Supramolecular Order and Dynamics of Discotic Materials Studied by Solid-State NMR Recoupling Methods

Dissertation
zur Erlangung des Grades

”Doktor der Naturwissenschaften”

am Fachbereich Chemie und Pharmazie der
Johannes Gutenberg-Universität
in Mainz

Ingrid Fischbach
geboren in Mainz

Mainz 2003

Tag der mündlichen Prüfung: 17. Dezember 2003

Contents

Abbreviations and Acronyms

AHT	*a*verage *H*amiltonian *t*heory
BABA	*ba*ck-to-*ba*ck
CODEX	*c*enterband-*o*nly *d*etection *o*f *ex*change
CSA	*c*hemical *s*hift *a*nisotropy
CP	*c*ross-*p*olarization
CW	*c*ontinuous-*w*ave
DD	*d*ipolar *d*ecoupling
DF	*d*irector *f*rame
DMS	dimethylsulfone $(CH_3)_2SO_2$
DQ	*d*ouble-*q*uantum
DSC	*d*ifferential *s*canning *c*alorimetry
ERM	*e*volution *r*otor *m*odulation
FET	*f*ield *e*ffect *t*ransistor
FID	*f*ree *i*nduction *d*ecay
FT	*f*ourier *t*ransformation
FWHM	*f*ull *w*idth at *h*alf *m*aximum
HATNA	*h*exa*aza**t**rin**a*phthylene
HBC	hexa-*peri*-*h*exa*b*enzo*c*oronene
HDOR	*h*eteronuclear *d*ipolar *o*rder *r*otor-*e*ncoding
HETCOR	*h*eteronuclear *c*orrelation
HMQ	*h*eteronuclear *m*ultiple-*q*uantum
HSQC	*h*eteronuclear *s*ingle-*q*uantum *c*orrelation
IMR	*i*ntermediate *m*otional *r*egime
INEPT	*i*nsensitive *n*uclei *e*nhanced by *p*olarization *t*ransfer
LAB	*lab*oratory frame
LC	*l*iquid *c*rystal
LED	*l*ight *e*mitting *d*iode
MAS	*m*agic-*a*ngle *s*pinning
MF	*m*olecular *f*rame
MQ	*m*ultiple-*q*uantum
NMR	*n*uclear *m*agnetic *r*esonance
PAH	*p*olycyclic *a*romatic *h*ydrocarbon
PAS	*p*rincipal *a*xes *s*ystem
PE	*p*oly*e*thylene
POM	*p*olarized *o*ptical *m*icroscopy
REDOR	*r*otational *e*cho, *d*ouble *r*esonance
REREDOR	*r*otor *e*ncoded *r*otational *e*cho, *d*ouble *r*esonance

REPT	*r*ecoupled *p*olarization *t*ransfer
RF	*r*adio *f*requency
RRE	*r*econversion *r*otor *e*ncoding
RT	*r*oom *t*emperature
SAXS	*s*mall-*a*ngle *X*-ray *s*cattering
SB	*s*ide*b*and(s)
SLF	*s*eparated *l*ocal *f*ield
SQ	*s*ingle-*q*uantum
SUPER	*s*eparation of *u*ndistorted *p*owder patterns by *e*ffortless *r*ecoupling
TEDOR	*t*ransferred *e*cho, *d*ouble *r*esonance
TOSS	*to*tal *s*uppression of spinning *s*idebands
TPPI	*t*ime *p*roportional *p*hase *i*ncrementation
TPPM	*t*wo-*p*ulse *p*hase-*m*odulated
WAXS	*w*ide-*a*ngle *X*-ray *s*cattering

Chapter 1

Introduction

> *"Just as there is a field of molecular chemistry based on the covalent bond, there is a field of supramolecular chemistry, the chemistry of molecular assemblies and of the intermolecular bond."* Jean-Marie Lehn [Lehn 78]

Since the introduction of the term supramolecular chemistry in 1978 by Jean-Marie Lehn [Lehn 78], the field of supramolecular chemistry has developed into a rapidly growing, highly interdisciplinary field of science. Its aims are the controlled formation and characterization of supermolecules (i.e. well-defined, discrete oligonuclear species) and organized polymolecular systems, which are held together by non-covalent interactions, e.g. electrostatic interactions, hydrogen bonding and van der Waals forces [Lehn 95]. The increasing complexity of the systems rendered their characterization more and more demanding. A comprehensive analysis of structure and properties became only possible by the development of the powerful physical methods of today, particularly mass spectrometry, X-ray diffraction and nuclear-magnetic resonance (NMR) spectroscopy.

The aim of the work presented here is the characterization of structure, order and dynamics in discotic liquid crystals by means of solid-state NMR. Discotic liquid crystals consist of a flat, disc shaped (usually aromatic) core surrounded by long alkyl sidechains [Chandrasekhar 98]. Hence, they typically form supramolecular, columnar stacks which are isolated from each other by the long alkyl sidegroups. This particular packing arrangement leads to high one-dimensional charge carrier mobilities along the columns which can ultimately be thought of as 'molecular wires' [Boden 99b]. Therefore, discotic liquid crystals are of particular interest as conducting media in optoelectronic device applications, such as field effect transistors (FETs), light emitting diodes (LEDs) or photovoltaic cells (PVs). Naturally, precise knowledge of the supramolecular packing arrangements and the properties associated with certain packing arrangements is crucial for a well-directed materials design.

The principles of the solid-state NMR experiments utilized here have recently been introduced in order to unravel such structure-property relations [Brown 01]. Especially in amorphous systems, which cannot be fully characterized by scattering methods, solid-state NMR has proven to be valuable [Percec 02, Wind 02, Goward 03b]. Moreover, it offers numerous ways to study dynamic aspects over a large range of motional correlation times from around 10^{-10} s to 10^{1} s [Schmidt-Rohr 94].

The success of NMR is based on its high selectivity. The observed resonance frequencies are not only isotope specific but also influenced by local fields, in particular by the distribution of electron density around the investigated nucleus. A typical solid-state spectrum consists of severely broadened lines which arise from the various anisotropic interactions a nuclear spin is subject to, such as dipole-dipole couplings with other nuclear spins. These line-broadening effects are particularly severe in ^{1}H NMR experiments, where often no spectral resolution is observed at all. In solution- or liquid-state NMR, the anisotropic interactions are averaged to zero by fast molecular motion and, hence, narrow lines are observed. This situation is mimicked to some degree by the magic-angle spinning (MAS) technique [Andrew 58, Lowe 59], where the sample is rapidly rotated around an axis inclined at the magic angle $\theta_M = 54.7°$. This rapid sample rotation makes it possible to obtain high-resolution solid-state NMR spectra. Technically, the Hamiltonians describing the anisotropic parts of the respective interactions consists of two terms, one modulated by the rotor frequency (ω_R) and the other modulated by twice the rotor frequency ($2\omega_R$). Over a full rotor period the contributions from both terms vanish. Thus, sufficiently fast MAS ensures averaging of the anisotropic interactions which are responsible for severe line broadening in static spectra and narrow lines result. However, this line narrowing comes at the price of the loss of the information which is inherent to these anisotropic interactions, e.g. the distance between two dipolar coupled spins. To overcome this problem, pulse sequences were developed, which selectively recouple the interaction of interest and, thereby, make the desired information available. After a general overview of the underlying theoretical concepts of solid-state NMR in **chapter 2**, **chapter 3** reviews the recoupling MAS experiments used in this thesis. The described sequences are based on recoupling the ω_R-modulated term of the respective interaction Hamiltonian under MAS. Naturally, it is also possible to recouple the $2\omega_R$-modulated term of an interaction Hamiltonian, which exhibits a different orientation dependence. Thereby, complementary information on orientation effects is provided and, hence, orientation effects can more accurately be quantified. This approach was first introduced by Glaubitz et al. [Glaubitz 01] and is applied in **chapter 4** to the sequences described in **chapter 3**. There, also several oriented systems are investigated exemplary. The advantage of this approach as compared to other established ones such as deuteron NMR (which is better as to its quantitativety) is that only small amounts of sample (around 10 mg) and no isotopic enrichment are required. Hence, quick analysis of as-synthesized materials becomes feasible. The knowledge of the influence of macroscopic sample orientation on the outcome of MAS recoupling experiments is of particular interest in samples which can easily be oriented, such as the discotic liquid crystals investigated in the

following chapters.

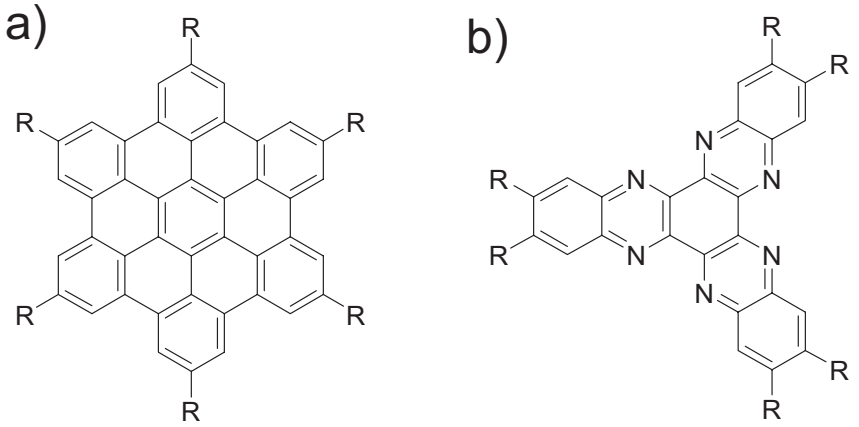

Figure 1.1: *Core structure of substituted HBC derivatives (a) and HATNA derivatives (b).*

In **chapters 5** and **6** the results of the investigation of derivatives of hexa-*peri*-hexabenzocoronene (HBC) are presented, whose general chemical structure is depicted in Fig. 1.1 a. Alkyl- or phenyl-alkyl-substituted HBCs form thermotropic liquid crystalline mesophases over exceptionally broad temperature ranges (up to 250 °C phase width). These systems are of particular interest in materials science, since they combine good processability and favorable physical and optoelectronical properties, in particular very high one-dimensional charge carrier mobilities up to 1.13 $cm^2V^{-1}s^{-1}$ [Craats 99]. Hence, they are envisaged as hole-conducting media in device applications, such as field effect transistors or photovoltaic cells. A hexaphenyl-substituted HBC (HBC-PhC_{12} [Fechtenkötter 99]) could already be successfully implemented in a photovoltaic device as an active medium for charge transport [Schmidt-Mende 01].

Since the synthesis of the first alkyl-substituted HBC reported in 1996 by Herwig [Herwig 96], a broad variety of HBCs has been synthesized, ranging from various symmetric compounds with six identical substituents [Fechtenkötter 99, Fechtenkötter 01b] over asymmetrically substituted HBCs [Ito 00b] to HBC dimers [Ito 00a] or polymers incorporating HBCs [Thünemann 99, Thünemann 00]. Interestingly, even slight changes in the substitution pattern were found to lead to tremendous changes in phase behavior, molecular packing arrangement and charge-carrier mobility. In **chapter 5** the influence of branched sidechains, as opposed to linear ones, is investigated in hexa-substituted HBCs. **Chapter 6** presents results from investigations on functionalized HBCs, where mainly the effects of hydrogen bonding and dimer formation are analyzed.

HBCs are hole carrying materials, but for device applications obviously electron carrying media are needed, too. Among discotic liquid crystals, substituted derivatives of hexaazatrinaphthylene (HATNA, Fig. 1.1 b) are of particular interest as potential electron carriers. In **chapter 7** the detailed investigation of the alkylsulfanyl-substituted HATNA-SC_{12} is de-

scribed.

Thus, **chapters 5 - 7** present solid-state NMR studies of new columnar liquid crystalline materials which are of current interest for optoelectronic device production, while the NMR experiments applied to these materials contain new recoupling schemes which make the desired information on molecular orientation and dynamics accessible.

Chapter 2

General Theoretical Background

In 1946 Bloch and Purcell [Bloch 46, Purcell 46] reported the first experimental evidence of nuclear magnetic resonance (NMR), a discovery, for which they were awarded the nobel prize in physics in 1952. Nuclear magnetic resonance occurs in strong external magnetic fields, when the magnetic moment of an atom's nuclear spin ($I \neq 0$) interacts with radio frequency fields (typical frequencies between 30-900 MHz). Since the magnetic moment of a nuclear spin is specific for each isotope, NMR is a very selective method. The observed resonance frequencies are influenced by local fields, particularly in a very sensitive fashion by the chemical surrounding of the investigated nucleus. Hence, today NMR is an indispensable analytical tool for structural characterization of liquids, compounds in solution, solids and even 'soft matter' materials like proteins, liquid crystals or other supramolecular systems [Breitmaier 93, Cavanagh 96, Evans 95, Emsley 85, Brown 01, Percec 02]. The successful development of NMR was only possible by changing the way of performing NMR experiments entirely. The initially used continuous-wave (CW) methods were replaced by Fourier transform (FT) techniques employing pulsing schemes prior to detection, which made the development of a great variety of NMR experiments including two- or multi-dimensional spectroscopy and multiple-quantum methods possible. In solid-state NMR it was in particular the introduction of the magic-angle spinning (MAS) technique, where the sample is rapidly rotated around an axis inclined at the magic-angle $\theta_M = 54.7°$, which made it possible to obtain high-resolution spectra.

The mathematical formalism of describing the effect of multipulse sequences under MAS on the spin system is well-developed and covered in most standard text books [Abragam 61, Slichter 96, Mehring 83]. In this chapter, a general overview of the underlying theoretical concepts will be provided, as well as a description of some basic solid-state NMR experiments.

2.1 NMR Interactions

In NMR, information is gathered from the strength of the various interactions a nuclear spin experiences. In the quantum mechanical formalism NMR interactions are described by the corresponding Hamilton operators. Solving the Schrödinger equation $\hat{\boldsymbol{H}}\psi = E\psi$ yields the energy levels and the corresponding resonance frequencies. The most important interactions are (ordered roughly from strongest to weakest) the ZEEMAN-interaction, the quadrupolar coupling, the interaction with radio frequency pulses, the chemical shift, the dipole-dipole coupling and the indirect spin-spin or J-coupling:

$$\hat{\boldsymbol{H}} = \hat{\boldsymbol{H}}_z + \hat{\boldsymbol{H}}_Q + \hat{\boldsymbol{H}}_{RF} + \hat{\boldsymbol{H}}_{CS} + \hat{\boldsymbol{H}}_D + \hat{\boldsymbol{H}}_J \tag{2.1}$$

In contrast to solution NMR or high-resolution magic-angle spinning NMR (HRMAS), the J-coupling, $\hat{\boldsymbol{H}}_J$, is in solid-state NMR usually negligible and will, therefore, not be discussed further in this thesis. The various NMR interactions are generally anisotropic, i.e. exhibit an orientation dependence with respect to the external static magnetic field, $\underline{\mathbf{B}_0}$. Thus, the spatial part of an interaction Hamiltonian is most conveniently expressed as a second rank tensor. In a general form, the complete Hamiltonian of an interaction can be represented as a bilinear product [Mehring 83]

$$\hat{\boldsymbol{H}} = \underline{\hat{\mathbf{I}}} \cdot \underline{\underline{\mathbf{A}}} \cdot \underline{\hat{\mathbf{S}}} = \begin{pmatrix} \hat{I}_x & \hat{I}_y & \hat{I}_z \end{pmatrix} \begin{pmatrix} A_{xx} & A_{xy} & A_{xz} \\ A_{yx} & A_{yy} & A_{yz} \\ A_{zx} & A_{zy} & A_{zz} \end{pmatrix} \begin{pmatrix} \hat{S}_x \\ \hat{S}_y \\ \hat{S}_z \end{pmatrix} \tag{2.2}$$

with the tensor $\underline{\underline{\mathbf{A}}}$ describing the space part. $\underline{\hat{\mathbf{I}}}$ and $\underline{\hat{\mathbf{S}}}$ are vector operators, which can be spin angular momentum operators of like or unlike spins (homonuclear and heteronuclear dipole-dipole coupling), of the same spin (quadrupolar coupling), or one of them can represent the cartesian vector of the magnetic field, $\underline{\mathbf{B}_0}$, (chemical shift interaction). The cartesian tensor of the space part can always be decomposed into three contributions

$$\underline{\underline{\mathbf{A}}} = a \cdot \mathbb{1} + \begin{pmatrix} 0 & b & c \\ -b & 0 & d \\ -c & -d & 0 \end{pmatrix} + \begin{pmatrix} e & g & h \\ g & f & i \\ h & i & -e-f \end{pmatrix} \tag{2.3}$$

The first term denotes the isotropic part *a*, which equals a third of the trace, $a = \frac{1}{3}\mathbf{Tr}\{A_{\alpha\beta}\}$, of the cartesian tensor. The second term is traceless and antisymmetric (3 components) and the third term is traceless and symmetric (5 components).
An alternative common representation for interaction tensors is the irreducible spherical representation, which is advantageous due to the favorable transformation behavior of spherical

tensor components. The latter transform identically to the spherical harmonics $Y_{L,m}$ with a multiplicity of *2L+1* and values for *m* ranging in integer steps from *-L...+L*. This greatly simplifies the mathematical description of rotations (which are inevitable in the description of most solid-state NMR experiments), since instead of costly matrix multiplications just linear combinations among the components need to be formed. The irreducible spherical tensor representation of $\underline{\underline{\mathbf{A}}}$ consists of a scalar, $\mathbf{A_0}$, a vector of dimension 3, $\underline{\mathbf{A}}_1$, and a vector of dimension 5, $\underline{\mathbf{A}}_2$. In spherical tensor representation Eq. (2.2) reads as

$$\hat{\boldsymbol{H}} = \hat{\underline{\mathbf{I}}} \cdot \underline{\underline{\mathbf{A}}} \cdot \hat{\underline{\mathbf{S}}} = \sum_{k=0}^{2} \sum_{q=-k}^{k} (-1)^q A_{kq} \hat{T}_{k-q} \tag{2.4}$$

where the $\hat{T}_{k-q}$ are irreducible spherical spin tensor operators of rank *k* and order *-q*. The relations for the transformation between the Cartesian and spherical representations of tensors are summarized in Appendix A. Another great simplification of the mathematical description arises from the fact that rotations in real space affect only the space part, given by the A_{kq}, whereas rotations in spin space (as caused by radio frequency pulses) affect only the spin part, given by the $\hat{T}_{k-q}$, of the interaction Hamiltonian. In the following sections the various interactions as listed in Eq. (2.1) will be discussed in detail.

2.1.1 ZEEMAN-Interaction

The by far strongest interaction in all experiments carried out in this thesis is the ZEEMAN interaction, which is the interaction of a nuclear spin ($I \neq 0$) with an external static magnetic field, $\underline{\mathbf{B}}_0$. The ZEEMAN interaction causes a splitting of the degenerated (2I+1) energy levels, which are defined by the magnetic nuclear spin quantum number m_I= -I, -I+1, ... +I. If the external magnetic field is oriented along the z-axis, only the z-component of the corresponding Hamiltonian deviates from zero:

$$\hat{H}_z = -\gamma \hbar B_0 \hat{I}_z \tag{2.5}$$

The energies of the levels are given by

$$E_m = -m \hbar \gamma B_0. \tag{2.6}$$

In the case of a spin-$\frac{1}{2}$-nucleus the energy splitting between the two levels is $\Delta E = \hbar \omega_L = -\gamma \hbar B_0$. ω_L is the so-called LARMOR frequency and amounts to roughly 300 MHz for protons in a magnetic field of 7 T strength. In the case of a strong external magnetic field B_0 the ZEEMAN interaction by far exceeds the other interactions listed in Eq. (2.1), i.e. $\|H_0\| \gg \|H_{int}\|$.

These other interactions are commonly referred to as internal or local, since they depend on the local surroundings of a nucleus- in contrast to the ZEEMAN interaction. Therefore, the internal interactions bear the important information on the local environment of a nucleus. The Hamiltonians of the internal interactions can be splitted in two parts, the *secular* part $\hat{\boldsymbol{H}}'_{int}$, which commutes with $\hat{\boldsymbol{H}}_0$, and the non-*secular* part $\hat{\boldsymbol{H}}''_{int}$, which does not commute with $\hat{\boldsymbol{H}}_0$. In first approximation only the $\hat{\boldsymbol{H}}'_{int}$ contribute to the observed spectrum. This is the *secular*- or high-field approximation, which is valid in all cases of interest here. Typical examples for the break down of the *secular* approximation are quadrupolar nuclei with very strong quadrupolar couplings, which can even exceed the ZEEMAN interaction. In spherical tensor representation, the *secular* part of an internal interaction reads as

$$\hat{\boldsymbol{H}}'_{int} = A_{00}\hat{T}_{00} + A_{10}\hat{T}_{10} + A_{20}\hat{T}_{20}, \tag{2.7}$$

All other terms from Eq. (2.4) vanish, since they do not commute with $\hat{H}_0$. Vividly spoken, the *secular* approximation is valid, since in the rotating frame the frequency of the ZEEMAN interaction is much higher than those of the other interactions, which, therefore, can be considered as time-independent within the rotating frame. Thus, only the parts commuting with $\hat{H}_0$ need to be considered.

2.1.2 Quadrupolar Coupling

Nuclei with a spin $I \geq 1$ exhibit a nuclear electric quadrupole moment, which interacts with the local electric field gradient in the molecule. The Hamiltonian for the quadrupolar coupling is

$$\hat{\boldsymbol{H}}_Q = \hat{\underline{\mathbf{I}}} \cdot \underline{\underline{\mathbf{Q}}} \cdot \hat{\underline{\mathbf{I}}} \ , \tag{2.8}$$

with $\underline{\underline{\mathbf{Q}}}$ being the quadrupolar interaction tensor, which is given by

$$\underline{\underline{\mathbf{Q}}} = \frac{e \cdot Q}{2I(2I-1)\hbar} \cdot \underline{\underline{\mathbf{V}}}. \tag{2.9}$$

$\underline{\underline{\mathbf{V}}}$ is the local electric field gradient tensor. For deuterons (I = 1) the quadrupolar splitting is around 125 kHz, which is sufficiently lower than the LARMOR frequency so that the *secular* approximation (which is a first-order perturbation approach) remains valid. Thus, deuteron NMR spectra are dominated by the quadrupolar interaction, which is strongly orientation dependent with

$$\omega_Q = \pm\frac{\delta_Q}{2}(3\cos^2\theta - 1 - \eta_Q \sin^2\theta \cos 2\phi), \tag{2.10}$$

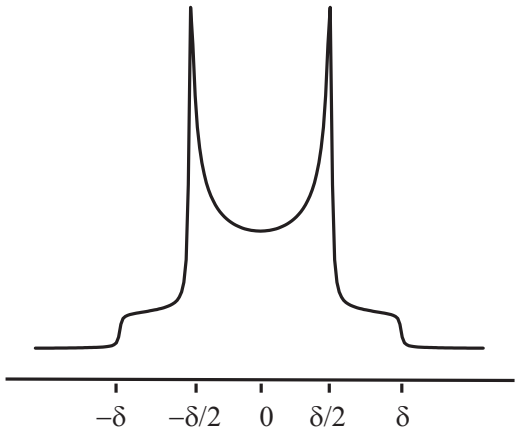

Figure 2.1: *Static* PAKE*-pattern for the* ^2H *quadrupolar coupling.*

where θ and ϕ are the polar coordinates of the B_0-field in the PAS of the quadrupole interaction tensor. In solids, where fast motions are absent, the orientation dependence of the quadrupolar coupling leads to the well-known PAKE-pattern for isotropic orientation distributions as it is shown in Fig. 2.1 [Pake 48]. Molecular motion leads to a characteristic narrowing of the PAKE-pattern. This is commonly utilized in ^{2}H NMR spectroscopy, where a line shape analysis of the motionally averaged pattern yields information on the geometry and the timescale of a dynamical process.

2.1.3 Chemical Shift

The chemical shift is the most important NMR interaction in terms of structure determination. Solution NMR experiments that are routinely carried out in organic synthesis for product structure determination or purity tests are based on the fact that different chemical surroundings of a nucleus usually lead to different resonance positions in the spectrum. The chemical shift is caused by the electrons surrounding a nucleus, which shield the external magnetic field in such a way that the nucleus experiences a smaller effective field $\underline{\mathbf{B}}_{eff} = \underline{\mathbf{B}}_0 - \underline{\underline{\sigma}} \cdot \underline{\mathbf{B}}_0$. This shielding is in general anisotropic and depends on the number of electrons and, as already pointed out above, on the chemical surrounding of the nucleus. In the *secular* approximation the chemical shift Hamiltonian is given by

$$\hat{\boldsymbol{H}}_{CS} = \gamma \hat{\underline{\mathbf{I}}} \cdot \underline{\underline{\sigma}} \cdot \underline{\mathbf{B}_0} = \gamma(\hat{I}_x\sigma_{xz} + \hat{I}_y\sigma_{yz} + \hat{I}_z\sigma_{zz})B_0, \tag{2.11}$$

where $\underline{\underline{\sigma}}$ is the chemical shift tensor and $\underline{\mathbf{B}_0} = \begin{pmatrix} 0 & 0 & B_0 \end{pmatrix}$ the external magnetic field. Following Eq. (2.3) the chemical shift tensor $\underline{\underline{\sigma}}$ can be decomposed into an isotropic, a symmetric and an antisymmetric part. The antisymmetric part σ_{asy} can be neglected within the

secular approximation. The symmetric part σ_{sy} can always be diagonalized, which equals to a transformation into its principal axis system (PAS). In the PAS $\underline{\underline{\sigma}}$ reads as

$$\underline{\underline{\sigma}} = \sigma_{iso} + \delta_{CS} \begin{pmatrix} -\frac{1+\eta_{CS}}{2} & 0 & 0 \\ 0 & -\frac{1-\eta_{CS}}{2} & 0 \\ 0 & 0 & 1 \end{pmatrix}. \tag{2.12}$$

δ_{CS} is the so-called anisotropy parameter and η_{CS} the so-called asymmetry parameter, given by

$$\delta_{CS} = \omega_L(\sigma_{zz}^{PAS} - \sigma_{iso}) \quad \text{and} \quad \eta_{CS} = \frac{\sigma_{yy}^{PAS} - \sigma_{xx}^{PAS}}{\sigma_{zz}^{PAS} - \sigma_{iso}}. \tag{2.13}$$

The isotropic part σ_{iso} is orientation independent and is commonly given in ppm of the LARMOR frequency of the corresponding nucleus. It should be noted that the chemical shift has to be referenced using calibration compounds with known isotropic shifts. If ν_{ref} is the resonance frequency of the reference compound and ν the resonance frequency of the resonance of interest, the chemical shift δ in ppm is defined as

$$\delta\,[ppm] = \frac{\nu - \nu_{ref}}{\nu_{ref}} \cdot 10^6. \tag{2.14}$$

The great advantage of the ppm-scale is its independence on the strength of the external magnetic field B_0, which greatly simplifies comparison between spectra measured at different spectrometers. The symmetric part of the chemical shielding tensor σ_{sy} is commonly referred to as *c*hemical *s*hift *a*nisotropy, CSA. In liquids and solutions, the CSA is averaged to zero by fast isotropic molecular motions. However, in solids, where fast isotropic motions are absent, the orientation dependence of the CSA generally leads to a significant broadening of the resonance lines. If θ and ϕ are the polar coordinates of the B_0-field in the PAS of the chemical shielding tensor, the anisotropic frequency of a spin is in analogy to Eq. (2.10) given by

$$\omega_{CS} = \frac{\delta_{CS}}{2}(3\cos^2\theta - 1 - \eta_{CS}\sin^2\theta\cos 2\phi). \tag{2.15}$$

For isotropic orientation distributions, a typical spectrum is shown in Fig. 2.2. The theoretical powder line shape has been calculated in general by [Bloembergen 53]. This derivation can also be found in most solid-state NMR textbooks, like [Mehring 83, Schmidt-Rohr 94]. The principal values of the CSA tensor can easily be identified in the spectra as the points of discontinuity as is indicated in Fig. 2.2. The assignment of the principal values follows the Spiess-convention [Spiess 78]: $|\sigma_{11}| \geq |\sigma_{22}| \geq |\sigma_{33}|$ with $|\sigma_{11}| = |\sigma_{xx}^{PAS} - \sigma_{iso}|$, $|\sigma_{22}| = |\sigma_{yy}^{PAS} - \sigma_{iso}|$ and $|\sigma_{33}| = |\sigma_{zz}^{PAS} - \sigma_{iso}|$. The advantage of this convention is that $0 \leq \eta \leq 1$, where $\eta = 0$ for an uniaxial tensor.

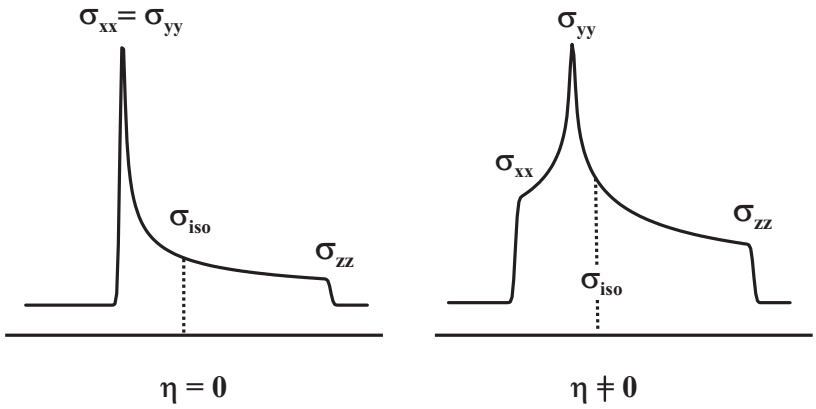

Figure 2.2: *Theoretical line shapes for isotropic samples for a symmetric CSA tensor (left) and an asymmetric CSA tensor (right). The principal values can easily be identified as the points of discontinuity in the pattern.*

2.1.4 Dipole-Dipole Coupling

Spins exhibit magnetic dipole moments, which are essentially proportional to the expectation value of their spin angular momentum, $\mu_i \sim \gamma_i \langle m | \hat{\boldsymbol{I}} | m \rangle$. A dipole moment creates a local magnetic field, with which the dipole moments of adjacent spins can interact. In the *secular* approximation the Hamiltonian for a homonuclear spin-pair $\mathbf{I}, \mathbf{J}$ reads as

$$\hat{\boldsymbol{H}}^{IJ}_{D,homo} = -\frac{\mu_0 \hbar \gamma^2}{4\pi r^3} \cdot \frac{1}{2}(3\cos^2\theta - 1)(3\hat{I}_z\hat{J}_z - \hat{\underline{\mathbf{I}}} \cdot \hat{\underline{\mathbf{J}}}). \tag{2.16}$$

The dipole-dipole coupling depends on the internuclear distance *r* and the angle θ between the internuclear axis and the B_0 field. In the heteronuclear case, i.e. the dipole-dipole coupling of two different spins $\mathbf{I}$ and $\mathbf{S}$ with vastly different LARMOR frequencies, the Hamiltonian is further truncated (so-called second averaging). It is given by

$$\hat{\boldsymbol{H}}^{IS}_{D,hetero} = -\frac{\mu_0 \hbar \gamma_I \gamma_S}{4\pi r^3} \cdot \frac{1}{2}(3\cos^2\theta - 1)2\hat{I}_z\hat{S}_z. \tag{2.17}$$

In the bilinear product representation,

$$\hat{\boldsymbol{H}}^{ij}_{D} = \hat{\underline{\mathbf{I}}} \cdot \underline{\underline{\mathbf{D}}} \cdot \hat{\underline{\mathbf{J}}}, \tag{2.18}$$

the corresponding dipole-dipole coupling tensor is traceless and symmetric. In its principal axis system, we can write

$$\underline{\underline{\mathbf{D}}}_{ij}^{PAS} = -2D_{ij} \begin{pmatrix} -\frac{1}{2} & 0 & 0 \\ 0 & -\frac{1}{2} & 0 \\ 0 & 0 & 1 \end{pmatrix}, \tag{2.19}$$

with the dipole-dipole coupling constant

$$D_{ij} = \frac{\mu_0 \hbar \gamma_i \gamma_j}{4\pi r_{ij}^3} \tag{2.20}$$

in units of angular frequency. The dipole-dipole coupling constant strongly depends ($\propto r^{-3}$) on the distance of the dipolar coupled nuclei. For protons with an internuclear distance of r = 1$\mathring{A}$ the dipole-dipole coupling is $\approx$ 122 kHz, whereas for a ^{1}H -^{13}C spin pair with an internuclear distance of r = 1$\mathring{A}$ the dipole-dipole coupling is due to the lower γ_{13C} only $\approx$ 31 kHz. From this it is clear that the dipole-dipole coupling dominates the shape of static ^{1}H solid-state spectra. However, in liquids or solutions dipole-dipole couplings are usually completely averaged to zero by fast molecular motion. Therefore, in solution NMR dipole-dipole couplings play a minor role. The distance dependence of the dipole-dipole coupling constant allows for a very precise determination of interatomic distances by measuring the dipole-dipole coupling constant. This is of particular interest for measuring distances in non-crystalline solids or distances to protons, where other methods like X-ray scattering cannot readily be used. Furthermore, due to the orientation dependence of the dipole-dipole coupling molecular motions on a timescale $> 10^4$ s^{-1} lead to a characteristic reduction of the dipole-dipole coupling constant. Thus, information on the geometry of molecular dynamics can be gained from the degree of reduction of the dipole-dipole coupling constant.

2.2 Density Operator and LIOUVILLE-VON-NEUMANN Equation

In a NMR experiment, the macroscopic magnetization resulting from an ensemble average over the individual spins in measured. The description of such a huge ensemble requires the introduction of a statistical operator, the density operator $\hat{\boldsymbol{\rho}}$. The density operator can be represented by the so-called density matrix, with the matrix elements given by

$$\hat{\rho}_{ij}(t) = \langle\, i \big| \hat{\boldsymbol{\rho}}(t) \big| j \,\rangle = \overline{c_i^*(t) c_j(t)}. \tag{2.21}$$

$\big|i\,\rangle$ denote the eigenstates of the nuclear spin Hamiltonian $\hat{\boldsymbol{H}}$. Since the density matrix is hermitian, the corresponding eigenvalues are real. The diagonal elements ρ_{ii} give the probability of the spin system occupying the state $\big|i\,\rangle$. The off-diagonal elements are the complex amplitudes of coherent superpositions of eigenstates, averaged over the ensemble. Depending on the corresponding change in the magnetic quantum number, these coherences are either transverse modes of magnetization (± 1) or multiple-quantum coherences.
The ensemble-averaged expectation value of an observable A described by the operator $\hat{\boldsymbol{A}}$ is given by

$$\langle \hat{\boldsymbol{A}} \rangle = \mathbf{Tr}\{\hat{\boldsymbol{\rho}} \cdot \hat{\boldsymbol{A}}\}. \tag{2.22}$$

The time-evolution of $\hat{\boldsymbol{\rho}}$ is described by the LIOUVILLE-VON-NEUMANN equation

$$\frac{\partial \hat{\boldsymbol{\rho}}}{\partial t} = -i[\hat{\boldsymbol{H}}, \hat{\boldsymbol{\rho}}(t)]. \tag{2.23}$$

The general solution of eq.(2.23) is

$$\hat{\boldsymbol{\rho}}(t) = \hat{U}(t) \hat{\boldsymbol{\rho}}(0) \hat{U}^{-1}(t). \tag{2.24}$$

$\hat{U}$ ist a so-called propagator. If $\hat{\boldsymbol{H}}$ is time independent, i.e. $\hat{U} = e^{-i\hat{\boldsymbol{H}}t}$, the solution of the LIOUVILLE-VON-NEUMANN equation simplifies to

$$\hat{\boldsymbol{\rho}}(t) = e^{(-i\hat{\boldsymbol{H}}t)} \hat{\boldsymbol{\rho}}_0 e^{(i\hat{\boldsymbol{H}}t)}. \tag{2.25}$$

Further simplification arises, if the components of the time independent Hamiltonian commute, since then the propagator $\hat{U} = exp\{-i(\hat{\boldsymbol{H}}_1 + \hat{\boldsymbol{H}}_2 + ... + \hat{\boldsymbol{H}}_N)t\}$ can be factorized: $\hat{U} = exp\{-i\hat{\boldsymbol{H}}_1 t\} exp\{-i\hat{\boldsymbol{H}}_2 t\} ... exp\{-i\hat{\boldsymbol{H}}_N t\}$. This complies with a separate calculation of the different contributions. In Eq. (2.25), a known starting point, $\hat{\boldsymbol{\rho}}_0$, has been assumed for

the evolution of the density matrix. For a spin ensemble in thermal equilibrium, i.e. $\frac{d\hat{\rho}}{dt} = 0$, this initial state is given by a BOLTZMANN distribution of the individual spins among the energy levels of the system. The spin system can then be described by [Abragam 61]:

$$\hat{\boldsymbol{\rho}}_B = \frac{exp(-\frac{\hbar \hat{\boldsymbol{H}}}{kT})}{\mathbf{Tr}\{exp(-\frac{\hbar \hat{\boldsymbol{H}}}{kT})\}} \tag{2.26}$$

Within the *secular* approximation only the contribution from the ZEEMAN interaction $\hat{\boldsymbol{H}}_z = -\gamma B_0 \hat{I}_z$ is taken into account, leaving the density matrix as

$$\hat{\boldsymbol{\rho}}_B = \frac{exp(-\frac{\gamma \hbar B_0 \hat{I}_z}{kT})}{\mathbf{Tr}\{exp(-\frac{\gamma \hbar B_0 \hat{I}_z}{kT})\}} \tag{2.27}$$

After TAYLOR expansion and truncation to terms of first order (feasible for $T > 1K$ and moderate B_0 fields) and assuming constant energy $E = \mathbf{Tr}\{\hat{\boldsymbol{\rho}}\hat{\boldsymbol{H}}\}$, the equilibrium density matrix is finally obtained as

$$\hat{\boldsymbol{\rho}}_{eq} \sim \hat{\mathbb{1}} + \frac{\gamma \hbar B_0}{kT} \hat{I}_z \tag{2.28}$$

The unity operator, $\hat{\mathbb{1}}$, does not evolve in time, since it commutes with any other operator describing internal interactions and can therefore be neglected. Thus, the initial equilibrium state in a static magnetic field oriented along the z-axis is given by a sum of the individual z-angular momentum operators, with relative weights determined by the different LARMOR frequencies. In the following the equilibrium state will be briefly described with $\hat{I}_z$.

2.3 The Effect of Radio Frequency Pulses

One of the reasons for the great success of Fourier-transformation (FT) NMR spectroscopy lies in the fact, that radio frequency (RF) pulses affect the spin system in a well-defined manner, which in turn allows for a defined manipulation of the system. The radio frequency corresponds to the transition frequency between the ZEEMAN energy levels. For the description of pulsed NMR, a transition into a rotating frame of reference, which rotates with the *Larmor* frequency ω_L around $\underline{\mathbf{B}}_0$, is convenient. A $\underline{\mathbf{B}}_1$ field oscillating with ω_L, which is applied perpendicular to the $\underline{\mathbf{B}}_0$ field, is static in the rotating frame. The applied $\underline{\mathbf{B}}_1$ field makes the spins precess around the $\underline{\mathbf{B}}_1$ direction. Hence, in the rotating frame, the effect of a pulse of the length t is a rotation of the initial z-magnetization in the xy-plane by an angle $\alpha = \omega_1(t) \cdot t = -\gamma B_1(t) \cdot t$. Consequently, the effect of a so-called 90° pulse applied along y is a flip of the magnetization from the z-axis on the x-axis as is depicted in Fig. 2.3[1].
Generally, the effect of radio frequency pulses on the spin system is calculated with the density matrix formalism. With the Hamilton operator of a +y pulse given by $\hat{\boldsymbol{H}} \sim \hat{I}_y\alpha$, the corresponding propagator is $\hat{U} = exp(-i\alpha\hat{I}_y)$. According to Eq. (2.25), the time evolution of the equilibrium density matrix $\hat{\boldsymbol{\rho}}_{eq} \sim \hat{I}_z$ during such a pulse is given by

$$\rho(t) \sim exp(-i\alpha\hat{I}_y)\hat{I}_z exp(i\alpha\hat{I}_y), \tag{2.29}$$

which is clearly describing a rotation in spin space. At this point, it is convenient to introduce the so-called product operator formalism, which was introduced by Ernst and co-workers [Sørensen 83]. The product operator formalism is based on the fact that propagators of the general form $\hat{U}(t)\hat{\boldsymbol{\rho}}(0)\hat{U}^{-1}(t)$ are describing rotations in spin space. More precisely spoken, the propagators are rotations in three-dimensional sub-spaces of the 'Liouville'-space, which are defined by the corresponding interactions. The effect of such rotations is given by simple equations like

$$\hat{I}_z \xrightarrow{\alpha\hat{I}_y} \hat{I}_z \cos\alpha + \hat{I}_x \sin\alpha \tag{2.30}$$

for the description of the effect of a radio frequency pulse. The most common rotations are listed in table 2.1. The product operator formalism is not restricted to the description of the

[1] It should be noted, that the direction of the flip (to +x or -x) can in principle be chosen arbitrarily, since the convention for the sense of the rotation of the RF-pulse does not change anything about the physical action of the $\underline{\mathbf{B}}_1$ field. However, once chosen, the flip direction must be consequently retained when describing a NMR experiment. In the right-handed, mathematically positive, convention a 90° y pulse rotates the magnetization from the +z direction into the +x direction. In the left-handed, "physical" convention the magnetization is rotated into the other, the -x direction. In this thesis the flip direction will throughoutly be given by the "right-hand-rule" (see also Fig. 2.3).

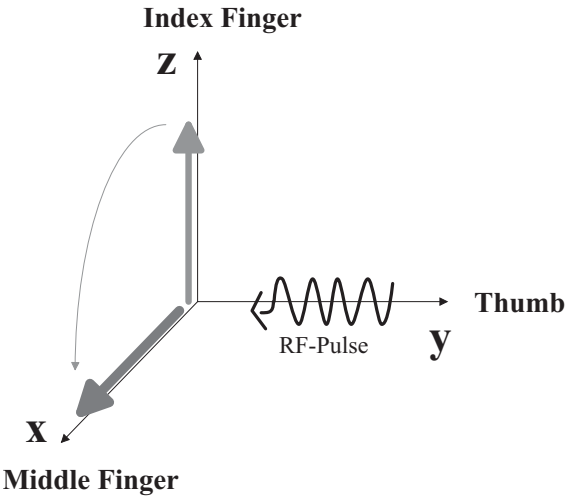

Figure 2.3: *The effect of a 90° y pulse on the initial equilibrium state $\hat{I}_z$ can within the rotating frame be seen as a rotation by the angle 90°. The rotation direction is by the convention used throughout this thesis given by the 'right-hand-rule': If the thumb is pointing at the direction of the RF-pulse and the index finger is pointing at the direction of the initial magnetization, the middle finger points at the direction of the magnetization after the pulse.*

Table 2.1: *The effect of $\hat{U}\hat{I}_\beta\hat{U}^{-1}$ for various $\hat{U}$ and for β=x,y,z.*

$\hat{U}$	$\hat{I}_x$	$\hat{I}_y$	$\hat{I}_z$
$e^{-i\alpha\hat{I}_x}$	$\hat{I}_x$	$\hat{I}_y\cos\alpha + \hat{I}_z\sin\alpha$	$\hat{I}_z\cos\alpha - \hat{I}_y\sin\alpha$
$e^{-i\alpha\hat{I}_y}$	$\hat{I}_x\cos\alpha - \hat{I}_z\sin\alpha$	$\hat{I}_y$	$\hat{I}_z\cos\alpha + \hat{I}_x\sin\alpha$
$e^{-i\alpha\hat{I}_z}$	$\hat{I}_x\cos\alpha + \hat{I}_y\sin\alpha$	$\hat{I}_y\cos\alpha - \hat{I}_x\sin\alpha$	$\hat{I}_z$

effect of RF-pulses. Rather, the time evolution under most NMR interactions can conveniently be described provided that the corresponding Hamiltonian is time independent or time averaged.

2.4 Magic-Angle Spinning (MAS)

Manipulation of spin interactions can not only be achieved by irradiation with radio frequency pulses, which affect the spin part T_{kq} of an interaction Hamiltonian, but also by rotating the sample mechanically around an axis, which is tilted with respect to the external magnetic field B_0 by an angle θ. Naturally, the latter only affects the space part A_{kq} of an interaction Hamiltonian. If the angle θ between the rotor axis and the external magnetic field B_0 is the magic-angle, $\theta_M = 54.7°$, the anisotropic parts of interactions represented by second rank tensors can be averaged out, since they depend on the second Legendre polynomial $P(\theta) = \frac{1}{2}(3cos^2\theta - 1)$, which is zero for $\theta_M = 54.7°$. The benefit of this is that the lines, which are severely broadened by the anisotropic interactions, are significantly narrowed with the line being centered at the isotropic frequency. Sample rotation at the magic-angle is referred to as magic-angle spinning (MAS) and was introduced first by Andrew [Andrew 58] and Lowe [Lowe 59]. However, a complete averaging to zero of an anisotropic interaction λ is only achieved, when the sample is spun rapidly enough, i.e. for a spinning frequency $\omega_R \gg \omega_\lambda$. This is the main reason why considerable effort is taken to reach higher and higher frequencies. Today, MAS equipment with rotors of an outer diameter of 2.5 mm capable of spinning up to 35 kHz is commercially available. In the literature, up to 50 kHz spinning speed are reported [Ernst 01] and a recent conference contribution presented spectra measured even at 70 kHz spinning frequency [Samoson 03].
The theoretical description of MAS is most conveniently carried out in the irreducible tensor representation. As already described in section 2.1, the *secular* part of a second rank tensor interaction in the static case is given by Eq. (2.7). For the dipole-dipole coupling, the chemical shift anisotropy and the quadrupolar coupling, $A_{10}\hat{T}_{10} = 0$, and, thus, Eq. (2.7) simplifies to

$$\hat{\boldsymbol{H}}_\lambda = A_{00}\hat{T}_{00} + A_{20}\hat{T}_{20}. \tag{2.31}$$

magic-angle spinning introduces a time dependence of the space part A_{kq} of the interaction Hamiltonian. Since $\hat{\boldsymbol{H}}(t)$ is now time dependent, Eq. (2.25) is no longer a solution of the LIOUVILLE-VON-NEUMANN equation (Eq. (2.23)). However, as long as the time dependent $\hat{\boldsymbol{H}}(t)$ does not contain non-commuting contributions for a specific time t, the problem can be solved by applying average Hamiltonian theory (AHT). If the problem is cyclic, an average time-independent Hamiltonian is calculated for one cycle of the sequence. MAS is a cyclic problem with the cycle time t_c being one rotor period τ_R, so the average Hamiltonian $\bar{\hat{\boldsymbol{H}}}$ has to be calculated for one rotor period

$$\hat{\boldsymbol{U}}(t_c) = e^{-i\hat{\boldsymbol{H}}_1\tau_1}e^{-i\hat{\boldsymbol{H}}_2\tau_2}\ldots e^{-i\hat{\boldsymbol{H}}_n\tau_n} = e^{-i\bar{\hat{\boldsymbol{H}}}\tau_R} \tag{2.32}$$

Since the average Hamiltonian $\hat{\bar{\boldsymbol{H}}}$ is time-independent, it commutes with itself at arbitrary times, $[\hat{\bar{\boldsymbol{H}}}(t_1), \hat{\bar{\boldsymbol{H}}}(t_2)] = 0$, and, hence, the propagator for N rotor periods can be written as

$$\hat{U}(N\tau_R) = exp\{-i\hat{\bar{\boldsymbol{H}}}N\tau_R\}. \tag{2.33}$$

Unfortunately, $\hat{\bar{\boldsymbol{H}}}$ cannot be calculated as a simple sum $\Sigma\hat{\boldsymbol{H}}_i\tau_i/\tau_R$, because generally $[\hat{\boldsymbol{H}}_i, \hat{\boldsymbol{H}}_j] \neq 0$. In the case of MAS it is advantageous to expand the propagators with two non-commuting $\hat{\boldsymbol{H}}$ according to the BAKER-CAMPBELL-HAUSDORFF relation

$$e^{\hat{\boldsymbol{B}}}e^{\hat{\boldsymbol{A}}} = exp\left\{\hat{\boldsymbol{B}} + \hat{\boldsymbol{A}} + \tfrac{1}{2}[\hat{\boldsymbol{A}}, \hat{\boldsymbol{B}}] + \tfrac{1}{12}([\hat{\boldsymbol{B}}, [\hat{\boldsymbol{B}}, \hat{\boldsymbol{A}}]] + [[\hat{\boldsymbol{B}}, \hat{\boldsymbol{A}}], \hat{\boldsymbol{A}}]) + \ldots\right\}. \tag{2.34}$$

The resulting average Hamiltonian is most clearly written as sum of different orders

$$\hat{\bar{\boldsymbol{H}}} = \hat{\bar{\boldsymbol{H}}}^{(0)} + \hat{\bar{\boldsymbol{H}}}^{(1)} + \hat{\bar{\boldsymbol{H}}}^{(2)} + \ldots, \tag{2.35}$$

where the order i indicates the overall power of τ_R, and the number of nested commutators involved. The zeroth-order average Hamiltonian now reads as

$$\hat{\bar{\boldsymbol{H}}}^{(0)} = \frac{1}{\tau_R}\sum_i \hat{\boldsymbol{H}}_i\tau_i. \tag{2.36}$$

Since under MAS the $\hat{\boldsymbol{H}}_i$ are not constant during the time-interval τ_i, the problem can only be treated in the limit of $\tau_i \to 0$ and $n \to \infty$. Eq. (2.32) can then be used to calculate the zeroth-order average Hamiltonian, because the commutators $[\hat{\boldsymbol{H}}(t), \hat{\boldsymbol{H}}(t + \Delta t)]$ vanish for infinitely small time steps. Therefore, in the limit $\Delta t \to 0$ the full average Hamiltonian can again be written as a sum of integrals, which is known as the MAGNUS expansion. The first three terms of the MAGNUS expansion are

$$\hat{\bar{\boldsymbol{H}}}^{(0)} = \frac{1}{\tau_R}\int_0^{\tau_R} \mathrm{d}t\, \hat{\boldsymbol{H}}(t), \tag{2.37}$$

$$\hat{\bar{\boldsymbol{H}}}^{(1)} = -\frac{i}{2\tau_R}\int_0^{\tau_R} \mathrm{d}t_1 \int_0^{t_1} \mathrm{d}t_2 [\hat{\boldsymbol{H}}(t_1), \hat{\boldsymbol{H}}(t_2)], \tag{2.38}$$

$$\hat{\bar{\boldsymbol{H}}}^{(2)} = -\frac{1}{6\tau_R}\int_0^{\tau_R} \mathrm{d}t_1 \int_0^{t_1} \mathrm{d}t_2 \int_0^{t_2} \mathrm{d}t_3 \Big([\hat{\boldsymbol{H}}(t_1), [\hat{\boldsymbol{H}}(t_2), \hat{\boldsymbol{H}}(t_3)]] + [\hat{\boldsymbol{H}}(t_3), [\hat{\boldsymbol{H}}(t_2), \hat{\boldsymbol{H}}(t_1)]]\Big). \tag{2.39}$$

For inhomogeneous interactions the commutator $[\hat{\boldsymbol{H}}(t_1), \hat{\boldsymbol{H}}(t_2)]$ vanishes [Maricq 79]. Since CSA, quadrupolar coupling and dipole-dipole coupling of an isolated spin pair are inhomogeneous interactions, for those interactions the higher-order terms in the MAGNUS expansion vanish. Then, one is left with the zeroth-order average Hamiltonian

$$\hat{\bar{\boldsymbol{H}}}_{\lambda}^{(0)} = \frac{1}{t}\int_0^t \hat{\boldsymbol{H}}_{\lambda}(t)dt = \hat{T}_{00}A_{00}^{LAB} + \hat{T}_{20}\frac{1}{t}\int_0^t A_{20}^{LAB}(\omega_R t)dt, \tag{2.40}$$

which describes the evolution under an interaction λ and sample rotation for arbitrary times. The explicit calculation of the average Hamiltonian according to Eq. (2.40) requires the knowledge of the space part A_{20}^{LAB} in the laboratory frame. Since an interaction tensor is defined in its principal axis system (PAS), it is necessary to transform it to the laboratory frame (LAB). This generally involves three subsequent Euler angle transformations, first from the PAS to the molecular frame (MF), second from the molecular frame to the rotor frame (R) and finally from the rotor frame to the laboratory frame:

$$\text{PAS} \xrightarrow{(\alpha_{PC},\beta_{PC},\gamma_{PC})} \text{MF} \xrightarrow{(\alpha_{MF},\beta_{MF},\gamma_{MF})} \text{Rotor} \xrightarrow{(\omega_R t,\beta_M,0)} \text{LAB}$$

tensor orientation *powder average* *MAS*

The time dependence enters the picture only in the last step, where the Euler angle α_{RL} depends on the rotor position (rotor phase), $\alpha_{RL} = \omega_R t$. In the course of this sequential transformations, the irreducible tensor representation proves its usefulness, since the rotation of a tensor is simply given by a linear combination of components with the same rank L:

$$A_{Lm}^{Y} = \sum_{m'=-L}^{L} A_{Lm'}^{X}\, \mathcal{D}_{m'm}^{(L)}(\Omega), \tag{2.41}$$

where the $\mathcal{D}_{m'm}^{(L)}(\Omega)$ are elements of the Wigner rotation matrices

$$\mathcal{D}_{m'm}^{(L)}(\alpha,\beta,\gamma) = d_{m'm}^{(L)}(\beta)e^{-im'\alpha}e^{-im\gamma}, \tag{2.42}$$

with $d_{m'm}^{(L)}(\beta)$ as the reduced matrix elements, which are listed in appendix A. For the three subsequent rotations A_{20}^{LAB} is obtained as

$$A_{20}^{\lambda,LAB}(t) \;=\; \sum_{m=-2}^{2} A_{2-m}^{\lambda,R}\, e^{im\omega_R t}\, d_{-m0}^{(2)}(\beta_M) \tag{2.43}$$

$$= \sum_{m=-2}^{2} \left[\sum_{m'=-2}^{2} A_{2-m'}^{\lambda,MF} \mathcal{D}_{-m'-m}^{(2)}(\Omega_{MF}) \right] e^{im\omega_R t} d_{-m0}^{(2)}(\beta_M) \tag{2.44}$$

$$= \sum_{m=-2}^{2} \left[\sum_{m'=-2}^{2} \left[\sum_{m''=-2}^{2} A_{2-m''}^{\lambda,PAS} \mathcal{D}_{-m''-m'}^{(2)}(\Omega_{PC}) \right] \mathcal{D}_{-m'-m}^{(2)}(\Omega_{MF}) \right] \times e^{im\omega_R t} d_{-m0}^{(2)}(\beta_M). \tag{2.45}$$

The full treatment including all three transformations is only necessary if more than one interaction is considered. Otherwise, a direct transformation from the PAS to the rotor frame and subsequently to the laboratory frame is sufficient. Then, the $A_{20}^{LAB}(t)$ can be calculated starting with Eq. (2.44) setting $A_{20}^{\lambda,MF} = A_{20}^{\lambda,PAS}$. Inserting the obtained expression for $A_{20}^{\lambda,LAB}(t)$ in Eq. (2.40) yields after integration a general expression for the complete averaged interaction Hamiltonian of an interaction λ under MAS

$$\hat{\bar{\boldsymbol{H}}}_{\lambda,MAS} = \hat{T}_{00} A_{00}^{\lambda,LAB} + \hat{T}_{20} \frac{1}{t} \int_0^t A_{20}^{LAB}(\omega_R t) dt = \hat{T}_{00} A_{00}^{\lambda,LAB} + \hat{T}_{20} \cdot \frac{1}{t} \cdot \sqrt{\tfrac{3}{2}} \cdot \Phi_\lambda \tag{2.46}$$

The first term is zero for the dipole-dipole and quadrupolar interaction, since $A_{00}^{quad,LAB} = A_{00}^{dip,LAB} = 0$. The integrated phase Φ_λ is given by

$$\Phi_\lambda(t) = \frac{C_1}{\omega_R} \{\sin(\gamma + \omega_R t) - \sin\gamma\} + \frac{C_2}{2\omega_R} \{\sin(2\gamma + 2\omega_R t) - \sin 2\gamma\} - \frac{S_1}{\omega_R} \{\cos(\gamma + \omega_R t) - \cos\gamma\} - \frac{S_2}{2\omega_R} \{\cos(2\gamma + 2\omega_R t) - \cos 2\gamma\}, \tag{2.47}$$

and

$$C_1 = -\frac{\delta_\lambda}{\sqrt{2}} \sin 2\beta (1 + \frac{\eta_\lambda}{3} \cos 2\alpha), \tag{2.48}$$

$$C_2 = \frac{\delta_\lambda}{2} \sin^2\beta - \frac{\delta_\lambda \eta_\lambda}{6} (1 + \cos^2\beta) \cos 2\alpha, \tag{2.49}$$

$$S_1 = \frac{\sqrt{2}\delta_\lambda \eta_\lambda}{3} \sin\beta \sin 2\alpha, \tag{2.50}$$

$$S_2 = \frac{\delta_\lambda \eta_\lambda}{3} \cos\beta \sin 2\alpha. \tag{2.51}$$

In the case of the dipole-dipole coupling (and for most ^2H quadrupolar couplings) the expression for $\Phi_\lambda(t)$ is greatly reduced by the fact that $\eta_\lambda = 0$.
When pulse sequence Hamiltonians are to be calculated, the lower limit for the integration in Eq. (2.46), i.e. the initial rotor phase, often needs to be different from zero. For an arbitrary initial rotor phase the acquired MAS phase for an interaction λ can be defined as

$$\Phi_\lambda \,|_{t_1}^{t_2} = \Phi_\lambda(t_2) - \Phi_\lambda(t_1) \tag{2.52}$$

From this some useful relations can readily be calculated:

$$\Phi_\lambda \,|_t^{t+\tau_R} = 0 \tag{2.53}$$

$$\Phi_\lambda \,|_0^{\frac{\tau_R}{2}} = -\Phi_\lambda \,|_{\frac{\tau_R}{2}}^{\tau_R} \tag{2.54}$$

The first relation expressing that the acquired phase over a full rotor period becomes zero is responsible for the averaging effect of MAS. After each rotor period the initial signal is fully refocused and the observed time signal (theoretically) does not decay, resulting in infinitely narrow spinning sidebands in the spectra.
With the expression for the averaged Hamiltonian under MAS (Eq. (2.46)) the evolution of an initial state $\hat{\boldsymbol{\rho}}(0) = \hat{\boldsymbol{I}}_x$ under an interaction under MAS is given by

$$\hat{\boldsymbol{I}}_x \xrightarrow{\bar{H}_{\lambda,MAS}(t)\,t} \hat{\boldsymbol{I}}_x \cos\Phi_\Lambda + \hat{\boldsymbol{W}} \sin\Phi_\Lambda, \text{ where} \tag{2.55}$$

$$\begin{aligned}
\Phi_{CS} &= \omega_{iso}t + \Phi_{csa}, \quad \hat{\boldsymbol{W}} = \hat{\boldsymbol{I}}_y, \\
\Phi_Q &= \sqrt{\tfrac{3}{2}}\Phi_{quad}, \quad \hat{\boldsymbol{W}} = i(\hat{\boldsymbol{T}}_{21} + \hat{\boldsymbol{T}}_{2-1}), \\
\Phi_{D_{ij}} &= \sqrt{\tfrac{3}{2}}\Phi_{dip,hom}, \quad \hat{\boldsymbol{I}}_x = \hat{\boldsymbol{I}}_x^{(i)} + \hat{\boldsymbol{I}}_x^{(j)}, \quad \hat{\boldsymbol{W}} = 2\hat{\boldsymbol{I}}_y^{(i)}\hat{\boldsymbol{I}}_z^{(j)} + 2\hat{\boldsymbol{I}}_y^{(j)}\hat{\boldsymbol{I}}_z^{(i)}, \\
\Phi_{D_{is}} &= \frac{1}{2}\Phi_{dip,het}, \quad \hat{\boldsymbol{W}} = 2\hat{\boldsymbol{I}}_y\hat{\boldsymbol{S}}_z.
\end{aligned}$$

Note that the acquired phase angles Φ_Λ differ from the integrated phase Φ_λ, since they include additional prefactors arising from the corresponding spin part $\hat{T}_{20}^{\lambda}$. The acquired phase angles Φ_Λ are functions of time and depend on the Euler-angles (α, β, γ) transforming the interaction from the PAS to the rotor frame. α and β are identical to the polar angles of the rotor axis in the PAS. A dependence on α is only given for asymmetric tensors ($\eta \neq 0$). γ denotes the initial rotor phase, because in Eq. (2.47) the time dependence, $\omega_R t$, always appears relative to this angle.
An important point for the techniques introduced in chapters 3 and 4 is the way the time dependence due to sample rotation enters the interaction Hamiltonian. Due the representation as a second rank tensor, elements of the Wigner rotation matrices up to second order (L=2) are involved in Eqs. 2.43 - 2.45. The Wigner rotation matrix elements introduce the time dependence as trigonometric functions of ω_R and $2\omega_R$. This suggests that the MAS Hamiltonian can be rewritten in terms of five Fourier components, $\omega_\lambda^{(m)} = A_{2-m}^{\lambda,R} d_{-m0}^{(2)}(\beta_M)$:

$$\hat{\tilde{\boldsymbol{H}}}_{\lambda,MAS}(t) = \hat{\boldsymbol{T}}_{20} \sum_{m=-2}^{2} \omega_\lambda^{(m)}\, e^{im\omega_R t} \tag{2.56}$$

Clearly, the time dependence is a mere rotor modulation that does not effect the spin part. If the latter is manipulated by suitably spaced RF-pulses, differently modulated components of

the Hamiltonian can independently be selected, which is the basis of the work presented in chapter 4.

2.5 Basic NMR Experiments

In the following section, some basic NMR experiments used throughout this thesis will be introduced. The theoretical treatment of the experiments will be carried out completely in the rotating frame with the initial state given by $\hat{\boldsymbol{\rho}}_{eq} \sim \hat{\boldsymbol{I}}_z$. In the first paragraph (section 2.5.1) the one-pulse experiment and the fundamentals of signal detection will be discussed. Afterwards dipole-dipole decoupling techniques (section 2.5.2) and cross-polarization (section 2.5.3) will be introduced, which represent tools that are essential for the observation of nuclei with low natural abundance nuclei, such as ^{13}C , in solids.

2.5.1 The One-Pulse Experiment and Signal Detection

The most simple experiment in FT-NMR is the one-pulse experiment, which is shown schematically in Fig. 2.4. By a 90°- (or $\frac{\pi}{2}$) pulse the magnetization is flipped from the *z* axis into the *x*-*y*-plane as follows from Eq. (2.30) for $\alpha = 90°$. After the pulse the LARMOR precession of the transverse magnetization induces a weak voltage in the RF-coil, which constitutes the actual observed signal S(t). Technically, this signal is mixed with the reference carrier frequency to obtain the response in the rotating frame. Modern spectrometers are capable of phase-sensitive detection, i.e. x- and y- components of the precessing magnetization can separately be detected. This is accomplished by mixing of the NMR signal S(t) with two reference signals with orthogonal phases and collection of the data points in complex form (Re[S],Im[S]).

Since transversal magnetization is a non-equilibrium state, the magnetization will return with time to its equilibrium state with no observable transversal magnetization. The decay of the transversal magnetization is described by the T_2 relaxation time, whereas the return towards the initial $\hat{I}_z$ state is characterized by the relaxation constant T_1. The acquired signal decaying with T_2 is called *free induction decay* (FID). With the density matrix formalism introduced in section 2.2 the signal is given as the expectation value of the transverse magnetization, which constitutes an *observable*. In order to obtain the full complex signal, the expectation value of the shift-operator $\hat{I}_+$ must be calculated. Using Eq. (2.22) the expectation value

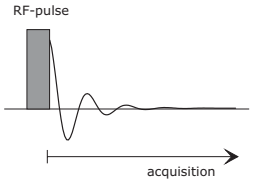

Figure 2.4: *The one-pulse experiment.*

results as

$$\langle \hat{\boldsymbol{I}}_+ \rangle = \mathsf{Tr}\left\{ \hat{\boldsymbol{I}}_+ \hat{\boldsymbol{\rho}} \right\} = \tfrac{1}{\sqrt{2}} \left(\mathsf{Tr}\left\{ \hat{\boldsymbol{I}}_x \hat{\boldsymbol{\rho}} \right\} + i\, \mathsf{Tr}\left\{ \hat{\boldsymbol{I}}_y \hat{\boldsymbol{\rho}} \right\} \right) = \tfrac{1}{\sqrt{2}} \left(\langle \hat{\boldsymbol{I}}_x \rangle + i \langle \hat{\boldsymbol{I}}_y \rangle \right). \tag{2.57}$$

By Fourier transforming $\langle \hat{\boldsymbol{I}}_+ \rangle(t)$ a spectrum including the full phase information is obtained.

2.5.2 Heteronuclear Dipolar Decoupling

When dealing with nuclei $\mathbf{S}$ in low natural abundance (like ^{13}C with about 1 % natural abundance) homonuclear couplings can safely be neglected. However, even at fast MAS up to 30 kHz the heteronuclear coupling between the $\mathbf{S}$ nuclei and high abundance nuclei $\mathbf{I}$ (in organic solids usually ^{1}H) still causes significant line broadening. To overcome this problem various decoupling schemes have been devised and the improvement and development of heteronuclear decoupling schemes is still a topic of ongoing research [Paëpe 03, Ernst 03, Khitrin 03]. In solid-state NMR under MAS, high-power continuous-wave (CW) decoupling was initially used to achieve heteronuclear spin decoupling. There, the high abundance spins $\mathbf{I}$ are continuously irradiated by high-power RF-fields as is depicted in Fig. 2.5. This requires a double-resonance probehead, where the RF-coil is addressed via two separate resonant circuits operating at the respective LARMOR frequencies. In order to achieve sufficient decoupling efficiencies and to avoid interference effects between the physical rotation from MAS and the rotation of the spins by the applied CW RF-field, high-power decoupling with strong RF-fields of 50-150 kHz is necessary. The most important interference effects arise from rotary-resonance [Dusold 00], either at the condition $n\omega_R = \omega_1$ or at the condition $\frac{1}{2}\omega_R = \omega_1$. The former condition leads to a recoupling of the heteronuclear dipole-dipole coupling [Oas 88] and the latter to recoupling of the homonuclear dipole-dipole coupling [Nielsen 94]. In terms of high-power decoupling these conditions are carefully avoided by choosing the decoupling frequency at least two times higher than the spinning frequency. It should be noted that with the high spinning frequencies achievable today low-power CW-decoupling becomes of interest. Especially in the field of protein NMR, where radiation heating proposes a severe problem, low-power decoupling with the RF-frequency being much lower than the spinning frequency is advantageous, since it reduces the power dissipation in the sample drastically [Ernst 01].

Today, high-power multiple-pulse decoupling schemes are established as the most efficient decoupling methods for solids under MAS. The first decoupling scheme, which gave significant improvement in both linewidth and line intensity under a wide range of experimental conditions, was the two-pulse phase-modulated (TPPM) decoupling sequence [Bennett 95], which is schematically depicted in Fig. 2.5b. TPPM decoupling consists of two pulses each corresponding to a flip angle of about 170°. The phase difference, ϕ, between the two pulses

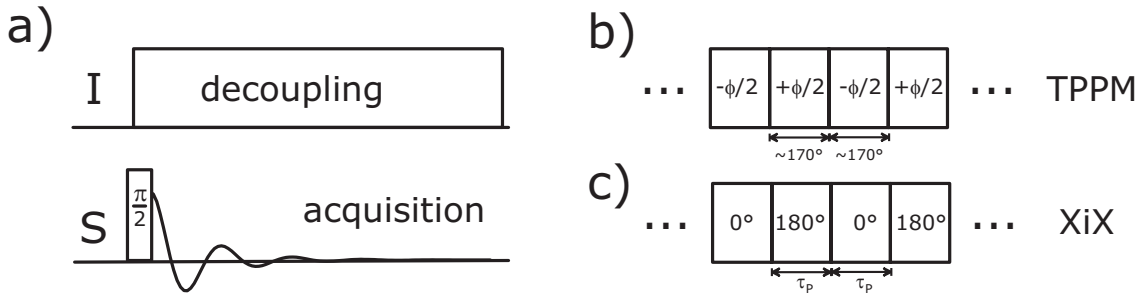

Figure 2.5: *Heteronuclear decoupling sequences. For CW-decoupling the RF-field is simply switched on for the whole decoupling period (a). In multiple-pulse decoupling schemes the constant RF-field is replaced by composite pulse trains as those shown for TPPM (b) and XiX (c) decoupling.*

is on the order of 10-50°. Experimentally, the decoupling efficiency depends on the precise setting of these two parameters, which have to be optimized empirically. The improvement in decoupling efficiency was ascribed to second averaging [Gan 97, Carravetta 00]. Provided the RF-field is much higher than the MAS frequency, the spin Hamiltonian is first truncated by the RF irradiation and then on a longer timescale averaged by the MAS rotation. CW decoupling leads only in zeroth-order approximation to a full decoupling of heteronuclear spin systems in solids under MAS. In a higher order approximation, a cross-term between the heteronuclear dipole-dipole coupling tensor and the chemical shielding tensor of the irradiated spins is reintroduced. This cross-term is strongly reduced by TPPM decoupling, thus leading to a significant reduction in linewidth. Meanwhile, several variants of the TPPM sequence were proposed but none of them offers significant improvement in rigid solids over a large range of experimental parameters [Gan 97, Yu 98, Fung 00, Takegoshi 01].

An alternative decoupling scheme is the XiX (X inverse-X) sequence introduced by Meier and co-workers [Detken 02]. The sequence, shown in Fig. 2.5c, consists of a windowless phase-alternating sequence, $(\theta_{+x}, \theta_{-x})_N$, which has only one parameter, namely the pulse width τ_P in units of the rotor period τ_R. The advantage of the XiX scheme is that it is easy to implement, because it is only sensitive on a single parameter, τ_P/τ_R. Based solely on the MAS frequency, a good initial value for the pulse width can be predicted. As a rule of thumb, good starting values for the pulse length are $\tau_P = 1.85\tau_R$ and $\tau_P = 2.85\tau_R$. Therefore, the experimentalist is only left with some fine-tuning to obtain a close-to-optimum performance.

Detailed comparisons between the XiX and the TPPM scheme have shown [Ernst 03, Detken 02] that XiX might lead to an increase in peak height of up to 29% as compared to TPPM. The gain was found to be primilarily obtained from the broad 'foot' in the TPPM spectra, which is reflected by the fact that the linewidths (FWHM) are very similar for both sequences. However, XiX performs well only at high spinning frequencies (>20 kHz) and at high RF-amplitudes (>100 kHz). The advantages of XiX over TPPM decoupling decrease with decreasing RF-field strength and decreasing MAS frequency. In those cases TPPM decoupling is often the better choice.

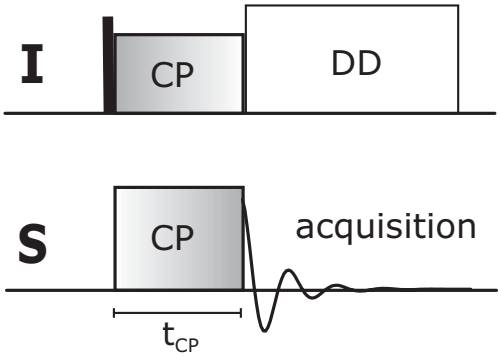

Figure 2.6: *The cross-polarization experiment.*

2.5.3 Cross-Polarization

The maximum polarization one can achieve in a homonuclear NMR experiment is governed by the magnetogyric ratio of the respective nucleus. Cross-polarization (CP) is a method to gain signal intensity in low-γ nuclei (**S**), like ^{13}C or ^{15}N, by polarization transfer from abundant high-γ nuclei (**I**), i.e. usually protons. This technique was first applied by A. Pines, M. Gibby and J. S. Waugh [Pines 72, Pines 73] and was originally referred to as 'Proton enhanced nuclear induction spectroscopy'. The basic CP experiment is shown in Fig. 2.6. Transverse magnetization of the **I** spins is generated by the initial 90° pulse. Afterwards the polarization is transferred to the **S** nuclei by simultaneous irradiation on both channels for typically 500 μs - 5 ms. Maximum transfer occurs, if the Hartmann-Hahn condition is met, i.e.

$$\omega_1(S) = \gamma_S B_1(X) = \gamma_I B_1(I) = \omega_1(I) \tag{2.58}$$

The matching condition corresponds to a degeneration of the ZEEMAN splittings in the lock-fields, i.e. each spin species precesses with the same frequency $\nu_1 = -\gamma B_1/2\pi$ around the axis of its RF-field in its own rotating frame. Since both rotating frames share the same z axis, there will be an oscillation of local I and S magnetization components along the z axis with the same frequency ν_1. By this frequency match, magnetization can be exchanged between both spin species. This exchange requires the presence of a mediating interaction, which is usually the heteronuclear dipole-dipole coupling. Formally, the matching reintroduces flip-flop terms (e.g. $2\hat{I}_z\hat{S}_z$) from the heteronuclear dipole-dipole coupling in the effective dipolar Hamiltonian, which are responsible for the polarization transfer. Hence, the efficiency of the cross-polarization process is governed by the size of the dipole-dipole interaction between **I** and **S** spins, with the maximum signal enhancement given by a factor of $\gamma(I)/\gamma(S)$. With increasing the contact time, t_{CP}, the **S** magnetization, $M_S(t_{CP})$, is first built up with a time constant T_{IS}, which is characteristic for the strength of the underlying dipole-dipole couplings.

However, since the spin-locked **I** and **S** magnetizations are also subject to relaxation, the **S** magnetization passes at longer CP times through a maximum before being attenuated by $T_{1\rho}^{I}$ and $T_{1\rho}^{S}$, which are the time constants for the relaxation in the rotating frame. In the case of dilute **S** spins in a large system of **I** spins the contact time dependence $M_S(t_{CP})$ is given by [Mehring 83, Slichter 96]

$$M_S(t_{CP}) = \frac{M_0}{\lambda} \cdot \left[1 - exp\left\{-\frac{\lambda t_{CP}}{T_{IS}}\right\}\right] \cdot exp\left\{-\frac{t_{CP}}{T_{1\rho}^{I}}\right\} , \tag{2.59}$$

where

$$\lambda = 1 + \frac{T_{IS}}{T_{1\rho}^{S}} - \frac{T_{IS}}{T_{1\rho}^{I}} \tag{2.60}$$

Eq. (2.59) can be derived on the basis of thermodynamics, which is appropriate considering the large system of coupled **I** spins in most organic solids. The contact time dependence of an isolated two-spin system would be oscillatory. Strongly coupled nuclei exhibit a small T_{CH} and hence build up quickly, whereas weakly coupled nuclei have a large T_{CH} and build up more slowly. Since molecular motions generally reduce dipole-dipole couplings, the CP build up behavior of a certain resonance provides qualitative insight into segment mobility. A quantitative analysis would require the knowledge of the individual relaxation time constants [Voelkel 88].
Another important advantage of the CP experiment is that T_1^I governs the recycle delay of the experiment. Since usually $T_1^I > T_1^S$, a lot of measuring time is saved, since shorter recycle delays are sufficient.
It should be noted that under MAS the Hartmann-Hahn condition, Eq. (2.58), changes to

$$\omega_1(S) = \omega_1(I) \pm n\omega_R \tag{2.61}$$

with maximum signal for $n = \pm 1$ at higher MAS frequencies. The Hartmann-Hahn matching profile in CP-MAS NMR shows a strong mismatch dependence, if the MAS frequency is in the order of the dipole-dipole couplings in the sample. This makes it experimentally difficult to establish and maintain an efficient matching condition. This problem can efficiently be overcome by using a ramped-amplitude cross-polarization sequence (RAMP-CP) as it was introduced by Metz et. al. [Metz 94]. In RAMP-CP the amplitude of the lock pulse on either channel is linearly increased over the contact time. This produces flat matching profiles over a wide range of matching conditions. Therefore, RAMP-CP was used for all MAS experiments presented in this thesis.

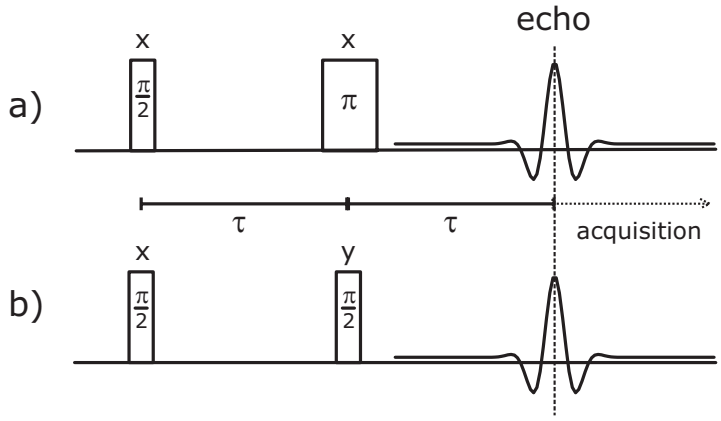

Figure 2.7: *Hahn spin echo (a) and solid echo (b) sequence. The acquisition starts at the echo maximum.*

2.5.4 Echo Experiments: Hahn Spin Echo and Solid Echo

For many samples in solid-state NMR the FID decays so fast that the coil has not yet recovered from the initial RF-pulse. An elegant way to overcome this dead-time problem is to form an echo. After the initial 90° pulse the spins are allowed to evolve for a time τ at which a suitable echo pulse is applied. The echo occurs at a time τ after the pulse, i.e. at a time 2τ after the initial 90° pulse. Depending on the type of interaction, which should be refocused, the effective flip angle of the echo pulse needs to be different. For interactions linear in $\hat{I}_z$ (chemical shift, resonance offset and heteronuclear dipole-dipole coupling) a 180° pulse is found to generate the echo. This is the familiar Hahn spin echo [Hahn 50]. Interactions bilinear in the same type of spins are refocused by a 90° echo pulse, which is phase shifted by 90° from the initial 90° pulse. This sequence is referred to as the solid echo. Examples are [Powles 63] for homonuclear dipole-dipole coupling and [Davis 76] for quadrupolar coupling. The two echo sequences are depicted if Fig. 2.7. The effect of the echo experiments can easily be derived by calculating the propagator at the time 2τ after the initial pulse. It is found to exactly recover the initial state at the time 2τ. A detailed derivation can be found in [Schmidt-Rohr 94]. The solid echo sequence is routinely used in deuteron NMR spectroscopy, namely for the study of molecular dynamics with correlation times in the range of approximately $1/\delta_Q < \tau_C < 10\tau$. Molecular reorientations during the echo time cause frequency changes during the quadrupolar evolution [Spiess 81]. This leads to very characteristic line shapes from which information on the geometry and the correlation time of the motion can be extracted [Macho 01].

Chapter 3

Recoupling Methods under MAS

The first chapter covered some fundamental aspects of solid-state NMR. Based on this, in this chapter the specific techniques comprising the methodological foundation of this thesis will be described. All techniques described involve recoupling of the anisotropic part of an NMR interaction under MAS and can consequently be viewed as recoupling experiments. In the first section, the general principle of recoupling will be explained, before turning to the particular techniques in detail in the following sections.

3.1 The Principle of Recoupling

As mentioned in the previous chapter, magic-angle spinning (MAS) provides a powerful tool to obtain spectral resolution in solid state NMR, which is a prerequisite for the elucidation of structure and dynamics in solid materials [Brown 01]. However, the line narrowing achieved by fast MAS comes at the price of a loss of the information, which is inherent to the anisotropic parts of the respective interaction tensors. This information includes all orientation dependent phenomena and, in the case of the dipole-dipole coupling, distance information, which is of very valuable for structure determination in solids. Methods, which allow such information to be selectively regained, while retaining the spectral resolution provided by MAS, are therefore of great value.
The first methods to partly regain the anisotropic information usually involved sacrificing a part of the spectral resolution just gained by MAS. Examples for retaining the chemical shift information are slow magic-angle spinning and *o*ff-*m*agic-*a*ngle-*s*pinning (OMAS). For slow MAS at medium spinning frequencies ($0 < \omega_R < \omega_{CSA}$) the isotropic signal is flanked on both sides by rotational sidebands at multiples of the spinning frequency ω_R. From an analysis of the MAS sideband intensities, information about the chemical shift tensor can be obtained [Herzfeld 80]. Spinning the sample fast at a known angle slightly different from the magic-angle (OMAS) preserves the anisotropic part of the interaction, but it is scaled down, so that

the overlap of the broad anisotropic line shapes is decreased [Stejskal 77, Blümich 90].
The aim of regaining anisotropic tensor information while, at the same time, keeping the full spectral resolution from MAS was finally reached by the recoupling approach [Gullion 89b, Carravetta 00]. Here advantage is taken from the fact that MAS as a rotation in real space affects only the space part of an interaction Hamiltonian (see Eq. (2.4)), whereas radio frequency pulses affect only the spin part of an interaction Hamiltonian. By the application of suitably designed pulse sequences it is possible to create a counter-rotation in spin space, which compensates for the averaging effect of MAS on the space part and selectively recouples the interaction of interest. Today a great variety of sequences recoupling the various NMR interactions is known [Gullion 97, Lee 95, deAzevedo 99, Dusold 00, Schnell 01b, Saalwächter 02c].
In principle, two main classes of recoupling experiments can be distinguished. The first class of experiments utilizes short, rotor-synchronized, high-power RF-pulses to achieve recoupling. These pulses are usually assumed to be δ-pulses for the calculation of the average Hamiltonian of the sequence. Since the calculation is carried out in the laboratory frame, these sequences are commonly referred to as laboratory frame pulse sequences. In order to be able to use the δ pulse approximation, the length of the pulses must be significantly shorter than the MAS rotor period. At increasing spinning speeds this becomes technically demanding in terms of pulse performance and spectrometer timing. The second class of recoupling experiments employs relatively long, continuously applied pulses. The $\underline{\mathbf{B}}_1$ field of those pulses causes a precession of the irradiated nuclear spins with the angular frequency $\omega_1 = \gamma_1 B_1$, which is matched to multiples of the MAS rotation frequency. Hence, the tilted rotating frame and the MAS rotor frame are synchronized and form the basis for the recoupling effect of these pulses sequences. Consequently, the latter pulse sequences are named tilted rotating frame pulse sequences. Since these experiments are very sensitive towards imperfections in the pulse power output, fast pulse-power switch and stable pulse power levels are technical prerequisites for employing these experiments. Since tilted rotating frame sequences were not used for the work presented here, the interested reader is referred to the literature covering these sequences in detail [Brinkmann 00, Zhao 01].
Apart from the SUPER experiment [Liu 02], which is described in section 3.6 and which, in a way, stands between the two classes of recoupling experiments, all recoupling sequences presented in the following belong to the class of the laboratory frame pulse sequences. Moreover, all these sequences are based on the application of rotor-synchronized pulse trains with the pulses spaced by exactly half (or a quarter of (chapter 4)) a rotor period. Thus, before turning to the particular experiments in detail in sections 3.3-3.5, the effect of such rotor-synchronized pulse trains is described in general first, providing a general understanding of the recoupling process.
As already mentioned above, recoupling experiments are based on the fact that the application of suitable pulse trains can be used to recouple anisotropic interactions, which would otherwise be averaged to zero by fast MAS. The approach of utilizing rotor-synchronized pulse trains with the pulses spaced by exactly half a rotor period was first employed in the RE-

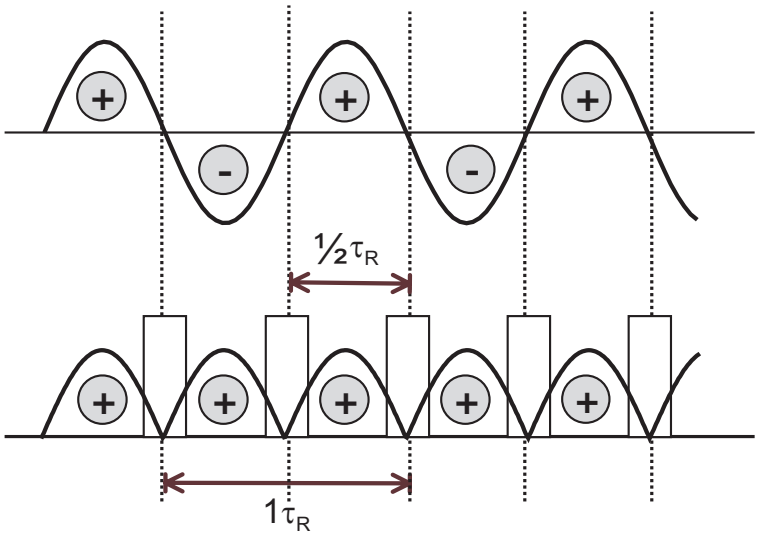

Figure 3.1: *Principle of recoupling by rotor-synchronized π pulse trains.*

DOR (*r*otational *e*cho, *d*ouble *r*esonance) experiment, which was introduced by Schaefer and Gullion [Gullion 89b, Gullion 89a] for recoupling the heteronuclear dipole-dipole coupling between two kinds of low-γ nuclei. In REDOR, recoupling is accomplished by a π pulse train with the pulses spaced by exactly half a rotor period. As will be shown below, REDOR-type π pulse trains can serve to recouple the anisotropic part of any interaction, which is linear in the (irradiated) spin. Hence, REDOR-type π pulse trains are also commonly used for CSA-recoupling [deAzevedo 99, Hong 00] or for recoupling the ^{1}H-X heteronuclear dipole-dipole coupling [Hing 92, Saalwächter 01b], where X denotes any low-γ spin-half nucleus.
In order to gain understanding of the recoupling effect of such a π pulse train, it is instructive, to regard the effect of MAS on an interaction Hamiltonian first. According to Eq. (2.46) the averaged Hamiltonian of an interaction λ under MAS is given by the sum of an isotropic (first term) and an anisotropic (second term) contribution:

$$\hat{\bar{\boldsymbol{H}}}_{\lambda,MAS} = \hat{T}_{00} A_{00}^{\lambda,LAB} + \hat{T}_{20} \cdot \frac{1}{t} \cdot \sqrt{\tfrac{3}{2}} \cdot \Phi_\lambda \tag{3.1}$$

MAS superimposes a $sin(\omega_R)$-modulation on the anisotropic part of $\hat{\bar{\boldsymbol{H}}}_{\lambda,MAS}$, which manifests itself in the acquired phase angle, $\Phi_\lambda(t)$, whose time-dependence is given in Eq. (2.47). From setting $t = \tau_R$ in Eq. (2.47), it directly follows that the acquired phase over a full rotor period is zero, $\Phi_\lambda(\tau_R) = 0$. Hence the anisotropic part of $\hat{\bar{\boldsymbol{H}}}_{\lambda,MAS}$, becomes zero over a full rotor period, too. This is the origin of the averaging effect of fast MAS, which is illustrated graphically on top of Fig. 3.1, where a $sin(\omega_R)$-modulation is schematically depicted. Intervals marked with $\oplus$ and $\ominus$ correspond to positive and negative lobes, respectively, of the *sine*-oscillation. Clearly, the contributions from the first and the second half of the rotor

period cancel for free evolution under MAS. Hence, it is obvious, how recoupling could be achieved: If the sign of the anisotropic part of the interaction Hamiltonian could be effectively inverted after every second $\tau_R/2$ interval, only positive lobes would be present and, thus, the anisotropic contributions from each $\tau_R/2$ interval would add up, i.e. be recoupled. Such a sign-inversion can easily be achieved by applying pulses after each half rotor period, which invert the sign of the spin part $\hat{T}_{20}$. This represents a "counter-rotation" to the MAS rotation in spin space and leads to the desired recoupling effect. The contributions from each $\tau_R/2$ interval add up, as is indicated on the bottom of Fig. 3.1, where only $\oplus$ lobes are present. The nature of the recoupling pulses depends on the nature of the spin part $\hat{T}_{20}$ of the respective interaction. For interactions linear in a certain type of spin (heteronuclear dipole-dipole coupling, CSA), the sign inversion of $\hat{T}_{20}$ is accomplished by π pulses. Since π pulses do not invert the sign of interactions bilinear in the same spin type (such as the homonuclear dipole-dipole coupling), the described π pulse trains cannot serve for recoupling the homonuclear dipole-dipole coupling. However, recoupling of the homonuclear dipole-dipole coupling can be achieved in an analogous fashion by the Back-to-Back (BABA) pulse sequence [Feike 96], which will be described in detail in section 3.3. In the Back-to-Back sequence the π pulses of a REDOR-type recoupling pulse train are replaced by a pair of $\pi/2$ pulses with orthogonal phases. This leads to a time-reversal of the homonuclear dipole-dipole coupling during the second half of each rotor period and, thus, to a recoupling of the homonuclear dipole-dipole coupling analogous to the heteronuclear or CSA recoupling.

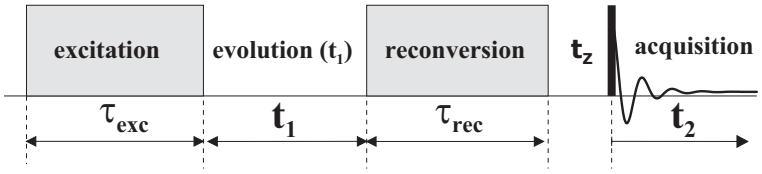

Figure 3.2: *Basic structure of a multiple-quantum experiment.*

3.2 Multiple-Quantum Techniques

An aspect not mentioned yet is that recoupling sequences are very often used for the selective excitation of multiple-quantum coherences. Since the multiple-quantum aspect is crucial for most of the presented sequences, in the following some aspects of multiple-quantum NMR spectroscopy will be discussed in general.
Since the first multiple-quantum NMR experiments in solids [Weitekamp 82, Munowitz 87], several multiple-quantum experiments have developed into established solid-state NMR methods, in particular for the determination of dipole-dipole coupling constants and, thereof, internuclear distances. Multiple-quantum (MQ) experiments involve the excitation of multiple-quantum coherences. A *m*-quantum coherence is defined by a change in the overall magnetic spin quantum number *M* by *m*. In spherical tensor notation a MQ coherence of order *m*, involving *L* spins of spin $\frac{1}{2}$, can always be written as a single tensor operator of rank *L* and order *m*, $\hat{T}_{L\pm m}$. In unperturbed systems, transitions with $\Delta M > 1$ are forbidden. However, those transitions become weakly allowed under the influence of a perturbing interaction like the dipole-dipole coupling. Since MQ coherences are not directly observable, they must be converted to detectable magnetization prior to detection. Hence, experiments that follow the evolution of a MQ coherence are inherently at least two-dimensional. Therefore, a typical MQ experiment consists of four stages, as is depicted in Fig. 3.2. During the excitation period, a suitable pulse sequence for the excitation of the desired MQ coherences is applied. Usually, an average Hamiltonian, $\bar{\hat{\boldsymbol{H}}}_{exc}$, can be used to describe the whole period. The resulting MQ coherence may then evolve during the t_1-period of the 2D experiment. During the reconversion period, described by the average Hamiltonian $\bar{\hat{\boldsymbol{H}}}_{rec}$, the MQ coherence is converted to observable magnetization, which is finally detected, after a possible z-filter of duration t_Z. The desired coherence, e.g. a pure double-quantum coherence evolution during t_1, must be selected by a appropriate phase cycling scheme. The evolution of the MQ coherence is then monitored indirectly as an amplitude modulation of the final signal as a function of t_1.
If sign discrimination in the indirect dimension (F1) is desired, a phase cycling of a part of the pulse sequence with respect to the indirect dimension has to be implemented in such a way that for subsequent time increments in t_1 (called "slices" of the 2D spectrum) the amplitude modulation is only due to the *cosine*- or *sine*-component of the indirectly detected signal. Common methods are TPPI (*t*ime *p*roportional *p*hase *i*ncrementation) [Marion 83] and states-TPPI [Marion 89]. Either method involves incrementing the phases of all excitation pulses

by 45° after recording each t_1 point. In TPPI the *sine*- and *cosine*-components are detected alternatingly from slice to slice. Hence, the effective t_1 increment (Δt_1) is doubled and the spectral width in the indirect dimension is divided by two: $SW(F1) = 1/(2\Delta t_1)$. If a larger spectral width in the indirect dimension is needed (given a restriction to a minimum Δt_1), the states-TPPI method is preferable. There, the *cosine*- and *sine*-components are subsequently detected for each t_1, resulting in a spectral width of $SW(F1) = 1/(\Delta t_1)$. Details concerning the required special processing of the obtained data sets can be found in [Schmidt-Rohr 94].
Homonuclear MQ experiments make the determination of dipole-dipole coupling constants possible by evaluating the build-up behavior of the MQ coherences [Graf 96], or by analyzing spinning sideband patterns in the MQ dimension of 2D experiments [Geen 95, Gottwald 95, Friedrich 98]. Heteronuclear MQ experiments, probing the ^{1}H -^{13}C dipole-dipole coupling, take advantage from the enhanced spectral width of the ^{13}C chemical shifts.
Limiting the MQ order or, equivalently, the minimum number of coupled spins to 2, leads to double-quantum (DQ) spectroscopy, by the use of which dipole-dipole-coupled networks can be analyzed in a pairwise manner with respect to the chemical shift of the involved nuclei.

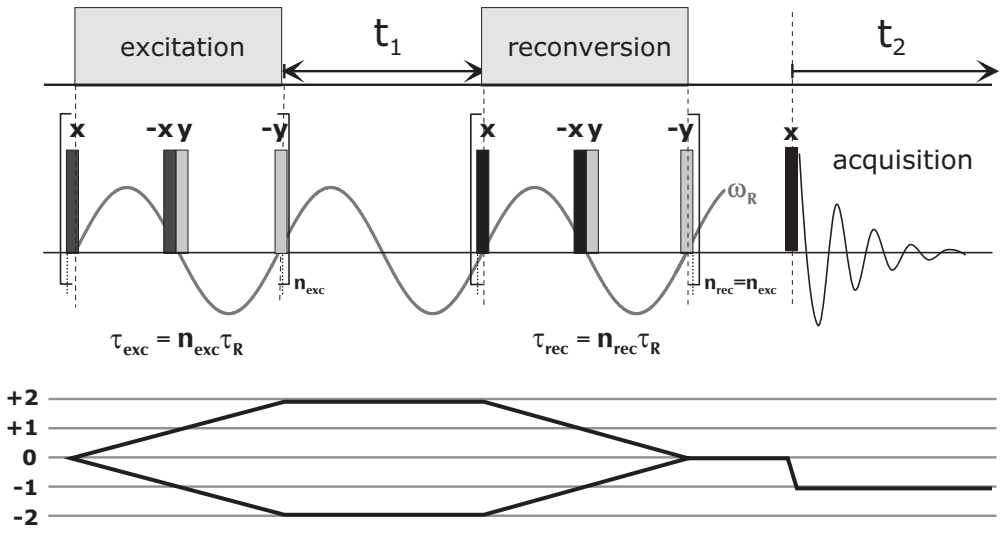

Figure 3.3: *The BABA sequence together with the coherence transfer pathway diagram for DQ excitation. For clarification the corresponding stages of a MQ experiment are depicted on top of the sequence.*

3.3 Back-to-Back

The BABA sequence [Feike 96] was introduced as a multiple-quantum technique under MAS based on recoupling the homonuclear dipole-dipole coupling. Today, the BABA sequence is routinely used for the determination of neighborhood relationships and ^{1}H-^{1}H internuclear distances, for a recent review see [Schnell 01b]. In the following, this discussion will be restricted to the use of BABA for double-quantum generation.
The BABA sequence, which is shown in Fig. 3.3, consists of repeating the basic segment $(90_x - \tau_R/2 - 90_{-x}90_y - \tau_R/2 - 90_{-y})$, which is often written in short-hand notation as $x - \bar{x}y - \bar{y}$. For longer excitation times (two, four and eight rotor periods) the signs of the pulse phases can be set in such a way that the sequence is compensated with respect to offset effects and pulse imperfections. It should be noted that the sequence has to undergo a phase cycling scheme (or alternatively a gradient dephasing/rephasing procedure) to select the desired coherence pathway. The BABA sequence recouples the homonuclear dipole-dipole coupling, which is described in a zeroth-order average Hamiltonian approach by

$$\hat{\tilde{\boldsymbol{H}}}_{dip,hom} = \hat{T}^{ij}_{20} \cdot \frac{1}{t} \cdot \int_0^t A^{LAB}_{20} = \hat{T}^{ij}_{20} \cdot \frac{1}{t} \cdot \sqrt{\frac{3}{2}} \Phi_{dip,hom}, \tag{3.2}$$

where according to Eq. (2.47)

$$\Phi_{dip,hom} = -\sqrt{2} D_{ij} \frac{sin2\beta}{\omega_R} \cdot (sin(\gamma + \omega_R t) - sin\gamma) + D_{ij} \frac{sin^2\beta}{2\omega_R} \cdot (sin(2\gamma + 2\omega_R t) - sin2\gamma) \tag{3.3}$$

Here, $\delta_{dip,hom}$ was replaced by the more familiar dipole-dipole coupling constant, $D_{ij} = \frac{1}{2}\delta_{dip,hom}$, which was defined in Eq. (2.20). The average Hamiltonian for a BABA segment $x - \bar{x}y - \bar{y}$ of one rotor period length can be calculated as [Schnell 01c]:

$$\hat{\bar{\boldsymbol{H}}}_{BABA} = \frac{1}{\tau_R} \cdot 3 \cdot \Phi_{dip,hom} \,|_0^{\frac{\tau_R}{2}} \left(\hat{T}^{ij}_{2,+2} + \hat{T}^{ij}_{2,-2} \right) = \frac{\Omega^{ij}(0, \frac{\tau_R}{2})}{\tau_R} \cdot \left(\hat{T}^{ij}_{2,+2} + \hat{T}^{ij}_{2,-2} \right), \quad (3.4)$$

where $\Omega^{ij}(0, \frac{\tau_R}{2}) = 3\Phi_{dip,hom} \,|_0^{\frac{\tau_R}{2}}$ was introduced in order to use the same notation as mostly found in the literature. As is reflected by the order $m = \pm 2$ of the tensor components, the BABA sequence as presented here generates DQ coherences. Calculating $\Omega^{ij}(0, \frac{\tau_R}{2})$ explicitly yields

$$\Omega^{ij}(0, \tfrac{\tau_R}{2}) = \frac{3\sqrt{2}D_{ij}}{\omega_R} sin2\beta_{ij} sin\gamma_{ij}. \quad (3.5)$$

Applying the BABA Hamiltonian to a spin-pair system in thermal equilibrium, i.e. $\rho_0^{ij} \propto \hat{I}_z^{(i)} + \hat{I}_z^{(j)}$, results in a DQ coherence, whose amplitude is modulated by $sin(\Omega^{ij}_{exc})$. During reconversion, a corresponding amplitude modulation by $sin(\Omega^{ij}_{rec})$ is introduced. For N rotor periods excitation and reconversion time, the relative double-quantum signal intensity can be described by multiplying the modulations from excitation and reconversion time

$$S^{(ij)}_{DQ}(t_1) \propto \langle sinN\Omega^{ij}_{exc} \cdot sinN\Omega^{ij}_{rec} \rangle_{\beta,\gamma'}, \quad (3.6)$$

where the brackets indicate the orientational averaging procedure required for powdered samples. As already indicated in Eq. (3.6) the DQ signal depends on the t_1 evolution time. Consequently, depending on the setting of t_1 and the t_1-increment, Δt_1, for a 2D experiment, the BABA experiment can be performed in various ways. In a one-dimensional experiment (t_1=0) the BABA sequence serves simply as a double-quantum filter (section 3.3.1), whereas two-dimensional BABA experiments can be carried out to yield either rotor-synchronized DQ spectra (section 3.3.2) or to generate ^{1}H -^{1}H DQ MAS spinning sideband patterns (section 3.3.3).

3.3.1 BABA: DQ Build-up Curves

The easiest way to perform a BABA experiment is in a one-dimensional fashion with $t_1 = 0$. Then, appropriate phase cycling provided, the BABA block serves as a double-quantum filter.

Since $t_1 = 0$, the integrated phases in Eq. (3.6) become identical, $\Omega_{exc}^{ij} = \Omega_{rec}^{ij}$. Hence, the DQ-filtered signal intensity is given by

$$\begin{aligned} S_{DQ}^{(ij)} &\propto sin\left(N\Omega_{exc}^{ij}\right) \cdot sin\left(N\Omega_{exc}^{ij}\right) && (3.7)\\ &\approx N\Omega_{exc}^{ij} \cdot N\Omega_{exc}^{ij} + ... && (3.8)\\ &\propto (D^{(ij)})^2 \cdot \tau_{exc}^2 + ... && (3.9)\\ &\propto \frac{\tau_{exc}^2}{r_{ij}^6} + ... && (3.10) \end{aligned}$$

In the limit for short excitation times, $\tau_{exc} = N\tau_R$, or weak couplings, D_{ij}, Eq. (3.7) can be approximated to Eq. (3.8). From the proportionality in Eq. (3.9) it is clear that only signal from protons involved in sufficiently strong (meaning $D_{ij}\tau_{exc}/2\pi \ll 1$) homonuclear dipole-dipole couplings is selected. Hence, for short excitation times, only the strongest dipole-dipole couplings contribute to the signal intensity, whereas at longer excitation times weaker couplings also contribute. Monitoring the double-quantum filtered signal intensity as a function of the excitation time leads to DQ build-up curves, from which the underlying dipole-dipole coupling strengths can be determined.

An important point not mentioned yet is that in "real" rigid ^{1}H samples the dense network of dipole-dipole couplings leads to the inevitable presence of multispin coherences, which are partly also excited by the BABA sequence. Precisely spoken, Eq. (3.7) was obtained as the first term from a series expansion for the evolution of the ^{1}H multispin system [Schnell 01b]. The truncation of this expansion to the first term is reasonable only for short recoupling times, where the double-quantum term dominates. However, with increasing recoupling time such a system develops its multispin character, leading to deviations from the ideal build-up behavior of an isolated spin pair. In Fig. 3.4 the ideal build-up curve for an isolated spin pair is depicted together with an experimental build-up curve obtained on tribromoacetic acid, which is a H-H spin pair model compound with a dipole-dipole pair coupling of $D_{ij} = 2\pi \cdot 6.5\,\text{kHz}$. The initial build-up is dominated by two-spin behavior, whereas at longer recoupling times the interference of several couplings of different strengths leads to the cancellation of the characteristic oscillations, because different frequencies are then destructively superimposed. The excited higher spin correlations and higher order coherences relax faster and, thus, reduce the overall DQ intensity at longer recoupling times.

In some fortunate cases the characteristic oscillations in the build-up curve can be detected, from which the dipole-dipole coupling constant can directly be extracted, provided that only one dipole-dipole coupling gives rise to the observed DQ peak. If those oscillations are smeared out, a more complicated procedure has to be applied, which is based on the fact that the DQ intensity can be expressed as a product

$$S_{DQ} = A \cdot D_{ij}^2 \tau_{exc}^2 \cdot e^{-\tau_{exc}/\tau_{DQ}}, \qquad (3.11)$$

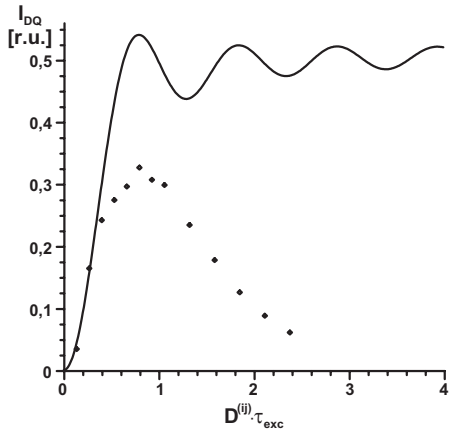

Figure 3.4: *Calculated DQ signal intensities for a single spin pair (solid line) and experimentally observed DQ signal intensities (data points) of tribromoacetic acid, a spin pair model compound. I_{DQ} was normalized with respect to the signal of a one-pulse experiment. Clearly, the initial slope of the experimental curve is dominated by two-spin behavior. This figure was adapted from [Schnell 01b].*

where A contains several constants and is fixed for a series of experiments. The exponential term is describing the decay of the DQ coherence with the time constant τ_{DQ}. Since A is usually unknown, only relative strengths of dipole-dipole couplings are obtained. For the absolute determination of dipole-dipole coupling strengths, more involved referencing procedures are required, some of which are described in [Graf 98a]. Strong dipole-dipole couplings give rise to pronounced decay effects and hence require high MAS spinning frequencies, which in turn puts high demands on the performance of the recoupling sequence. As a consequence of these complications, DQ build-up measurements are usually only carried out in systems, where the dipole-dipole couplings are weaker than in rigid ^{1}H spin systems. Examples are either very mobile systems, like liquid crystals [Langer 01] or polymer melts [Graf 98b], or nonproton systems with weaker homonuclear couplings, e.g. ^{31}P-^{31}P in crystalline phosphates [Schnell 96].
Due to the described limitations the build-up approach is not used in this thesis for the determination of homonuclear dipole-dipole coupling constants. Instead, analysis of sideband patterns, which will be described in section 3.3.3, which is particular useful for determining strong dipole-dipole couplings, is applied. Nonetheless, drawing attention to the ease with which the one-dimensional DQ experiments can be performed, ^{1}H DQ MAS spectra provide quick qualitative information on the strength of dipole-dipole couplings.

3.3.2 BABA: Rotor-Synchronized Two-dimensional DQ MAS Spectra

As already mentioned above, two-dimensional BABA spectra are obtained by increasing the t_1 evolution time for subsequent slices of the 2D experiment. Depending on the length of the

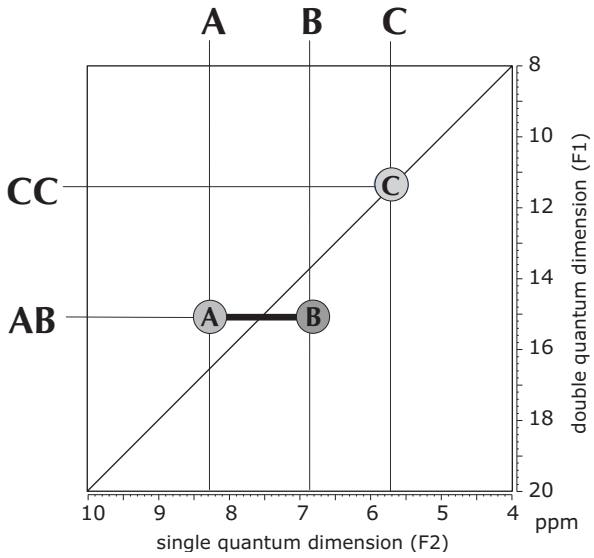

Figure 3.5: *Schematical rotor-synchronized BABA spectrum, indicating a diagonal peak arising from a DQ coherence between two like spins C and two cross peaks arising from a DQ coherence between two unlike spins A and B.*

t_1 increment, Δt_1, two variants of the 2D BABA spectra can be distinguished. Setting the t_1 increment to exactly one rotor period, $\Delta t_1 = \tau_R$, yields rotor-synchronized 2D spectra. Incrementing in smaller steps leads to spinning sidebands, which are described in the next section. The benefit of the rotor-synchronized spectra lies in the fact that with a spectral width along the indirect dimension of $SW(F1) = 1/\Delta t_1 = 1/\tau_R = \omega_R$ no spinning sidebands are observed or, in other words, all spinning sidebands in F1 can be considered to fold back onto the centerband position. Therefore, the peak position in the indirect dimension depends only on the evolution during t_1 of the excited DQ coherence. In this way, the experiment correlates the evolution of the selected DQ coherence during the first spectral dimension (t_1) with the SQ signal detected during the final acquisition period (t_2). The DQ coherence evolves during t_1 namely under the influence of the isotropic chemical shift and dipole-dipole interactions. The evolution of a DQ coherence between two spins i and j under the respective chemical shifts results in a modulation of the form $exp\left\{i(\omega_{CS}^{(i)} + \omega_{CS}^{(j)})t_1\right\}$. If only the mediating pair coupling between the spins i and j forming the DQ coherence is present, no evolution due to the dipole-dipole interaction occurs during t_1. However, any spin outside the coherence gives rise to an evolution of the DQ coherence during t_1 and, in this way, usually to a loss of signal, because those contributions are not refocussed by the subsequent reconversion period. From this it is clear, that the spectral position in t_1 is purely governed by the isotropic chemical shift evolution of the DQ coherence with the resonance frequency being the sum of of the resonance frequencies of the two involved spins. Therefore, it is convenient to display the two-dimensional rotor synchronized spectrum in such a way that the ω_1 frequency axis (t_1 dimension) is scaled by a factor of two as compared to the ω_1 frequency axis (t_2 dimension).

A schematic rotor-synchronized DQ spectrum is depicted in Fig. 3.5. The peak positions are denoted as (ω_2, ω_1), where ω_2 is the SQ frequency and ω_1 the DQ frequency of the respective peak. In the two-dimensional correlation spectrum two types of signal patterns can be distinguished: A DQ coherence between like spins **CC** (identical chemical shift) gives rise to a single peak at the position $(\omega_C, 2\omega_C)$ on the diagonal of the spectrum. A DQ coherence between unlike spins **AB** (different chemical shifts) leads to a pair of cross-peaks at the positions $(\omega_A, \omega_A + \omega_B)$ and $(\omega_B, \omega_A + \omega_B)$, i.e. symmetrically on either side of the diagonal. The two DQ cross-peaks of an **AB** coherence ideally have equal intensity, since the intensity of a cross-peak corresponds to the number of involved spins, which is naturally identical for both cross-peaks.
It should be noted that even though the homonuclear dipole-dipole coupling term does not contribute to to the rotor-synchronized amplitude modulation with respect to t_1, it nonetheless governs the overall signal intensity of a peak in the 2D DQ MAS spectrum. Therefore, it is crucial to choose the excitation time appropriately for the detection of a certain DQ coherence. Under fast MAS, DQ coherences are usually observed for $r_{HH} \leq 3.5\mathring{A}$.

3.3.3 BABA: ^{1}H -^{1}H DQ MAS Spinning Sideband Patterns

In contrast to the rotor-synchronized experiments presented in the previous section, incrementing the t_1 evolution time in steps $\Delta t_1 < \tau_R$ leads to spinning sideband patterns along the indirect dimension. The sideband intensities significantly depend on the excitation time and the strength of the underlying dipole-dipole coupling, which predestines them for the determination of dipole-dipole coupling strengths.
Since for an isolated spin pair there is no anisotropic evolution of the DQ coherences during t_1, the sidebands observed here cannot arise from evolution rotor modulation (ERM), which is the "normal" sideband generation mechanism, also responsible for the generation of the spinning sideband (SB) patterns observed in 1D slow MAS SQ spectra. SB patterns generated by ERM, i.e. the evolution of an anisotropic interaction under MAS, would map out the anisotropy of the evolving spin interaction. However, under the fast MAS conditions applied here, ERM contributes (almost) only to the centerband intensity. Hence, the sidebands present in ^{1}H -^{1}H DQ MAS spinning sideband patterns are due to another mechanism, namely the *r*econversion *r*otor *e*ncoding (RRE) mechanism. RRE arises from the rotor-phase dependence of the average Hamiltonians used for excitation and reconversion. Conversely speaking, the average Hamiltonians must depend explicitly on the rotor phase in order to allow for RRE. The laboratory frame recoupling sequences presented here meet this condition, but many rotor frame sequences like C7 cannot be used for generating sidebands by RRE, since their average Hamiltonians do not depend on the initial rotor phase. Note that RRE does not require concomitant spin evolution in t_1. Hence, for the description of the encoding mechanism, terms arising from evolution during t_1 (particularly the chemical shift evolution) are left out. In Fig. 3.6 the principle of RRE is illustrated. When t_1 equals zero, excitation and

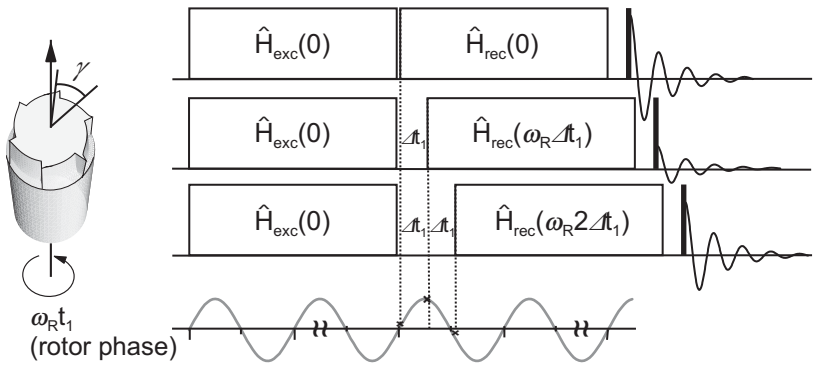

Figure 3.6: *Schematic illustration of the principle of reconversion rotor encoding (RRE).*

reconversion period have the same initial rotor phase, which is manifested in the integrated phase Ω^{ij} (Eq. (3.5)). As t_1 is incremented, the rotor phase dependence of the reconversion period changes relative to that of the excitation period. Therefore, the integrated phases for excitation and reconversion differ with respect to their initial rotor phases

$$\Omega^{ij}_{exc}\left(0, \tfrac{\tau_R}{2}\right) = \frac{3\sqrt{2}D_{ij}}{\omega_R} sin2\beta_{ij} sin\gamma_{ij} \tag{3.12}$$

$$\neq$$

$$\Omega^{ij}_{rec}\left(\tfrac{\tau_R}{2} + t_1, \tau_R + t_1\right) = -\frac{3\sqrt{2}D_{ij}}{\omega_R} sin2\beta_{ij} sin(\omega_R t_1 + \gamma_{ij}). \tag{3.13}$$

As compared to the integrated phase of the excitation period, the integrated phase of the reconversion period is shifted or -in other words- rotor encoded by the term $\omega_R t_1$ in the argument of the *sine*-function. Thus, without any further "real" evolution, MAS modulates the amplitudes of DQ coherences by means of a phase encoding. Clearly, no rotor modulations occur if t_1 is incremented in steps of rotor periods, i.e. in the case of the rotor-synchronized experiment. Consequently, rotor echoes occur in the t_1-signal for evolution times $t_1 = n\tau_R$ with sidebands spaced by multiples of the rotor period in the indirect dimension. Note that this sideband generation mechanism inherently requires at least two-dimensional experiments. In analogy to Eq. (3.6) the DQ signal is now given by

$$S^{(ij)}_{DQ}(t_1) \propto sin\left(N\Omega^{ij}\left(0, \tfrac{\tau_R}{2}\right)\right) \cdot sin\left(N\Omega^{ij}\left(\tfrac{\tau_R}{2} + t_1, \tau_R + t_1\right)\right). \tag{3.14}$$

By inserting Eq. (3.12) into Eq. (3.14) and summarizing all terms, which do not depend on t_1, into the coefficient C_{ij}, Eq. (3.14) becomes to

$$S^{(ij)}_{DQ}(t_1) \propto sin(C_{ij} \cdot sin(\omega_R t_1 + \gamma)). \tag{3.15}$$

Using the relation [Abramowitz 72]

$$sin(xsin(\omega_R t_1 + \gamma)) = 2\sum_{n=0}^{\infty} J_{2n+1}(x) sin((2n+1)\omega_R t_1 + (2n+1)\gamma), \tag{3.16}$$

the DQ signal intensity can be rewritten as a Fourier series, whose terms contain Bessel functions $J_n(C_{ij})$ of *n*th order

$$S_{DQ}^{(ij)}(t_1) \propto 2\sum_{n=1}^{\infty} J_{2n+1}(C_{ij}) sin((2n-1)\omega_R t_1 + (2n+1)\gamma). \tag{3.17}$$

From the Fourier series it is clear that the DQ signal is modulated by odd multiples of the spinning frequency only. Thus, after a Fourier transformation in t_1, the sideband pattern consists of solely odd-order sidebands. The intensity distribution over the sidebands is determined by the Bessel functions and the coefficients C_{ij}, which depend on the orientation (β, γ) and on the ratio D_{ij}/ω_R. Hence, DQ sideband patterns bear information on sample orientation and dipole-dipole coupling strengths. In samples with a known orientation distribution, e.g. isotropic powder samples, the orientation distribution can be taken into account, by e.g. a powder averaging procedure, and finally the dipole-dipole coupling constant can be extracted. The essential parameter determining the envelop of the sideband pattern is the product $D_{ij}\tau_{exc}$. In Fig. 3.7 DQ spinning SB patterns are shown for various $D_{ij}\tau_{exc}$. Clearly, by choosing a suitable excitation time, the number of observed sidebands can be pumped to the desired level. Experimentally, it has proven advantageous to choose $D_{ij}\tau_{exc} \approx 1.2$, which is a compromise between enough sidebands for numerical fitting and not too many sidebands over which the intensity is distributed.

The analysis of the spinning sideband patterns is usually carried out by comparison of the relative sideband intensities with calculated sideband patterns. The analytical equations commonly used in the simulation assume the presence of an isolated spin pair. In organic solids, protons rarely exist as well-isolated spin pairs. An important question to be asked then is the validity of this spin-pair approximation and the strength of the effect of remote protons. It could be shown, that under sufficiently fast MAS the weak dipole-dipole couplings are averaged out first, leaving only the strongest dipole-dipole couplings, i.e. ideally an isolated spin pair. Even if weak dipole-dipole couplings are still present, they contribute only to the first-order sidebands, because these couplings are significantly weaker. Hence, restricting the analysis to the higher order SB leads to reliable results in those cases. Another observation made frequently in multispin systems is the presence of even-order sidebands. These sidebands arise ERM or, more precisely spoken, from the evolution of a DQ coherence during t_1 under the influence of dipole-dipole coupling to other spins not involved in the actual DQ coherence. Since ERM is suppressed by fast MAS, spinning faster generally leads to a more efficient suppression of the unwanted centerband and even-order sideband intensity.

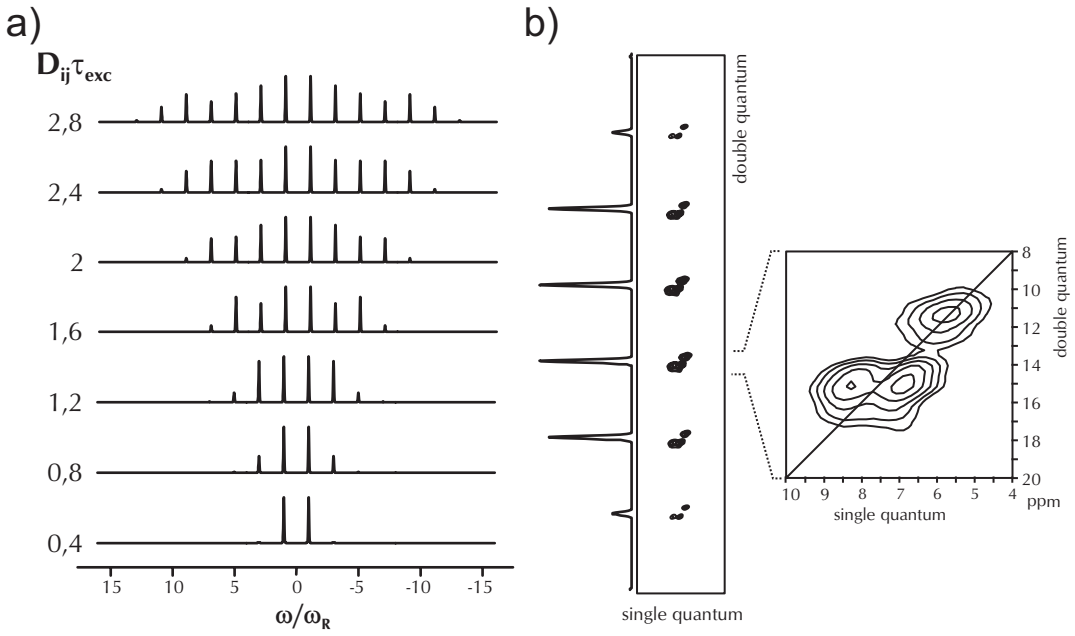

Figure 3.7: *(a) Calculated DQ spinning sideband patterns for various $D_{ij}\tau_{exc}$. (b) Idealized full 2D DQ sideband spectrum providing chemical shift resolution as well. The magnification shows that each "sideband" in fact consists of a full chemical shift resolved spectrum.*

Experimentally, the t_1 increment is chosen to give 20-25 points per rotor period, i.e. $\Delta t_1 = \frac{\tau_R}{n_P}$ with n_P being the number of points per rotor period. A point not mentioned yet, is that, of course, chemical shift evolution during t_1 is still present. Therefore, DQ sideband patterns have to be recorded with the evolution time covering a sufficient number of rotor periods, in order to obtain the chemical shift information as well. This requires usually a lot of slices in the t_1 dimension (512 or more points in F1), but allows one to separate the sideband patterns arising from the dipole-dipole coupling of a spin A to a spin B and another spin C, provided that B and C have different chemical shifts. Each sideband contains an intensity weighted full "rotor-synchronized" spectrum, and sideband patterns arising from the various couplings can be distinguished. In Fig. 3.7(b) a schematic representation of a full 2D spectrum is shown.

3.4 REDOR-based Heteronuclear Dipole-Dipole Recoupling Experiments

In this section a variety of techniques based on recoupling the ^{1}H -X heteronuclear dipole-dipole coupling will be presented. Compared to homonuclear ^{1}H methods, the heteronuclear approach benefits from the higher chemical shift resolution of most X nuclei. All experiments rely on the homonuclear decoupling efficiency of very fast MAS and are based on REDOR-type π pulse trains in order to achieve heteronuclear dipolar recoupling.
Before turning to the particular experiments in detail, the average Hamiltonian under a REDOR-type π pulse train needs to be considered. Starting from initial proton transversal magnetization (the treatment for initial S transversal magnetization is analogous), the evolution over one rotor period of the recoupling π pulse train reads as

$$\hat{I}_x \xrightarrow{\Phi\, 2\hat{I}_z\hat{S}_z} \hat{I}_x\cos\Phi + 2\hat{I}_y\hat{S}_z\sin\Phi \tag{3.18}$$

$$\xrightarrow{\pi\hat{S}_x} \hat{I}_x\cos\Phi - 2\hat{I}_y\hat{S}_z\sin\Phi \tag{3.19}$$

$$\xrightarrow{\Phi'\, 2\hat{I}_z\hat{S}_z} \hat{I}_x\left(\cos\Phi\cos\Phi' + \sin\Phi\sin\Phi'\right) - 2\hat{I}_y\hat{S}_z\left(\sin\Phi\cos\Phi' - \cos\Phi\sin\Phi'\right)$$
$$\overset{\Phi=-\Phi'}{=} \hat{I}_x\cos 2\Phi - 2\hat{I}_y\hat{S}_z\sin 2\Phi \tag{3.20}$$

$$\xrightarrow{\pi\hat{S}_y} \hat{I}_x\cos 2\Phi + 2\hat{I}_y\hat{S}_z\sin 2\Phi \tag{3.21}$$

For clarity, the shorthand notations $\Phi = -\Phi_{D_{is}}\big|_0^{\frac{\tau_R}{2}}$ and $\Phi' = -\Phi_{D_{is}}\big|_{\frac{\tau_R}{2}}^{\tau_R}$ are used with $\Phi_{D_{is}}\big|_{t_1}^{t_2}$ being defined in Eq. (2.55). The equality $\Phi' = -\Phi$ used in Eq. (3.20) corresponds to the effective inversion of the space part of the Hamiltonian by MAS. The second π pulse in Eq. (3.21) needs to be included in order to describe a full cycle, i.e. one rotor period, of the recoupling pulse train. Comparing Eq. (3.18) with Eq. (3.21) shows that the evolution over one rotor period of the recoupling π pulse train can conveniently be described by an average Hamiltonian,

$$\hat{\bar{\boldsymbol{H}}}_{is} = \bar{\Phi}\, 2\hat{I}_z\hat{S}_z\tfrac{1}{\tau_R}, \quad \text{where} \tag{3.22}$$

$$\bar{\Phi} = 2\Phi = -2\Phi_{D_{is}}\big|_0^{\frac{\tau_R}{2}} = \frac{D_{is}}{\omega_R}2\sqrt{2}\sin 2\beta\sin\gamma \tag{3.23}$$

Consequently, the evolution over a pulse train of N rotor periods length is given by

$$\hat{I}_x \xrightarrow{\hat{\bar{\boldsymbol{H}}}_{is} N\tau_R} \hat{I}_x\cos\left(N\bar{\Phi}\right) + 2\hat{I}_y\hat{S}_z\sin\left(N\bar{\Phi}\right). \tag{3.24}$$

As can be shown easily by applying π pulses with arbitrary phases in Eq. (3.18)– Eq. (3.21), neither the phase nor the channel where the π pulses are applied have any influence on the average Hamiltonian. This freedom marks a great advantage, since it allows schemes of π pulse trains to be implemented, which are compensated for offsets, chemical-shift anisotropy, and pulse imperfections. The (xy-4) phase cycling scheme [Gullion 90] has turned out to be particular useful and was implemented in all experiments presented here.
Typically, a heteronuclear dipolar correlation experiment can as well be separated into the characteristic four stages of a MQ experiment. In the case of the experiments presented here, excitation and reconversion are achieved by π pulse trains, which are typically intersected by the evolution time t_1. The first π pulse train results (according to Eq. (3.24)) in a *cosine*-modulation of the initial coherence and a *sine*-modulated antiphase coherence. Analogously, an antiphase coherence can be converted back into a transverse coherence state by the reconversion π pulse train. The differences in the various techniques arise from the fact that different coherences can be created and probed during the t_1 evolution time. The experiments are distinguished by: (i) the nucleus from which the recoupling process is started (either ^{1}H or any X-nucleus whose polarization is enhanced by CP), (ii) the detected nucleus (either conventional X or inverse ^{1}H -detection), and (iii) in the coherence state probed in the indirect dimension of the 2D experiment. In table 3.1 the various experiments are listed. Fig. 3.8 shows some of the corresponding pulse sequences.
The TEDOR experiment [Hing 92] was the first of such experiments. However, as the t_1 evolution period is placed at the beginning of the experiment, it lacks the possibility to create sidebands by reconversion rotor encoding and will therefore not be discussed in more detail here. The other experiments can be distinguished further by the symmetry of the coherence pathway and by the question whether polarization is transferred between the nuclei. From those experiments only the class of the DIP experiments [Saalwächter 01b] is symmetric with respect to the recoupling procedure, i.e. the direction of recoupling is from S to I to S again. The other experiments are asymmetric with respect to the recoupling procedure, with the polarization being transferred from I to S. This important aspect of using initial proton magnetization for the generation of HMQ coherences, via which the polarization is later transferred to the carbon channel, is reflected in the name of this class of experiments, namely the REPT (*re*coupled *p*olarization *t*ransfer) techniques. In solution-state NMR this concept is very famous under the acronym INEPT (*i*nsensitive *n*uclei *e*nhanced by *p*olarization *t*ransfer) [Morris 79], where J-couplings are responsible for the generation of the HMQ coherences. The obvious advantage of the REPT techniques is that no initial CP step is involved, which is usually not very efficient under fast MAS conditions. Recently, inversely detected experiments were introduced [Schnell 01a], which again are symmetric with respect to the recoupling procedure.
Of relevance for the work presented here are mainly three of the techniques listed in table 3.1, namely REPT-HSQC, REPT-HDOR and REREDOR. In the following three sections these experiments will therefore be discussed in more detail.

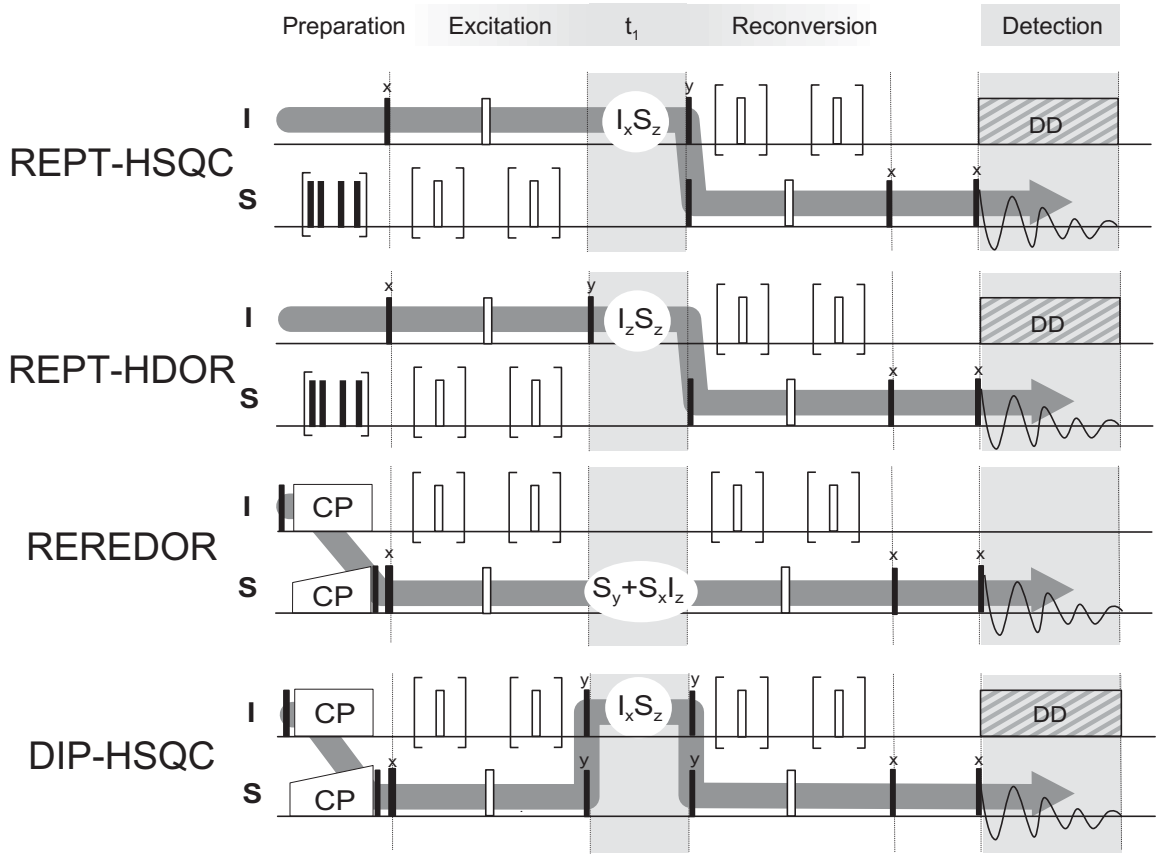

Figure 3.8: *Pulse sequences for heteronuclear correlation spectra based on REDOR. The grey arrows indicate the possible pathways for the transverse components of the coherence states present in the indirect dimension* t_1.

Table 3.1: *Heteronuclear correlation experiments based on REDOR-type π pulse trains*

	(i) starting from	(ii) detected on	(iii) coherence during t_1	Reference
TEDOR	$\hat{I}_{x/y}$	S	$\hat{I}_{x/y}$	[Hing 92]
REPT-HMQC	$\hat{I}_{x/y}$	S	$2\hat{I}_x\hat{S}_x$	[Saalwächter 99] [Saalwächter 01a]
REPT-HSQC	$\hat{I}_{x/y}$	S	$2\hat{I}_x\hat{S}_z$	[Saalwächter 01a]
REPT-HDOR	$\hat{I}_{x/y}$	S	$2\hat{I}_z\hat{S}_z$	[Saalwächter 01a]
DIP-HMQC	$\hat{S}_{x/y}$	S	$2\hat{S}_y\hat{I}_x$	[Saalwächter 01b]
DIP-HSQC	$\hat{S}_{x/y}$	S	$2\hat{S}_z\hat{I}_x$	[Saalwächter 01b]
DIP-HDOR	$\hat{S}_{x/y}$	S	$2\hat{S}_z\hat{I}_z$	[Saalwächter 01b]
REREDOR	$\hat{S}_{x/y}$	S	$\hat{S}_y + 2\hat{S}_y\hat{I}_z$	[Saalwächter 02c]
RELM	$\hat{S}_{x/y}$	S	$\hat{S}_z$	[De Paul 00]
inv. det. HSQC	$\hat{I}_{x/y}$	I	$2\hat{I}_x\hat{S}_z$	[Schnell 01a]
inv. det. TEDOR/REPT	$\hat{S}_{x/y}$	I	$\hat{S}_x$ / $2\hat{S}_z\hat{I}_z$	[Schnell 02]

3.4.1 REPT-HSQC

The REPT-HSQC experiment [Saalwächter 01a], whose pulse sequence is depicted in Fig. 3.8, can, in a way, be seen as the heteronuclear equivalent of the BABA experiment. Like the BABA experiment, it can be performed in three different ways: (i) Setting $t_1 = 0$ in the one-dimensional version and varying the length of the recoupling period leads to HSQC build-up curves, which are sensitive to the strength of the underlying heteronuclear dipole-dipole coupling. (ii) Incrementing t_1 in steps of full rotor periods in a two-dimensional experiment provides heteronuclear correlation (HETCOR) spectra, correlating the S spin chemical shift in the direct dimension with the I-spin chemical shift in the indirect dimension. (iii) Incrementing t_1 in smaller steps leads to spinning sidebands by RRE, from which the dipole-dipole coupling constant can be derived. Since the REPT-HDOR and the REREDOR experiment presented in the next section provide more elegant and - most importantly- time-saving ways to determine dipole-dipole coupling constants, this REPT-HSQC sidebands are not used in practice.

For the theoretical description, the t_1 dependence of the S-detected experiment needs to be

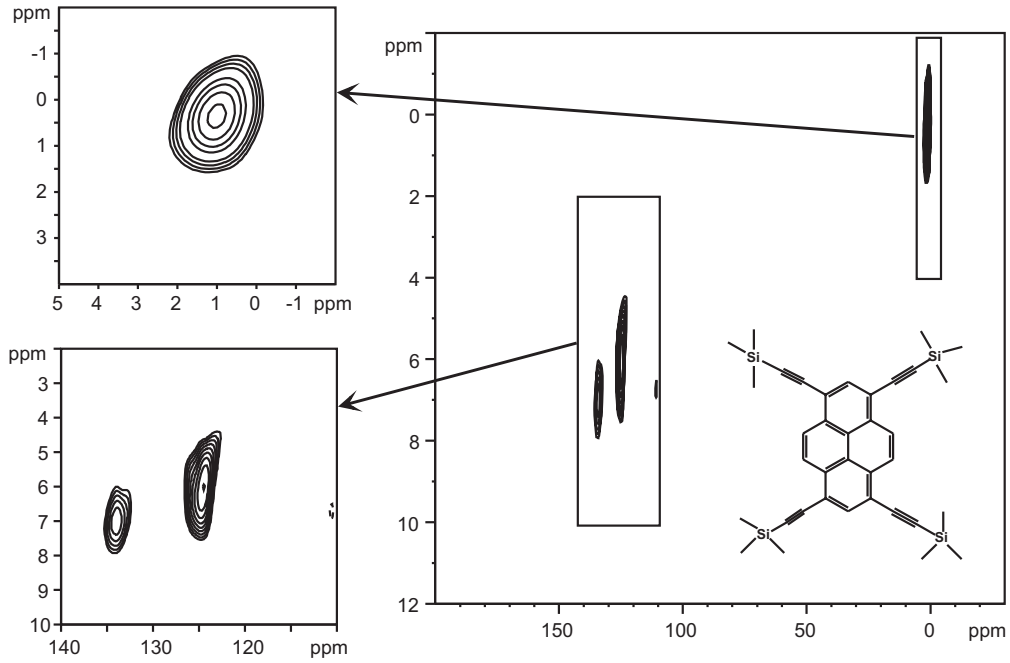

Figure 3.9: *Heteronuclear correlation spectrum of a pyrene derivative obtained with the REPT-HSQC sequence at 30 kHz MAS and a excitation time of $1\tau_R$. Clearly, well-resolved correlation peaks for the various sites can be distinguished, allowing for an assignment of the resonances.*

considered. The antiphase coherence, $\hat{I}_x\hat{S}_z$, which was created by the first π pulse train, evolves during t_1 under the influence of the chemical shift and the dipole-dipole couplings. Considering only the isotropic chemical shift evolution of the I spins, the x- and y- components of the signal are modulated in addition by *cosine* and *sine* factors which are functions of $\omega_{CS,I}t_1$. Proton CSA is usually small and can therefore be neglected. After reconversion to observable SQ coherence, the two components of the S-detected signal read as:

$$S_x(t_1) = \langle sin(N_{exc}\bar{\Phi}_0)sin(N_{rec}\bar{\Phi}_{t_1})cos(\omega)_{CS,I}t_1)\rangle, \tag{3.25}$$

$$S_y(t_1) = \langle sin(N_{exc}\bar{\Phi}_0)sin(N_{rec}\bar{\Phi}_{t_1})sin(\omega)_{CS,I}t_1)\rangle. \tag{3.26}$$

In order to obtain the full phase information for the indirect dimension, the *cosine* and *sine* modulated components need to be acquired separately. This is usually done by the TPPI procedure, which was described in section 3.2. From Eq. (3.25) it follows immediately that in the rotor-synchronized experiment (i.e. $\Delta t_1 = \tau_R$) the t_1 dependent signal is modulated only by the isotropic chemical shift of the I spins. Hence, a heteronuclear correlation spectrum is recorded, in which the intensity of the correlation peaks is determined by the strength of the underlying dipole-dipole coupling and the number of recoupling cycles N_{rcpl}. As an example, the correlation spectrum of a pyrene derivative is shown in Fig. 3.9. At the short recoupling time ($1\tau_R$ at 30 kHz MAS) chosen for this experiment, correlation peaks occur almost only for

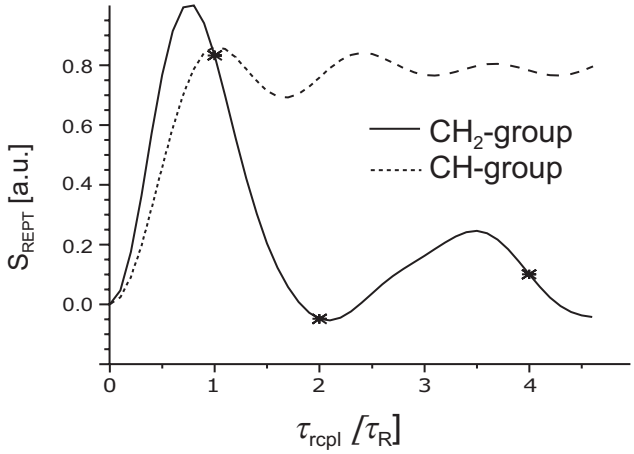

Figure 3.10: *Theoretical HSQC build-up curve for a CH group and a CH_2 group at 25 kHz MAS. Note that at a recoupling time of two rotor periods the CH_2 signal becomes zero.*

directly bonded, i.e. strongly coupled, ^{1}H -^{13}C pairs. Thus, HETCOR spectra are particular useful for spectral assignment purposes.
The build-up behavior, i.e. the change of the one-dimensional filtered signal intensity with increasing recoupling time, provides a quick way to get an estimate for the strength of the underlying dipole-dipole couplings. In Fig. 3.10 calculated build-up curves for a rigid, directly bonded CH spin pair and a CH_2 group are shown. Naturally, the build-up behavior of the CH_2 group strongly deviates from the build-up behavior of a spin pair. For CH_2 groups (and CH_3 groups) it is necessary to expand the treatment to the three (four) involved spins. The full treatment for multispin systems (including CH_2 and CH_3 groups) can be found in [Saalwächter 01a]. Regarding the theoretical build-up curve of a CH_2 group, a peculiarity of CH_2 groups meets the eye, namely that the signal intensity becomes zero at a recoupling time of around 80μs (two rotor periods at 25 kHz MAS). This proposes a problem when rigid CH_2 groups are to be detected, but this problem can easily be circumvented by using the REREDOR approach, which is described in section 3.4.3.

3.4.2 REPT-HDOR

The REPT-HDOR experiment, whose pulse sequence is depicted in Fig. 3.8, is based on creating a state of dipolar longitudinal order, $\hat{I}_z\hat{S}_z$, during t_1. After the build-up of antiphase coherence, $2\hat{I}_x\hat{S}_z$, during the excitation time, the antiphase coherence is converted into a state of longitudinal dipolar order, $\hat{I}_z\hat{S}_z$, by a 90° pulse on the I spins. After t_1 this state is converted back into antiphase coherence,$\hat{I}_z\hat{S}_y$, by a 90° pulse on the S spins. During the subsequent reconversion period this antiphase coherence evolves back into observable SQ coherence. The advantage of creating a state of heteronuclear dipolar order is that it does not evolve during t_1.

Hence, the S-detected signal of the HDOR experiment simply reads as

$$S_x(t_1) = \langle sin(N_{exc}\bar{\Phi}_0) sin(N_{rec}\bar{\Phi}_{t_1})\rangle, \tag{3.27}$$
$$S_y(t_1) = \langle sin(N_{exc}\bar{\Phi}_0) sin(N_{rec}\bar{\Phi}_{t_1})\rangle. \tag{3.28}$$

Clearly, the amplitude modulation measured as a function of t_1 is solely due to rotor encoding and leads to odd-order spinning sidebands only, which are centered around the zero offset frequency in the indirect dimension. Also, due to the absence of I spin chemical shift contributions, no phase sensitive detection in t_1 is needed. The acquisition of a *cosine* data set in t_1 thus reduces the experiment time by a factor of two. Another great benefit in terms of experiment time arises from the fact that the signal in t_1 is periodic with respect to the rotor period, apart from a signal decay arising from T_1 relaxation of the respective spins. Since the T_1 relaxation times are usually much longer than the timescale of the MAS, a decay is mostly not observed. Hence, all information is comprised in only one rotor period of t_1 evolution. Practically, two rotor periods evolution are recorded in t_1 and concatenated prior to Fourier transformation in order to avoid *sinc* cut-off wiggles. This bears the advantage that the spinning sidebands can be artificially narrowed and no strong gaussian line-broadening is required to suppress *sinc* cut-off wiggles, as might be necessary for the directly 2D Fourier-transformed spectrum. However, the concatenation procedure results in the appearance of correlated noise that contributes randomly to the sideband intensities. Using two rotor periods of evolution for the concatenation leads to such correlated noise also at half rotor period intervals, which allows the overall noise contribution to the sideband intensities to be estimated. The resulting sideband patterns can be fitted to yield the heteronuclear dipole-dipole coupling constant. In Fig. 3.11 the REPT-HDOR spectrum of a pyrene derivative is exemplary shown together with an extracted sideband pattern.

In the case of multispin systems (e.g. CH_2 and CH_3 groups) the simple spin pair formula from Eq. (3.27) must also be replaced by appropriate multispin formulas as described in [Saalwächter 01a]. It should be noted that in the REPT-HDOR experiment CH_2 groups also exhibit zero signal at around 80μs recoupling time. Hence, the generation of spinning sideband patterns for CH_2 groups with REPT-HDOR is virtually impossible. If CH_2 groups are to be investigated, the REREDOR experiment presented in the next section provides an excellent alternative.

Like in any other recoupling experiment generating spinning sidebands by reconversion rotor encoding, the number of spinning sidebands can deliberately be adjusted by the length of the recoupling time, since it depends on the product $D_{is}\tau_{rcpl}$. Note that the master plot showing calculated sideband patterns for REPT-HDOR (Fig. 3.12) deviates from the corresponding plot of the BABA experiment due to the difference between homonuclear and heteronuclear dipole-dipole coupling by a factor of $\frac{3}{2}$. In Fig. 3.12 sideband patterns for various values of $D_{is}\tau_{rcpl}$ are shown together with the corresponding build-up curve. Practically, the recoupling time is chosen in such a way that $D_{is}\tau_{rcpl} \approx 1.6$.

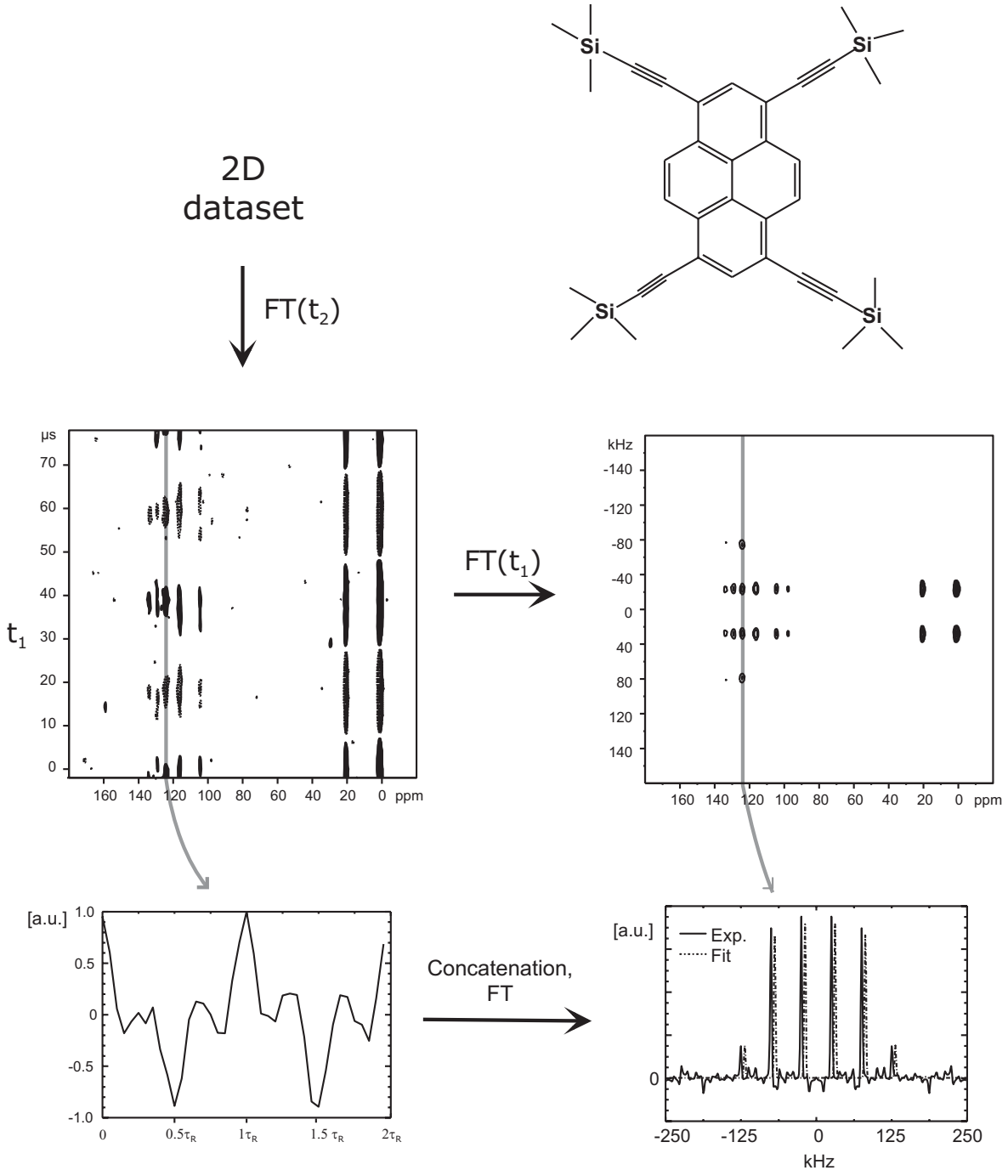

Figure 3.11: *REPT-HDOR experiment of a pyrene derivative (shown on the upper right) at 25 kHz MAS and $\tau_{rcpl} = 2\tau_R$. The two-dimensional data set can directly be subjected to a 2D Fourier transformation to yield the sideband patterns as slices along the indirect dimension. Alternatively, after FT along the direct (F2) dimension slices along t_1 can be extracted and (possibly) concatenated before the second FT, which saves experiment time, because less slices in t_1 are required. The resulting sideband patterns were fitted to yield the dipole-dipole coupling constants. A coupling constant of $D_{is}/2\pi$=22.2 kHz was obtained for the aromatic CH resonance at 124 ppm, which is typical for rigid aromatic CH pairs.*

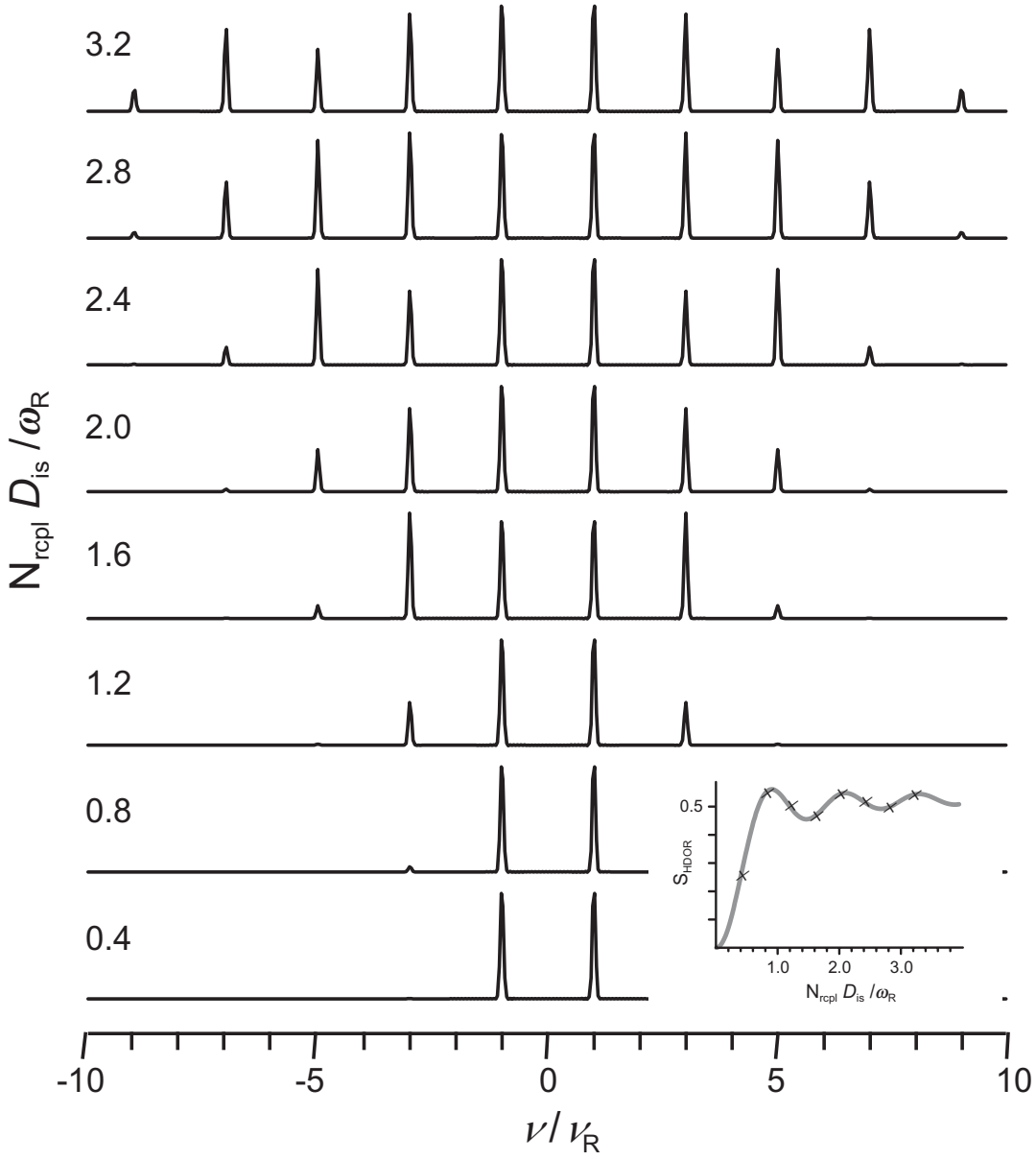

Figure 3.12: *Calculated REPT-HDOR sideband patterns for various $D_{is}\tau_{rcpl}$. The inset shows the corresponding build-up curve with the experimentally accessible points marked by asterisks.*

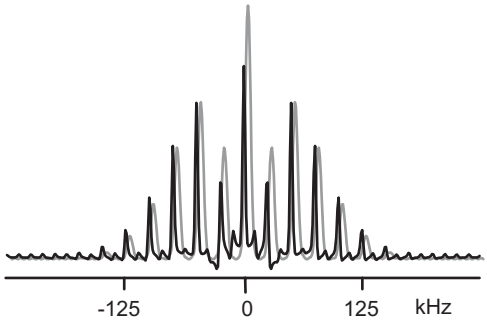

Figure 3.13: *REREDOR sideband patterns of the CH group in L-Alanine measured at 25 kHz MAS and $\tau_{rcpl} = 2\tau_R$. The underlying grey pattern is a simulation with $D_{is}/2\pi = 21kHz$.*

In conclusion, the REPT-HDOR experiment makes the determination of heteronuclear dipole-dipole coupling constants in samples with ^{13}C in natural abundance possible within reasonable measuring times. Most HDOR spectra presented in this thesis were measured within less than 12 hours of experiment time.

3.4.3 REREDOR

The REREDOR (*r*otor *e*ncoded REDOR) experiment [Saalwächter 02c] is based on simply inserting a t_1 delay after *both* excitation *and* recoupling period (see Fig. 3.8). Like the REPT-HDOR experiment it can be used to generate spinning sideband patterns by reconversion rotor encoding. The REREDOR time evolution is calculated by summation of the phases acquired under the action of the whole sequence $(excitation - t_1 - reconversion - t_1)$:

$$S \propto \langle \prod_i cos\left(N_{exc}\bar{\Phi}_0^{(i)} - \Phi^{(i)}|_0^{t_1} - N_{rec}\bar{\Phi}_{t_1}^{(i)} + \Phi^{(i)}|_{t_1}^{2t_1}\right)\rangle. \tag{3.29}$$

The product already includes the possibility of couplings to more than one spin. The REREDOR experiment has two main advantages as compared to the REPT-HDOR experiment: First, CH_2 groups do not exhibit zero signal at around 80 μs recoupling time. Hence, a sufficient number of sidebands can be created allowing for the precise determination of the dipole-dipole coupling constant. Thus, the REREDOR experiment is particular interesting for CH_2 groups. Second, the experiment results in even *and* odd order sidebands. This fact becomes clear when neglecting the two $\Phi|_{t_a}^{t_b}$ terms in Eq. (3.29), which is feasible under conditions of very fast MAS and/or weak dipole-dipole coupling constants, since these terms describe the residual dipolar evolution during the two t_1 intervals. Restricting to the dominating recoupling terms and a single pair coupling, Eq. (3.29) becomes

$$S \propto \langle cos(N_{exc}\bar{\Phi}_0 - N_{rec}\bar{\Phi}_{t_1})\rangle \tag{3.30}$$

$$\propto \langle sinN_{exc}\bar{\Phi}_0 sinN_{rec}\bar{\Phi}_{t_1}\rangle + \langle cosN_{exc}\bar{\Phi}_0 cosN_{rec}\bar{\Phi}_{t_1}\rangle. \tag{3.31}$$

Clearly, both odd-order (*sin-sin* term) and even order (*cos-cos* term) sidebands are created. Hence, restricting to the approximation in Eq. (3.30), formally a REREDOR sideband pattern can be decomposed into a sum of a REPT-HDOR (only *sin-sin* term, only odd-order SB) and a RELM (only *cos-cos* term, only even-order SB) experiment. From this it is clear that the REREDOR experiment should be more sensitive than the other heteronuclear recoupling methods presented here, since it generates more sidebands.
In conclusion, the REREDOR experiment provides the most efficient way for the determination of dipole-dipole coupling constants, provided that the initial CP is efficient. As will be shown in the course of this thesis, in mobile samples the initial CP step sometimes becomes very problematic. Exemplary, Fig. 3.13 shows the REREDOR sideband patterns extracted for the CH group in L-Alanine corresponding to $D_{is}/2\pi$ = 22 kHz.

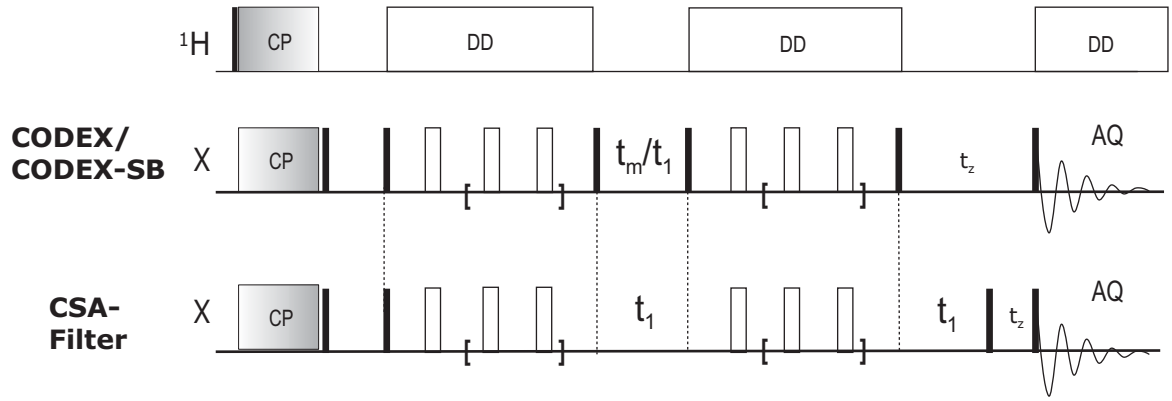

Figure 3.14: *Pulse sequence of the CODEX experiment and the CSA-Filter experiment, which deviates from the CODEX experiment only by omitting the two central 90° pulses for z-storage and by an additional t_1 delay before the final z-filter. In the case of the CODEX experiment a trigger is commonly used to ensure that the mixing time t_m is a multiple of the rotor period, $t_m = n\tau_R$. Replacing the mixing time by a t_1 period which is incremented in steps smaller than the rotor period leads to sidebands which are solely due to RRE. This is the CODEX-SB experiment used for most of the experimental work presented here.*

3.5 Recoupling the Chemical Shift Anisotropy: CODEX and CSA-sideband Patterns

In all the experiments presented in the previous section, even though not explicitly mentioned, much care was taken to *not* recouple the chemical shift anisotropy by placing at least one of the recoupling π pulses on the second channel. Of course, the chemical shift anisotropy can be recoupled on purpose by applying all π pulses on one channel. Then, a decoupling scheme must be applied during the π pulse trains on the other channel in order to avoid recoupling of the heteronuclear dipole-dipole coupling.
Recoupling the CSA by means of REDOR-type π pulse trains was first utilized in the CODEX experiment developed by Schmidt-Rohr and co-workers [deAzevedo 99, deAzevedo 00], whose pulse sequence is depicted in Fig. 3.14. In the CODEX experiment, the magnetization is stored on $\pm z$ for a mixing period $t_m = n\tau_R$, during which chemical exchange can be probed. By means of the phase cycle both the *sine* and the *cosine* modulated signal compound are selected for t_1 in subsequent scans. Since the mixing time is kept at integers of the rotor period (which is usually ensured by a trigger), the CODEX signal is simply given by

$$S \propto \langle cos(N_{exc}\bar{\Phi}_{CSA})cos(N_{rec}\bar{\Phi}'_{CSA}) + sin(N_{exc}\bar{\Phi}_{CSA})sin(N_{rec}\bar{\Phi}'_{CSA})\rangle. \tag{3.32}$$

The prime on the average phase of the reconversion period denotes that $\bar{\Phi}_{CSA}$ might change in the course of the long mixing time due to slow (*ms* timescale) molecular reorientation

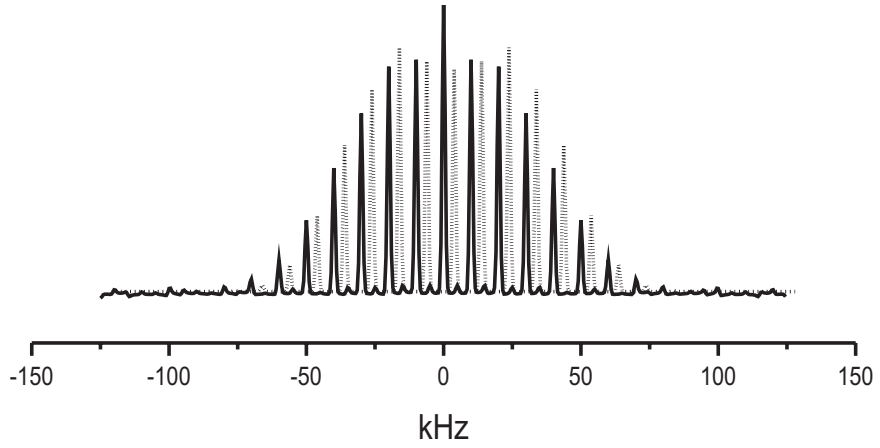

Figure 3.15: *CODEX-SB pattern of the COOH carbon of L-Alanine measured at 10 kHz MAS,* $\tau_{rcpl} = 2\tau_R$ *and a* ^{13}C *-*LARMOR *frequency of 125 MHz (solid line). Also shown is a simulation (dotted line) with the CSA-tensor values of* $\delta = 2\pi \cdot 5400Hz$ *and* $\eta = 0.83$*, which were taken from the literature [Naito 81].*

processes. Hence, with CODEX motional correlation times as well as information on the geometry of the underlying motional process become accessible.
The first CSA recoupling experiment probing the CSA as such was introduced by Mei Hong and co-workers [Hong 00]. There, CSA recoupling was used as a filter incorporated in a more complex sequence for identification of secondary protein structure and was consequently named CSA-filter experiment. The detailed analysis showed that the CSA-filter experiment is not sensitive to the asymmetry parameter η of the CSA, but rather to the width $\Delta\sigma$ of the CSA tensor. The t_1 dependent signal of the CSA-filter experiment is given by

$$S \propto \langle cos(N_{exc}\bar{\Phi}_{CSA}) - cos(N_{rec}\bar{\Phi}'_{CSA}) - \Phi'_{CSA}|_{0}^{t_1} + \Phi_{CSA}|_{t_1}^{t_2} \rangle. \tag{3.33}$$

The CSA-filter experiment can be used for the generation of spinning sidebands by RRE as is discussed in detail in [Fischbach 00]. Since sidebands created with the CSA-filter experiment also contain contributions from evolution during t_1, it can be seen as the CSA-analogue of the REREDOR experiment. Practically, for the work presented here, it has turned out to be more advantageous to create CSA sidebands with the CODEX experiment by replacing the mixing time by a t_1 evolution period with the increment during t_1 being a fraction of the rotor period. The advantage of these CODEX-SB is that they are solely due to RRE. Fig. 3.15 exemplarily shows the CODEX-SB pattern for the COOH-carbon of L-Alanine. The sidebands are spaced by the rotor frequency with even and odd sidebands present as is expected from Eq. (3.32).

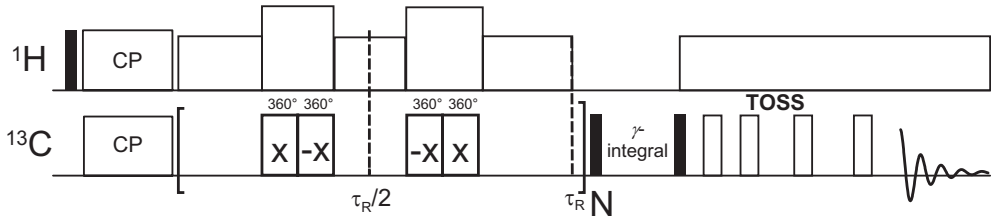

Figure 3.16: *Pulse sequence of the SUPER experiment.*

3.6 The SUPER Experiment

As mentioned above, the CSA-SB experiment is not suited for an accurate measurement of the asymmetry parameter η of the CSA. If the full CSA tensor information, i.e. all three principal values, is required in a site-resolved fashion, the SUPER experiment introduced by Schmidt-Rohr and co-workers [Liu 02] is the technique of choice. The SUPER (*s*eparation of *u*ndistorted *p*owder patterns by *e*ffortless *r*ecoupling) experiment is derived from the older technique of Tycko and co-workers [Tycko 89], which was suffering from a great sensitivity towards pulse length errors and other imperfections. These problems are largely overcome in the SUPER experiment by using 360° recoupling pulses instead of the 180° pulses, which are used for Tyckos experiment.
The pulse sequence of the SUPER experiment is shown in Fig. 3.16. Application of properly positioned 360° recoupling pulses leads to a quasi-static evolution during the recoupled evolution period

$$\bar{\omega} = \chi\prime\omega_{ani,stat} + \xi\prime\omega_{iso}, \tag{3.34}$$

where $\chi\prime$ and $\xi\prime$ are scalar scaling factors determined by the actual pulse positions. Since the 360° pulses alone would also recouple the heteronuclear dipole-dipole coupling, care needs to be taken to apply sufficiently strong dipolar decoupling during the recoupling pulses. Since the required pulse field strengths are multiples of the rotor frequency (typically $\omega_{360°rot} = 12.12\omega_R$ and $\omega_{1Hdec.} \geq 25\omega_R$), the SUPER experiment is limited to lower spinning frequencies of up to 7 kHz. Hence, it is usually necessary to suppress MAS spinning sidebands. This is accomplished by applying the four-pulse TOSS (*t*otal *s*uppression *o*f *s*pinning *s*idebands) scheme [Dixon 82] before detection. Since the TOSS scheme alone does not provide full sideband suppression in two-dimensional MAS experiments, it is combined with an incrementation of the preceding z period in four steps of $\tau_R/4$, which provides a "γ integral" that suppresses sidebands up to fourth order [deAzevedo 00]. For $\omega_R < |\sigma_{11} - \sigma_{33}|/2$, the CSA line shapes observed will not be perfect powder patterns, since some differential suppression of signals from different segmental orientations occurs. However, as long as the centerband is larger than the sidebands, this will lead only to an overall modulation of the CSA powder

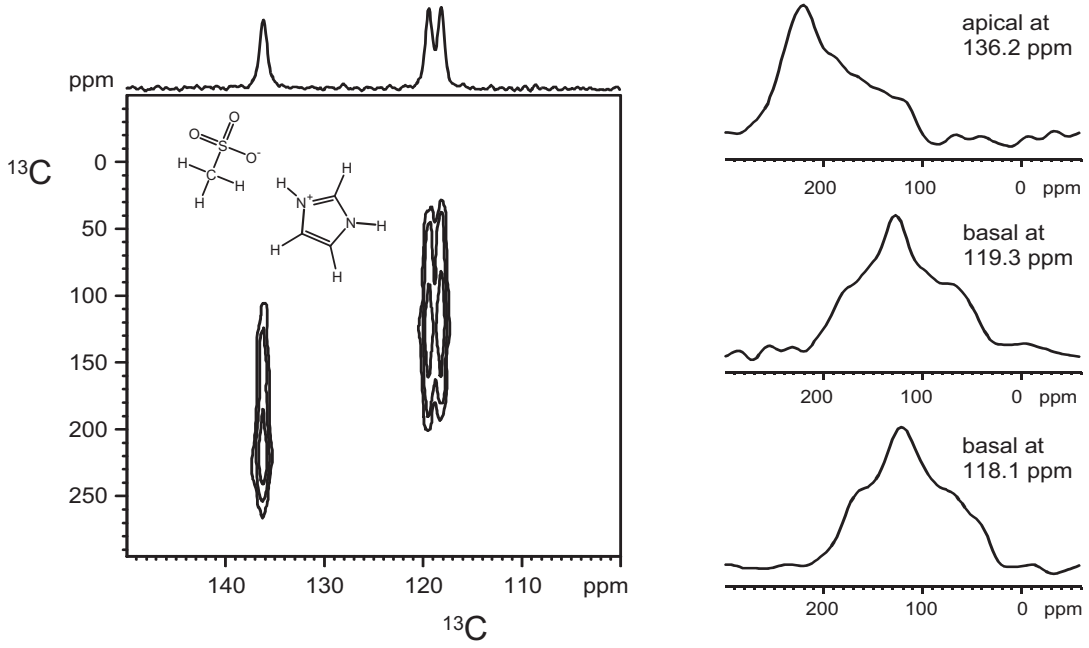

Figure 3.17: *^{13}C SUPER spectrum of imidazolium-methylsulfonate at 7 kHz MAS and 270 K. On the right the quasi-static powder patterns extracted as slices along the indirect dimension are shown. Since the spectrum was not subject to the shearing procedure described in [Liu 02] only the patterns of the peaks close to the offset at 118.7 ppm are roughly at the correct position. The pattern of the peak at 136.2 ppm needs to be shifted according to the scaled isotropic shift term in order to yield the correct CSA tensor values.*

line shape, but not to a change in the positions of the steps and the maximum on the spectrum, from which the chemical-shift principal values are determined. Due to the isotropic chemical shift term in Eq. (3.34), only the on-resonant signal will be in the indirect dimension at its genuine position. All other signals are shifted according to the scaled isotropic shift term as can be seen in the 2D SUPER spectrum of imidazolium-methylsulfonate, which is exemplary shown in Fig. 3.17. Since the frequency offset is known, it is usually not necessary to carry out a shearing procedure as it is described in [Liu 02]. Instead, the obtained tensor values can afterwards simply corrected for the known offset term. Since the SUPER experiment is very sensitive and remarkably robust with respect to pulse imperfections, field inhomogeneities and other imperfections, it can readily be used for CSA determination under MAS conditions.

Chapter 4

ω_R- and $2\omega_R$- Recoupling Experiments and Sample Orientation

In the previous chapter, MAS recoupling experiments were introduced as expedient tools for structure determination in solids. It was shown that they allow internuclear distances to be determined, neighborhood relationships to be elucidated and, furthermore, dynamic processes to be investigated, as the latter lead to a characteristic reduction of dipole-dipole coupling constants. The question addressed in this chapter is the influence of macroscopic sample orientation on the outcome of those recoupling experiments. This question becomes in particular interesting for liquid crystalline samples, such as the discotics studied in this thesis, since liquid crystalline systems can easily be oriented by various means [Chandrasekhar 98]. As will be shown on several oriented systems, macroscopic sample orientation can have very pronounced effects on the outcome of recoupling MAS NMR experiments.

Based on this, the question arises whether and to which extent recoupling experiments under MAS can be used for the determination of orientational order parameters and orientation distributions.
As it will turn out, the results from a single recoupling experiment can be quite ambiguous, when only the ω_R-modulated term of the respective interaction Hamiltonian is recoupled. This is due to its orientational dependence, which is given by the ambiguous term sin2β (Eq. (2.47)), where β denotes the angle between the rotor axis and the *z*-axis of the PAS of the respective interaction tensor. As is clear from Fig. 4.1 the sin2β function is unambiguous only over the interval $\beta = [0, \frac{\pi}{4}]$, i.e. the inverse function exists only over this interval. For measurements of tensor orientations usually unambiguity over the interval

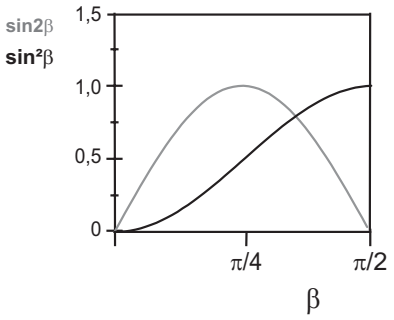

Figure 4.1: *sin*2β *and sin*$^2\beta$.

$\beta = [0, \frac{\pi}{2}]$ is desired. Hence, purely ω_R-recoupled experiments are unsuited for the determination of sample orientation. In the case of asymmetric tensors an additional dependence on the Euler-angle α has to be taken into account, but since this effect is not very pronounced it will be left out in the following general treatment.
As was shown in [Glaubitz 01] for CN_n^ν pulse sequences, the ambiguity of the term $\sin 2\beta$ can be overcome by simply recoupling the $2\omega_R$-modulated term of the respective interaction Hamiltonian, which exhibits an orientation dependence of $\sin^2\beta$ (also plotted in Fig. 4.1). Since the $\sin^2\beta$ function is invertable over the interval $\beta = [0, \frac{\pi}{2}]$, $2\omega_R$-recoupling provides unambiguous orientation information over this interval. Hence, $2\omega_R$-recoupling is advantageous for the determination of sample orientation.
Since $2\omega_R$-recoupling is a new variant of the laboratory frame recoupling experiments presented in chapter 3, the first section introduces $2\omega_R$-recoupled experiments as such. In the following sections results on various model systems will be presented.

4.1 Principles and Experimental Realization of $2\omega_R$-Recoupling

In section 3.1 of the previous chapter, the general principle for recoupling the ω_R-modulated term of an interaction Hamiltonian was explained. However, the Hamiltonian of a second rank tensorial interaction under MAS has also a term modulated by $2\omega_R$, as can directly be seen in Eq. (2.47) and was already pointed out in Eq. (2.56). The $2\omega_R$-modulated term was left out in the treatment in chapter 3, because it is averaged to zero under the recoupling conditions described there. This is graphically depicted Fig. 4.2. Clearly, for π pulses spaced by half a rotor period the contributions from the $2\omega_R$-modulation cancel. From Fig. 4.2 it also becomes immediately clear how $2\omega_R$-recoupling could be achieved. Since recoupling is based on a "counter-rotation" to the MAS rotation in spin space, the recoupling π pulses just need to be spaced by a quarter of a rotor period in order to recouple the $2\omega_R$-modulated term instead of the ω_R-modulated term. Naturally, for ω_R-recoupling a full echo occurs after one rotor period of t_1-evolution, whereas for $2\omega_R$-recoupling the echo already occurs after half a rotor period. Hence, in the $2\omega_R$-recoupled sideband patterns the spacing of the sidebands is twice the spacing in the ω_R-recoupled patterns. The recoupling time of the $2\omega_R$-recoupled experiment needs to be significant larger than in the ω_R-recoupled experiment. This becomes immediately clear, when regarding the integrated phase $\Phi_\lambda(t)$ (Eq. (2.47)) of an uniaxial ($\eta = 0$) interaction Hamiltonian

$$\Phi_\lambda(t) = -\frac{1}{\omega_R}\sin 2\beta\frac{\delta_\lambda}{\sqrt{2}}\{\sin(\gamma+\omega_R t)-\sin\gamma\} \tag{4.1}$$

$$+ \frac{1}{\sqrt{2}}\cdot\frac{1}{2\omega_R}\sin^2\beta\frac{\delta_\lambda}{\sqrt{2}}\{\sin(2\gamma+2\omega_R t)-\sin 2\gamma\}\,. \tag{4.2}$$

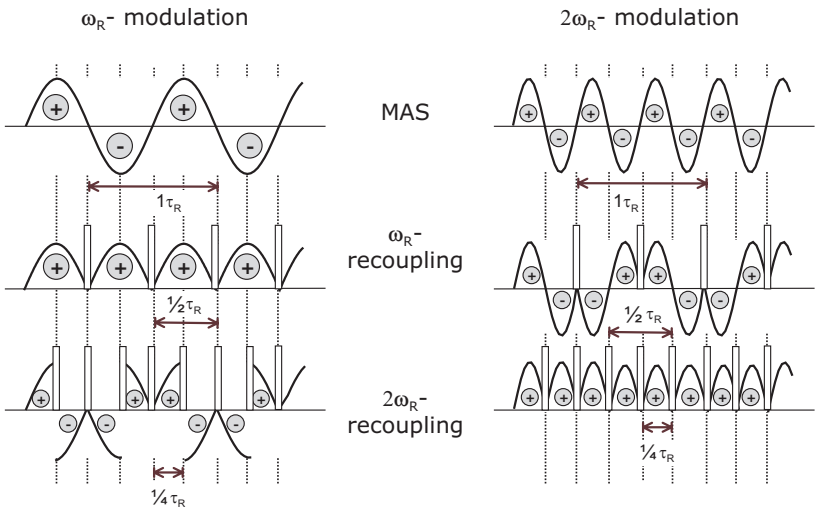

Figure 4.2: *Principle of $2\omega_R$-recoupling compared to ω_R-recoupling. On top the modulations under MAS are shown. Clearly, both the ω_R- and the $2\omega_R$- modulated term are averaged to zero by MAS. Employing a REDOR-type π pulse train with the pulses spaced by exactly half a rotor period (ω_R-recoupling) recouples the ω_R- modulated term, whereas the $2\omega_R$-modulated term is still averaged to zero, since the integrals over a full rotor period cancel as indicated by the $\oplus$ and $\ominus$ signs. In contrast, spacing the π pulses by a quarter of a rotor period recouples the $2\omega_R$-modulated term and averages the ω_R-modulated term to zero.*

Clearly, the $2\omega_R$-modulated term (Eq. (4.2)) exhibits an additional prefactor of $\frac{1}{\sqrt{2}}$, which scales the respective interaction and, hence, longer recoupling times are needed in order to generate a sufficient number of sidebands. Since a longer recoupling time implies less signal due to the increased number of recoupling pulses, $2\omega_R$-recoupling is in general less favorable unless sample orientation is investigated. Also, the increased number of recoupling pulses should lead to an increased sensitivity towards finite-pulse effects and pulse imperfections. Fig. 4.2 is somewhat misleading, since it suggests that excitation times being multiples of half a rotor period, $\tau_{exc} = n \cdot \frac{\tau_R}{2}$, can be used to obtain recoupling. However, regarding both the ω_R- and the $2\omega_R$- contributions, it is obvious that the periodicity of the recoupled integrated phase is still a rotor period for both ω_R- and $2\omega_R$-recoupling. Hence, care needs to be taken to keep the recoupling time at integers of a full rotor period.
In the following subsections the experimental realization of $2\omega_R$-recoupling will be presented for most of the experiments described in the previous chapter. It will turn out, that 'pure' $2\omega_R$-recoupling (i.e. no contributions to the average Hamiltonian, which are modulated by ω_R) is only achieved, if the coherence state present during t_1 is a longitudinal state, which is not subject to evolution. Otherwise, from the evolution during t_1 an ω_R-modulated term is introduced into the average Hamiltonian as will be discussed in detail on the example for the CSA-recoupling experiments in subsection 4.1.5.

4.1.1 BABA

In this subsection the practicability of $2\omega_R$-recoupling is proven for the BABA pulse sequence. In order to achieve $2\omega_R$-recoupling the spacing of the pulses was simply changed from $\tau_R/2$ to $\tau_R/4$. In Fig. 4.3 1D-filtered spectra and rotor-synchronized 2D-spectra are compared for ω_R- and $2\omega_R$-recoupling. As a model compound HBC-C_{12} deuterated at the α position of the sidechains was chosen, whose structure is depicted on top of Fig. 4.3. HBC-C_{12} is a well-studied system in terms of homonuclear ^{1}H DQ NMR [Brown 99]. As is clear from the structure, the aromatic protons form spin pairs with an internuclear distance of 2.0$\mathring{A}$. The advantage of the deuteration of the α positions of the sidechains is that in the spectra multispin effects for the aromatic protons are significantly reduced. In the middle of Fig. 4.3 1D DQ filtered spectra are shown for excitation times of 1, 2 and 4 rotor periods at 30 kHz MAS. The build-up behavior clearly reflects the difference in the scaling of the dipole-dipole coupling by the factor of $\frac{1}{\sqrt{2}}$. Whereas the maximum of the build-up curve for ω_R-recoupling is at around $\tau_{exc} = 1\tau_R$ (and not detected as such), the maximum for $2\omega_R$-recoupling is at a longer recoupling time of around $\tau_{exc} = 2\tau_R$. Clearly, for the estimation of the dipole-dipole coupling strength from the build-up behavior, $2\omega_R$-recoupling is preferable due to its smaller scaling factor. The smaller scaling factor shifts the maximum of the build-up curve towards longer recoupling times and, hence, the initial slope is less steep and, thus, provides a better estimation of the dipole-dipole coupling strength.
In the spectra, three aromatic proton peaks can be distinguished. These could be attributed to three different environments of the aromatic protons in the packing of the aromatic cores of the molecules [Brown 99]. The core packing is depicted on the right top of Fig. 4.3. In the 2D DQ spectra the splitting of the aromatic protons peaks is more pronounced, the detailed peak assignment can be found in [Brown 99]. Clearly, the ω_R- and the $2\omega_R$-recoupled 2D DQ spectra are identical, and provide basically the same information about neighborhood relationships. Only the relative peak intensities change, which is again due to the changed scaling factor of the dipole-dipole coupling in the $2\omega_R$-recoupled experiment.
The most significant differences between ω_R- and $2\omega_R$-recoupled BABA occur in the sideband patterns. In Fig. 4.4, BABA sideband patterns of the aromatic protons at 8.3 ppm are compared. As will be explained in detail in subsection 4.1.2, the spacing of the sidebands is twice the spacing of the sidebands in the corresponding ω_R-recoupled experiment. Also, a longer recoupling time of $4\tau_R$ instead of $2\tau_R$ needed to be employed in order to get a sufficient number of sidebands. In order to estimate the influence of multispin effects of the $2\omega_R$-recoupled BABA, a sideband pattern of non-deuterated HBC-C_{12} is shown in Fig. 4.4. The sideband patterns of the α-deuterated HBC-C_{12} can be simulated by a spin pair coupling with a dipole-dipole coupling constant of $D_{ij}/2\pi$=15 kHz corresponding to a distance between the aromatic protons of 2.0$\mathring{A}$. In contrast, for the simulation of the SB pattern of the non-deuterated HBC-C_{12} a third perturbing spin had to be taken into account, in order to yield the correct intensity ratios of the sidebands. A peculiarity occurring in

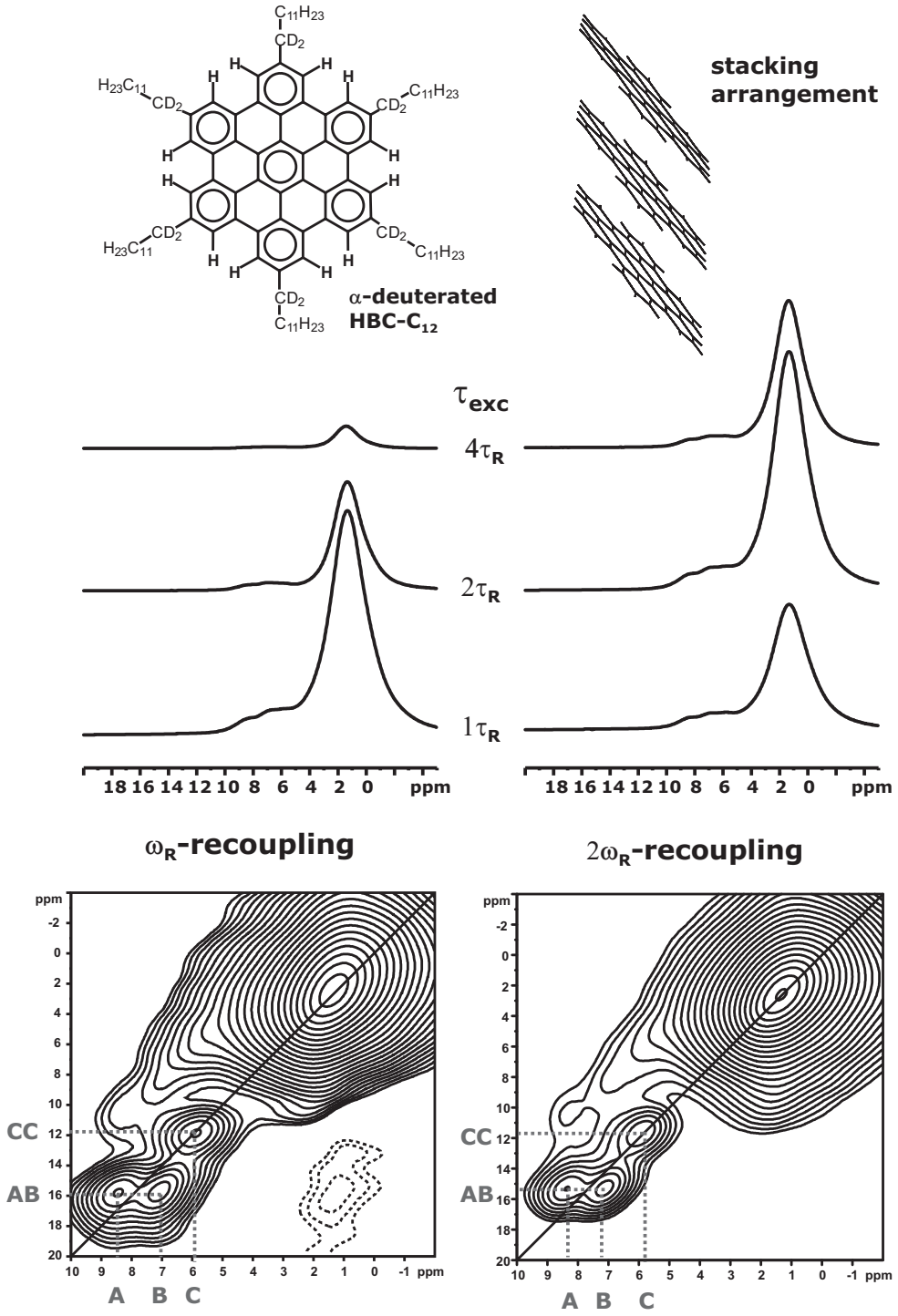

Figure 4.3: *ω_R- and $2\omega_R$-modulated BABA on α-deuterated HBC-C_{12}, whose structure is depicted on the top. In the middle 1D-DQ filtered spectra are shown for excitation times τ_{exc} of 1, 2 and 4τ_R at 30 kHz MAS. On the bottom 2D DQ spectra with $\tau_{exc} = \tau_R$ and $\tau_{exc} = 2\tau_R$, respectively, are shown. The aromatic proton signal is split into three distinct peaks. This could be attributed to the tilted packing arrangement in HBC-C_{12} [Brown 99], which is depicted on the upper right. Apart from different intensities due to the different scaling factors, the ω_R- and $2\omega_R$-recoupled experiments provide basically the same information.*

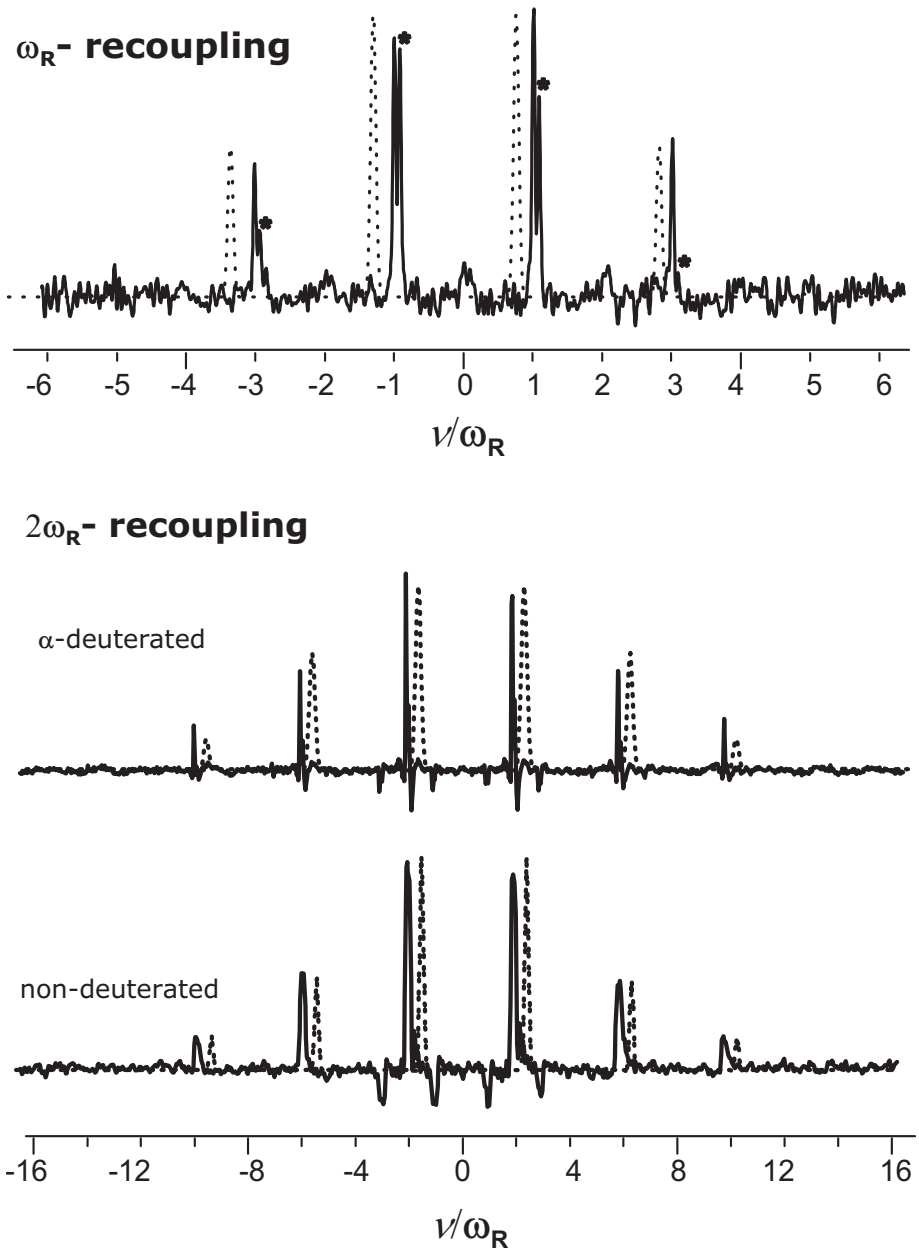

Figure 4.4: *BABA-SB patterns of the aromatic protons of HBC-C_{12} at 8.3 ppm:*
top: *α-deuterated HBC-C_{12}, ω_R-recoupling, $\tau_{exc} = 2\tau_R$, 35 kHz MAS (taken from [Brown 99]).*
middle: *α-deuterated HBC-C_{12}, $2\omega_R$-recoupling, $\tau_{exc} = 4\tau_R$, 30 kHz MAS.*
bottom: *non-deuterated HBC-C_{12}, $2\omega_R$-recoupling, $\tau_{exc} = 4\tau_R$, 30 kHz MAS.*
The dashed lines are simulations for a spin pair with $D_{ij}/2\pi$=15 kHz (top and middle) and a three spin system with the third spin being at the position of an α-CH_2 proton (bottom). The asterisks denote sidebands arising from the coupling to aliphatic protons.

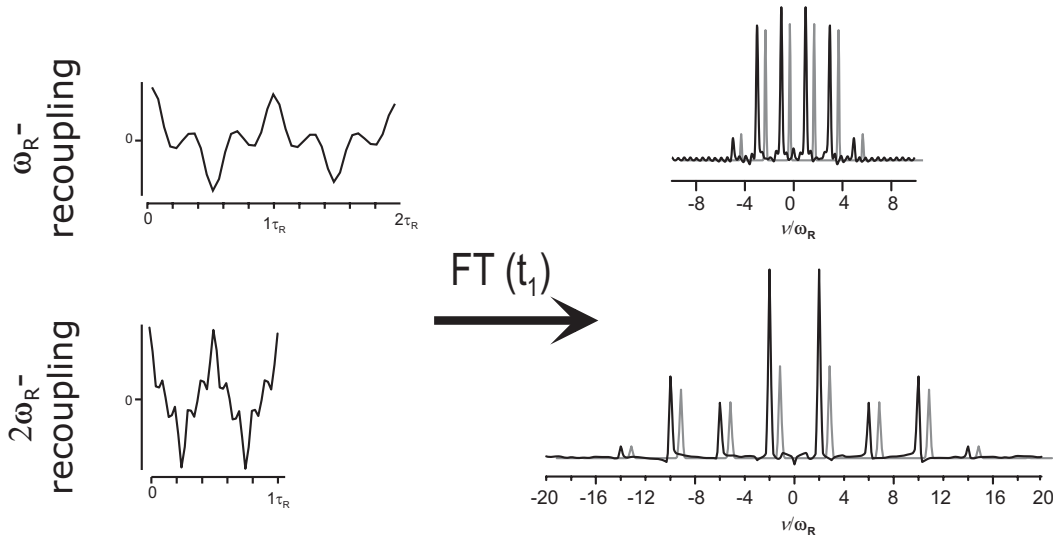

Figure 4.5: *ω_R- and $2\omega_R$-modulated HDOR SB-patterns and the corresponding t_1-modulations of the CH resonance of L-Alanine measured at 25 kHz MAS and $\tau_{rcpl} = 2\tau_R$ and $\tau_{rcpl} = 4\tau_R$ respectively. The grey SB-patterns are simulations for $r_{CH} = 1.13\mathring{A}$*

the $2\omega_R$-recoupled SB patterns is the occurrence of a superimposed 'negative' pattern with odd-order sidebands. Since this effect seems to be more pronounced in the patterns of the non-deuterated compound, it can be most probably be attributed to a multi-spin effect, even though such negative sidebands do not occur in the simulations including a third perturbing spin.

4.1.2 REPT-HDOR

For the $2\omega_R$-recoupled REPT-HDOR experiment, the pulse sequence also only needs to be modified by changing the spacing of the recoupling π pulses from half a rotor period to a quarter of a rotor period. In addition, in order to provide a sufficient spectral width in the indirect dimension, the t_1-increment is divided by two as compared to the ω_R-recoupled experiment. Due to the periodicity of half a rotor period of the $2\omega_R$-recoupled experiment, only one rotor period of evolution is sufficient for concatenation, allowing the total number of points in the t_1-dimension to be kept identical. In Fig. 4.5 ω_R- and $2\omega_R$-recoupled REPT-HDOR t_1-modulations and sideband patterns of the CH group of L-Alanine are shown. As expected, for ω_R-recoupling the full echo occurs after a full rotor period. For $2\omega_R$-recoupling the echo occurs after half a rotor period. Since in ω_R-recoupled REPT-HDOR spectra only odd (2n+1) order sidebands are present, it follows directly that the $2\omega_R$-recoupled spectra exhibit only sidebands of order $(2n+1)\cdot 2 = 4n+2$. Since during t_1 the coherence state is of longitudinal dipolar order ($2\hat{I}_z\hat{S}_z$) and, hence, not subject to evolution, no ω_R-modulated contribution (i.e.

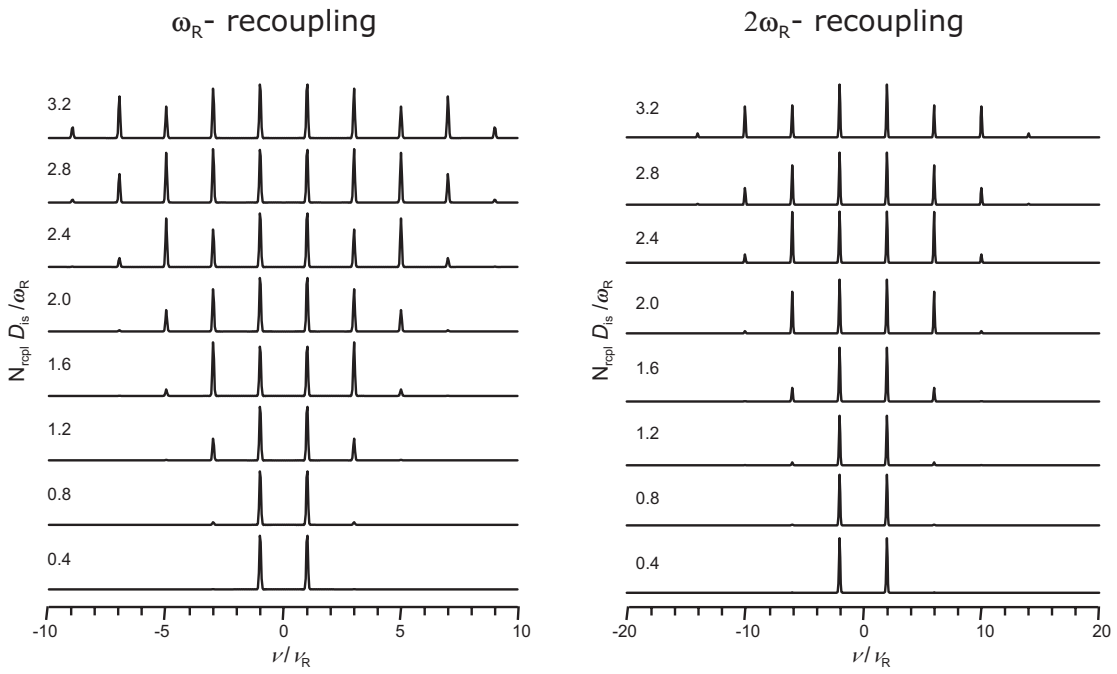

Figure 4.6: *Calculated REPT-HDOR SB patterns for ω_R- (left) and $2\omega_R$-recoupling (right).*

odd-order SB) arising from evolution during t_1 is present in the $2\omega_R$-recoupled SB patterns. It should be noted that the recoupling time of the $2\omega_R$-recoupled experiment needed to be $4\tau_R$ instead of $2\tau_R$ in order to get a sufficient number of sidebands due to the additional prefactor of $\frac{1}{\sqrt{2}}$ in Eq. (4.2). This necessity is illustrated in Fig. 4.6, where calculated ω_R- and $2\omega_R$-recoupled sideband patterns are compared for identical $D_{is}\tau_{rcpl}$. Clearly, in order to achieve an equal number of sidebands, the recoupling time for $2\omega_R$-recoupling has to be increased by $\sqrt{2}$ compared to ω_R-recoupling.

4.1.3 Influence of Remote Couplings

In the $2\omega_R$-recoupled SB pattern shown in Fig. 4.5, the second order SB are significantly too high. This observation is frequently made for ω_R-recoupled experiments and is discussed in detail in [Wind 02]. Excessive first order sidebands can be attributed to additional remote couplings, which are naturally weaker and therefore give rise to only first order SB. In dynamically heterogeneous systems, the additional first order SB intensity can arise from mobile fractions undergoing fast large-amplitude motions. The dipole-dipole couplings of these fast moieties are strongly reduced and, hence, contribute only to first order SB. Also, partial sample orientation might give rise under some circumstances to excessive first order SB as will be shown in the following sections. For the L-alanine sample both partial sample orientation (the sample was thoroughly ground before packing the rotor) and large amplitude motions

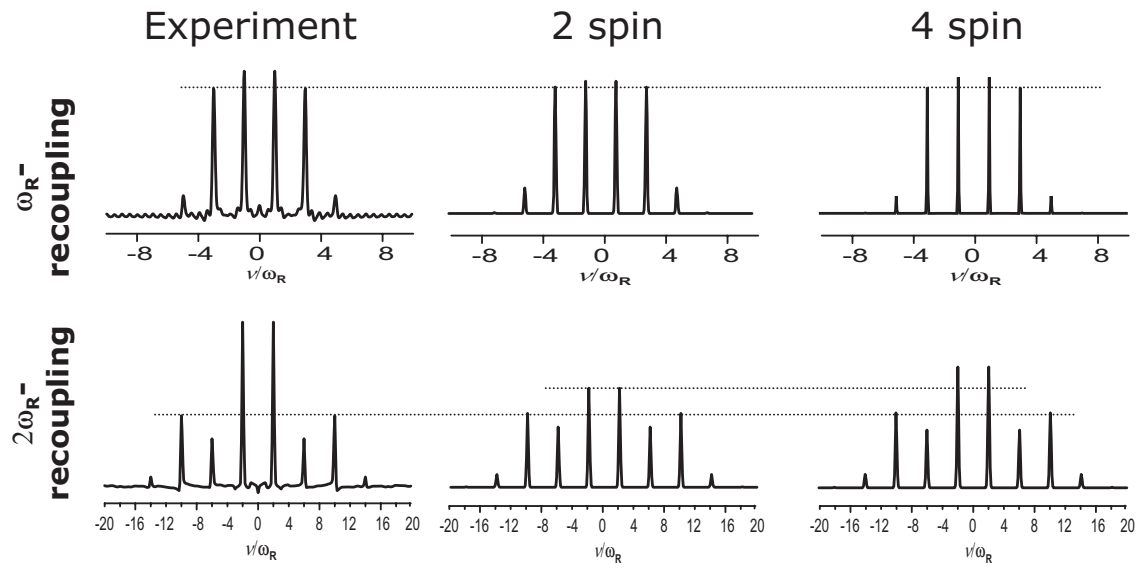

Figure 4.7: *Experimental REPT-HDOR SB patterns of L-Alanine compared with 2 spin simulations and 4 spin simulations.*

can be excluded. Hence, the excessive first order SB should be due to remote couplings. Consequently, additional simulations were carried out with the SIMPSON program [Bak 00] including couplings to remote protons.

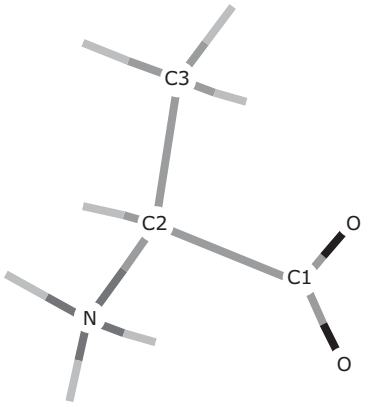

Figure 4.8: *Structure of L-Alanine.*

The next nearest protons to the C2 carbon in L-Alanine are the CH_3 and NH_3^+ protons at a distance of roughly $2.2\mathring{A}$, corresponding to additional couplings of around 3.3 kHz. The distances to protons of neighboring molecules in the crystal structure are much longer and thus, couplings to those protons are neglected. Nonetheless, one would be left with an 8 spin system for the calculation, which would require extensive calculation time. The calculation is further complicated by the fact that at room temperature the CH_3 and NH_3^+ group rotate fast around their internal C_3 symmetry axes. For the simulations this rotation was taken into account by reducing the dipole-dipole coupling to these protons by a factor of $\frac{1}{2}(3cos^2\theta - 1)$, where $\theta \approx 28°$ is the angle between the C-H axis and the rotation axis, which lies along the C2-C3 bond and N-C2 bond respectively. The reduced dipole-dipole coupling is then around 2.2 kHz. Thus, instead of six additional protons only two more protons need to be considered, which lie on the respective rotation axis at a distance from the C2 carbon given by the averaged dipole-dipole coupling. The fact that each of these 'dummy' protons represents three protons is taken into account

by the crude approximation that the dipole-dipole couplings can be added up according to $\bar{D}_{is} = \sqrt{D_{1,is}^2 + D_{2,is}^2 + D_{3,is}^2} = \sqrt{3}D_{is} \approx 2\pi * 3.2kHz$. Thus, one is left with a 4 spin simulation (the strongly coupled C-H pair and two remote protons causing additional couplings of 3.2 kHz each) to get an impression of the influence of remote couplings. The calculated SB patterns are shown in Fig. 4.7 together with the 2 spin simulations and the experimental patterns from Fig. 4.5 for comparison. Clearly, remote couplings lead to a significant increase of the second order sidebands in the $2\omega_R$-recoupled experiment. Interestingly, the effect is much less pronounced in the ω_R-recoupled patterns, which is probably due to the longer recoupling time (four rotor periods instead of two) of the $2\omega_R$ recoupled experiment, but as well might be coincidental insofar as only for this special spin system geometry the $2\omega_R$-recoupled experiment is more sensitive towards multispin effects than the ω_R-recoupled experiment. Nonetheless, the simulation does not lead to such a strong increase as it is observed in the experiment. This can be attributed to the fact that the used approximation is too crude and thus can only reflect the principal features, but not the details. Namely, the calculation was carried out assuming δ-pulses and, thus, does not account for finite-pulse effects. Previous investigations revealed that the main effect of finite pulses in REDOR experiments manifests in a duty cycle-dependent factor, which reduces the dipole-dipole coupling constant [Jaroniec 00]. Under normal experimental conditions for isolated spin pairs this reduction is only very small and usually negligible. In multi-spin systems the description of finite-pulse effects is more involved. Extensive simulations of a methyl group DQ signal of a BABA sequence with finite pulses revealed that the overall effect of finite pulses is still very weak and does not hamper the extraction of dipole-dipole coupling constants within reasonable accuracy [Saalwächter 02a], but still might slightly contribute to excessive intensity of the inner sidebands. Nevertheless, the 4 spin simulation clearly proves that the excessive second order sideband intensity in the $2\omega_R$-recoupled experiment must mainly attributed to remote couplings.

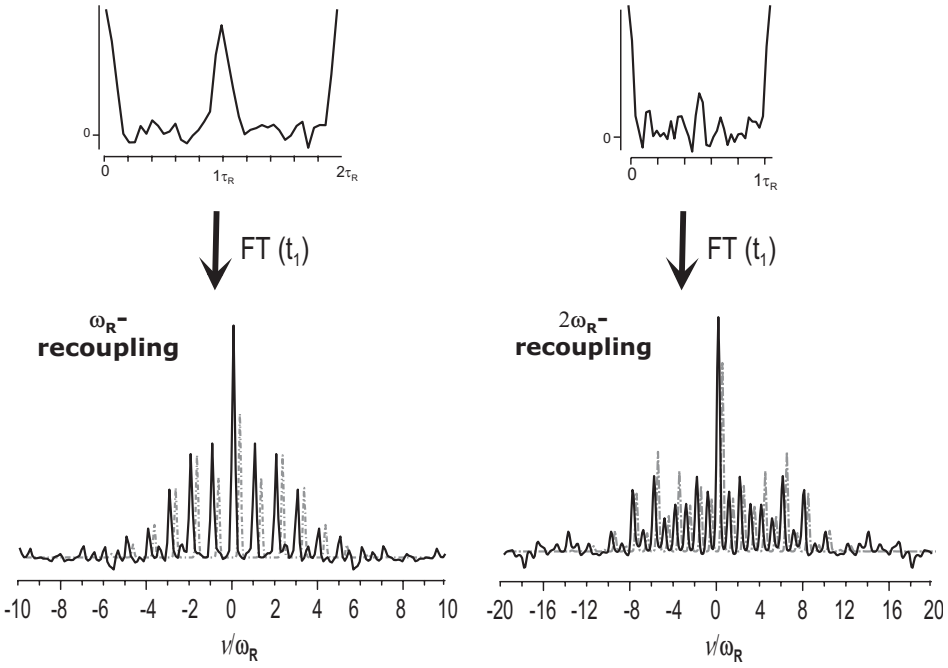

Figure 4.9: *t_1-modulations and REREDOR-SB patterns of the aromatic core CH peak at 119 ppm of α-deuterated HBC-C_{12} (structure shown in Fig. 4.3) measured at 25 kHz MAS and recoupling times of $\tau_{rcpl} = 2\tau_R$ (ω_R-recoupling) and $\tau_{rcpl} = 3\tau_R$ ($2\omega_R$-recoupling), respectively. The underlying grey patterns are simulations carried out with a dipole-dipole coupling constant of $D_{is}/2\pi = 21kHz$.*

4.1.4 REREDOR

Naturally, it is also possible to perform the other experiments described in section 3.4 as $2\omega_R$-recoupled experiments. For the $2\omega_R$-recoupled REREDOR experiment again only the spacing of the π pulses needs to be changed from $\frac{\tau_R}{2}$ to $\frac{\tau_R}{4}$. Also, the t_1-increment is divided by two in order to insure a sufficient spectral width. In Fig. 4.9 t_1-modulations and the corresponding REREDOR-SB patterns of the aromatic core CH peak of α-deuterated HBC-C_{12} are shown. Regarding the t_1-modulations, it immediately stands out that the periodicity of the $2\omega_R$-recoupled experiment is not half a rotor period as one would expect for $2\omega_R$-recoupling, but one rotor period. Equally, the $2\omega_R$-recoupled REREDOR SB pattern exhibits not only sidebands of order $4n + 2$, but also odd-order SB, which is clearly due to an additional contribution, which is modulated by ω_R. The origin of this ω_R-modulated contribution lies in the fact that in the REREDOR experiment transversal coherence states are present during t_1, which are subject to evolution. From this period of free evolution the ω_R-modulated contribution arises.

Comparing the calculated SB patterns, which are shown in Fig. 4.9 as underlying grey lines, with the experimental patterns, it becomes obvious that the fit of the $2\omega_R$-recoupled pattern is not too good. This is due to the fact that the periodicity of the $2\omega_R$-recoupled t_1-signal is a

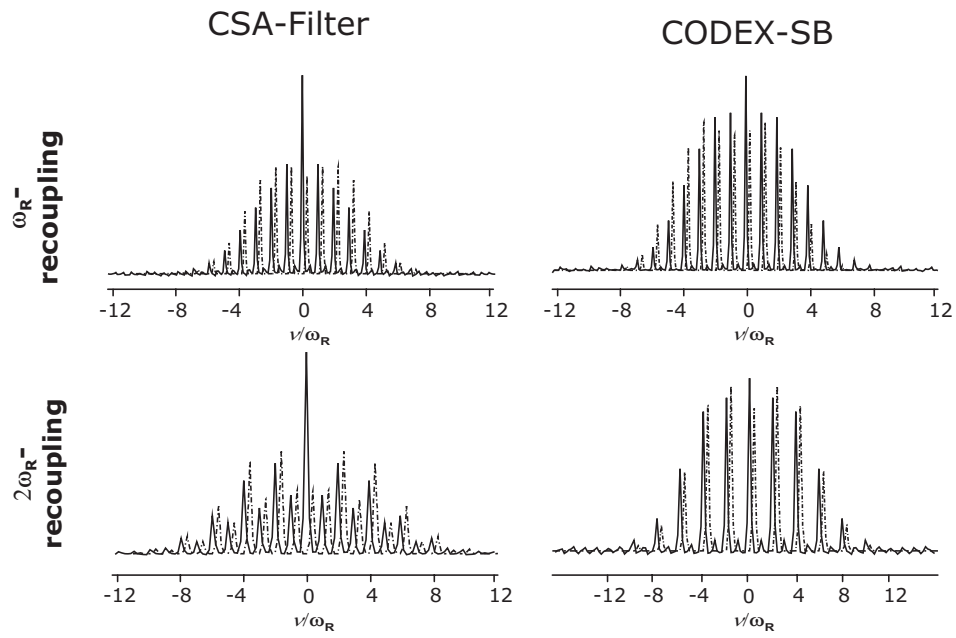

Figure 4.10: *CSA sideband patterns of the COOH carbon of L-alanine obtained with the different recoupling approaches at 10 kHz MAS and a recoupling time of $2\tau_R$. The dashed lines are simulations with the tensor values taken from the literature [Naito 81].*

full rotor period and not, like in $2\omega_R$-recoupled REPT-HDOR only half a rotor period. Since only one rotor period of t_1-modulation was acquired, the concatenation procedure described in section 3.4.2 correlates the noise with the same periodicity as the actual signal, which consequently leads to strong noise contributions on the sideband intensities. In order to reduce this noise contribution, obviously at least two rotor periods of evolution need to be acquired. However, this would imply a doubled experiment time. This is the reason, why in all the experimental work presented later in this thesis $2\omega_R$-recoupled REPT-HDOR is chosen for heteronuclear dipolar recoupling and not $2\omega_R$-recoupled REREDOR.

4.1.5 CSA-SB Patterns

In this subsection $2\omega_R$-recoupled CSA sideband patterns are presented. As a model compound, L-alanine was chosen again, but now the sidebands of the acid group carbon (C1) are considered. In section 3.5 two experiments for the generation of CSA sideband patterns were distinguished, the CSA-filter experiment and the CODEX-SB experiment. These experiments differ just in the coherence state present during t_1. While the latter experiment employs a *z*-filter in order to provide a longitudinal state, $\hat{S}_z$, during t_1, the CSA-filter experiment retains a transversal state, $\hat{S}_{x/y}$, during t_1. Fig. 4.10 shows experimental (solid lines) and calculated (dashed lines) SB patterns of the various experiments. As can be seen

in the figure, the different coherence states present during t_1 lead to significant differences in the $2\omega_R$-recoupled patterns. As was already observed in the case of the $2\omega_R$-recoupled REREDOR experiment in the previous section, in the $2\omega_R$-recoupled CSA-Filter experiment also ω_R-modulated contributions are present. These contributions also arise from the free evolution during the t_1 delays, which introduces both ω_R- and $2\omega_R$-modulated components. Notably, in the CSA-filter experiment the centerband is significantly too high as compared to the simulations. This can be attributed to evolution of the transversal coherence state under perturbing interactions. This loss of coherence leads effectively to an additional offset in t_1, which after FT is reflected in additional centerband intensity. In the case of the CODEX-SB experiment, this effect is by far less pronounced. The reasons for this are that the longitudinal coherence state is not subject to evolution and also that the *z*-filter acts as a coherence filter, which selects only the desired longitudinal coherence during t_1.

4.1.6 Conclusions

Summarizing this section, it can be concluded, that $2\omega_R$-recoupled experiments work equally well as ω_R-recoupled experiments and provide identical results on the strength of the underlying interactions. ω_R-recoupled experiments are often preferable, since they require only shorter recoupling times and, hence, provide better S/N. However, for the same reason, in cases of very strong interactions $2\omega_R$-recoupling might be advantageous. For example, in the BABA build-up curves shown in Fig. 4.3 a maximum of the build-up behavior is only observed for $2\omega_R$-recoupling, which allows the underlying dipole-dipole coupling strength to be better estimated. Having proven the practicability of 2ω-recoupling, we can now turn towards possible applications. In the following sections, the particular usefullness of $2\omega_R$-recoupled experiments for the investigation of sample orientation will be demonstrated for various (partially) oriented systems.

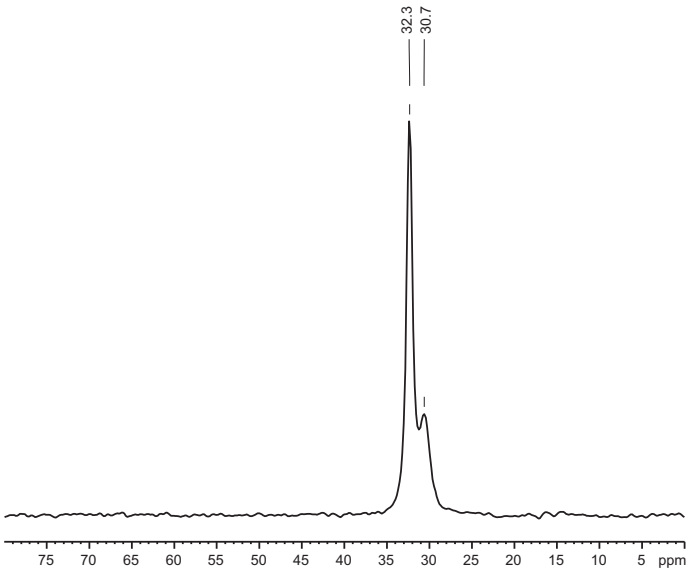

Figure 4.11: *^{13}C CP spectrum of unoriented PE at 10 kHz MAS.*

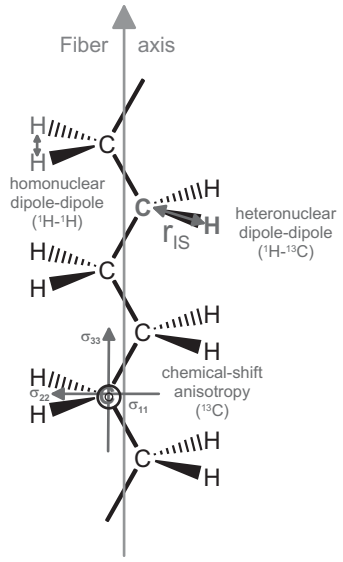

Figure 4.12: *Structure of polyethylene together with the relevant tensor orientations.*

4.2 Recoupling Experiments on Highly Oriented Polyethylene as a Model System.

As already pointed out above, the different orientation dependence for ω_R- and $2\omega_R$-recoupled experiments should be most apparent in experiments on (partly) oriented samples. In order to study the influence of sample orientation on the outcome of recoupling experiments, highly oriented polyethylene (PE) was chosen as a model system. The advantages of PE for such model purposes lie at hand: first, sample orientation can easily be obtained by macroscopic stretching and, second, PE is a well-studied system also in terms of solid-state NMR [Opella 77, Schmidt-Rohr 92, Graf 96, Schnell 01c]. In Fig. 4.11 the ^{13}C CP MAS spectrum of unoriented PE is shown. Clearly, the spectrum exhibits a very sharp signal at 32.3 ppm arising from the crystalline parts in the sample and a broader signal at 30.7 ppm arising from the amorphous parts in the sample. In crystalline PE, the chains are packed parallel in a very well-defined manner, which excludes any molecular motion apart from jumps along the chain axis during which the σ_{33} principle axis is retained [Schmidt-Rohr 91]. However, even in drawn, oriented PE some amorphous domains are present, in which the chains are irregularly packed and thus exhibit considerably higher mobility. Hence, only the sideband patterns corresponding to the crystalline peak are used for probing sample orientation, since they are not affected by molecular motion.

In principle, the various experiments probing the different anisotropic interactions in PE (whose orientation in the molecular frame is shown in Fig. 4.12), could be used for probing sample orientation. However, since PE is among the materials with the highest proton

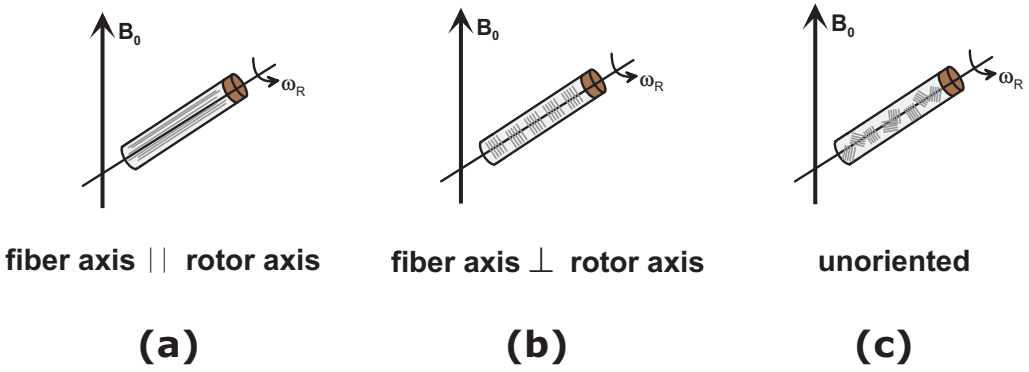

Figure 4.13: *PE samples used for the study of orientation effects: (a) drawn PE with the fiber axis oriented parallel to the rotor axis. (b) drawn PE with the fiber axis oriented perpendicular to the rotor axis. (c) unoriented PE for comparison. Since the drawn fibers did not fill out the rotor completely, anhydrous Na_2SO_4 was used to fill out the cavities and, thus, provide stable spinning.*

density, multispin effects strongly dominate the outcome of any experiment probing dipole-dipole couplings involving protons. This leads to strong signal decay during the t_1 evolution time, which makes data processing difficult. Also, in the ^{1}H -^{1}H BABA-SB pattern (not shown here) strong even order SB appear indicating significant multispin contributions, which make an analysis virtually impossible. For these reasons, the ^{13}C chemical shift anisotropy is the interaction of choice for the study of orientation effects in polyethylene. In the following, we therefore restrict ourselves to CSA-SB patterns obtained with the CSA-filter experiment (see section 3.5). The CSA of highly oriented PE was already studied in detail by Opella and Waugh [Opella 77], who could determine the CSA-tensor orientation in the molecular frame by separated local field (SLF) spectroscopy. In fibers of highly oriented polyethylene, which are characterized by the PE chains being parallel aligned, the σ_{zz} tensor value was found to be oriented exactly along the chain axis (as indicated in Fig. 4.12). The tensor values were determined as σ_{zz} = 12 ppm, σ_{yy} = 35 ppm and σ_{xx} = 49 ppm. The orientation distribution of drawn polyethylene was already investigated by Schmidt-Rohr et. al. [Schmidt-Rohr 92] with the DECODER technique. It could be shown that the chains were aligned parallel to the drawn direction with a full width at half-maximum (FWHM) of $\Delta\Theta = 8°$. This narrow orientation distribution makes drawn PE an ideal model system for the study of orientation effects.

Three samples of PE were prepared as depicted in Fig. 4.13: Two samples of drawn PE with the fiber axis parallel (a) and perpendicular (b) to the rotor axis and one unoriented sample (c), where the PE was melted and cooled down in order to get an isotropic distribution of crystallite orientations. In Fig. 4.14 ω_R- and $2\omega_R$-recoupled CSA-SB patterns of the three samples obtained with the CSA-filter experiment (see section 3.5) are shown. Clearly, the patterns of the oriented samples differ strongly from the powder sample. The grey patterns in the background are simulations using an isotropic powder angle file for sample (c) and powder angle

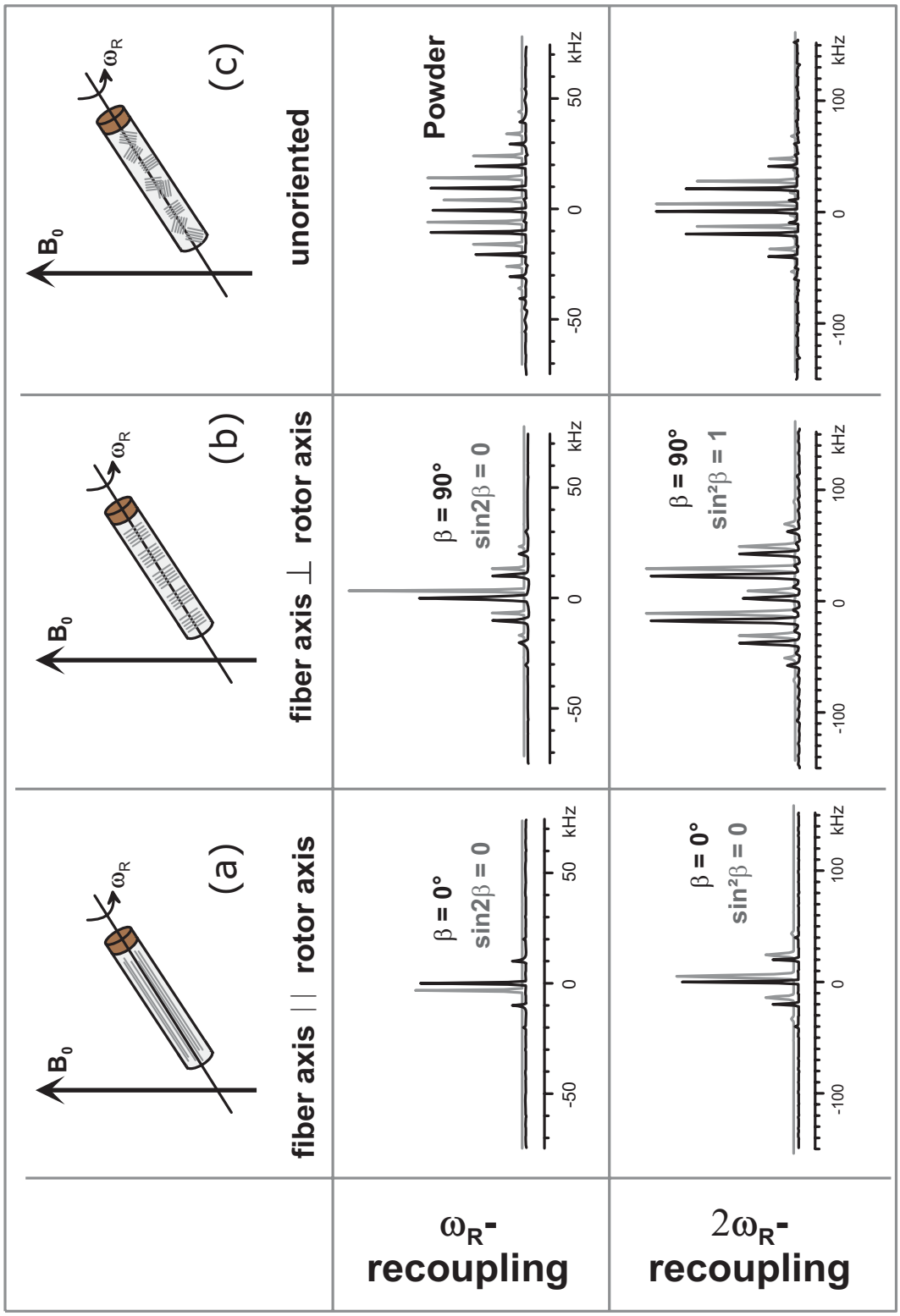

Figure 4.14: *CSA-SB patterns of the three PE samples obtained with the CSA-filter experiment (10 kHz MAS, $\tau_{rcpl} = 4\tau_R$).*

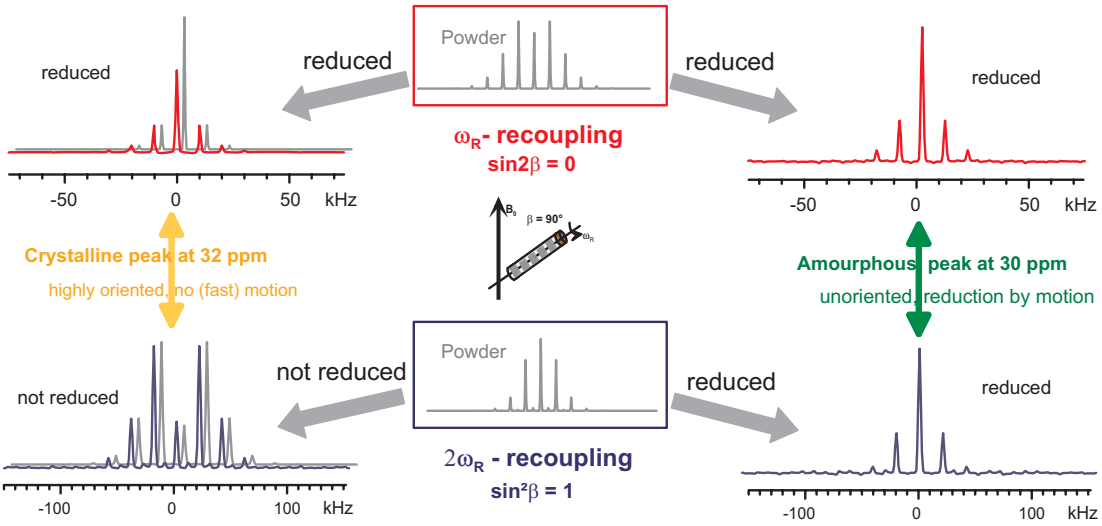

Figure 4.15: *CSA-SB patterns of the crystalline peak (left) and the amorphous peak (right) of PE sample (b). In the middle simulations for an isotropic powder are shown. Clearly, both the ω_R- and the $2\omega_R$-recoupled sideband pattern of the amorphous peak are reduced, indicating that the observed reduction is due to molecular dynamics. In contrast, the $2\omega_R$-recoupled sideband pattern of the crystalline peak is not reduced but exhibits more intense higher order SB, which clearly indicates sample orientation. The underlying grey SB patterns are simulations for perfect orientations with a single $\beta = 90°$.*

files with only one β-angle for sample (a) and sample (b), namely $\beta = 0°$ and $\beta = 90°$, respectively. Since in drawn PE the chains are oriented parallel to the drawing direction and the σ_{zz} principal value points along the chain axis, for perfect orientation only a single β angle is present, which is in this special case the angle between the rotor axis and the fiber axis. Hence, the simulations for samples (a) and (b) were carried out for only a single β angle. The deviation between experiment and simulation for the oriented samples can be attributed to deviations from the perfect sample orientation, which will be discussed in detail below.
Comparing the SB-patterns in Fig. 4.14, it becomes immediately clear that depending on the prefactor sin2β or sin$^2\beta$ the sideband patterns change significantly. As a rule of thumb, for small prefactors (sin2β or sin$^2\beta$) the SB patterns are strongly reduced, i.e. exhibit lower order SB as compared to the powder pattern. For large prefactors the outer sidebands gain intensity as compared to the powder pattern. The difference in the β angle dependence of ω_R- and $2\omega_R$-recoupling is most prominent in the spectra for the sample oriented perpendicular to the rotor axis, since there the orientation dependent prefactor changes from zero (sin$(2 \cdot 90°)$=0) to one (sin$^2 90°$=1). This is an important aspect when it comes to distinguishing effects of molecular dynamics and effects of macroscopic sample orientation on the sideband patterns. Molecular dynamics generally averages and thus reduces anisotropic NMR interactions. Hence, a sideband pattern from a mobile system is reduced relative to the rigid system. From a single

sideband pattern, like the ω_R-recoupled CSA-SB pattern of the parallel oriented PE sample, it would not be possible to distinguish whether the observed reduction is due to sample orientation or molecular dynamics. This ambiguity can be overcome by carrying out a second experiment applying $2\omega_R$-recoupling. This becomes immediately clear when comparing the SB patterns from the crystalline, oriented peak at 32.3 ppm with those from the amorphous, unoriented peak at 30.7 ppm as explained in Fig. 4.15. Of course, the example chosen here represents the case with the most prominent differences and was deliberately considered to illustrate the general principle. Usually, the differences in the SB patterns are not as pronounced.

Nonetheless, with these experiments a general strategy is available which allows for the distinction, whether a SB pattern changed relative to the rigid powder is due to sample orientation or molecular dynamics: Provided that the strength of the underlying interaction is known, it is necessary to measure both the ω_R- and the $2\omega_R$-modulated sideband pattern and to fit both experiments for the strength of the underlying interaction (e.g. for a dipole-dipole coupling constant or for the width of the CSA tensor). If both fits arise from an isotropic angle distribution (powder), they should yield *identical* values of the respective interaction strength for isotropic samples. However, if significant differences of these values occur or if the fit does not reflect the shape of the SB pattern, this is an indication for sample orientation.

For a more detailed analysis of sample orientation, the inherent strength of the underlying interaction needs to be known. For dipole-dipole couplings, this does usually not pose a problem, since the internuclear distances are commonly known, from which the dipole-dipole constant can easily be calculated. If the strength of the underlying interaction is not known, the easiest approach is to prepare a powdered and, hence, isotropic sample and to measure the SB pattern of this definitely isotropic sample and compare it to the SB pattern of the possibly oriented sample.

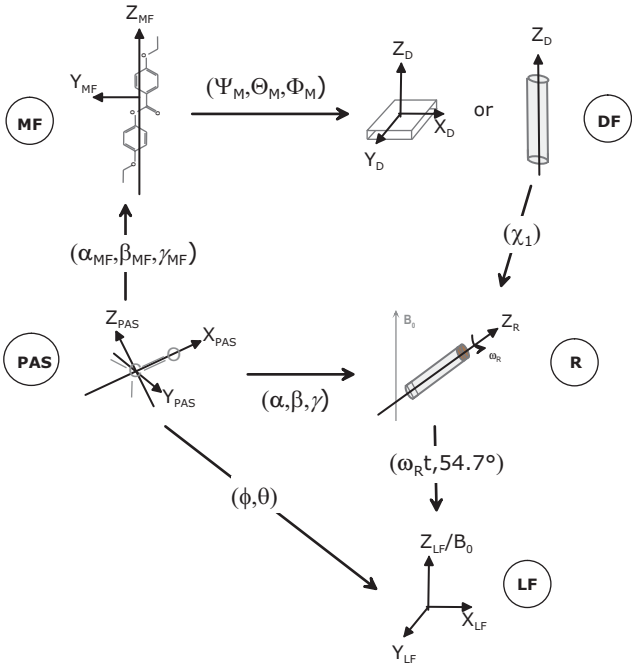

Figure 4.16: *Definition of the angles and coordinate systems used in this chapter.*

4.3 Orientation Distributions from Recoupling MAS-NMR Experiments.

The obvious question arising now is to which extent orientation distributions can be reconstructed from the experiments described above. The methodology for extracting angle dependent orientation distributions from frequency dependent NMR spectra is well-developed and described in detail in the literature, for example in chapter 11 and 12 of [Schmidt-Rohr 94]. In Fig. 4.16 the relevant angles and coordinate systems are defined, which are necessary for describing sample orientation for experiments under MAS. The respective interaction tensor is defined in its principle axis frame (PAS). The orientation of the PAS in the molecular frame (MF) is specified by the Euler angles $\alpha_{MF}, \beta_{MF}, \gamma_{MF}$. If oriented samples, such as liquid crystals, are investigated, it is useful to specify the orientation of the molecule with respect to the director frame (DF), which defines the direction of primary order in the sample, by the Euler angles Ψ_M, Θ_M, Φ_M. In the following, we restrict the consideration to uniaxial director frames. Then, the orientation of the director frame in the rotor frame (R) is given by a single angle χ_1, since both rotor and director frame are uniaxial. The transformation from the rotor frame into the laboratory frame is already included in the equations used for the description of MAS NMR experiments (see section 2.4). In the description of recoupling MAS NMR experiments the relevant orientation for the outcome of the experiment is the orientation of the PAS in the rotor frame, which is specified by the Euler angles α, β and γ. Only if more than

one interaction is considered, the transformation to the molecular frame is absolute necessary. In the following, we will restrict the consideration to only one interaction and assume that the orientation of the PAS in the molecular frame is known. This condition is usually met for dipole-dipole couplings, but not necessarily for CSAs and, hence, in some cases it has to be determined separately.

If sample orientation is to be studied, the information of interest is the orientation distribution of the molecules in the director frame. Since the orientation of the director in the rotor frame is usually known from sample preparation, the orientation distribution of the PAS in the rotor frame can, under these circumstances, be easily converted to the orientation distribution of the molecules in the director frame. Hence, in the following, we will focus on extracting the orientation distribution of the PAS in the rotor frame. Since the γ angle denotes only the initial rotor phase and the α angle is only necessary for asymmetric interactions, in the easiest case of an uniaxial interaction, it is sufficient to extract the orientation distribution P(β). If the underlying orientation distribution exhibits cylindrical symmetry, even for an asymmetric interaction one can restrict the consideration to an orientation distribution P(β), while keeping the α angles isotropically distributed.

Basically, there are three ways to obtain an orientation distribution P(β) from an NMR spectrum, which is given by a frequency dependent intensity distribution S(ω):

(i) direct reconstruction

(ii) direct expansion (best fit of delta-function subspectra)

(iii) moment expansion (best fit of Legendre-polynomial-weighted spectra).

A direct reconstruction (i) requires spectra which directly reflect the angle distribution, that is, a single spectral peak for each angular peak, and no coincidence of spectral peaks as is e.g. the case in static CSA powder spectra. Then, the distribution can be directly reconstructed according to the principle of conservation of the area of corresponding intervals, $S(\omega)d\omega = P(\beta)d\beta$. For recoupling MAS experiments this condition is obviously not met and, hence, the direct reconstruction will not be discussed any further here.

For the direct expansion (ii), the experimental spectrum $S^{exp}(\omega)$ is divided into subspectra $S^{th}(\omega, \beta)$ for individual β:

$$S^{exp}(\omega) = \int_{0^\circ}^{90^\circ} S^{th}(\omega, \beta) P(\beta) \mathrm{d}\beta \tag{4.3}$$

$$= \sum_{\beta} S^{th}(\omega, \beta) P(\beta) \tag{4.4}$$

With the discrete formulation Eq. (4.4) the orientation distribution can be obtained from a best fit of δ-function subspectra.

For the third approach, the moment expansion (iii), the angle distribution is written as a sum of Legendre polynomials:

$$\tilde{R}(\beta) = \sum_{L} (2L+1) \langle P_L \rangle P_L(cos\beta), \tag{4.5}$$

where the weighting factor $\langle P_L \rangle$ can be seen as an order parameter and $P_L(cos\beta)$ is the *n*-th order Legendre polynomial. The experimental spectrum is decomposed into the contributions from the various moments:

$$S^{exp}(\omega) = \sum_L (2L+1)\langle P_L \rangle \int_{0^\circ}^{90^\circ} S^{th}(\omega, \beta) P_L(cos\beta) d\beta. \tag{4.6}$$

A best-fit procedure with the $\langle P_L \rangle$ as coefficients yields the contributions from the various moments. The moment expansion is particular useful for broad orientation distributions and yields order parameters which can directly be related to order parameters obtained with other methods like X-ray scattering.
For reasons of simplicity and, in particular, sheer lack of information content (Note that a typical sideband pattern exhibits only a few sidebands, which certainly under-determines the problem.), none of these approaches to extract information about the orientation distribution will be used. Instead a specific orientation distribution is assumed, which (optimally) depends only on one variable parameter. This parameter will be varied until the calculated SB pattern calculated for this orientation distribution fits the experimental SB pattern best. The advantage of this approach is that the orientation function, i.e. the probability $P(\beta)$ of finding a given angle β, can easily be incorporated into the simulations by just changing the weighting factors in the corresponding powder angle files as is explained in detail in appendix C. Due to the facility of this approach, it will be the most used one within this thesis, even though in the literature commonly the third approach, the moment expansion (iii) is found. As already suggested by [Harbison 87], an gaussian shaped orientation distribution will be used:

$$P(\beta) = exp\left(-\frac{sin^2(\beta - c)}{k}\right) \tag{4.7}$$

Here, c specifies the β angle around which the distribution is centered. Using $\sin^2\beta$ instead of β^2 in the exponential makes the orientation distribution periodic, i.e. in particular $P(\beta) = P(180^\circ - \beta)$. The constant *k* is related to the FWHM $\Delta\beta$ of the orientation distribution as follows

$$k = -\frac{sin^2\left(\frac{\Delta\beta}{2}\right)}{ln\frac{1}{2}} \tag{4.8}$$

The advantage of a gaussian orientation distribution is that the probability $P(\beta)$ of finding a given angle β is determined only by $\Delta\beta$, the width of the orientation distribution[1]. The choice

[1] In the literature the width of a distribution is often given by the standard deviation σ, which is related to the FWHM $\Delta\beta$ of the gaussian by $\Delta\beta = 2.35\sigma$.

of a gaussian orientation distribution can often be validitated by the physics of the orientation process; e.g. for samples aligned in a magnetic field, the gaussian shape of the orientation distribution arises directly from the Boltzman distribution of the energy of a molecule with anisotropic magnetic susceptibility in an external, static magnetic field. Naturally, one has to be aware of the fact that the order parameters extracted on the basis of this model are not model-free and, hence, might strongly differ in those cases where the gaussian model is inappropriate, from model-free order parameters which were determined by other methods.
Turning now back to the model PE sample (a), whose fiber axis is oriented parallel to the rotor axis, we will now determine the width $\Delta\beta$ (FWHM) of the orientation distribution from the ω_R-recoupled CSA-SB pattern. In Fig. 4.17 the experimental pattern is shown together with simulated SB patterns for a powder sample, a perfectly oriented sample ($\beta = 0°$) and simulations including orientation distributions of various widths, which are given by Eq. (4.7) with c = 0°. Comparing experimental and calculated spectra yields that the width (FWHM) of the orientation distribution is $\Delta\beta \approx 15°$.
Having determined the width $\Delta\beta$ of the orientation distribution $P(\beta)$, it is now possible to calculate the order parameter S as follows [Zannoni 94]

$$S = \langle P_2(cos\beta)\rangle = \frac{\int_0^1 \frac{1}{2}(3cos^2\beta - 1)P(\beta)d(cos\beta)}{\int_0^1 P(\beta)d(cos\beta)}. \tag{4.9}$$

This order parameter has the nice feature of being zero for an isotropic distribution $P(\beta)$. It becomes 1 for perfect alignment parallel to the director and -0.5 for perfect alignment perpendicular to the director.
It should be noted, that often the order parameter $S^{(1)}$ in a system 1 (e.g. the director frame) is of interest, but can be measured only in a system 2 (e.g. the laboratory frame). If the angle β_0 transforms between system 1 and 2, the two order parameters are simply related by

$$S^{(2)} = \langle P_2(cos\beta^{(2)})\rangle = P_2(cos\beta_0)\langle P_2(cos\beta^{(1)})\rangle \tag{4.10}$$

This relation is for example often used, when dynamic order parameters are determined, for example for rotations, where the order with respect to the rotation axis is of interest, which naturally can not be directly measured.
The necessary integrals in Eq. (4.9) can be solved numerically, and the resulting dependence of the order parameter S on the width $\Delta\beta$ of the orientation distribution is plotted in Fig. 4.18 for a distribution centered around $c = 0°$ and in Fig. 4.19 for a distribution centered around $c = 90°$. As expected, the curve in Fig. 4.18 for $c = 0°$ decays from 1 for perfect orientation towards 0 for broad orientation distributions. Also, the curve for the distribution centered around $c = 90°$ increases from -0.5 for perfect alignment towards 0.

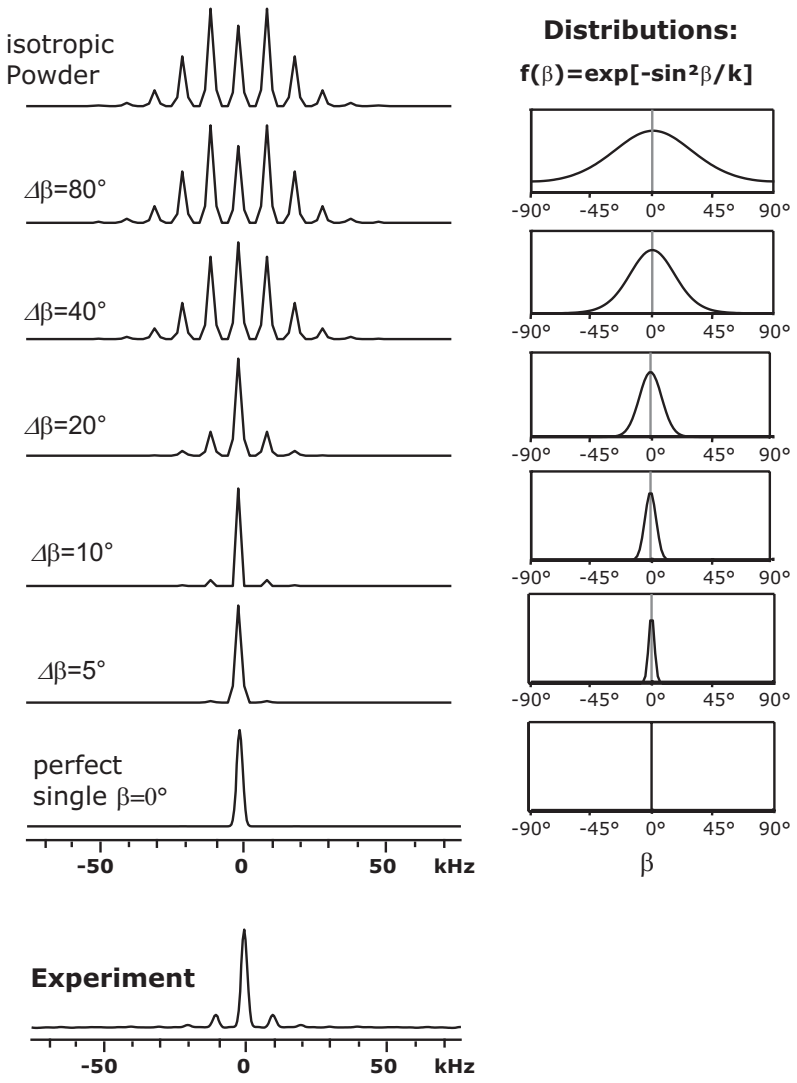

Figure 4.17: *Comparison between calculated (top) and the experimental (bottom) CSA-SB patterns of the crystalline peak of the drawn PE sample (a) with the fiber axis being parallel to the rotor axis. The calculations were carried out for an isotropic powder, perfect orientation with $\beta = 0°$ and orientation distributions of various widths centered around $c = 0°$. For illustration, the corresponding orientation distributions are depicted on the right of the respective spectrum. Comparing the experimental spectrum with the calculated spectra reveals that the width (FWHM) of the orientation distribution is between $\Delta\beta = 10° - 20°$.*

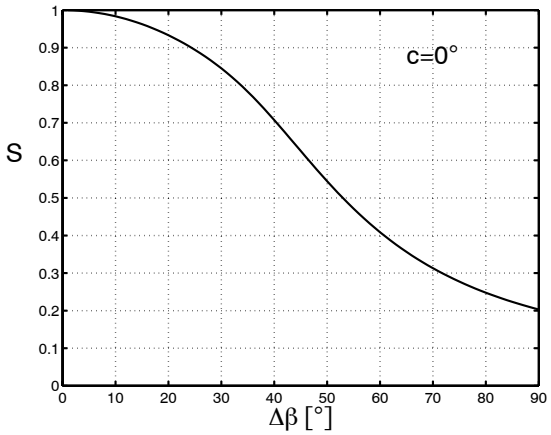

Figure 4.18: *Dependence of the order parameter S on the width $\Delta\beta = 2.35\sigma$ of the gaussian orientation distribution for $c = 0°$.*

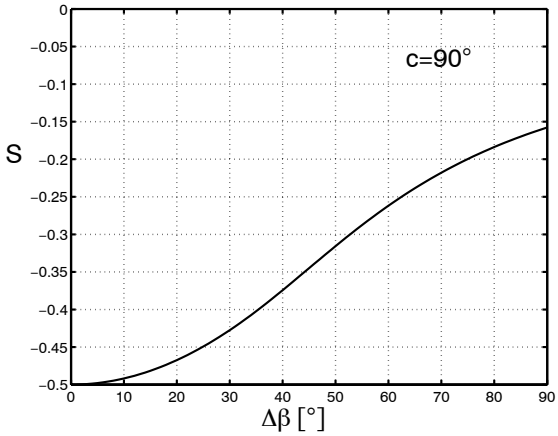

Figure 4.19: *Dependence of the order parameter S on the width $\Delta\beta = 2.35\sigma$ of the gaussian orientation distribution for $c = 90°$.*

Since in the PE example the orientation distribution is centered around $c = 0°$, the order parameter S can simply be read off from Fig. 4.18. For $\Delta\beta = 15°$ one obtains S = 0.96, which is a very high order parameter, as it is expected for such a drawn PE sample.

4.4 Results on a Nematic Liquid Crystal

As already mentioned before, liquid crystals can easily be oriented by various means. An important goal in materials science is the optimization of alignment procedures, since the quality of the alignment often governs the performance of devices based on liquid crystals. The degree of alignment is usually studied by X-ray scattering. NMR investigations of order in liquid crystalline systems were previously mainly carried out by deuteron NMR on isotopically enriched samples [Emsley 85]. However, this is afflicted with a high synthetic expense which is not feasible for routine testing on many samples. Alternative methods using ^{13}C NMR can be found as well, which benefit from the fact that they do not require isotopic labelling, but are experimentally quite involved [Titman 93, Chmelka 93]. In this section, the possibility to determine orientation distributions in a nematic liquid crystal by recoupling MAS NMR experiments is explored.
As thermotropic nematic model compound, 4-hexyloxy-benzoic acid-(4'-ethoxy-)phenyl ester, whose structure is shown in Fig. 4.20, was chosen.

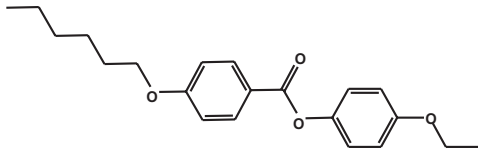

Figure 4.20: *Structure of the nematic model compound.*

At room temperature this compound forms white crystalline needles, which melt at T = 341 K into the nematic phase and melt at T = 353 K isotropically. Previous investigations by deuteron [Boeffel 83] and fast MAS proton DQ NMR [Neidhöfer 03] were focusing on the determination of the local order parameter in the nematic liquid crystalline phase. The deuteron NMR studies also revealed that the material aligns macroscopically in a static magnetic field in such a way that the aromatic discs are parallel to the magnetic field. Alignment of liquid crystalline materials in strong external magnetic fields is a well-known phenomenon caused by the anisotropy of the magnetic susceptibility of the liquid crystalline molecules. Due to this anisotropy some orientations in the magnetic field are preferred and, hence, (partial) sample alignment takes place.
In Fig. 4.21 the proton spectra of the unoriented sample in the crystalline phase and the liquid crystalline phase are shown together with the corresponding peak assignment. Clearly, the spectrum in the crystalline phase lacks sufficient resolution, since only two broad featureless peaks arising from the aromatic and aliphatic protons can be distinguished. Hence, ^{13}C detected experiments, i.e. namely REPT-HDOR, were chosen for the study of orientation effects. Fig. 4.22 shows ^{13}C spectra of the unoriented sample in the crystalline and liquid crystalline phase measured at 25 kHz MAS. Interestingly, the spectra differ significantly in the chemical shift of the aromatic protons, which is due to additional shift effects in the crystalline packing. In the following we concentrate on the peak at 118.0 ppm in the crystal spectrum, which can be assigned to carbons *3* and/or *3'*, respectively. For the study of sample orientation presented here, the oriented sample was simply prepared by heating the material in a NMR rotor in

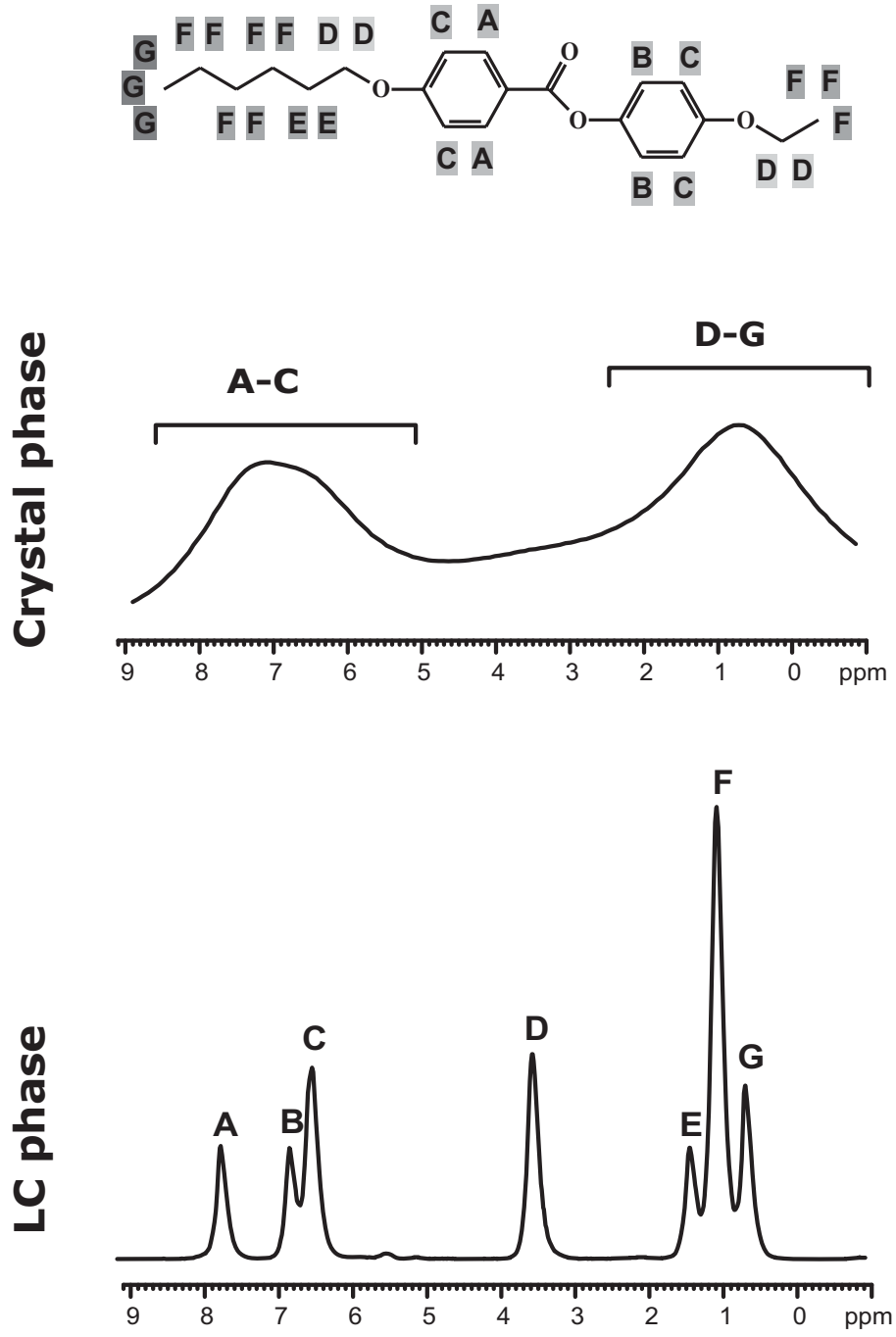

Figure 4.21: ^1H *spectra of the nematic model compound in its crystalline and liquid crystalline phase measured at 25 kHz MAS. The corresponding peak assignment is shown on the top.*
[The LC phase spectrum was taken from [Neidhöfer 03].]

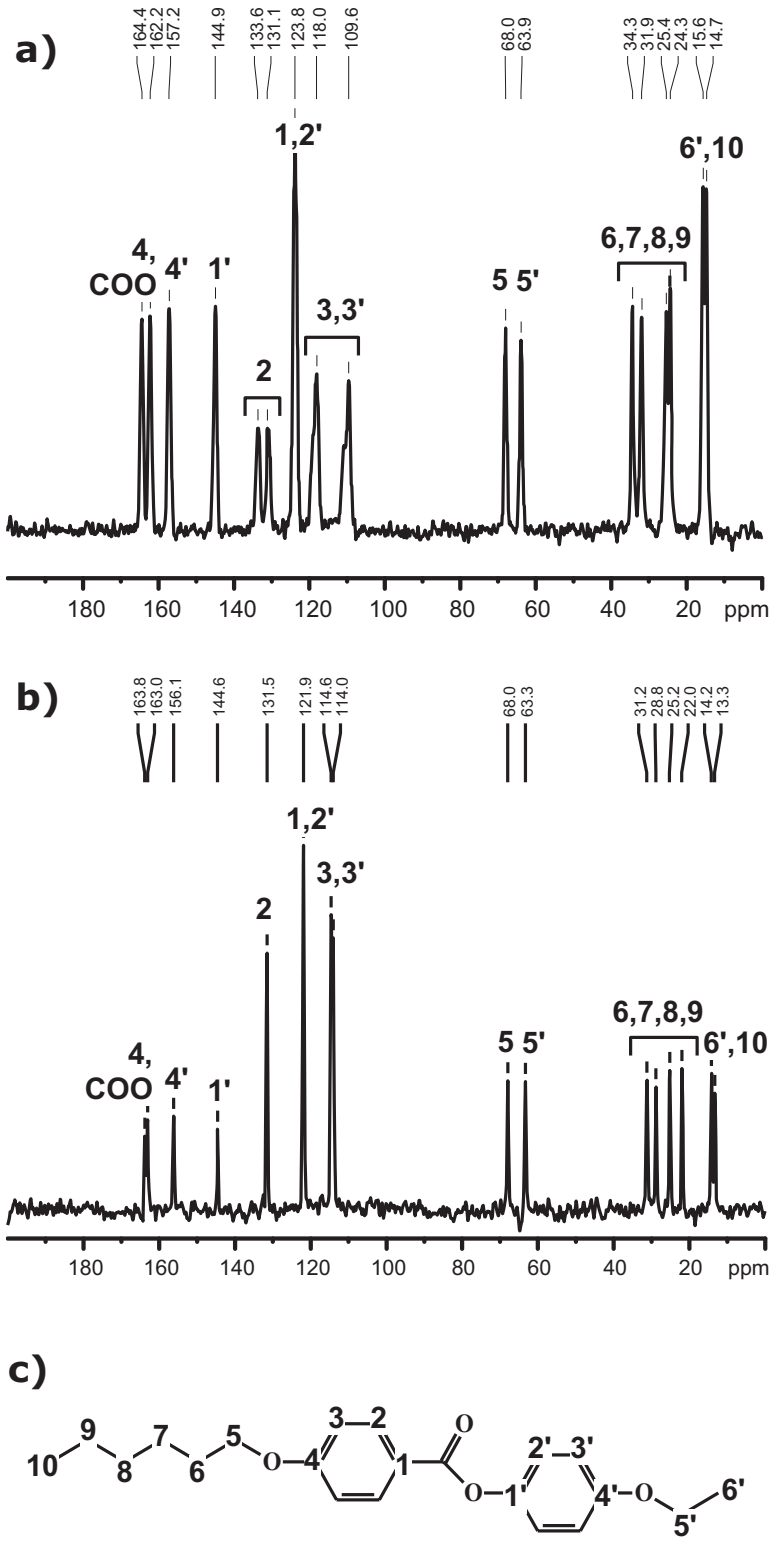

Figure 4.22: *^{13}C spectra of 4-hexyloxy-benzoic acid-(4'-ethoxy-)phenyl ester:*
(a) ^{13}C CP spectrum in the crystalline phase measured at 25 kHz MAS and T = 312 K.
(b) ^{13}C one-pulse spectrum in the LC phase measured at 10 kHz MAS and T = 343 K [provided by Michael Neidhöfer].
(c) Numeration of the carbons as used for the peak assignment.

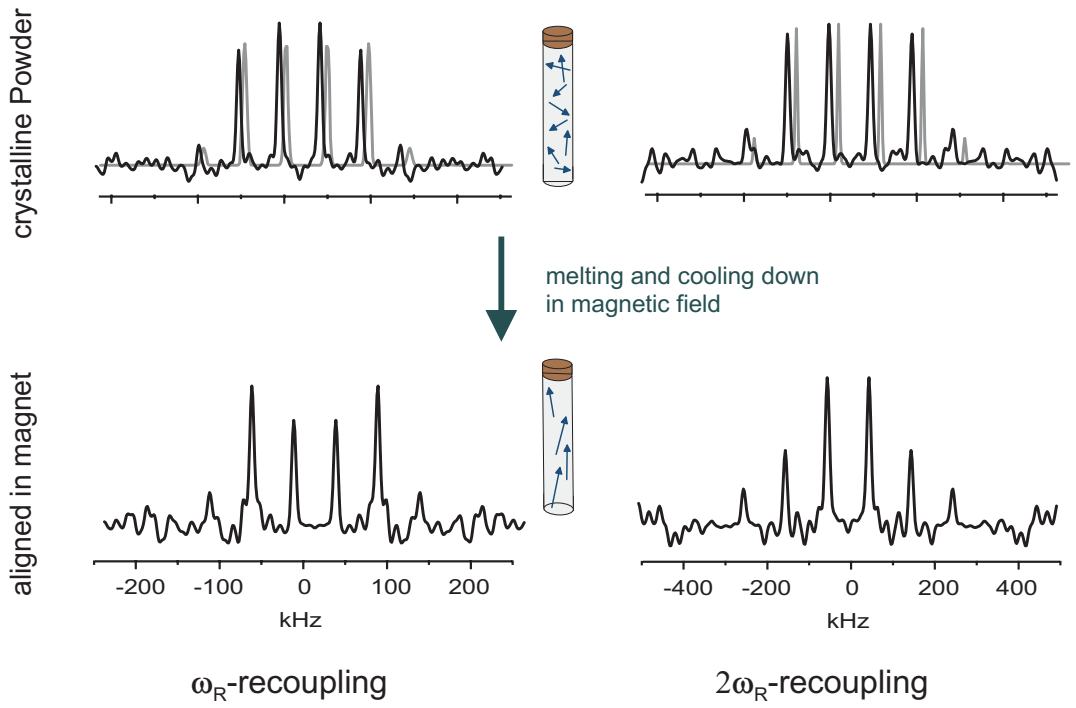

Figure 4.23: *REPT-HDOR SB pattern of the peak at 118.0 ppm of the unoriented and the oriented nematic model compound. The spectra were measured at 25 kHz MAS, T = 312 K (i.e. in the crystal phase) and $\tau_{rcpl} = 2\tau_R$ for ω_R-recoupling and $\tau_{rcpl} = 3\tau_R$ for $2\omega_R$-recoupling, respectively. The underlying grey patterns are simulations for a crystalline powder with a dipole-dipole coupling constant of $D_{is}/2\pi$ = 21 kHz.*

an external magnetic field (7.05 T) to the isotropic phase and subsequently cooling it slowly down. The rotor was put in the magnetic field in such a way that its rotor axis was parallel to the field direction. Hence, as previously shown by ^{2}H NMR, the material is aligned in such a way that the aromatic planes are parallel to $\underline{\mathbf{B}}_0$, i.e. the ring normal is perpendicular to $\underline{\mathbf{B}}_0$ [Boeffel 83]. The unoriented crystalline powder sample was obtained by grinding the crystalline material.

In Fig. 4.23 HDOR-SB patterns of the unoriented crystalline powder sample and the sample oriented in the magnetic field are shown. The patterns of the crystalline powder sample fit nicely to the simulations for an isotropic powder sample with a dipole-dipole coupling constant of $D_{is}/2\pi = 21$ kHz, which is typical for rigid aromatic CH pairs. Clearly, the spectra of the sample oriented in the magnetic field differ from those of the crystalline powder sample. Since the rotor was oriented parallel to the external magnetic field during the alignment process, one would intuitively expect the rod-like nematic molecules to be aligned parallel to the rotor axis, resulting in a $\beta = 60°$ (C-H vector relative to B_0) for perfect alignment. However, comparison with calculated SB patterns for perfect orientations with various β angles (Fig. 4.24) shows that an angle of $\beta = 60°$ is not consistent with the experimental SB

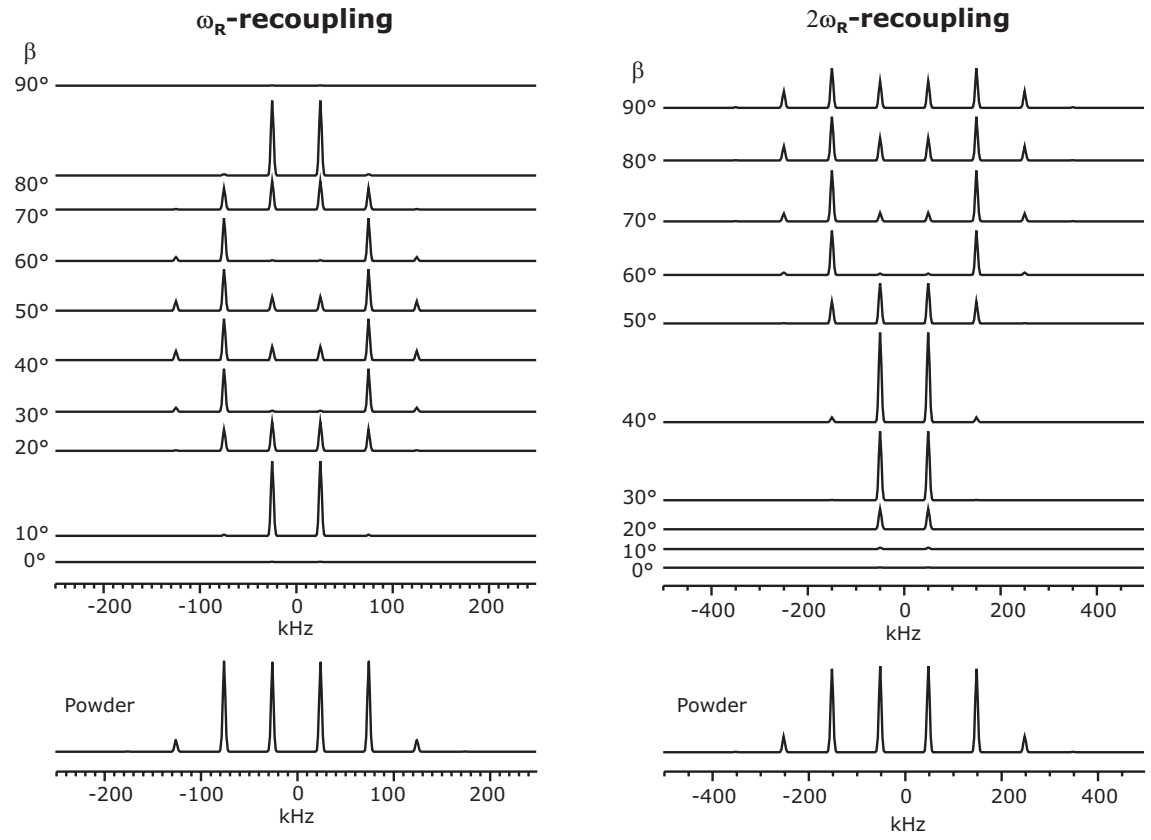

Figure 4.24: *Calculated REPT-HDOR SB patterns of a C-H spin pair ($D_{is}/2\pi$ = 21 kHz) for single orientations β (top spectra) and an isotropic powder sample (bottom).*
Left: ω_R-recoupling, $\tau_{rcpl} = 2\tau_R$. *Right: $2\omega_R$-recoupling, $\tau_{rcpl} = 3\tau_R$.*

patterns. Instead an angle β of around 50° seems to fit the experimental patterns best.
At this point of the discussion it is important to note that the nematic molecules are not linear because the internal C_2 axes of the two phenylene rings are not parallel, but slightly inclined. Also the phenylene rings are probably not coplanar, but rather twisted with respect to each other. This is a typical observation for other nematic mesogens with the same core structure. For example, in the crystal structure of 4'-Cyanophenyl-4-n-pentylbenzoate the two aromatic ring planes enclose a dihedral angle of 75° [Baumeister 82]. An energy minimization carried out with the CS Chem3D Software package yielded a dihedral angle of 46°. The structure obtained with the energy minimization is depicted in Fig. 4.25. From this, it is clear that the alignment axis cannot be parallel to the internal C_2 symmetry axes of the two phenylene rings. In Fig. 4.25 this is betokened by the gray line in the chemical structure. Such a situation would imply that the angles between the rotor (= alignment) axis and the C-H axis are not identical for the CH groups located at the two sides of the phenylene rings (also indicated in the figure). Also, most crystal structures of similar rod-like nematic mesogens contain two molecules per unit cell, which might lead to even more different orientations of the CH groups. Hence, cal-

culations were carried out assuming a superposition of two orientation distributions centered at β = 45° and β = 75°, respectively. The orientation distribution used for the simulation of the HDOR sideband pattern was

$$P(\beta) = sin(\beta) \cdot \left(exp\left\{ -\frac{sin^2(\beta - c_1)}{k} \right\} + exp\left\{ -\frac{sin^2(\beta - c_2)}{k} \right\} \right), \tag{4.11}$$

where k was set to 0.1681, which corresponds to a FWHM of $\Delta\beta$ = 40°. The orientation distributions and the corresponding sideband patterns are shown in Fig. 4.25. Even though c_1 and c_2 were simply guessed, such a bimodal orientation distribution can qualitatively account for the observed sideband patterns. Due to the comparably low signal-to-noise ratio a more detailed or quantitative analysis yielding the precise values of c_1 and c_2 or the width of the orientation distribution (which was arbitrarily chosen to $\Delta\beta = 40°$) is not possible. Nonetheless, it should be stressed that the sideband patterns were sensitive enough to distinguish between a bimodal and a single exponential orientation distribution.

An interesting observation was made for a an unoriented crystalline powder sample, which was heated into the liquid crystalline phase several times while spinning at the magic-angle up to 30 kHz in order to carry out other experiments. As was proven by [Courtieu 82], magic-angle spinning at precisely the magic-angle ($\beta_M = 54.7°$) in a magnetic field does not lead to sample alignment. In contrast, spinning at angles different from the magic-angle is well known to cause sample alignment in liquid crystalline media. Since this nematic sample was only spun precisely at the magic-angle, it should not be aligned and exhibit spectra corresponding to an isotropic powder. Surprisingly, the SB patterns of this sample are more or less identical to the SB patterns of the sample oriented in the magnetic field (not shown here). Obviously, the sample was (partially) aligned by heating, spinning and subsequent cooling down. An explanation for this unexpected alignment phenomenon might be that the sample crystallized in an oriented way while it was still spinning in the magnetic field. This might, for example, be due to surface effects which are known to induce oriented crystallization. Even though one can so far only speculate about the alignment mechanism, the occurrence of alignment stresses the importance of carefully checking the possibility of sample orientation before evaluating the outcome of recoupling NMR experiments.

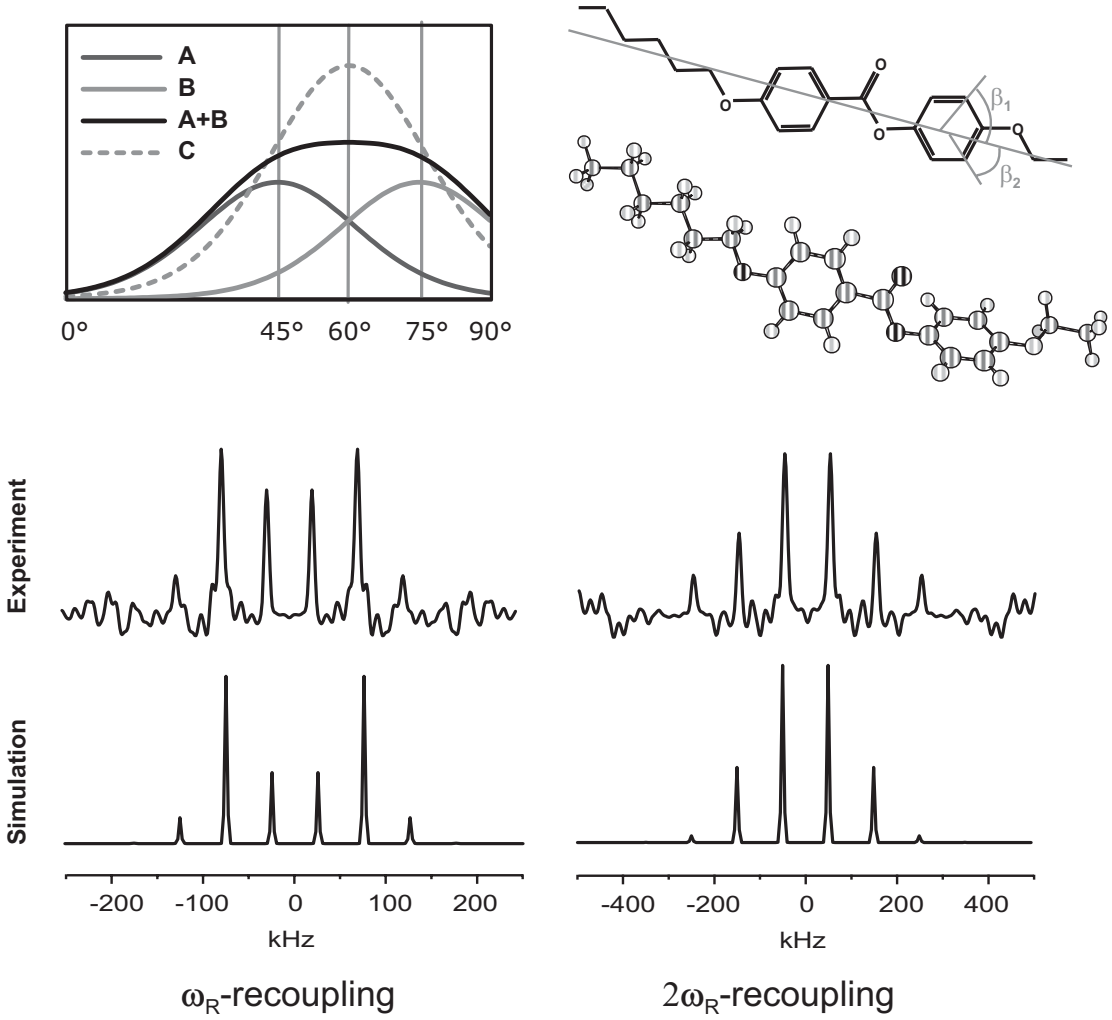

Figure 4.25: *Experimental and calculated REPT-HDOR SB patterns for the aligned nematic liquid crystal. The simulations were carried out for a C-H spin pair ($D_{is}/2\pi$ = 21 kHz) with the bimodal orientation distribution of Eq. (4.11), where c_1=45° and c_2=75°. For illustration, the orientation distribution is plotted on top (denoted with A+B) together with the two single gaussian contributions (A and B). For clarity, the sin-factor in Eq. (4.11) was omitted in the plots of the orientation distributions. For comparison also a single gaussian distribution function of same width centered around c = 60° (C) is plotted.*

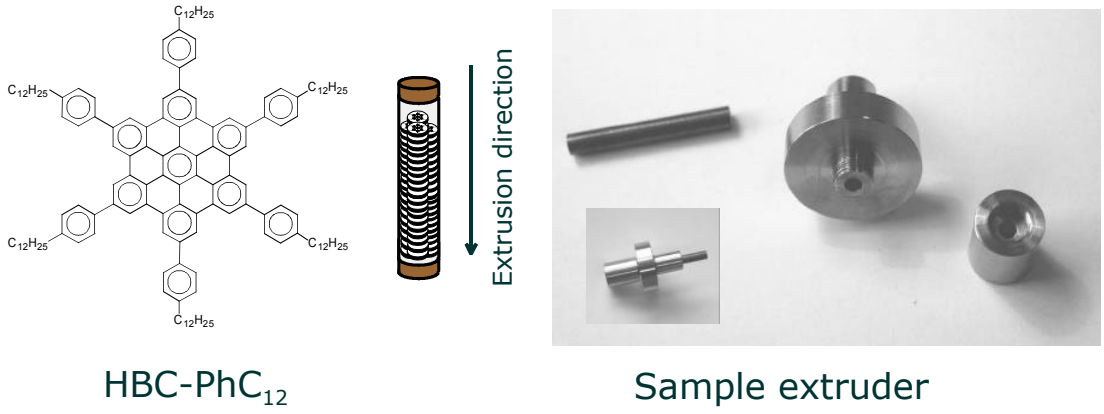

Figure 4.26: *Structure of HBC-PhC$_{12}$ (left) and photograph of the device used for extrusion of oriented fibers (right).*

4.5 Results on a Discotic Liquid Crystal

As already mentioned above, the quality of sample alignment in liquid crystals is crucial for the performance of optoelectronic devices based on liquid crystals. The material investigated in this section is a columnar discotic liquid crystal, hexa(*para-n*-dodecylphenyl-)-*peri*-hexabenzocoronene, HBC-PhC$_{12}$ [Fechtenkötter 99], whose chemical structure is depicted in Fig. 4.26. This material exhibits a high charge carrier mobility along the column axis and can, for example, be envisaged as a hole conducting medium in devices like organic thin film transistors or solar cells. Various methods to achieve sample orientation in this material are described in the literature [Tracz 03, Craats 03]. The by far easiest among those is simple extrusion through a nozzle, yielding a fiber of highly oriented material. For the NMR investigations presented here, a special extruder was built, which is shown in Fig. 4.26. With this extruder the material can be directly extruded into the 2.5 mm MAS rotor and, hence, the material fills the rotor completely. This is crucial in order to avoid the orientation being disrupted by the centrifugal forces during spinning, which press the material on the walls of the rotor. The fiber is extruded through the rotor in such a way that excessive material sticks out at the end of the rotor and can be used for other analytical purposes, namely X-ray diffraction. The great advantage of this lies in the fact that material with identical history (preparation and thermal history) can be used for both analytical techniques. Since discotic liquid crystalline materials are known to exhibit a strong dependence on the thermal history and the actual sample preparation, this is an important point when it comes to comparing NMR results with results obtained from X-ray diffraction.

For the investigation of sample orientation in an extruded fiber of HBC-PhC$_{12}$, the material was extruded at room temperature into the MAS rotor. At room temperature HBC-PhC$_{12}$ forms a solid columnar phase, in which the aromatic discs are oriented perpendicular to the columnar axis. A detailed investigation of packing and dynamics in this phase can be found

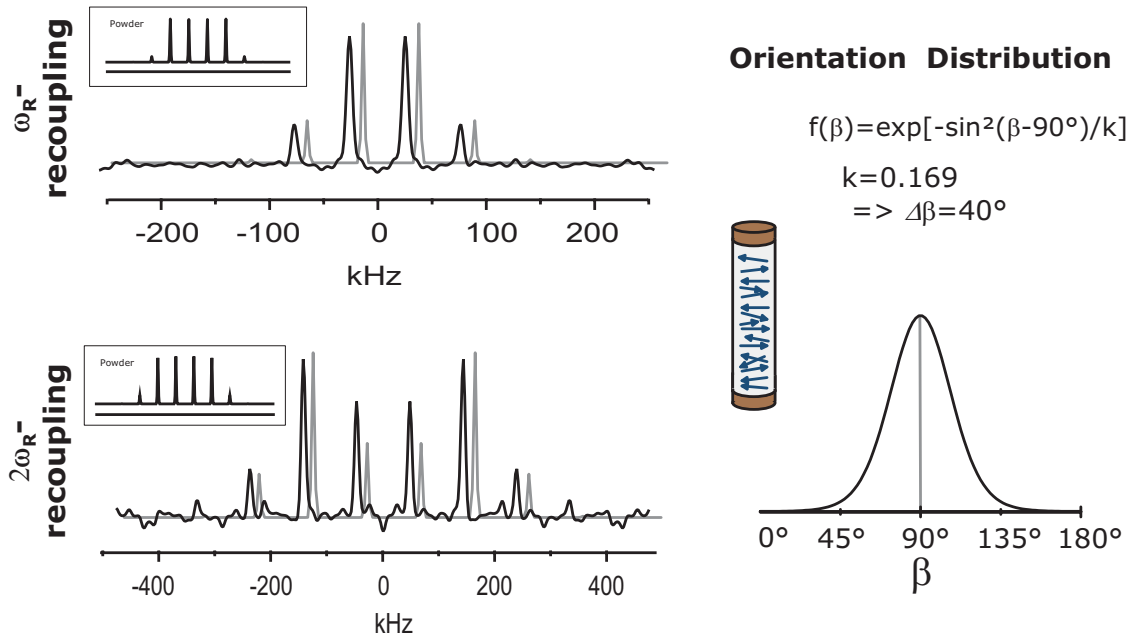

Figure 4.27: *REPT-HDOR SB patterns of the aromatic core CH of an oriented fiber of HBC-PhC$_{12}$ measured at 25 kHz MAS with a recoupling time of $\tau_{rcpl} = 2\tau_R$ (ω_R-recoupling) and $\tau_{rcpl} = 3\tau_R$ ($2\omega_R$-recoupling). The underlying grey patterns were calculated assuming Gaussian orientation distributions with widths $\Delta\beta$ = 40 ° and centered around β_0 = 90 ° (depicted on the right). The insets show simulations of the corresponding powder patterns.*

in [Fischbach 02]. In an extruded fiber, the columns are more or less oriented parallel to the fiber axis, as is depicted in the middle of Fig. 4.26.

First, SB patterns of the core CH resonance obtained with the REPT-HDOR experiment are discussed, which are shown in Fig. 4.27. The center of the orientation distribution is $\beta_0 = 90°$, since the aromatic discs are oriented perpendicular to the columnar/fiber axis and the internuclear vectors of all core CH pairs lie in the aromatic plane. This can easily be verified by comparing to the calculated SB patterns for various β angles shown in Fig. 4.24. A broad orientation distribution of $\Delta\beta = 40°$ was found to fit the experimental SB patterns best. According to Eq. (4.9), this corresponds to an order parameter S = -0.37 $\pm$ 0.06.

Alternatively, the width of the orientation distribution can be determined by CSA-recoupling. Exemplary, in Fig. 4.28 the $2\omega_R$-recoupled CODEX-SB pattern of the core CH is shown. Since the CSA-tensor is oriented differently to the heteronuclear dipole-dipole coupling tensor, the β angle is changed, around which the orientation distribution is centered. Since in aromatic carbons the lowest tensor value (σ_{33}) is oriented perpendicular to the ring plane and the aromatic cores are oriented perpendicular to the fiber axis, the center of the orientation distribution of the CSA is $\beta = 0°$, as is depicted on the right of Fig. 4.28. The experimental CODEX-SB pattern also fits best to an orientation distribution with a width of $\Delta\beta \approx 40°$.

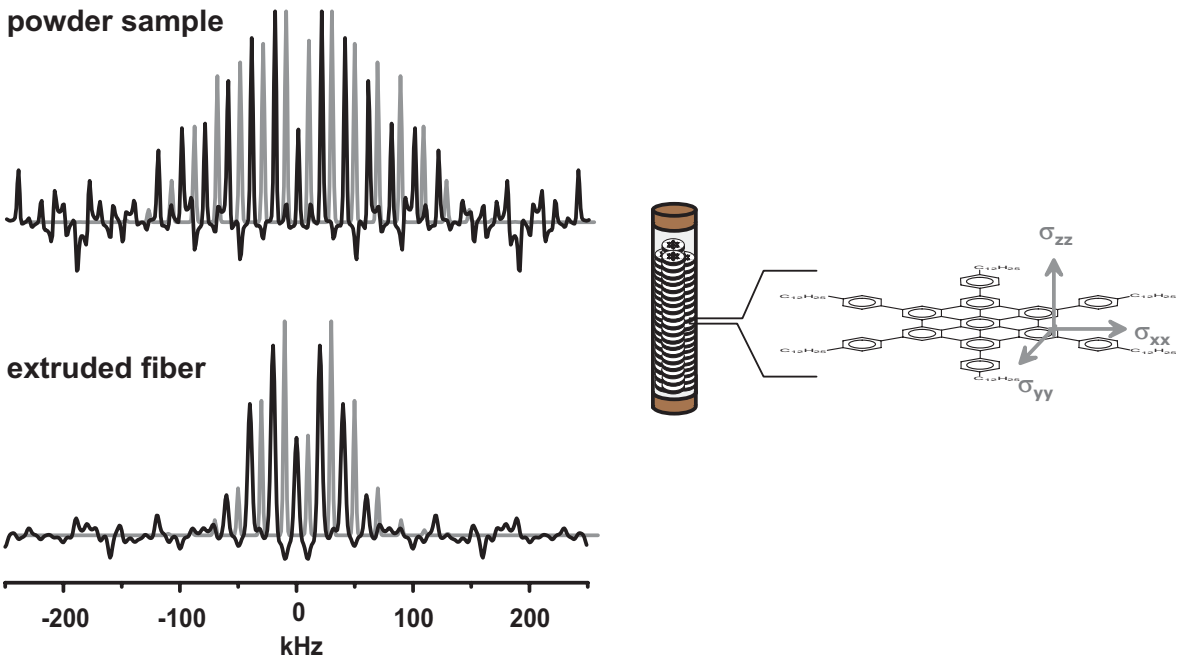

Figure 4.28: *$2\omega_R$-recoupled CODEX-SB patterns (10 kHz MAS, $\tau_{rcpl} = 2\tau_R$, T = RT) of the aromatic core CH of an unoriented powder sample (top) and an oriented fiber (bottom) of HBC-PhC$_{12}$. The underlying grey patterns are simulations for an isotropic powder (top) and for a Gaussian orientation distribution centered around β = 0° with a width $\Delta\beta$ = 40° (bottom). The CSA-tensor values used for the simulation were σ_{11} = 210 ppm, σ_{22} = 144 ppm and σ_{33} = 2 ppm (taken from [Fischbach 02]). On the right the orientation of the CSA-tensor in the molecular frame is depicted, which leads to β = 0° for perfect orientation.*

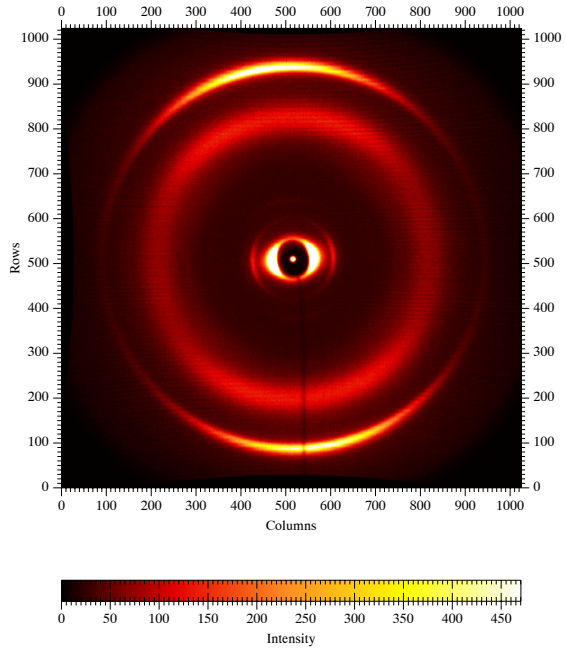

Figure 4.29: *WAXS pattern of the extruded fiber of HBC-PhC$_{12}$.*

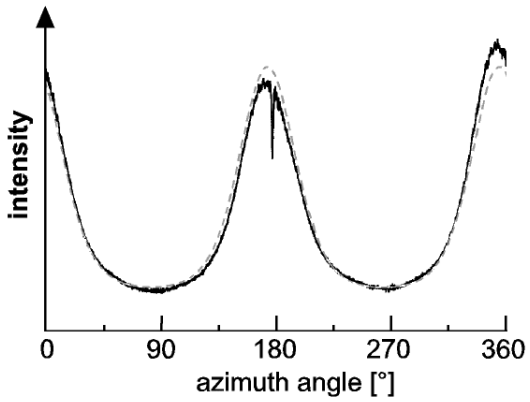

Figure 4.30: *Azimuth scan of the (001)-reflex of the 2D WAXS pattern of HBC-PhC$_{12}$. The dashed line represents the best fit according to the procedure described in [Ebert 03] with an order parameter of S = 0.59 ± 0.05.*

This corresponds, according to Eq. (4.9), to an order parameter of S = 0.71 ± 0.15.[2]
For comparison, a WAXS pattern was recorded, which is shown in Fig. 4.29. The indexing of the reflexes is analogous to the indexing published in [Fischbach 02] for an extruded fiber with smaller diameter and is therefore not listed in detail here. From an azimuthal scan of the (001)-reflex at $2\theta = 25.6°$ (Fig. 4.30) an order parameter of S = 0.59 ± 0.05 is extracted. Since the (001)-reflex arises from the interdisc spacing, the order parameter of this reflex should be comparable to the order parameter determined with the CODEX-SB. Within the error margins, the order parameters obtained with X-ray and solid-state NMR agree.

Having determined the order parameter of the aromatic discs, the recoupling experiments can be further explored. Regarding the sideband patterns of the *exo*-Ph CH, it is now possible to determine the average position of the phenylene rings. Since the σ_{zz} principal value of the CSA tensor of the *exo*-Ph CH is perpendicular to the phenylene ring plane, the angle β between σ_{zz} and the rotor axis directly reflects the tilt of the phenylene ring with respect to the core plane in the case of perfect alignment (i.e. the cores are perpendicular to the rotor axis). Of course, the cores are not perfectly aligned, but it is justified to assume that the width of the orientation distribution is basically the same for *exo*-phenylene rings and core, because

[2]Note that this order parameter differs from the one obtained from above REPT-HDOR, because the two order parameters are defined for different principal axes of orientation. Since an angle of 90 ° transforms between the CSA frame and the C-H frame, Eq. (4.10) can be easily applied to convert the two order parameters into each other ($-0.5 \cdot 0.71 \approx -0.37$, the slight deviation must be attributed to the errors occuring when numerically solving the integrals in Eq. (4.9)).

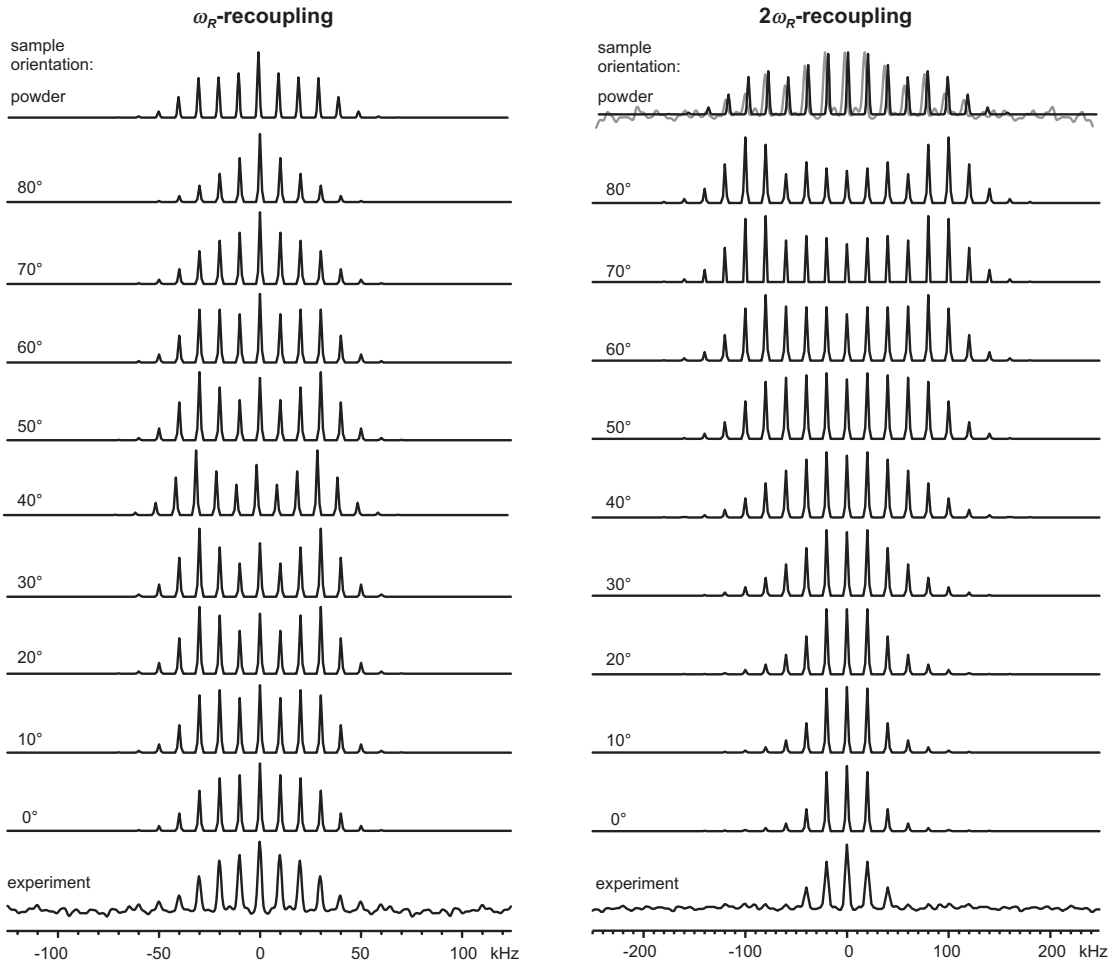

Figure 4.31: *ω_R- (left) and $2\omega_R$- (right) recoupled CODEX-SB pattern of the* exo*-Ph CH of an oriented fiber of HBC-PhC$_{12}$ for a recoupling time of $\tau_{rcpl} = 1\tau_R$ and $\tau_{rcpl} = 2\tau_R$, respectively, at 10 kHz MAS. The simulations were carried out assuming Gaussian orientation distributions with widths $\Delta\beta = 40°$ centered around the β_0 angles indicated in the figure. Clearly, the experimental data fits best to the patterns with β_0 = 0°. On the top, calculated powder patterns are shown. For $2\omega_R$-recoupling also an experimental pattern of an unoriented sample is shown for comparison (grey line).*

the phenylene rings are directly bonded to the core. For the analysis of the phenylene ring orientation it must be taken into account that the rings perform fast 180° flips around their internal C_2 axis, as was shown in [Fischbach 02]. There, the flip-averaged CSA tensor values were determined to σ_{xx} = 217 ppm, σ_{yy} = 175 ppm and σ_{zz} = -1 ppm. Since the flip leaves σ_{zz} and its orientation unchanged, the analysis of CSA SB patterns can simply be carried out with the flip-averaged tensor values and an orientation of the σ_{zz} principal value perpendicular to the phenylene ring plane. It is now possible to compare the experimental CSA SB patterns of the *exo*-PhC with simulated patterns, which were calculated for orientation distributions with $\Delta\beta$ = 40° centered around various β_0 angles. Of course, this analysis can again be carried out

for both ω_R- and $2\omega_R$-recoupled CSA SB patterns. The various SB patterns are compared in Fig. 4.31. Clearly, the experimental SB patterns fit best to β_0 = 0°. This is quite surprising, since- at first sight- this implies that the phenylene rings are coplanar to the core in their average flip position. However, for steric reasons, this can not be the case. At this point, it must be noted that the measured orientation distribution is the orientation distribution of the phenylene rings with respect to the rotor axis (= fiber axis) and *not* with respect to the core plane. The assumption that the measured orientation distribution directly reflects the orientation of the phenylene rings with respect to the aromatic core is obviously not fullfilled. Since it is well-known from structurally related systems that the coplanar arrangement is unfavorable for sterical reasons, a model including a tilt of the phenylene rings out of the core plane should be devised. In the quantum chemical calculations described in section 5.2 a tilt of the phenylene rings out of the molecular plane by around 20° was obtained. Obviously, the assumption of a single gaussian orientation distribution for the phenylene rings is inaccurate, since the phenylene rings can be tilted out of the core plane by angles +ϕ or -ϕ. Only if the core is oriented perpendicular to the rotor axis ($\beta = 0°$ for the CSA of the core CH), the two tilt directions lead to an identical β (with respect to the rotor axis) of the CSA of the phenylene rings. Hence, a bimodal orientation distribution centered around β = +ϕ and β = -ϕ seems to be the more appropriate model.

In Fig. 4.32 such a bimodal orientation distribution, which is composed of two gaussian orientation distributions, is shown. Clearly, for sufficiently broad individual gaussian distributions as the ones chosen here, the bimodal orientation distribution gets centered around β_0=0°, which would fit to the experimental observation. Obviously, large tilt angles ϕ can be excluded, since then the bimodal orientation distribution would not resemble a gaussian orientation distribution centered around β_0 = 0°. Detailed analysis and calculations of the maximum tilt angle are currently underway. Nonetheless, it should be kept in mind, that the analysis was crude from the beginning by just taking the flip averaged tensor values. If the flip motion is ill defined, i.e. not a perfect 180° flip, additional complications arise. Even though an ill-defined flip motion seems improbable from previous investigations [Fischbach 02], this possibility will be tested for in on-going investigations by repeating the experiments at temperatures at which the phenylene flip is frozen.

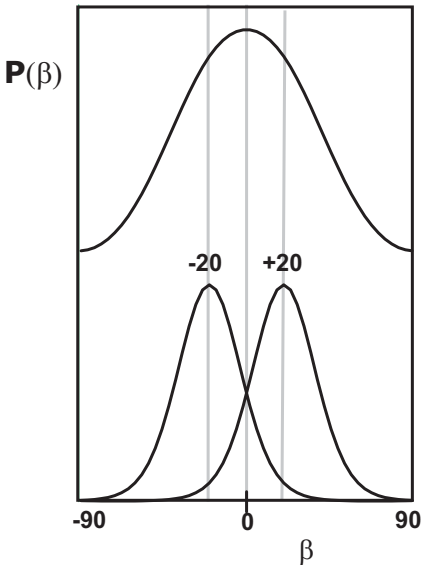

Figure 4.32: *'Bimodal' orientation distribution resulting for the phenylene rings as described in the text.*

The investigation on the oriented fiber of HBC-PhC_{12} has shown that the experiments described at the beginning of this chapter provide quantitative information on sample orientation analogous to information obtainable from X-ray. Nevertheless, it should be kept in mind that X-ray and solid-state NMR are based on different principles: while X-ray probes long-range order, NMR is a local method probing local order. Hence, as shown for the phenylene ring orientation, NMR in principle can also provide orientation information on the orientation of individual molecular segments (as resolved in a ^{13}C MAS spectrum), which can not be gained from X-ray.

Chapter 5

Structure and Dynamics in Hexa-substituted Hexa-*peri*-hexabenzocoronene Derivatives

In this chapter, the various solid-state NMR methods described in the previous chapters will be employed for the determination of structure and dynamics in hexa-substituted derivatives of hexa-*peri*-hexabenzocoronene (HBC) **1**. The investigations presented in this chapter represent the continuation of previous work on the characterization of structure and dynamics in HBCs by solid-state NMR [Herwig 96, Brown 99, Brown 00a, Fechtenkötter 99, Fischbach 02], which is briefly summarized in the first section (5.1). As shown by [Ochsenfeld 01] for HBC-C_{12}, the observed solid-state NMR ^{1}H shifts can be interpreted with the help of quantum chemical calculations. In section 5.2, it will be shown, that ^{13}C shifts and, in particular, the principal values of the ^{13}C chemical shift anisotropy are also sensitive to the solid-state packing. As already indicated by the title of this chapter, only hexa-substituted HBCs, i.e. HBCs carrying six identical substituents R (as depicted in Fig. 5.1), will be treated here. Due to their high molecular symmetry (C_6-symmetry axis), these hexa-substituted HBCs are often classified as symmetric HBCs. In section 5.3, HBCs carrying branched sidechains will be considered and compared to their counterparts with linear sidechains. The last section (5.4) is dedicated to C96, a material with an extended polycyclic aromatic hydrocarbon core, which is of particular interest, since the $\pi - \pi$ contact along the columnar stack is supposedly larger than in HBCs, which should lead to a further improve-

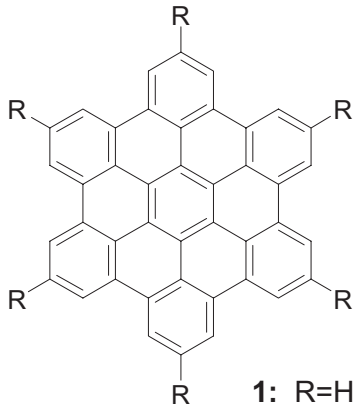

Figure 5.1: *Structure of hexa-substituted HBCs.*

Figure 5.2: *Discotic liquid crystalline materials. Some common examples, which were taken from [Chandrasekhar 98], are benzene-hexa-n-alkanoates* **2***, hexa-alkanoyloxytriphenylenes* **3** *and phthalocyanines* **4**.

ment of charge carrier mobilities.
All investigated materials were synthesized and provided by a number of colleagues, who are listed in the acknowledgement section. Consequently, the synthesis of these materials is not presented here; the interested reader is referred to the indicated literature.

5.1 Introduction to Hexa-*peri*-hexabenzocoronenes

Alkyl-substituted hexa-*peri*-hexabenzocoronenes often form liquid crystalline mesophases. Since their structure is composed of a flat disc-shaped polycyclic aromatic hydrocarbon (PAH) core, they belong to the class of the discotic mesogens, which will be briefly introduced in the following.

5.1.1 Discotic Liquid Crystals

The liquid crystalline (LC) state is defined as a mesomorphic state exhibiting long-range orientational order and either no or only partial positional order. Hence, it is an intermediate state of order between a liquid and a crystal. One distinguishes *thermotropic* liquid crystals, in which the mesophase is formed by heating a solid or cooling an isotropic liquid, and *lyotropic* liquid crystals, in which the mesophase is formed by dissolving an amphiphilic mesogen in suitable solvents under the appropriate conditions. In general, thermotropic mesogens have a stiff, (usually) aromatic core with anisotropic shape and flexible tails. Depending on their shape, LCs are divided into *calamitic* mesogens, characterized by the rod-like shape of the molecules, and *discotic* mesogens, characterized by the disc-like shape of the molecules.

The discovery of discotic liquid crystals is attributed to the work of Chandrasekhar on benzene-hexa-*n*-alkanoates (**2** in Fig. 5.2), which was published in 1977 [Chandrasekhar 77]. Over the last 25 years, the field of discotic liquid crystals has developed rapidly. Currently, more than 1500 different discotics are known. Some of the most common discotics are presented in Fig. 5.2, all of which feature a flat or nearly flat core with alkyl chain substituents. Although many applications have been suggested for discotic liquid crystalline systems, the only proven (profitable) application so far has been the production of optical compensation films for liquid crystal displays (Fuji Film Company) [Okazaki 00]. These films of a nematic discotic are being used to increase the angle of view in most modern liquid crystal displays. The list of potential applications for discotics ranges from their use in photovoltaics [Schmidt-Mende 01, Schmidt-Mende 02], OLEDs [Seguy 00] and electrically tuneable cholesteric mirrors [Kruerke 00]. This broad range of possible uses is the reason for the extensive research activities on discotic liquid crystals. For a recent review over discotic materials see [Bushby 02]. A more general overview can be found in [Chandrasekhar 98].

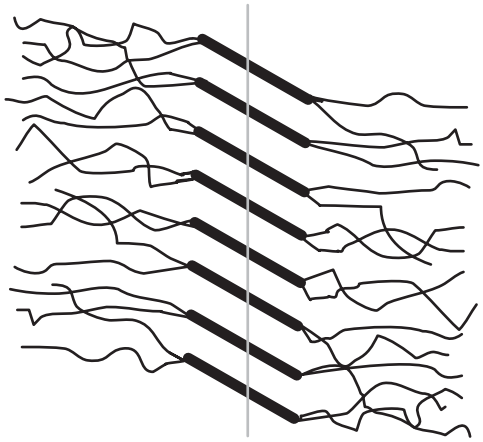

Figure 5.3: *The structure of a column, in which the molecular cores are tilted with respect to the column axis and the chains are in a highly disordered state.*

Discotic liquid crystals can be broadly classified into three types: *columnar* (Col), *nematic* (N_D) and *lamellar* (D_L). Examples of lamellar and nematic phases are rather scarce in comparison to the plethora of columnar materials. An overview over the columnar phases formed by discotic molecules is shown in Fig. 5.4. It should be noted that in older publications the notation 'D' is often found for columnar phases instead of 'Col'. The subscripts distinguish the different modifications, for example the subscript 'h' stands for a hexagonal lattice of columns, as indicated in Fig. 5.4. A common feature in columnar phases is a tilt of the molecular core with respect to the columnar axis, as depicted in Fig. 5.3. In contrast to the highly ordered cores, the sidechains are usually in a highly disordered state, as schematically shown in Fig. 5.3. The packing of the columns can be described by two-dimensional lattice structures, which have been identified by Levelut [Levelut 83] and are depicted in Fig. 5.5. The space groups indicated in Fig. 5.5 constitute a subset of the 230 space groups, when symmetry elements relating to translations along one of the axes (in this case the column axis) are absent.

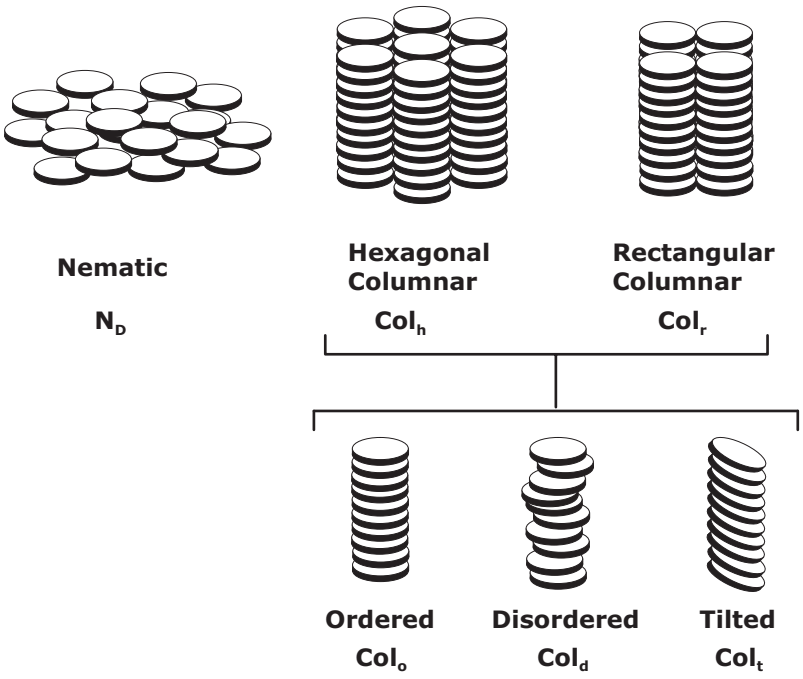

Figure 5.4: *Classification of the phases formed by disc-like molecules: Primarily, the phases are characterized by the degree of positional order and symmetry (top). The columnar phases can be sub-classified according to the degree of order within the columns (bottom).*

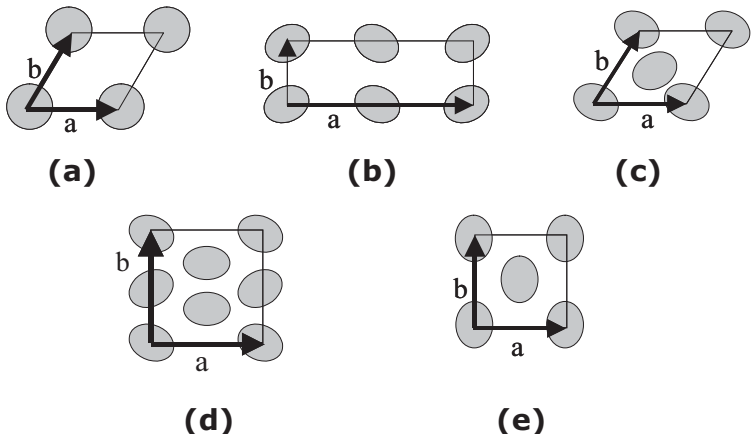

Figure 5.5: *Planar views of two-dimensional lattices of columnar phases; ellipses denote discs that are tilted with respect to the column axis: (a) hexagonal (P6 2/m); (b) rectangular ($P2_1/a$); (c) oblique (P_1); (d) rectangular ($P2_2/a$); (e) rectangular, face-centered, tilted columns (C2/m). The space groups are* planar *space groups, where symmetry elements relating to translations along the column axes are absent. [adapted from [Chandrasekhar 98].]*

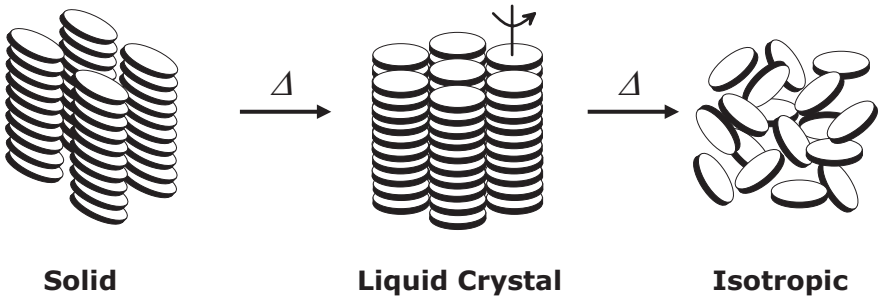

Figure 5.6: *Schematic representation of the phases typically encountered in HBCs.*

5.1.2 Phase Behavior of Hexa-*peri*-hexabenzocoronenes

Due to the disc-like shape of the HBC core, alkyl-substituted HBCs typically self-assemble into columnar aggregates and often exhibit thermotropic liquid crystalline behavior. The typical phases encountered in HBCs are depicted in Fig. 5.6. The cohesion of the molecules along the columns is caused by the microphase separation of the alkyl chains from the aromatic cores. In the LC phase, the columns are not tilted and usually packed in a two-dimensional hexagonal lattice. The sidechains are molten, and the aromatic cores undergo fast rotations about the columnar axis. Transition to the isotropic state, i.e. breaking of the columnar aggregates, requires high energy and occurs at usually very high temperatures, which are often even higher than the onset of decomposition. The low temperature phases are characterized by a higher order and by the loss of mobility of the aromatic cores. Typically, but not necessarily, a tilt of the molecules with respect to the columnar axis is observed. In the literature some dissension is found with respect to the nomenclature of the low temperature phases. On the one hand, the high order of the aromatic cores suggests to call them 'crystal' phases; however, since the alkyl chains can still be mobile and are usually amorphous, the term 'crystalline' phase is considered to be inadequate. On the other hand, alternative suggestions like 'plastic' crystals or 'defect-rich' crystals seem to be even more inappropriate. Therefore, in the following the neutral term 'solid' phase will throughoutly be used to refer to the low temperature phases. Here, the word 'solid' indicates the absence of any fast motion of the aromatic cores.

The phase behavior of HBCs is commonly studied by differential scanning calorimetry (DSC), polarized optical microscopy (POM), thermogravimetric analysis (TGA) and X-ray scattering. DSC is used to determine the temperatures, at which structural transitions occur in the sample. However, DSC does not yield any information about the kind of the structural changes. With the help of POM liquid crystalline phases can be distinguished from isotropic or crystalline phases, because they exhibit characteristic textures. Powder X-ray diffractometry provides some information on the nature of the phases as well. However, since in powder X-ray diffractometry reflections arising from intercolumnar and intracolumnar order cannot be distinguished, nowadays 2D diffractograms are mea-

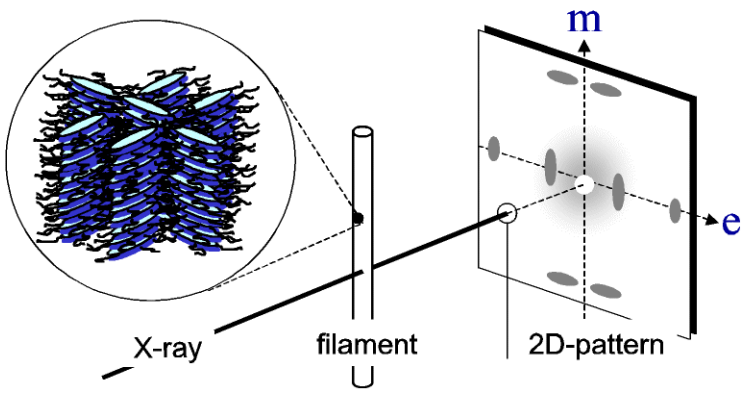

Figure 5.7: *Experimental setup for the X-ray analysis of extruded filaments.*

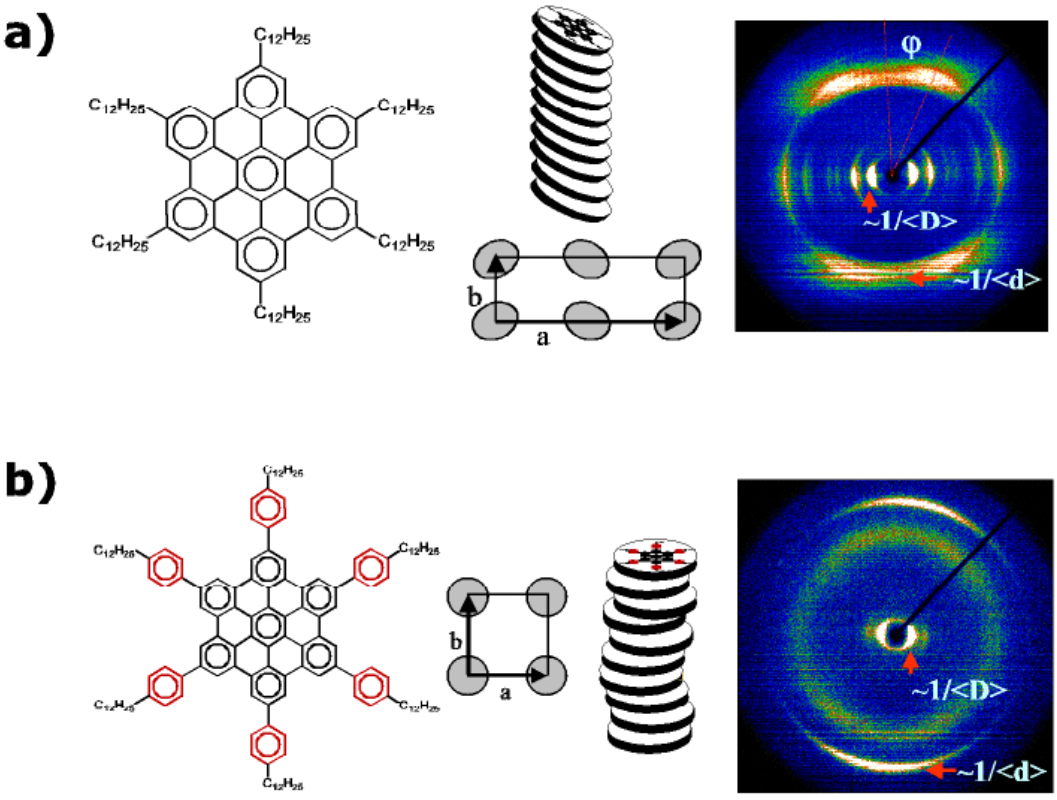

Figure 5.8: *Two-dimensional scattering patterns of oriented filaments of HBC-C_{12} (a) and HBC-PhC_{12} (b) measured in their solid phases at 300K [Fischbach 02]. The 2D lattices of the intercolumnar arrangements and the orientation of the discs within the column are shown schematically.*

sured on macroscopically oriented samples, which allow these reflections to be distinguished [Fechtenkötter 01a, Fischbach 02, Ito 00b]. These wide angle X-ray scattering (WAXS) measurements are recorded with vertical orientation of the extruded filaments perpendicular to the incident X-ray beam, as depicted in Fig. 5.7. In the resulting scattered intensity distributions, reflections on the equatorial (e) direction correspond to intercolumnar order, whereas reflections on the meridional (m) correspond to intracolumnar order. The oriented filaments are prepared with an extruder like the one shown in Fig. 4.26. With the aid of these patterns, tilted columnar structures can often be distinguished from upright columnar structures, as shown in Fig. 5.8, where WAXS patterns of extruded fibers of HBC-C_{12} (**5** in Fig. 5.9) and HBC-PhC_{12} (**6** in Fig. 5.9) are compared. The pattern of **5** corresponds to a rectangular, tilted columnar structure, whereas the pattern of **6** corresponds to a rectangular, non-tilted columnar structure.

5.1.3 Previous Solid-State NMR Investigations of Hexa-*peri*-hexabenzocoronenes

As shown by Brown et. al. [Brown 99, Brown 00a], the relative arrangement of neighboring discs in the columnar packing of hexa-*peri*-hexabenzocoronenes can easily be determined by ^{1}H solid-state MAS NMR, which is a powerful tool for unravelling the stacking arrangement within the columns. For example, the tilted arrangement of the discs in the solid phase of HBC-C_{12} (**5**) leads to different electronic environments of the aromatic protons in the packing. Therefore, in the ^{1}H MAS spectrum (Fig. 5.10) three distinct aromatic ^{1}H resonances are observed. The pronounced splitting reflects the different degrees to which the protons experience aromatic ring current effects from adjacent layers. Hence, the splitting is a packing effect due to the relative arrangement of the aromatic discs in the solid state. To address the question whether the three resonances arise from molecules in three different packing arrangements or from the protons of a single molecule, a two-dimensional ^{1}H -^{1}H double-quantum (DQ) spectrum was recorded, which is shown in Fig. 5.11b. In such a DQ spectrum, DQ coherences are only observed if the underlying dipole-dipole couplings between the respective nuclei are strong enough. This is only the case for nuclei which are not further apart than $\sim$ 0.35 nm. In this way, detailed information about internuclear proximities is obtained from the signals in the 2D DQ spectrum. This in turn made it possible to identify the structure as a so-called 'herringbone'-type arrangement, which is shown in Fig. 5.11a. Since the signal pattern observed for the aromatic protons will turn out to be a characteristic pattern for many HBC derivatives, it will be discussed in more detail in the

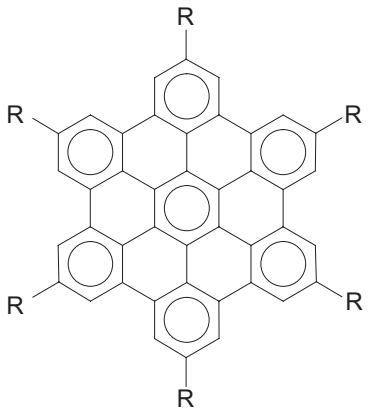

5: R= $C_{12}H_{25}$ (HBC-C_{12})
6: R= $PhC_{12}H_{25}$ (HBC-PhC_{12})

Figure 5.9: *Chemical structures of HBC-C_{12} (**5**) and HBC-PhC_{12} (**6**).*

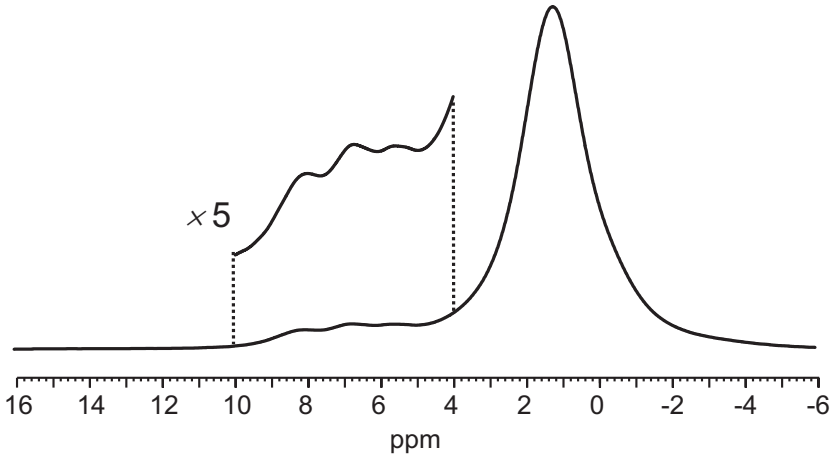

Figure 5.10: *^1H spectrum of HBC-C_{12} (**5**) measured at 35 kHz MAS and T = 60 °C [Brown 99].*

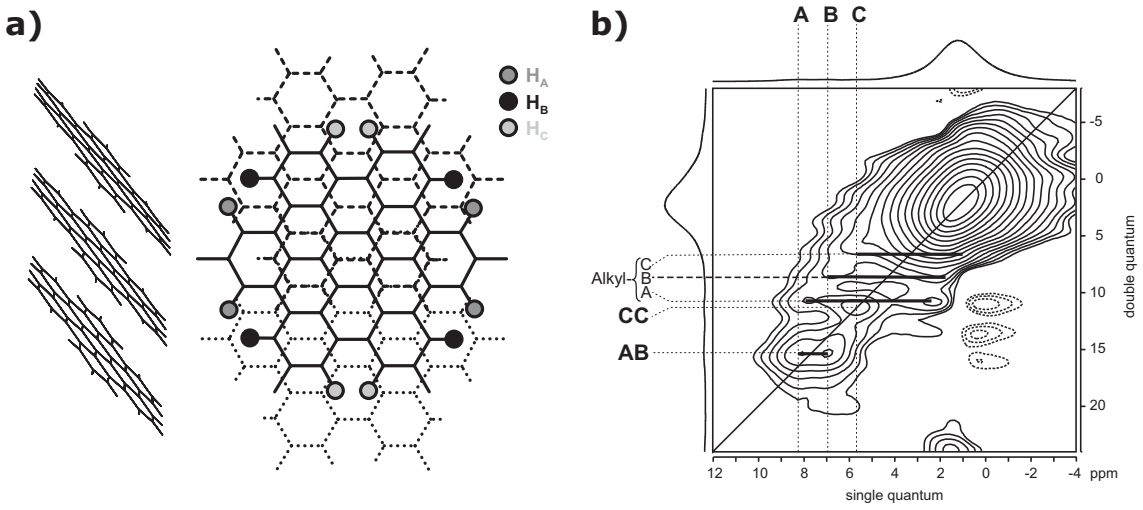

Figure 5.11: *(a) Stacking arrangement of **5** in the solid phase. As indicated, this 'herringbone'-type of stacking leads to three different environments for the aromatic protons. (b) ^1H DQ spectrum of **5** recorded at 35 kHz MAS using one cycle of the BABA recoupling sequence (taken from [Brown 99]).*

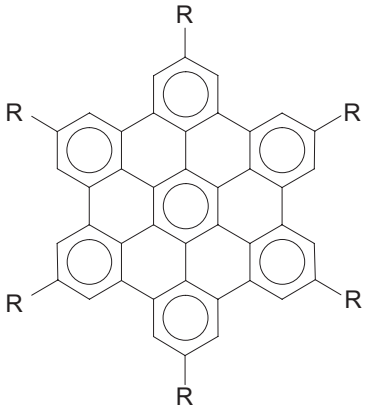

7: R= $CH(CH_3)_2$ (HBC-*i*Pr)
8: R= $C(CH_3)_3$ (HBC-*t*But)

Figure 5.12: *Chemical structures of HBC-*i*Pr and HBC-*t*But.*

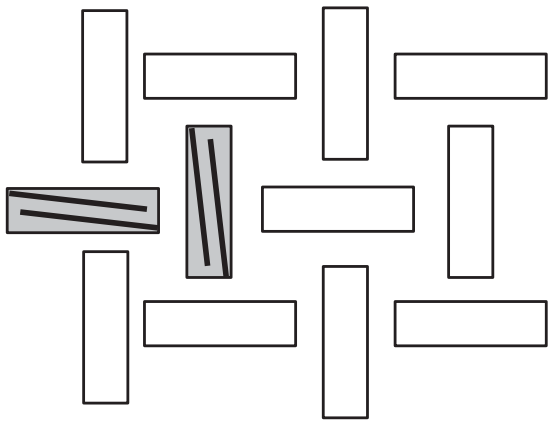

Figure 5.13: *The packing of HBC-tBut molecules as determined by a X-ray single crystal investigation [Herwig 00].*

following: The signal pattern of the aromatic protons consists of two off-diagonal peaks AB and one diagonal peak CC. While the cross-peaks indicate a close proximity of two aromatic protons with different chemical shifts A and B, the diagonal peak is due to a close proximity of two protons with identical chemical shift C. From the relative signal intensities it is clear that the two type of pairs, AB and CC, are present in a ratio 2:1. This characteristic DQ signal pattern is perfectly explained by a tilted disc arrangement as it is shown in Fig. 5.11a. The three proton positions distinguishable in this packing arrangement can quantitatively explain the deshielding effects, the types of pairs and the signal intensities observed in the ^{1}H -^{1}H DQ spectrum. *Ab initio* quantum chemical calculations of NMR shifts proved that there is no other packing arrangement which would give rise to the observed ^{1}H spectra [Ochsenfeld 01]. Similarly, the solid-state structures of HBC-*i*Pr (**7** in Fig. 5.12) and HBC-*t*But (**8** in Fig. 5.12) could be determined [Brown 00a]. The ^{1}H -^{1}H DQ MAS spectra showed that HBC-*i*Pr adopts the same packing arrangement as HBC-C_{12}. The packing of HBC-*t*But molecules could be determined by a X-ray single crystal investigation [Herwig 00] and is schematically depicted in Fig. 5.13. The structure consists of pairs of molecules in a sandwich-like arrangement, which then form a three-dimensional array. The aromatic cores of each sandwich are situated in a T-like fashion approximately perpendicular to the aromatic cores of each neighboring sandwich. This much more complicated packing arrangement was also consistent with ^{1}H DQ MAS NMR, which proved the ability of using ^{1}H DQ MAS for structure elucidation even in more complicated cases.

The development of heteronuclear correlation techniques for fast MAS NMR [Saalwächter 01a] opened up the possibility to acquire ^{1}H -^{13}C heteronuclear correlation spectra, which benefit from the greater resolution in ^{13}C spectra. With these techniques, structural information can be gained in those cases where ^{1}H spectra lack sufficient peak resolution. For example, in the ^{1}H spectrum of HBC-PhC_{12} (**6**) the peaks of the aromatic

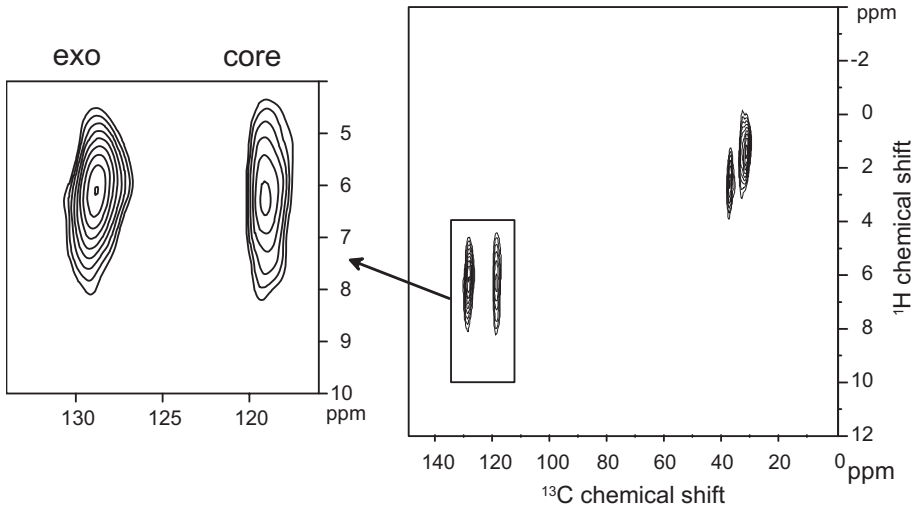

Figure 5.14: *Heteronuclear correlation spectrum of HBC-PhC$_{12}$ [Fischbach 02]. Clearly, only one ^{1}H -^{13}C correlation peak of the core CH is observed indicating the absence of a tilted columnar arrangement, which would lead to a splitting of this peak.*

core protons and the protons of the *exo*-phenylene rings overlap, which renders a structure elucidation based on protons impossible. However, in the 2D heteronuclear correlation spectrum (Fig. 5.14), the ^{1}H -^{13}C correlation peaks of the directly bonded core C-H pairs[1] and the directly bonded *exo*-phenylene C-H pairs[2] are resolved [Fischbach 02]. Clearly, the ^{1}H chemical shift is exactly the same for the core and the *exo* resonances. Since the correlation peak of the core CH is not split, HBC-PhC$_{12}$ adopts a non-tilted arrangement of the discs within the column, because a tilt would lead to an observable splitting of the core CH peak.

As already mentioned above, solid-state NMR can also be used to study molecular dynamics in HBCs. In fact, the first solid-state NMR investigations were carried out on core-deuterated HBC-C$_{12}$ and focused on the determination of the dynamic order parameter for the disc rotation in the columnar mesophase [Herwig 96, Kayser 99]. This is the most prominent dynamic process in columnar mesophases. With the development of recoupling experiments under fast MAS, this order parameter could also be determined by ^{1}H DQ NMR [Brown 99] and by REPT-HDOR [Fechtenkötter 99]. For all approaches, the order parameter is determined by measuring the rigid and the motionally reduced coupling strength D of the respective interaction (quadrupolar coupling or homo- or heteronuclear dipole-dipole coupling). If the symmetry axes of the tensors (the CH bond vector and the H-H internuclear vector of the two core CH protons) lie in a plane perpendicular to the rotational axis, the coupling constants are reduced by a factor of 0.5. Any further reduction is due to additional out-of-plane motion. Hence, the order parameter S for the column rotation was defined as $S_{col.rot.} = \frac{2D^{mobile}}{D^{rigid}}$. With all three methods employed, identical (within the experimental errors) order parameters were obtained of around $S_{col.rot.}$ = 0.80. This order parameter, which is <1, was taken as an indica-

[1] Henceforth referred to as core CH.

[2] From now on referred to as *exo*-Ph CH.

tion for additional out-of-plane motion.
In the solid phases at lower temperatures, the aromatic cores are rigid on the μs timescale, as is clear from the observation of rigid-like dipole-dipole coupling constants. This leaves only the possibility of slow jump motions of the aromatic cores on the *ms-s* timescale. These can conveniently be observed and investigated by the one-dimensional CODEX experiment. In HBC-PhC_{12} slow jumps about the C_6-symmetry axis of the molecule could be detected [Fischbach 02].
Of course, not only the motion of the core can be probed by solid-state NMR, but also the motion of the sidechains. Since the alkyl-sidechains are usually amorphous or only partly crystalline, they are generally more mobile than the aromatic cores. As shown in [Saalwächter 00] the REPT-HSQC build-up behavior makes it possible to draw (qualitative) conclusions about the sidechain mobility in HBCs. Expectedly, a mobility gradient along the chain was observed, with the chain ends being most mobile. As shown on other discotic liquid crystalline materials [Goldfarb 83, Hirschinger 91, Werth 93], information on sidechain dynamics is also accessible by deuteron NMR, provided that samples can be prepared with selective deuteration on the sidechains. As shown in subsection 5.3.3, the REREDOR experiment [Saalwächter 02c] enables a quantitative investigation of sidechain dynamics without the need of isotopic enrichment.

5.2 Core Packing as Reflected in Calculated and Experimental NMR Shifts

As already mentioned above, the combination of quantum chemical calculations with NMR experiments is a particular powerful tool, when it comes to unravelling solid-state structures [Facelli 93, Salzmann 98]. In the case of HBC-C_{12}, the quantum chemical calculation could relate the observed ^{1}H chemical shifts in a *quantitative* manner to the intermolecular structure [Ochsenfeld 01]. In this section, the core packing in HBC-PhC_{12} is investigated in more detail by comparing experimental and *ab initio* calculated NMR shifts. The intracolumnar packing arrangement in HBC-PhC_{12} could already be identified by X-ray scattering and solid-state NMR as a non-tilted arrangement of the discs within the column (see previous section). This arrangement plus the tilted packing of, for example, HBC-C_{12} are the typical packing arrangements in alkyl-substituted HBCs. Therefore, the detailed characterization of the solid-state packing in HBC-PhC_{12} presented here, also exhibits some kind of model character for other HBCs with similar solid-state structures. For example, since the calculations do not include the alkyl-substituents, their results can equally well be compared to the experimental findings of HBC-PhC_{12} and HBC-Ph$C^*_{8,2}$ (considered in section 5.3). While the previous studies on HBC-C_{12} focused on ^{1}H NMR shifts [Ochsenfeld 00, Ochsenfeld 01], the quantum chemical calculations automatically provide chemical shift data also for the other nuclei present in the molecular structure. As will be shown below, the isotropic ^{13}C chemical shift data and also the principal values of the ^{13}C chemical shift anisotropy are sensitive with respect to the solid-state packing, too, even though, admittedly, the absolute effect (in ppm) is on the same order of magnitude as for ^{1}H . Hence, relative to the total width of the spectra, the shifts induced by packing effects are by far not as pronounced for ^{13}C as for ^{1}H .

The *ab initio* calculations were performed by Prof. Jürgen Gauss (University of Mainz) using the program package TURBOMOLE [Ahlrichs 89]. Geometry optimization was carried out at the RI (resolution of identity)- DFT (density functional theory) level using the BP86 functional [Parr 89, Perdew 86, Becke 88] and a polarized split-valence (SVP) basis [Schäfer 92]. To avoid the gauge-origin problem in the calculation of the NMR chemical shifts, the gauge-including atomic orbitals (GIAO) approach [London 37] was used at the HF (Hartree-Fock) level [Ditchfield 74, Wolinski 90, Häser 92] with a 3-21G basis. The results of the calculations are preliminary, since with the used 3-21G basis no basis set convergence was reached for all reported shifts. Further calculations with improved basis sets are currently underway. The results of those calculations and further details of the calculations reported here will be subject of a separate future publication [Gauss 03a].

The quantum chemical calculations were restricted to a single HBC column, which can be justified by the isolating effect of the long alkyl sidechains. Also, only stacks of a few HBC molecules (i.e. small fractions of the column) were computed. This is feasible, because NMR chemical shifts are basically 'local' properties, which are influenced only by the next few neighbors. As mentioned above, the alkyl-substituents were replaced by hydrogen atoms.

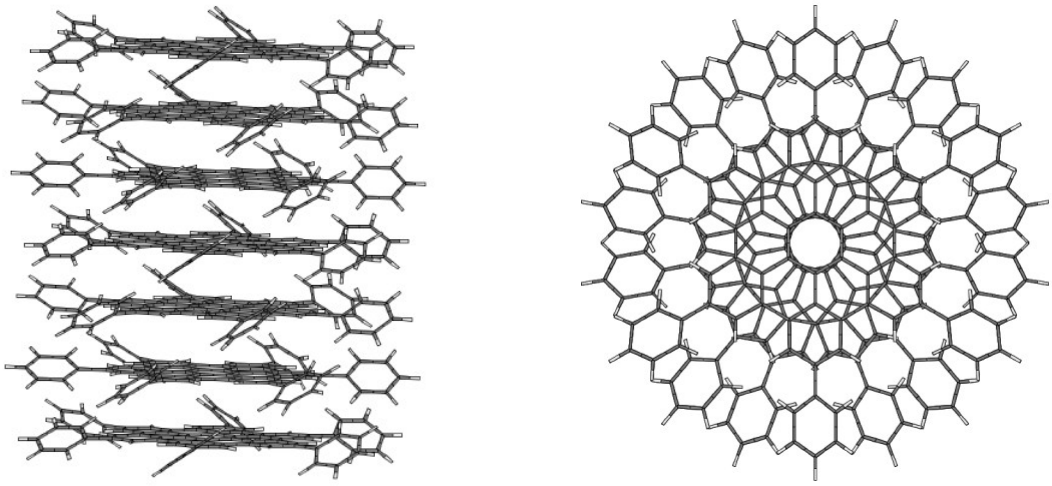

Figure 5.15: *Stacking of the HBC-PhC_{12} molecules in the model heptamer.*

This not only keeps the calculation time reasonably short, but also circumvents the problem of choosing the correct conformation of the alkyl-substituents. Of course, the results for the resonances close to the replaced alkyl-substituents are then inflicted with a substantial error, which needs to be accounted for separately. Of course, the validity of the chosen model system needs to be verified, and, in particular, the properties computed for small systems need to converge towards the properties of the bulk samples studied experimentally.

The quantum chemical calculations were performed starting with an optimization of the geometry of a single HBC-Ph molecule. From biphenyl it is known that the phenylene rings are tilted out of the molecular plane by 17.34° due to energetical reasons. For the calculations here, the phenylene rings were found to be tilted by around 20° out of the molecular plane. With this geometry, model stacks of three, five and seven HBC-Ph molecules were built as depicted in Fig. 5.15. In the stack, neighboring molecules are rotationally displaced by 20°. This angle was chosen, since then the structure still exhibits D_6 symmetry, which simplifies the calculations substantially. In a model stack of two HBC-Ph molecules, the relative energy was found to be lowest for an angle of 18°, as depicted in Fig. 5.16. Such a rotational displacement fits to recent results from X-ray, where a helical arrangement with every third molecule in the columnar stack being crystallographically identical was observed [Pisula 03]. Convergence of the calculated NMR shifts with stack size can then be checked by comparing the calculated shifts from a single molecule and stacks of three, five and seven molecules.
Since HBCs are known to have a strong aggregation tendency in solution, the convergence of the NMR chemical shifts with increasing stack size can experimentally be monitored by NMR on solutions with decreasing concentrations. Generally, the lower the concentration, the smaller the average size of the aggregates formed in solution. Finally, in infinite dilution, only isolated molecules are present. Practically, the concentrations are lowered until a plateau is reached, i.e. the observed chemical shifts no more change upon lowering the concentra-

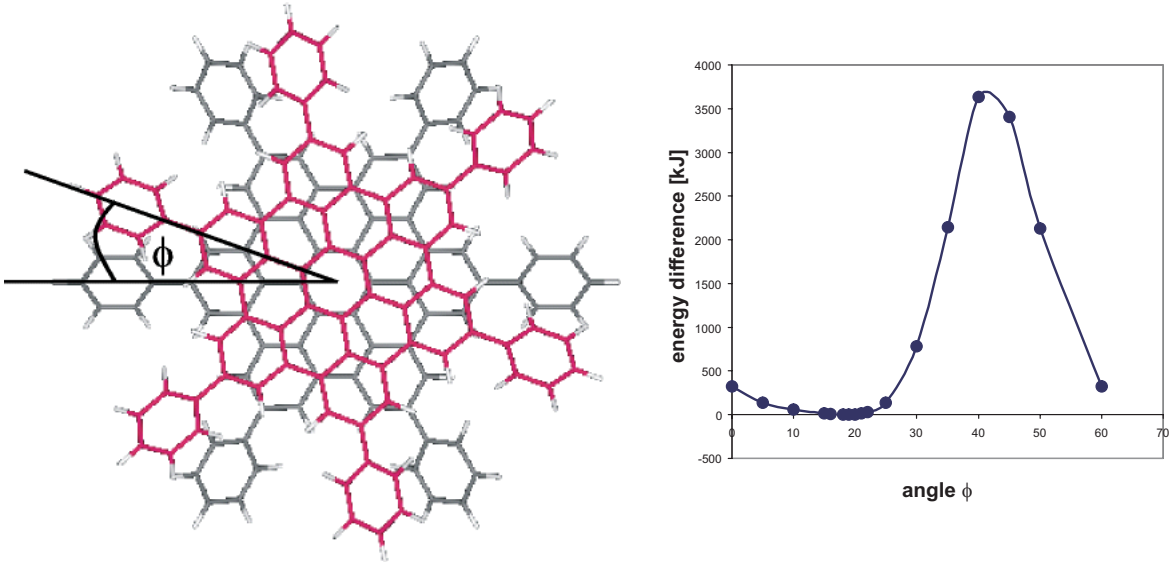

Figure 5.16: *Rotational displacement of the HBC-PhC$_{12}$ molecules in the columnar stack. On the right the dependence of the relative energy of the dimer on the rotation angle ϕ is plotted.*

tion. The plateau value of the chemical shift should reflect the chemical shift of an isolated molecule in the respective solvent.

Since HBC-PhC$_{12}$ exhibits an exceptional strong aggregation tendency even at elevated temperatures, the solution spectra needed to be measured at 130 °C in deuterated *o*-dichlorobenzene in order to ensure sufficiently narrow peaks. Spectra for various concentrations were measured, some of which are depicted in Fig. 5.17. Clearly, a strong dependence of the chemical shift of the aromatic protons on the concentration is observed. As it turned out, a plateau could be reached only for the Phenyl-H2 within experimentally accessible concentrations. Spectra at lower concentrations (c = $6.7 \cdot 10^{-6}$ mol/l and c = $1.8 \cdot 10^{-6}$ mol/l) were measured, but no signal of the aromatic protons was observed even after 4 days of signal acquisition. The solid-state ^{1}H NMR chemical shifts were taken from the heteronuclear correlation spectrum (Fig. 5.14 and [Fischbach 02]). In Table 5.1 the calculated proton chemical shifts are listed together with experimental values from solution and solid-state NMR experiments. Clearly, when increasing the size of the stacks in the calculations, the chemical shifts of all aromatic ^{1}H resonances are shifted upfield, which can be attributed to additional shielding from the "ring currents" of nearby molecules. This trend is also found in the solution spectra. The solid-state chemical shift of the core protons is in good agreement with the calculated shift for the stack of seven molecules. This shows that even the third nearest neighbors induce an observable shift effect. Since the chemical shifts listed in table 5.1 do not include the influence of the alkyl-chain substituents, it is not surprising that the solid-state chemical shifts of the protons attached to the phenylene ring do not agree with the calculated shifts. As mentioned above, the discrepancy between experiment and theory might also be attributed to the not yet optimal basis used for the calculations. Probably the phenyl shifts will better be accounted for by the ongoing calculations with an improved basis set.

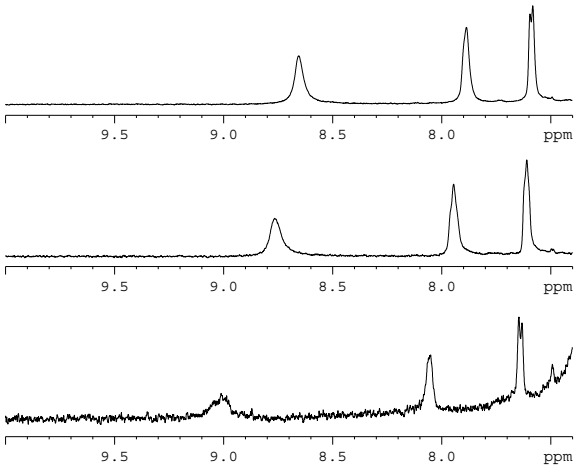

Figure 5.17: *^{1}H NMR spectra of HBC-PhC_{12} in deuterated* o*-dichlorobenzene at 130 °C and three exemplary concentrations: c = 2.3·10$^{-3}\frac{mol}{l}$ (top), c = 1.1·10$^{-3}\frac{mol}{l}$ (middle) and c = 2.0·10$^{-4}\frac{mol}{l}$ (bottom).*

Table 5.1: *Calculated (HF/3-21G) and experimental ^{1}H NMR shifts of the aromatic protons of HBC-PhC_{12}. All chemical shifts are given in ppm relative to the commonly used TMS (tetramethylsilane) standard.*

	Core	**Phenyl H1**	**Phenyl H2**
Theory			
Single Molecule	10.09	8.57	8.04
Three Molecules Stack (middle sheet)	8.8	8.84	7.99
Five Molecules Stack (middle sheet)	7.52	8.12	7.71
Seven Molecules Stack (middle sheet)	6.57	7.43	7.26
Experiment			
Solid-State NMR (T = 48 °C) [a]	6.3	6.1	6.1
Solution[b]:			
$2.3 \cdot 10^{-3}$mol/l	8.66	7.89	7.59
$1.4 \cdot 10^{-3}$mol/l	8.72	7.92	7.60
$1.1 \cdot 10^{-3}$mol/l	8.77	7.95	7.61
$5.0 \cdot 10^{-4}$mol/l	8.89	8.00	7.63
$4.6 \cdot 10^{-4}$mol/l	8.91	8.01	7.63
$2.0 \cdot 10^{-4}$mol/l	9.01	8.06	7.64
$1.0 \cdot 10^{-4}$mol/l	-	8.08	7.65
$3.5 \cdot 10^{-5}$mol/l	-	8.14	7.64

[a] from ^{1}H -^{13}C correlation (REPT-HSQC)
[b] o-$C_6D_4Cl_2$, 130 °C

Table 5.2: *Calculated (HF/3-21G) and experimental NMR shifts of the tertiary aromatic ^{13}C of HBC-PhC_{12}. All chemical shifts are given in ppm relative to the commonly used TMS (tetramethylsilane) standard. The signals of most of the quarternary carbons are not resolved in the solid-state spectrum and are therefore not listed in the table.*

	Core	**Ph 1**	**Ph 2**	**Ph with R**
Theory[a]				
Single Molecule	117.76	124.31	124.85	131.06
Three Molecules Stack (middle sheet)	117.20	122.98	124.85	129.59
Five Molecules Stack (middle sheet)	115.68	122.43	124.32	128.95
Seven Molecules Stack (middle sheet)	114.62	121.77	123.78	128.39
Experiment				
Solid-State NMR	118.1	127.3	126.5	139.20
Solution[b]:	120.31	128.93	129.83	

[a] with correction for the alkyl-substituent
[b] $C_2D_2Cl_4$, 85 °C

In the following, the ^{13}C chemical shifts are compared, which are listed in table 5.2. Not all solution and solid-state chemical shifts could be assigned unambiguously. Hence, in table 5.2 only the identified shifts are listed. Clearly, the changes of the isotropic ^{13}C chemical shifts are by far too small to be unambiguously detected as such in NMR experiments. Nonetheless, calculations of isotropic ^{13}C shifts are extraordinary useful for spectral assignment purposes. Even though the isotropic ^{13}C chemical shifts change only slightly by packing effects, the effect might be much more pronounced when regarding the principal values of the CSA tensor. As depicted in Fig. 4.28 the σ_{zz}-principal value of the core CH points perpendicular to the core plane. Hence, it should be influenced most by the "ring currents" of the neighboring molecules in the column. The principal values of the ^{13}C CSA were measured with the SUPER experiment [Liu 02] which correlates quasi-static CSA powder patterns with isotropic chemical shifts and, in this way, separates overlapping patterns. The SUPER spectrum is shown together with the extracted patterns in Fig. 5.18. The extracted tensor values are listed in table 5.3 together with the calculated values. The experimental σ_{xx} and σ_{zz} principal values are in nice agreement with the calculated values for the stack of seven molecules. The strong deviation of the experimental and theoretical σ_{yy} principal value can be attributed to the insufficient basis set used in the calculations. Calculations on benzene revealed that the errors arising from this are large for σ_{xx} and σ_{yy}, but small for σ_{zz} [Gauss 03b]. Hence, the observed agreement between the experimental and the calculated value of σ_{zz} is real and not coincidental. Surprisingly, the σ_{zz}-principal value changes by over 17 ppm from the single molecule to the stack of seven molecules. This effect is definitely strong enough to be detected experimentally. Since the SUPER experiment provides a facile way to determine the

Table 5.3: *Calculated (HF/3-21G) and experimental ^{13}C CSA tensor values in ppm of the core CH of HBC-PhC_{12}.*

	σ_{xx}	σ_{yy}	σ_{zz}	σ_{iso}
Theory				
Single Molecule	205.5	126.4	21.4	117.8
Three Molecules Stack (middle sheet)	208.0	131.2	12.4	117.2
Five Molecules Stack (middle sheet)	208.4	131.4	7.2	115.7
Seven Molecules Stack (middle sheet)	208.3	131.2	4.4	114.6
Experiment				
Solid-State NMR	210 ± 5	144 ± 3	2 ± 5	118.1

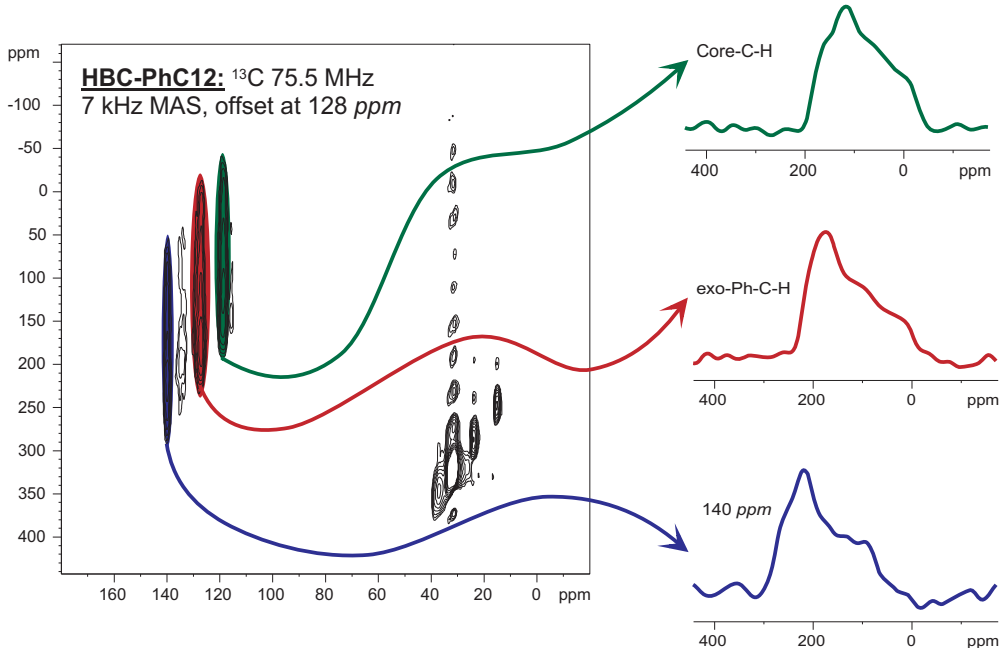

Figure 5.18: *SUPER spectrum of HBC-PhC_{12} together with the extracted quasi-static powder patterns for the aromatic resonances. The experimental details are listed in appendix D.1. Since the spectrum was not subjected to the shearing procedure described in [Liu 02], the extracted patterns are shifted by the scaled isotropic shift term (see section 3.6). The values listed in Table 5.3 were corrected to yield the correct tensor values.*

^{13}C CSA in a site-resolved fashion, the combination of quantum chemical calculations with experimental ^{13}C chemical shift anisotropies comprises an additional way to investigate solid state structures with respect to aggregation phenomena. This might be of particular interest in those cases where no ^{1}H are present in the chemical structure at the position of interest.

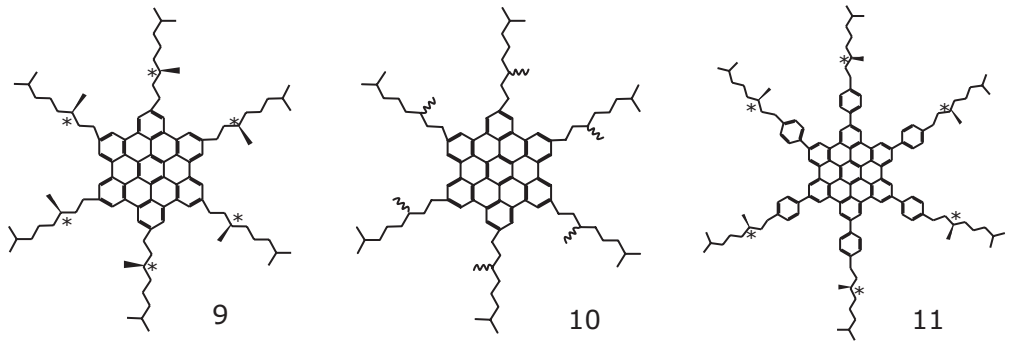

Figure 5.19: *Chemical structures of the investigated symmetric HBC derivatives with branched sidechains.*

5.3 HBC Derivatives with Branched Sidechains

In this section, results on symmetrically substituted (i.e. six identical sidegroups) HBCs are presented. As described above, some symmetrically substituted HBCs are already well-studied in terms of solid-state NMR. However, all these materials had either unbranched (HBC-C_{12}, HBC-PhC_{12}) or very short sidegroups (HBC-*i*Pr, HBC-*t*But). The need of materials with low LC phase transition temperatures and better solubility led to the introduction of long, branched sidechains [Fechtenkötter 01b]. The question arising immediately is to which extent the columnar order is influenced by the substitution with the more bulky, branched sidegroups. In order to answer this question, three materials with branched alkyl-chains were investigated, namely HBC-$C^*_{8,2}$ (**9**), HBC-$C^{rac}_{8,2}$ (**10**) and HBC-Ph$C^*_{8,2}$ (**11**), whose chemical structures are shown in Fig. 5.19. Material **10** is, strictly speaking, not a pure compound, but a mixture of all possible diastereomers and enantiomers, which is be produced when the a racemic precursor is used during synthesis[3]. Since this fact does not necessarily matter for potential applications, but in some respect even might be an advantage due to the lowered phase transition temperatures, the racemic mixture **10** is investigated as well for comparison. Previous studies already characterized the phase behavior of these three materials by DSC and optical polarization microscopy experiments [Fechtenkötter 01b, Fechtenkötter 01a]. The results of those studies are summarized in table 5.4 together with the results for the unbranched materials HBC-C_{12} and HBC-PhC_{12}. As expected, the phase transition temperatures of the materials with branched sidechains are significantly lowered as compared to the corresponding materials with unbranched sidechains. At room temperature, both the chiral **9** and the racemic mixture **10** are yellow solids. Upon heating, these compounds enter a columnar discotic mesophase Col_{ho}, which is chiral in the case of **9**, as was determined by circular dichroism spectroscopy. **9** is therefore denoted as Col^*_{ho}. In the case of HBC-Ph$C^*_{8,2}$ (**11**), no

[3]Note that by the random combination of the six stereogenic centers during synthesis up to $6^2 = 64$ different stereoisomers can be produced. From now on **10** will be referred to as racemic mixture HBC-$C^{rac}_{8,2}$, keeping in mind that this is not completely accurate, since **10** presumably contains also different diastereomers

Table 5.4: *Optical, thermal and thermodynamical data for compounds* **5**, **6**, **9**, **10** *and* **11** *(K = crystalline phase, Col_{ho} = ordered hexagonal columnar mesophase, I = isotropization)*

Compound		Transition	T(°C)	literature
HBC-$C^{*}_{8,2}$	**9**	K $\rightarrow$ Col^{*}_{ho}	96	[Fechtenkötter 01a]
		Col^{*}_{ho} $\rightarrow$ I	430	
HBC-$C^{rac}_{8,2}$	**10**	K $\rightarrow$ Col_{ho}	81	[Fechtenkötter 01a]
		Col_{ho} $\rightarrow$ I	420	
HBC-C_{12}	**5**	K_1 $\rightarrow$ K_2	42	[Herwig 96]
		K_2 $\rightarrow$ Col_{ho}	107	
HBC-Ph$C^{*}_{8,2}$	**11**	K $\rightarrow$ Col^{*}_{ho}	<-100	[Fechtenkötter 01b]
HBC-PhC_{12}	**6**	K_1 $\rightarrow$ K_2	18	[Fechtenkötter 99]
		K_2 $\rightarrow$ Col_{ho}	80	

phase transition was observed over the whole DSC temperature range (-100 to 250 °C). At room temperature, **11** is a very soft yellow solid. This and the presence of birefringence at room temperature, which was detected by means of polarized optical microscopy, were taken as a prove for the fact that **11** is liquid crystalline over the entire temperature range monitored with DSC [Fechtenkötter 01a].

5.3.1 Packing in the Low Temperature Phases

Before turning to the molecular dynamics, the molecular packing arrangement in the solid phases is investigated. As already described in section 5.1, the packing arrangement within the columns can easily be probed by ^{1}H -^{1}H DQ NMR. Figure 5.20 shows the 2D DQ spectra of **9** and **10**. Similar to the ^{1}H NMR spectra of the parent compound HBC-C_{12} (**5**), three aromatic proton resonances can be distinguished. The isotropic shifts of the these three aromatic resonances are virtually identical for **9** and **10**. Hence, differences in the π stacking arrangements must be negligible. Comparing the DQ signal pattern of the aromatic protons with the pattern observed for **5** (Fig. 5.11), it is clear that the patterns of all these three compounds are identical. Notably, no difference is observed between the enantiopure compound **9** and the racemic mixture **10**. Hence, it can be concluded that both **9** and **10** adopt a 'herringbone'-type packing arrangement of the aromatic cores in their solid phases, in analogy to their parent compound **5**. This is in good agreement with results from WAXS measurements, where also

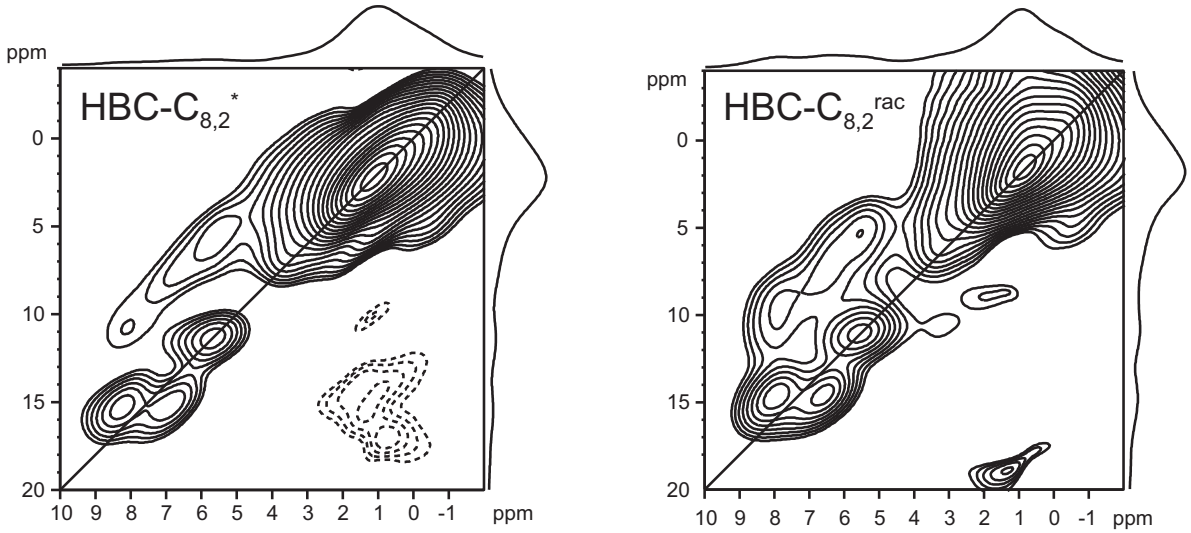

Figure 5.20: *^{1}H DQ spectra of HBC-$C^*_{8,2}$ (left) and HBC-$C^{rac}_{8,2}$ (right) measured at T = 48 °C, 30 kHz MAS and $\tau_{exc} = 1\tau_R$.*

a tilted columnar arrangement was found [Fechtenkötter 01b]. Obviously, the introduction of the more bulky branched sidechains instead of linear sidechains does not influence the core packing arrangement in the solid phases. It seems that only the actual phase transition temperatures, but not the encountered core packing structures are affected by the introduction of the branched sidechains.

This also seems to be the case for the compounds with a phenylene ring inserted between the core and the sidechain. Fig. 5.21 shows the ^{1}H -^{1}H DQ spectrum of HBC-Ph$C^*_{8,2}$ (**11**). Similar to the spectra of the parent compound, HBC-PhC_{12} (**6**), the peaks of the core protons and the protons of the *exo*-phenylene ring overlap. In the ^{1}H -^{1}H DQ spectrum, only one broad diagonal peak of the aromatic protons is observed, which already hints at the absence of a tilted structure, but naturally does not allow for a final conclusion because of the peak overlap. This limitation is overcome by the ^{1}H -^{13}C -heteronuclear correlation approach, which benefits from the enhanced site-resolution of the detected ^{13}C nuclei (described in section 3.4.1). In the ^{1}H -^{13}C heteronuclear correlation spectrum (Fig. 5.22), the *exo*-phenylene CH signal at 130 ppm is separated from the core CH signal at 120 ppm. The absence of any splitting of the core CH correlation peak indicates that HBC-Ph$C^*_{8,2}$ – like its parent compound HBC-PhC_{12} – does not adopt a tilted disc arrangement. Nonetheless, the observed chemical shift of the core protons (6.2 ppm) is shifted by around 2.0 ppm with respect to the chemical shift in solution (8.27 ppm, p-$C_6D_4Cl_2$, 150 °C [Fechtenkötter 01b]), which proves that the discs in HBC-Ph$C^*_{8,2}$ are also strongly interacting. Since HBC-PhC_{12} and HBC-Ph$C^*_{8,2}$ seem to exhibit the same packing arrangement, the results of the quantum chemical calculations presented in section 5.2 also apply for HBC-Ph$C^*_{8,2}$.

WAXS studies showed that HBC-Ph$C^*_{8,2}$ adopts a non-tilted arrangement in the columns. A

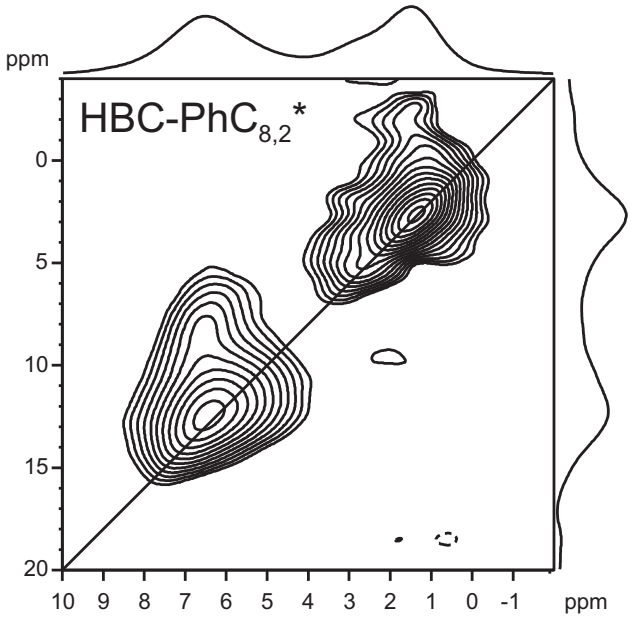

Figure 5.21: *^{1}H DQ spectrum of HBC-PhC$^{*}_{8,2}$ measured at T = 42 °C, 27.5 kHz MAS and $\tau_{exc} = 1\tau_R$.*

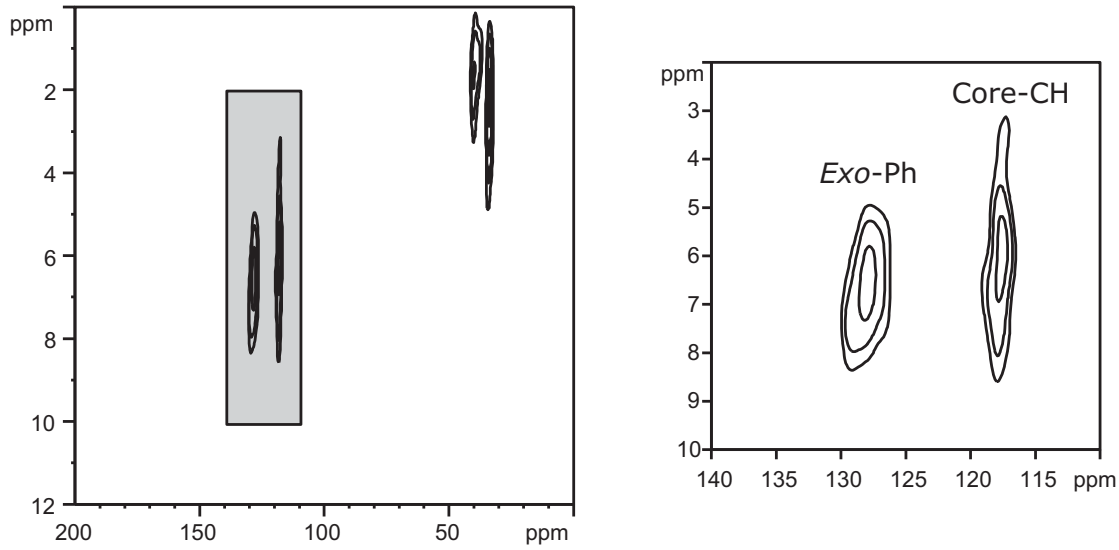

Figure 5.22: *Heteronuclear correlation spectrum of HBC-PhC$^{*}_{8,2}$ measured at T = 42 °C, 27.5 kHz MAS and $\tau_{rcpl} = 1\tau_R$. On the right the grey region is enlarged. Clearly, only one broad ^{1}H -^{13}C correlation peak of the core CH is observed. This indicates a non-tilted arrangement of the discs within the column.*

helical structure was found with every third molecule in the columnar stack being crystallographically identical [Pisula 03]. This is in good agreement with the results from the quantum chemical calculations, where also such a helical arrangement was proposed for the model stacks, which is depicted in Fig. 5.15.
Summarizing the results on the packing behavior in the low temperature phases, it can be concluded that the introduction of branched sidechains instead of linear ones does not lead to changes in the core packing arrangement. Only the transition temperatures to the respective mesophases are significantly lowered.

5.3.2 Core Dynamics in the LC Phases

The lowered transition temperatures of the materials with branched sidechains suggest that the branched sidechains introduce a significant amount of disorder. This increased amount of disorder should also be reflected in a lower dynamical order parameter for the column rotation in the columnar mesophases. As shown by X-ray investigations, in the columnar mesophases of **9** and **10** the discs are oriented perpendicular to the column axis. This is also reflected in the ^{1}H solid-state NMR spectra, where the three aromatic lines are merged into one (not shown here). In order to obtain the desired order parameter, heteronuclear dipole-dipole coupling constants D_{is} were measured with the REPT-HDOR experiment (section 3.4.2) for both the crystal and the LC phase. As can be seen in the ^{13}C CP spectra (Fig. 5.23), the core CH peak at 119 ppm is well resolved. In Fig. 5.24 the REPT-HDOR sideband patterns of the core CH of **9** and **10** are shown. At T = 38 °C rigid dipole-dipole coupling constants are obtained, namely $D_{is}/2\pi$ = (21.1 ± 0.7) kHz for the core CH of **9** and to $D_{is}/2\pi$ = (21.7 ± 0.6) kHz for the core CH of **10**. In the LC phase, significantly reduced dipole-dipole couplings are observed. For comparison, the spectra of both **9** and **10** were measured at identical T-T_m = 24 °C. For the core CH of **9**, the extracted dipole-dipole coupling constant is $D_{is}/2\pi$ = (7.0 ± 0.2) kHz (T = 121 °C), whereas for the core CH of **10** a dipole-dipole coupling constant of $D_{is}/2\pi$ = (8.6 ± 0.3) kHz is measured (T = 105 °C). The observed reduction of the dipole-dipole coupling can be attributed to the onset of fast (μs timescale or faster) rotation about the column axis in the LC phase. As explained in subsection 5.1.3, the dynamical order parameter for the column rotation can be defined as

$$S_{col.rot.} = \frac{2D_{is}^{LC}}{D_{is}^{rigid}}. \tag{5.1}$$

From this, $S_{col.rot.}$ = 0.66 for **9** and $S_{col.rot.}$ = 0.79 for **10** is obtained. These quite different order parameters are quite surprising, especially since the order parameter of the enantiopure HBC is lower than the one of the racemic mixture. Intuitively, a higher order parameter would be expected for the enantiopure compound, especially since the enantiopure compound is known to form a highly ordered helical superstructure from X-ray [Fechtenkötter 01a]. However, a

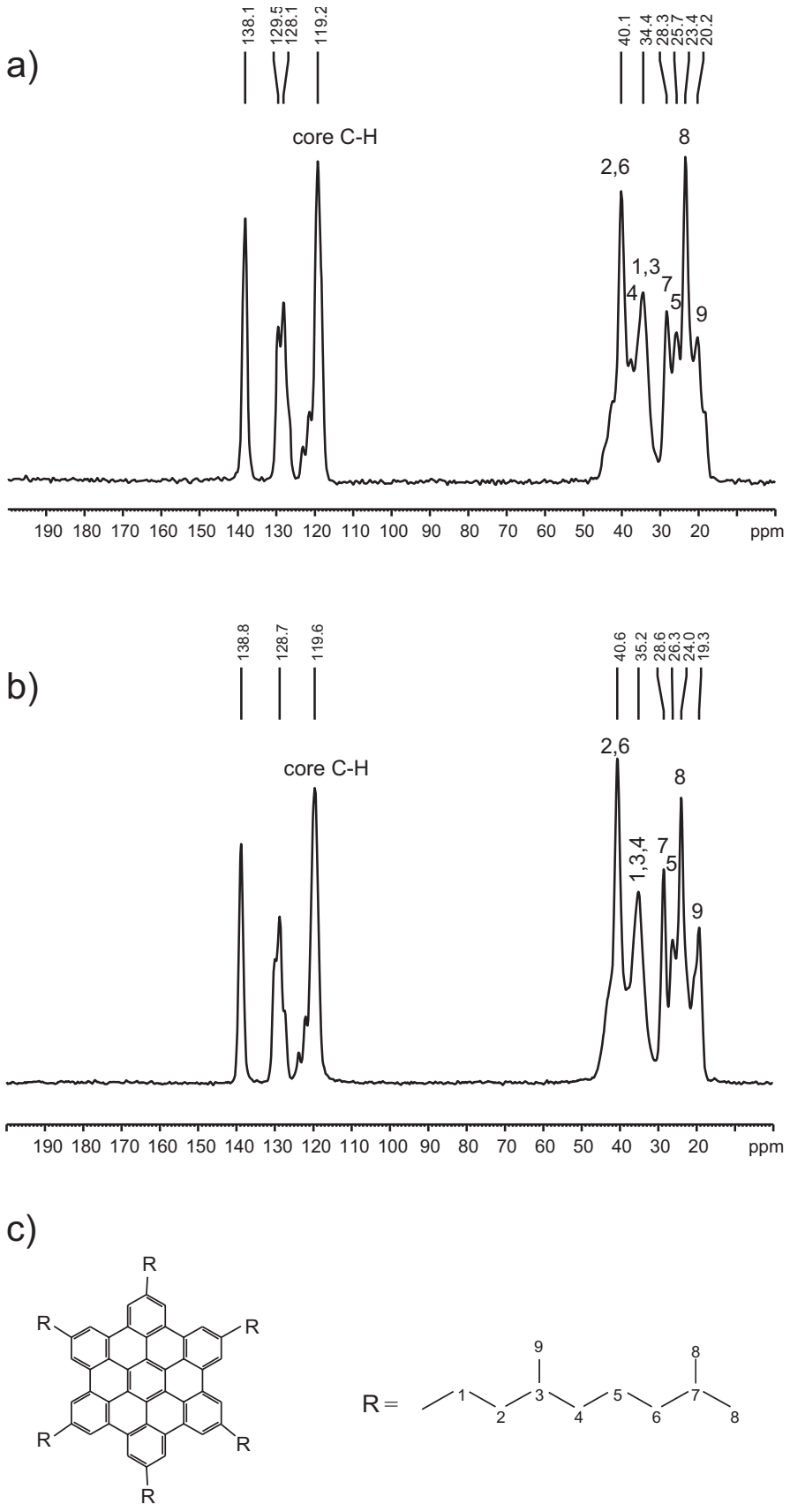

Figure 5.23: ^{13}C *CP spectra of HBC-*$C^{*}_{8,2}$ *(a) and HBC-*$C^{rac}_{8,2}$ *(b) at 25 kHz MAS and T = 38 °C.*

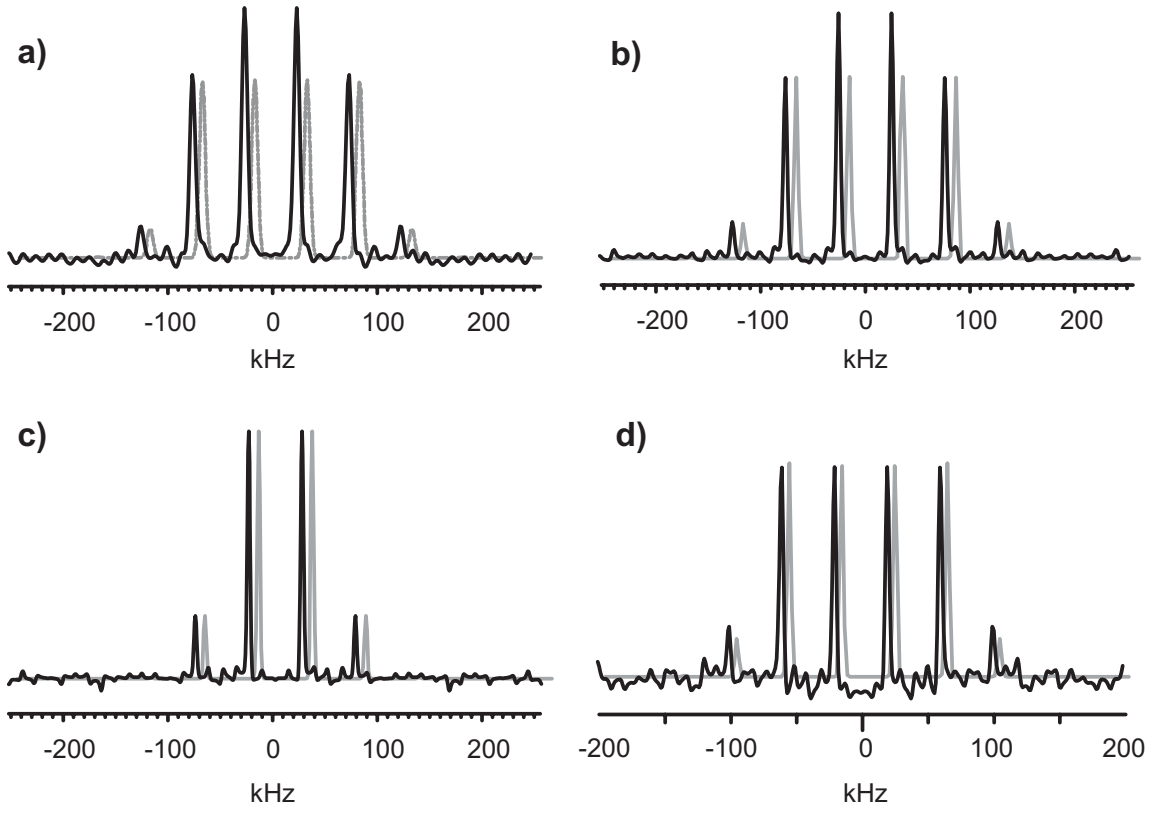

Figure 5.24: *REPT-HDOR SB patterns of the core CH resonance at 119 ppm of HBC-$C^{*}_{8,2}$ (***9***) and HBC-$C^{rac}_{8,2}$ (***10***).*
a) **9***: 25 kHz MAS, $\tau_{rcpl} = 2\tau_R$, T = 38 °C*
b) **10***: 25 kHz MAS, $\tau_{rcpl} = 2\tau_R$, T = 38 °C*
c) **9***: 25 kHz MAS, $\tau_{rcpl} = 4\tau_R$, T = 121 °C*
d) **10***: 20 kHz MAS, $\tau_{rcpl} = 4\tau_R$, T = 105 °C*

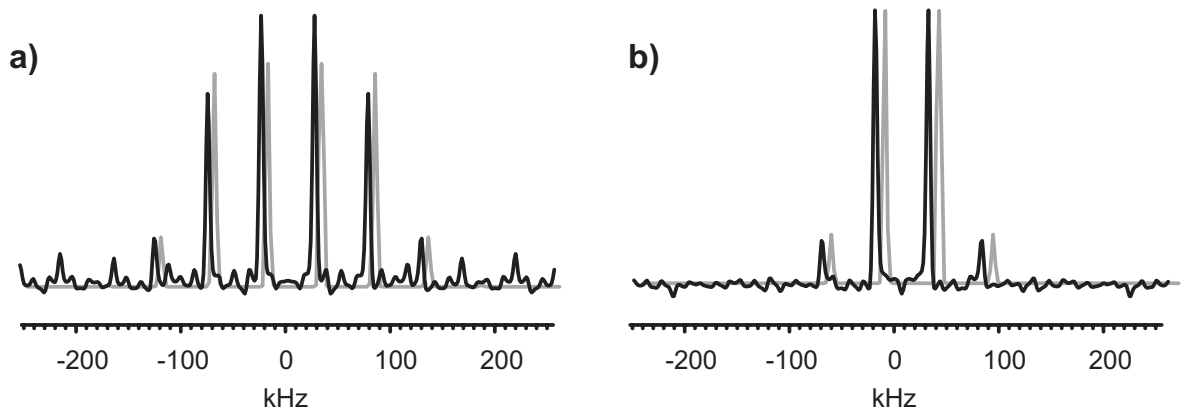

Figure 5.25: *REPT-HDOR SB patterns of HBC-PhC$^*_{8,2}$ (**11**) at 25 kHz MAS, T = 38 °C and $\tau_{rcpl} = 2\tau_R$: a) core CH resonance at 118 ppm and b)* exo*-Ph CH resonance at 127.5 ppm.*

peculiarity of the enantiopure sample needs to be mentioned at this point: It was impossible to detect any core CH signal at recoupling times longer than 160 μs. Hence, only a sideband pattern with sidebands up to third order could be generated. This is, of course, not sufficient for a reliable fit, since the first order SB are known to be inflicted with a considerable systematic error. Hence, the extracted order parameter for **9** is not reliable. The signal loss at longer recoupling times is presumably a relaxation effect due to molecular motions. Namely, intermediate motions (i.e. on the experimental timescale) are known to cause severe signal losses in MAS recoupling experiments such as the REPT-HDOR experiment employed here [Saalwächter 02b]. Hence, it might be the other way around, i.e. that **9** has the higher ordered phase with less mobility, which might be associated with longer motional correlation times in **9** than in **10**. If **10** is assumed to be in the fast motional limit with short motional correlation times, **9** might still exhibit intermediate motions with longer motional correlation times, which would cause the signal loss at longer recoupling times. A facile way to check this hypothesis would be to measure the sideband pattern of **9** at higher temperatures. This is unfortunately for experimental reasons not feasible, since the instrumention is not designed for higher temperatures. Therefore, and since other origins for the different order parameters (including issues of sample purity, etc.) cannot be excluded, it will not be discussed any further here. A brief, general account on the effects of intermediate motions on the outcome recoupling MAS experiments is given in appendix E; a more detailed analysis can be found in [Saalwächter 02b].

According to the assignment given in the literature, HBC-PhC$^*_{8,2}$ (**11**) forms a Col$^*_{ho}$ phase at room temperature. Hence, fast column rotation is expected as one of the dynamical processes. However, the REPT-HDOR sideband pattern shown in Fig. 5.25a corresponds to a dipole-dipole coupling constant of $D_{is}/2\pi$ = (22.3 $\pm$ 1.1) kHz, which indicates rigid core C-H groups. Hence, it must be concluded that the room temperature phase of **11** is not a true liquid crystalline phase, since the cores are not significantly mobile. Obviously, the phase

encountered in HBC-PhC8* is similar to the room temperature phase of HBC-PhC_{12} (**6**). There, slow (on the *ms* - *s* timescale) jumps about the C_6-symmetry axis were observed as the only motion of the core [Fischbach 02]. Future work will certainly address the question whether such slow jump processes take place in **11** as well. In Fig. 5.25 also the extracted sideband pattern for the *exo*-Ph CH resonance is shown, which corresponds to a significantly reduced dipole-dipole coupling constant of $D_{is}/2\pi$ = (13.0 $\pm$ 0.7) kHz. This proves that in **11** the phenylene rings of the sidechains perform fast 180° flips about their internal C_2 symmetry axis. Such a flip process was already observed in the parent compound HBC-PhC_{12} (**6**) [Fischbach 02].

5.3.3 Sidechain Dynamics

In this subsection, the dynamics of the sidechains is investigated. Since the introduction of branched $C_{8,2}$ sidechains lowers the phase transitions temperatures compared to compounds with linear C_{12} sidechains, one might expect higher sidechain mobilities for the branched sidechains. So far, sidechain mobility in HBCs has only been addressed *qualitatively* by studying the REPT-HSQC build-up behavior of the ^{13}C resonances of the sidechains of HBC-C_{12} (**5**) and HBC-PhC_{12} (**6**) in the solid phases [Fischbach 02]. As expected, a mobility gradient along the chain was observed, with the α-CH_2 groups being more or less as rigid as the core and the chain ends being most mobile. With the novel REREDOR experiment ([Saalwächter 02c] and section 3.4.3) SB patterns for CH_2 groups can be generated and, hence, sidechain dynamics can be investigated *quantitatively*.
First, we consider the sidechain dynamics in **5**. In the ^{13}C CP spectrum of **5** (Fig. 5.26), four ^{13}C alkyl resonances can be distinguished, the assignment of which is also shown in Fig. 5.26. In order to investigate the temperature dependence of the sidechain mobility, two-dimensional REREDOR spectra were measured at temperatures ranging from 0 °C to 110 °C. In Fig. 5.27, the extracted REREDOR SB patterns of the central chain carbons (β- to $(\omega-2)$-CH_2) are shown. Clearly, no significant change in the extracted sideband patterns is present until the transition to the Col_{ho} phase, which is associated with a significant reduction of the sideband pattern. Interestingly, also no change is observed upon the transition from the K_1 to the K_2 phase at 42 °C. The sideband patterns at lower temperatures correspond to a heteronuclear dipole-dipole coupling constant of $D_{is}/2\pi \approx 13$ kHz, which is the average over the whole central part of the sidechain. Since the exact geometry of the sidechain motion is not known, an order parameter like the one for the core CH (see Eq. (7.1)) cannot be defined. Instead, reduction factors will be calculated according to

$$S = \frac{D_{is}^{observed}}{D_{is}^{rigid}} \tag{5.2}$$

In those cases where the rigid heteronuclear dipole-dipole coupling constant cannot be measured (e.g. the motion can not be frozen out completely within the experimentally accessible

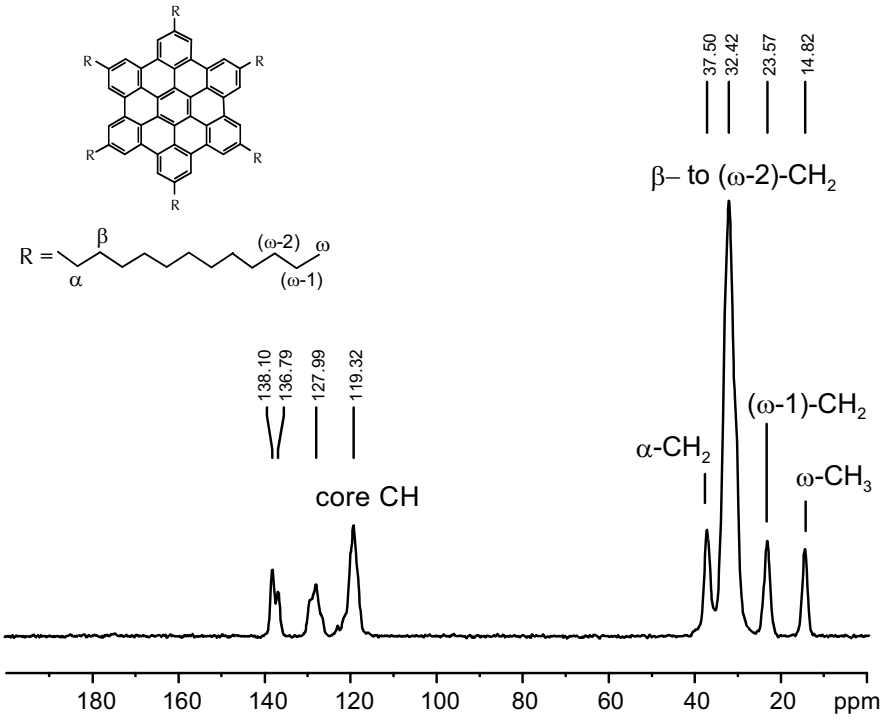

Figure 5.26: *^{13}C CP spectrum of HBC-C_{12} (**5**) at 25 kHz MAS and T = 38 °C.*

temperature range), a dipole-dipole coupling constant of $D_{is}/2\pi \approx 21$ kHz is assumed, which is typical for directly bonded, rigid C-H pairs. The observed heteronuclear dipole-dipole coupling constant of $D_{is}/2\pi \approx 13$ kHz therefore corresponds to a reduction factor of S $\approx$ 62%. From these observations, it can be concluded that in the crystal phases K_1 and K_2 the sidechains of **5** carry out fast (μs timescale and faster), but locally restricted motions. Of course, the sideband patterns of the other resonances can be evaluated as well. Basically, the temperature dependence of the SB patterns for these other resonances is identical to the temperature behavior observed for the central chain CH_2 groups in Fig. 5.27, i.e. the patterns do not change significantly up to the transition into the mesophase. In Fig. 5.28, the REREDOR sideband patterns of the core CH and the four distinguishable alkyl resonances are shown for two temperatures, namely at 50 °C in the K_2 phase and at 110 °C in the Col_{ho} phase. While the aromatic core is rigid in the K_2 phase, the alkyl chain is mobile with a strong mobility gradient along the chain: While the α-CH_2 groups are almost rigid (S $\approx$ 86%) the (ω-1)-CH_2 groups are significantly more mobile (S $\approx$ 43%). The reduction factor of the ω-CH_3 is even stronger S $\approx$ 19%, which can be attributed to the fact that CH_3 groups carry out fast rotations about their internal C_3-symmetry axis, which reduces the observed dipole-dipole coupling constant by an additional factor of $\sim$3.

Having quantified the sidechain mobility in **5**, it is now interesting to compare the results with the sidechain mobility the compounds with branched chains **9** and **10**. In Fig. 5.29 ex-

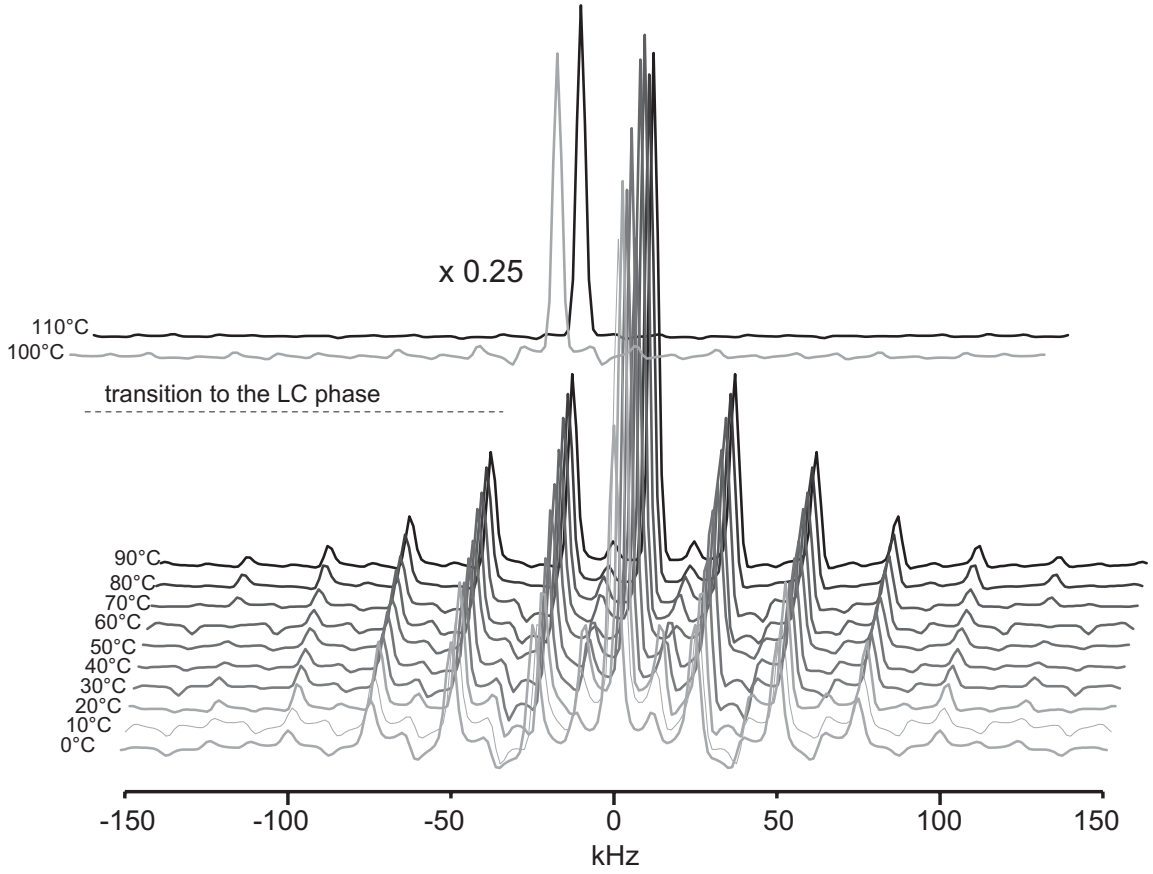

Figure 5.27: *Extracted REREDOR SB patterns of the resonance at 119.3 ppm corresponding to the central chain carbons (β to $(\omega - 2)$ position) of* **5**. *The experiments were carried out at 25 kHz MAS and $\tau_{rcpl} = 2\tau_R$. The patterns were normalized by setting the rotor echo amplitude in the time-domain signal to one. The LC phase sideband patterns were scaled down by a factor of 0.25.*

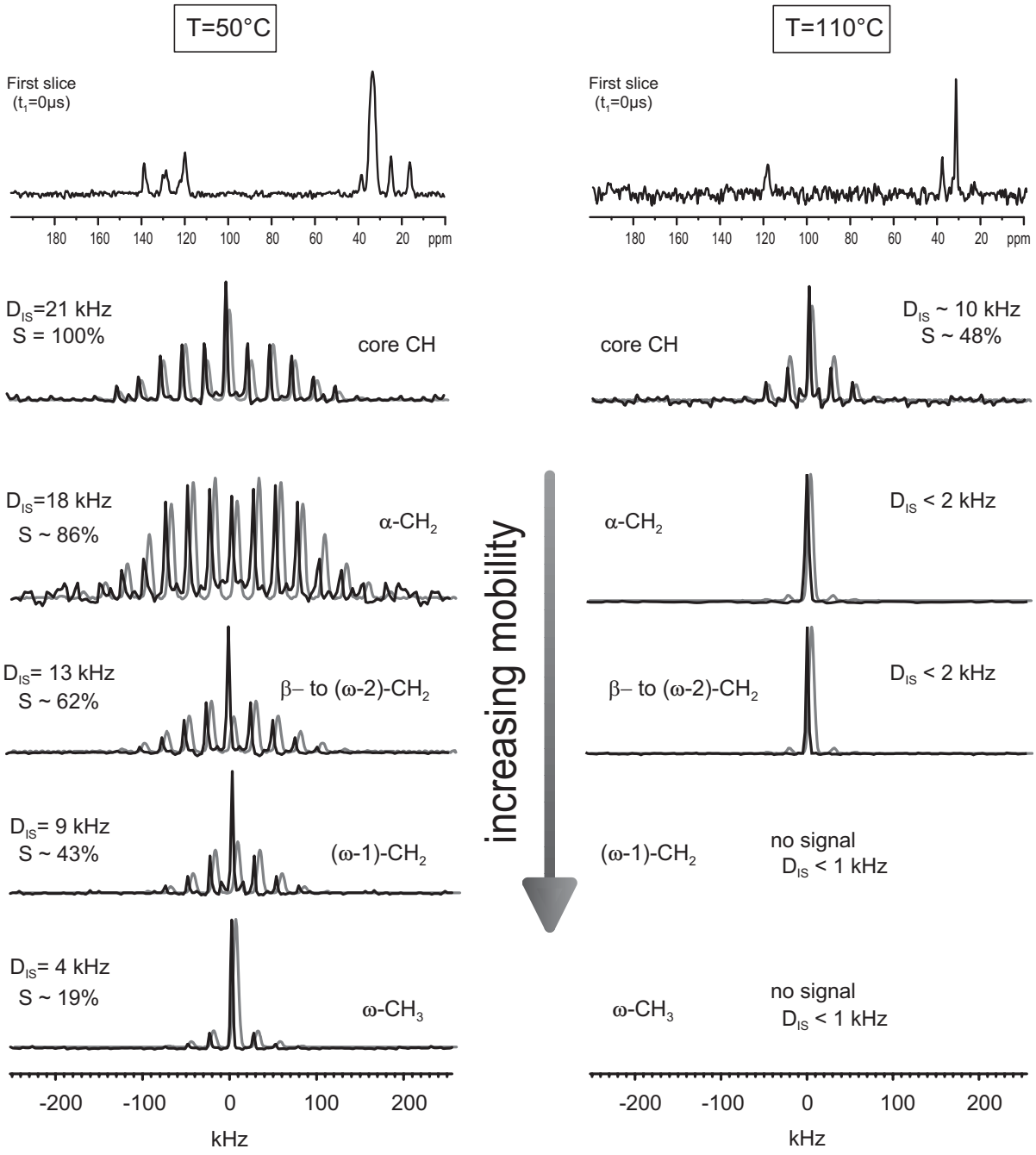

Figure 5.28: *REREDOR of HBC-C_{12} (**5**) at 25 kHz MAS and $\tau_{rcpl} = 2\tau_R$ in the crystal phase at T = 50 °C (left) and in the Col_{ho} phase at T = 110 °C (right). On the top, the first slices (t_1=0) of the two-dimensional experiments are shown. Below, the extracted sideband patterns for the core CH resonance and the four distinguishable alkyl resonances are shown. The underlying grey patterns are simulations with the corresponding dipole-dipole coupling constants and reduction factors indicated in the figure. Clearly, a mobility gradient along the sidechains is present with the mobility increasing towards the chain ends.*

tracted REREDOR sideband patterns for HBC-$C^{*}_{8,2}$ (**9**) and HBC-$C^{rac}_{8,2}$ (**10**) measured in the solid phase at 38 °C are shown. Since the patterns of **9** and **10** are basically identical, it can be concluded that the sidechain dynamics of both compounds are the same. For comparison, the patterns of the aromatic core CH are shown as well, which – as expected – correspond to a rigid dipole-dipole coupling constant of $D_{is}/2\pi \approx 21$ kHz. The patterns of four alkyl peaks are depicted, whose assignment is given by the color coding in the figure. The observed reduction factors decrease from $S \approx 62\%$ for the C1,C3 peak to $S \approx 43\%$ for the C7 peak. This proves that in HBC-$C_{8,2}$ a strong mobility gradient towards higher mobilities at the chain ends is present. The dipole-dipole coupling constants of the CH_3 groups are again additionally reduced by the rotation of the CH_3 groups. Nonetheless, comparing the SB patterns of the inner CH_3 group (C9) with the sideband pattern of the outer CH_3 groups (C8), it is found that the inner CH_3 group is less mobile than the outer CH_3 groups, which is also evidence of a mobility gradient along the chain.

The obtained reduction factors of the compounds with branched sidechains HBC-$C_{8,2}$ are similar to the reduction factors obtained for the compound with linear sidechains HBC-C_{12}. Hence it can be concluded that the sidechain dynamics in both materials is similar.

With a few approximations, it is possible to arrive at an estimate of the maximum motional amplitude from the observed reduction factors. First, it is assumed that the sidechain motion does not introduce any asymmetry into the motionally averaged dipole-dipole coupling tensor. Motional processes are known to introduce significant asymmetry to the averaged tensors [Macho 01, Goward 03a]. Since the HDOR SB patterns are not particularly sensitive to the asymmetry parameter η, this approximation is nonetheless acceptable here. Second, it should be noted that the observed reduction factor is a time-average over all occupied positions. An orientational order parameter, in contrast, represents an ensemble average over the various possible orientations at a given time. Hence, it is a feasible approximation to use the relations between the angular width of an orientation distribution and the orientational order parameter for the dynamical problem and to extract the width of the reorientation angle distribution from those relations. In Fig. 4.18, the dependence of the orientational order parameter on the width (FWHM) of the orientation distribution was already plotted. From this the width of the reorientational angle distribution for the various resonances can roughly be estimated. Clearly, the alkyl-sidechains move only in a restricted volume, which can be (in a simplified fashion) viewed as a cone with an increasing opening angle, as visualized in Fig. 5.30.

The similarity of the depicted cones shows that the volume which is encompassed by sidechain motion is similar for both linear and branched sidechains.

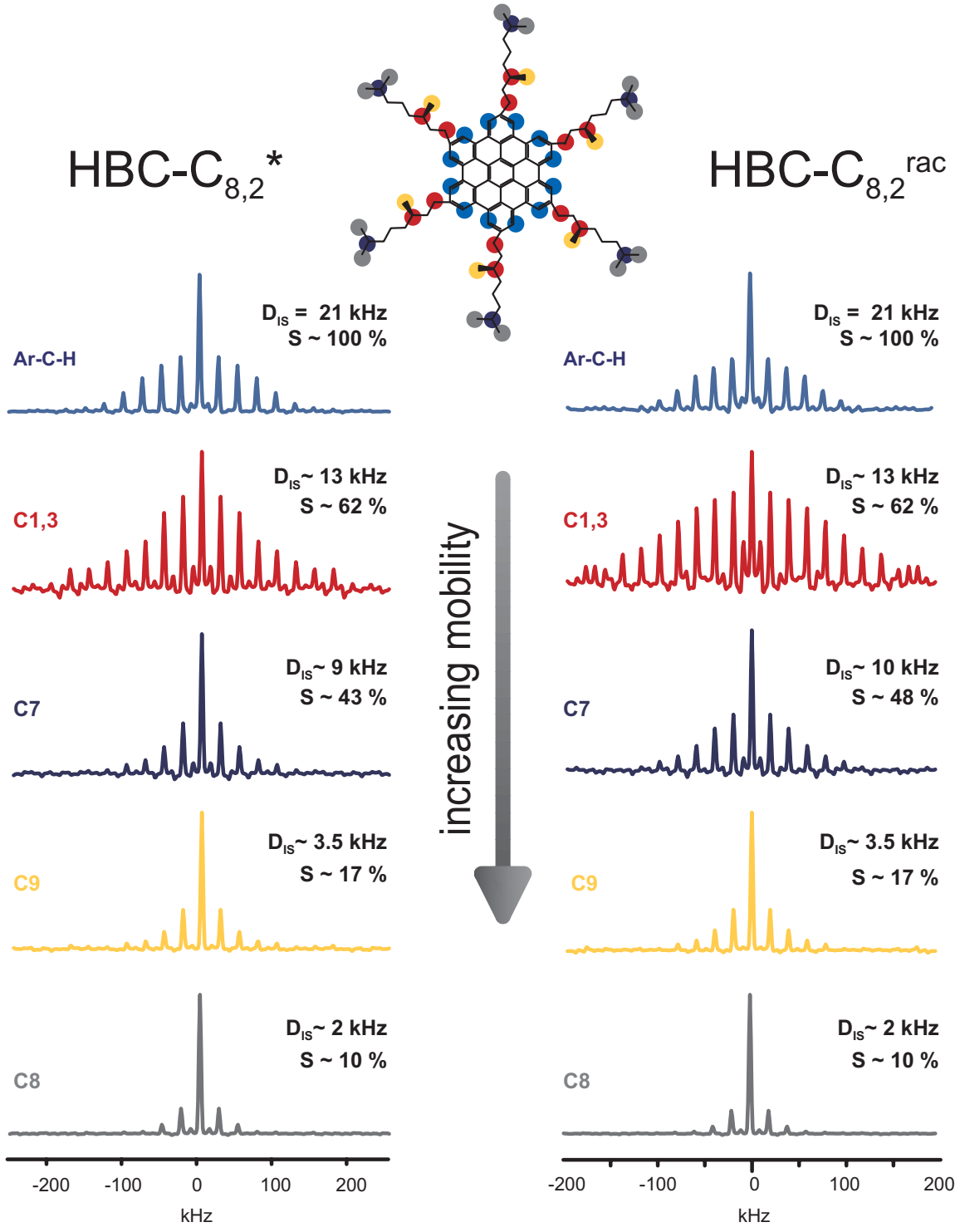

Figure 5.29: *REREDOR SB patterns of HBC-$C^{*}_{8,2}$ (**9**, left) and HBC-$C^{rac}_{8,2}$ (**10**, right) at 25 kHz MAS and T = 38 °C. The recoupling times were $\tau_{rcpl} = 2\tau_R$ for the core CH and $\tau_{rcpl} = 4\tau_R$ for the alkyl signals. The extracted dipole-dipole coupling constants and reduction factors are indicated in the figure as well. Obviously, the sidechain dynamics of both compounds is basically the same with a mobility gradient towards higher mobilities at the chain ends.*

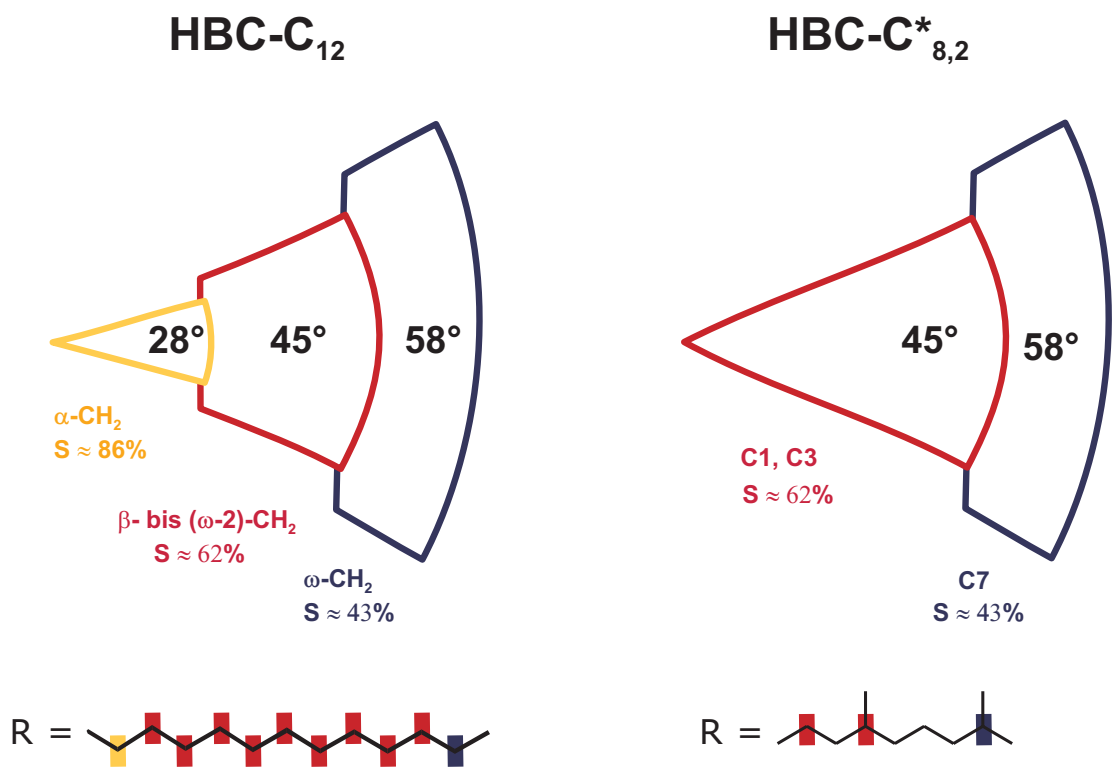

Figure 5.30: *Visualization of the restricted volume, which is encompassed by sidechain motion. From the reduction factors of the dipole-dipole coupling of the various sidechain groups, the width (FWHM) $\Delta\beta$ of the reorientational angle distribution (assumed to be gaussian) can be estimated as described in the text. This width is illustrated as the opening angle of the cones drawn in the figure. Clearly, the sidechain mobility in HBC-C_{12} and HBC-$C^*_{8,2}$ is very similar.*

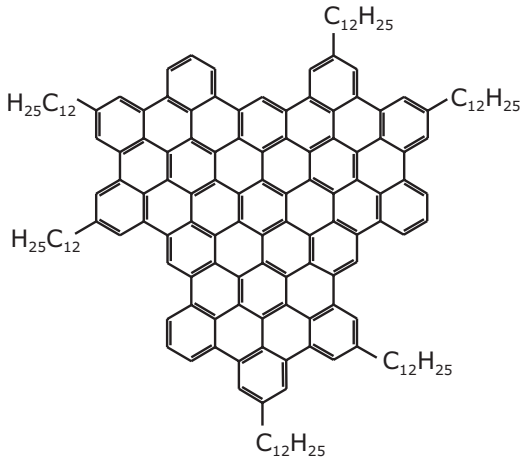

12

Figure 5.31: *Chemical structure of C96-C_{12} (***12***).*

5.4 Investigation of C96, a Compound with an Extended Aromatic Core

As discussed in the introduction, HBCs are favored for potential device applications because of their advantageous optoelectronic properties, namely the very high one-dimensional charge carrier mobilities. The observed high mobilities are attributed to the fact that the aromatic cores are exceptionally large. Thus, the π-π contact in the columnar stack is huge, which is responsible for the observed high one-dimensional charge carrier mobilities [Craats 00]. In order to increase the π-π contact even further, materials with even bigger or extended aromatic cores were synthesized [Dötz 00].

C96-C_{12} (**12** in Fig. 5.31) [Tomovic 03], the material discussed in the following, is strictly spoken not an HBC, since its polycyclic aromatic hydrocarbon (PAH) core is considerably larger than the HBC core. Its trivial name 'C96' denotes the number of carbon atoms in the core. Materials with larger cores than HBC are of interest, because they are considered to be two-dimensional graphite sections whose electronic properties are expected to converge to those of macroscopic graphite while still being molecularly well-defined. Among the alkyl-substituted PAHs, C96 is of particular interest, because the unperturbed $\pi - \pi$ contact can be assumed to be exceptionally large. The presumption of a very favorable $\pi - \pi$ contact is supported by the fact that C96 has a very strong aggregation tendency even though the aggregation tendency is actually driven by the microphase separation rather than the $\pi - \pi$ interactions. In fact, the aggregates are so strong that even under aggregate breaking conditions (high temperatures, unpolar solvents) the solution NMR spectra still feature only broad peaks. Despite numerous attempts under various experimental conditions, the peaks of the aromatic protons could so far not be resolved in solution ^{1}H NMR. The formation of excep-

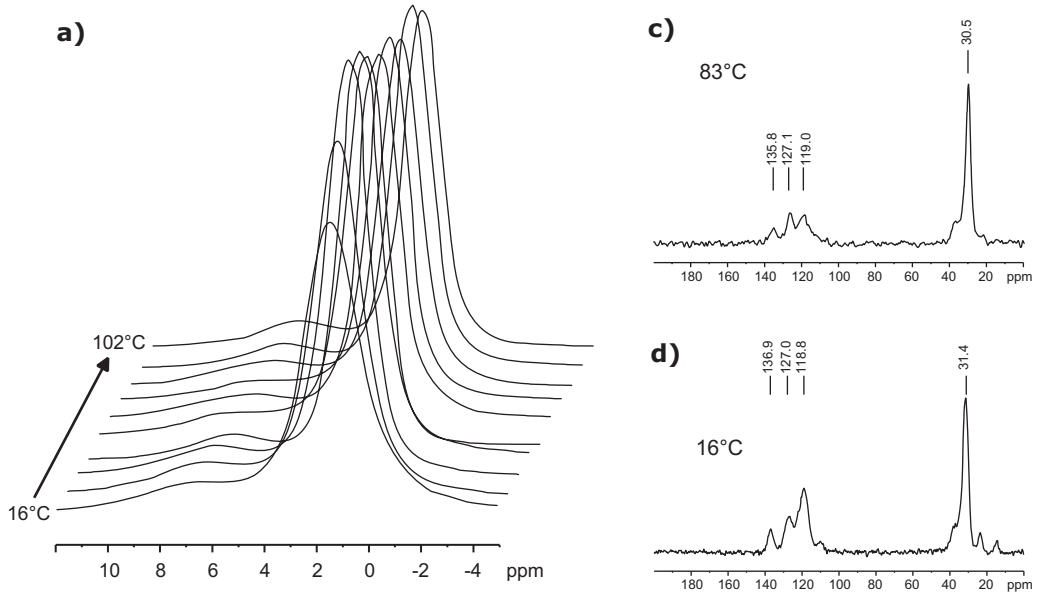

Figure 5.32: *^{1}H and ^{13}C CP MAS spectra of C96-C_{12} (**12**) at variable temperatures and 25 kHz MAS.*

tionally strong aggregates is also reflected by the fact that the material is difficult to purify by GPC. The bulk material is a waxy, dark red-brown material with a first order phase transition at around 38 °C in the DSC curve. The WAXS patterns in the two phases are very similar and correspond to highly ordered columnar hexagonal phases with a non-tilted arrangement of the discs in the column. Solid-state NMR experiments were conducted in order to further characterize the core packing arrangement. The one-dimensional ^{1}H and ^{13}C spectra in both phases look rather similar with very few resolved peaks in both cases. The alkyl proton peak narrows upon increasing the temperature due to increasing mobility of the sidechains. In order to gain more resolution, two-dimensional spectra were recorded. In the ^{1}H -^{1}H DQ spectra of both phases, only a broad featureless aromatic diagonal peak is observed, which does not provide any information about the solid-state packing apart from the fact that the absence of clear features indicates the absence of a well-defined highly ordered *intra*columnar packing arrangement of neighboring discs. Note that this does not contradict the observation of a very well-defined *columnar* packing in X-ray studies, since the columns as a whole still might be packed in a very regular fashion. The heteronuclear correlation spectrum (also shown in Fig. 5.33) does not provide deeper insight, either. Since the recoupling time was chosen short (40 μs), only correlation peaks of directly bonded ^{1}H -^{13}C pairs occur. Hence, the resonance at 118 ppm can be assigned to (probably overlapped) tertiary aromatic carbons.
Even though precise information on the packing could not be derived from solid-state NMR, information on the molecular dynamics in the different phases could be gained. Fig. 5.34 shows the REPT-HDOR SB pattern of the resonance at 118 ppm at 16 °C. From this, a dipole-dipole coupling constant of $D_{is}/2\pi$ = (21.5 $\pm$ 1.2) kHz was extracted, which corresponds to rigid C-H groups. Hence, the low temperature phase of C96-C_{12} is a solid phase without fast,

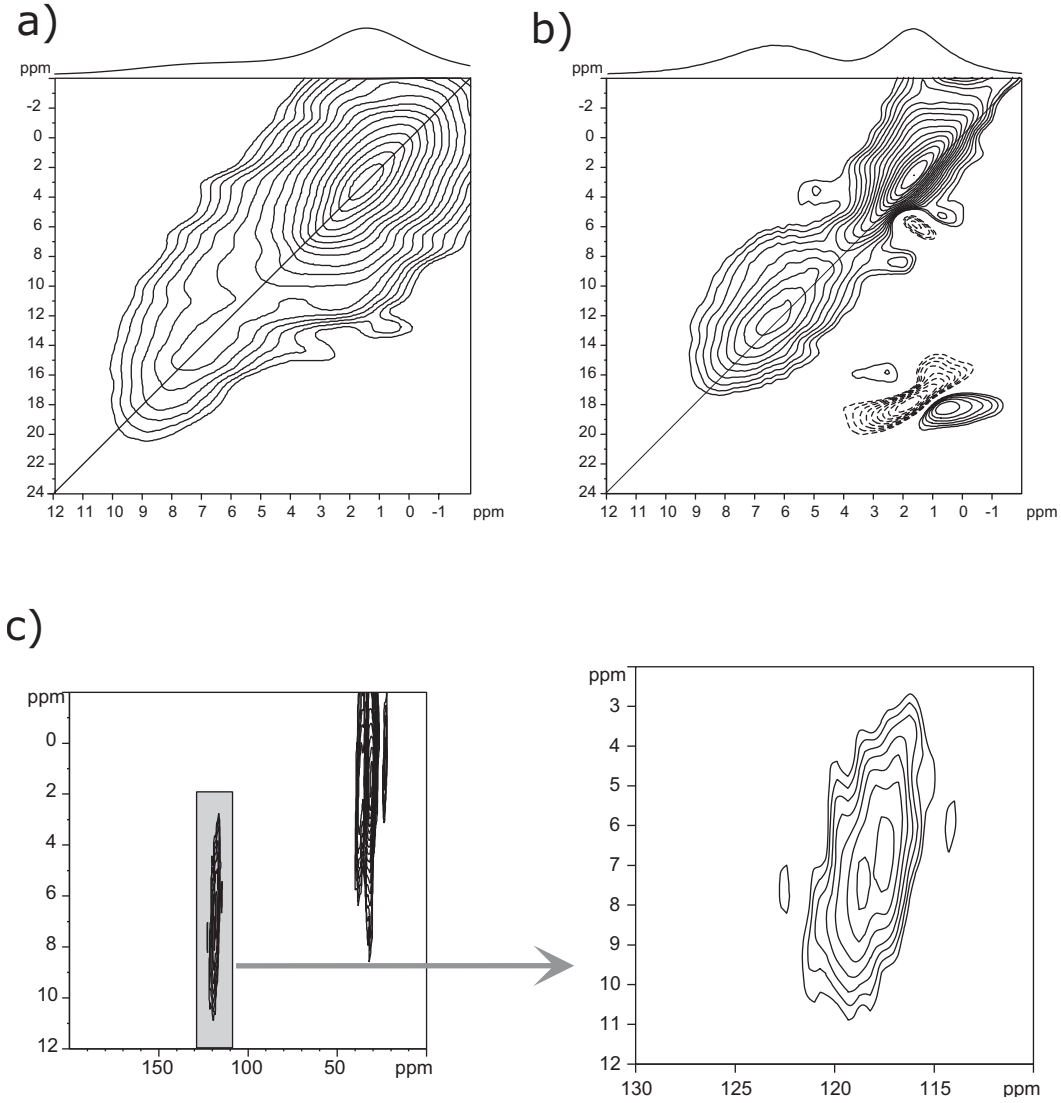

Figure 5.33: *Correlation spectra of C96-C_{12}* **12***:*
a) ^{1}*H -*^{1}*H DQ spectrum at 25 kHz MAS,* $\tau_{exc} = 1\tau_R$ *and T = 16 °C.*
b) ^{1}*H -*^{1}*H DQ spectrum at 30 kHz MAS,* $\tau_{exc} = 1\tau_R$ *and T = 83 °C.*
c) ^{1}*H -*^{13}*C correlation spectrum at 25 kHz MAS,* $\tau_{rcpl} = 1\tau_R$ *and T = 16 °C.*

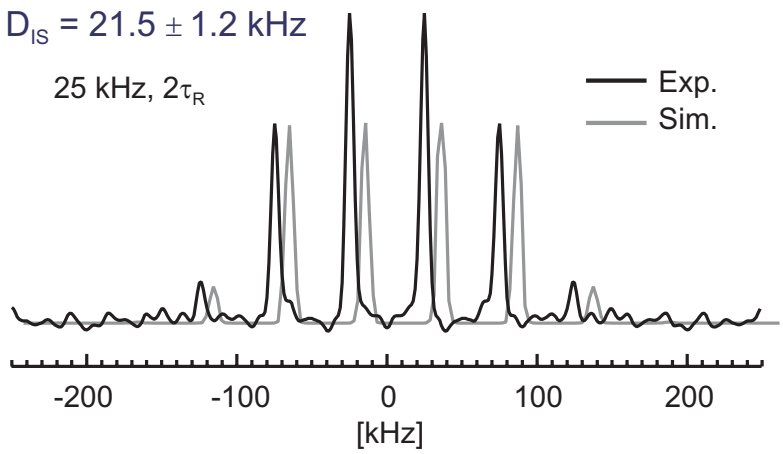

Figure 5.34: *REPT-HDOR SB pattern of the peak at 118 ppm of* **12** *measured at 25 kHz MAS,* $\tau_{rcpl} = 2\tau_R$ *and T = 16 °C. The grey line is the best fit pattern with* $D_{is}/2\pi$ *= (21.5 ± 1.2) kHz.*

large amplitude core motions. Upon heating above the phase transition, no ^{1}H -^{13}C REPT filtered signal could be obtained for the aromatic carbons at all, regardless of the chosen recoupling time or temperature (up to around 100 °C). This impossibility to create a coherence state surviving the course of the heteronuclear experiment strongly indicates the presence of significant intermediate molecular motion. Hence, C96-C_{12} melts at 38 °C and forms a LC phase with significant molecular motion of the cores, which is apparently more restricted than in HBC-C_{12}.

Summarizing the results on C96-C_{12}, a material with an extended aromatic core, it can be said that the increased size of the core on the one hand bears the advantage of a better ordered columnar packing, but on the other hand makes sample purification and in-depth characterization very difficult. Neither ^{1}H nor ^{13}C solid-state NMR spectra provide sufficient peak resolution for unravelling the solid-state packing. This points out the limitations of solid-state NMR for structure elucidation, which inevitably requires peak resolution for unambiguous structure determination. Nonetheless, dynamical information could be gained concerning the core dynamics in the respective phases. In the low temperature phases, the C96 cores are rigid, as determined by REPT-HDOR. The LC phase at elevated temperatures, however, is characterized by significant motions of the aromatic cores.

5.5 Summary

This chapter was dedicated to the investigation of structure and dynamics in hexa-substituted HBC derivatives.

As shown in section 5.2, with the relatively new SUPER experiment [Liu 02] ^{13}C chemical-shift anisotropies (CSA) can be determined in a site-resolved fashion in natural abundance even in complex materials such as HBC-PhC_{12}. This not only provides valuable dynamical information (as discussed in detail in [Fischbach 02]), but also the CSA principal tensor values themselves. As discussed in the text, comparison of the experimental ^{13}C CSA data with calculated ones (calculations performed by Prof. Dr. J. Gauss) revealed that the σ_{zz} value of the core CH carbons is particular sensitive to neighboring π systems in the columnar stack. Of course, ^{1}H chemical shifts are much more sensitive to stacking effects and, hence, the analysis of ^{1}H shifts is preferable to the analysis of ^{13}C shifts. Nonetheless, in cases where the ^{1}H spectra are not sufficiently resolved or where no protons are present in the chemical structure, the analysis of ^{13}C chemical shifts might provide a valuable alternative.

The comparison of materials with linear and branched alkyl-sidechains (section 5.3) revealed that the differences arising from the branching are very small apart from lowering the respective phase transition temperatures. The encountered phase structures are isomorphic in the corresponding materials with linear and branched sidechains. Also, the sidechain mobility was found to be very similar: In the solid phases, the sidechains exhibit fast motions in a restricted volume with a mobility gradient along the chain and higher mobilities at the chain ends. This is in pronounced contrast to the functionalized HBC derivatives, which are subject of the next chapter where even slight changes in the sidechain functionalization were found to lead to significant differences in phase behavior and solid-state structure and dynamics.

Chapter 6

Supramolecular Order and Dynamics in Functionalized HBC Derivatives

In this chapter, functionalized hexa-*peri*-hexabenzocoronene derivatives with lower symmetry (e.g. different sidechain substituents) are investigated. Controlling the supramolecular arrangement of materials is an important step on the way towards the creation of effective devices. In HBCs, further control of the supramolecular arrangement can be achieved by functionalization of the alkyl sidegroups. In particular, the introduction of groups capable of hydrogen bonding, e.g carboxylic acid or amide groups, is of interest to provide new structures in which hydrogen bonding and $\pi - \pi$ interactions compete for governing the intracolumnar organization of the bulk material. To further understand the organizational principles of these materials and especially gain insight into the hydrogen bonding arrangements, various HBC derivatives with carboxylic acid (section 6.1) or amide functionalities (section 6.2) were investigated. Another method to control the supramolecular arrangement is the formation of hexa-*peri*-hexabenzocoronene dimers, which are discussed in section 6.3. The materials as well as the DSC, X-ray and solution state NMR characterization were provided by N. Tchebotareva, D. Wasserfallen, J. Wu and Z. Wang from the group of Prof. Müllen at the MPI-P.

6.1 HBCs with One or Two Carboxylic Acid Groups

Hydrogen bonds play a significant role in supramolecular chemistry due to their ability to form reversible but directional bonds [Fredericks 96, Prins 01]. In large (supramolecular) systems, the van-der-Waals interaction usually dominates, since it scales with the size of the interacting molecules. To increase the strength of the comparably weak hydrogen-bonding interaction, multiple H-bonds are commonly used or H-bonds are supported by additional forces [Brunsfeld 01]. In the field of discotic liquid crystals, hydrogen bonding has been utilized for both the formation of discotic cores [Kraft 99,

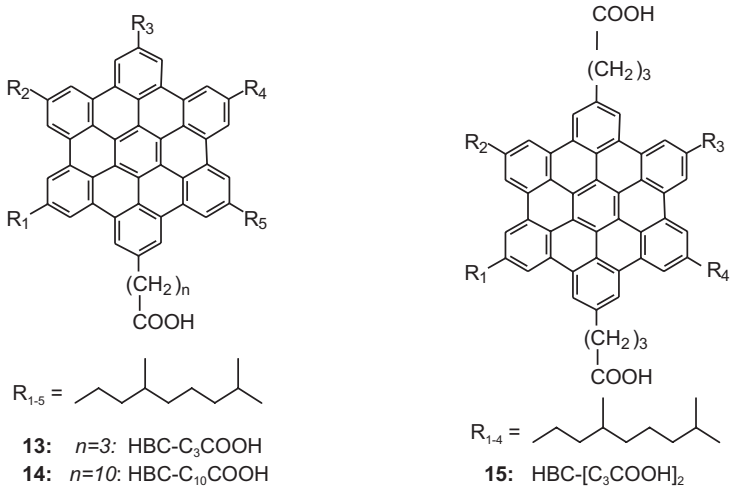

Figure 6.1: *Chemical structures of the investigated HBC derivatives with carboxylic acids groups.*

Kleppinger 97, Suarez 98] and as a tool to control the order within columns [Lee 02]. In this work the influence of hydrogen bonding on the phase behavior of hexa-*peri*-hexabenzocoronenes is first studied on three different HBC derivatives bearing carboxylic acid groups, namely 2-(4-Carboxipropyl)-5,8,11,14,17-penta-(3,7-dimethyloctanyl)-hexa-*peri*-hexabenzocoronene (HBC-C_3COOH, **13**), 2-(10-Carboxidecyl)-5,8,11,14,17-penta-(3,7-dimethyloctanyl)-hexa-*peri*-hexabenzocoronene (HBC-C_{10}COOH, **14**) and 2,11-di-(4-Carboxipropyl)-5,8,14,17-tetra-(3,7-dimethyloctanyl)-hexa-*peri*-hexabenzocoronene (HBC-[C_3COOH]$_2$, **15**).

6.1.1 DSC and X-ray

In this subsection, the results from the characterization of the three HBC acids by DSC and X-ray are briefly summarized [Tchebotareva 03, Wasserfallen 03]. HBC-C_{10}COOH (**14**) has a transition to the mesophase at 70 °C, which is slightly lower than the transition temperature of the symmetric parent compound HBC-$C^{rac}_{8,2}$ (**10**) at 81 °C. In contrast, HBC-C_3COOH (**13**) has a transition to the mesophase at 221 °C, which is extremely high compared with other HBCs carrying mainly branched alkyl sidechains. The diacid HBC-[C_3COOH]$_2$ (**15**) exhibits no phase transition over the whole DSC temperature range (-100 °C-250 °C). The DSC curves of **13** and **14** are shown in Fig. 6.2. On the first DSC scan of **13**, an additional irreversible exothermic transition occurs at around 70 °C in the DSC curve, which can be attributed to the melting of non equilibrated structures which are kinetically trapped in the sample during synthesis. In contrast, the first and second (not shown) heating curve of **14** do not differ. This tremendous difference in the phase behavior of samples, which differ only in the length of a single sidechain, is quite surprising.

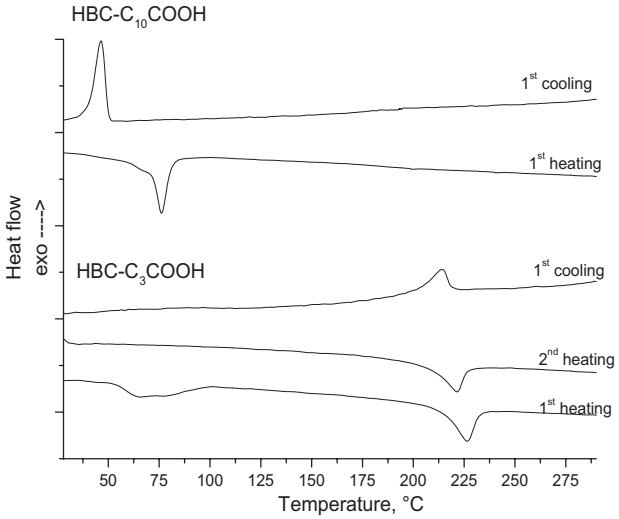

Figure 6.2: *DSC traces of HBC-C_3COOH (***13***) and HBC-C_{10}COOH (***14***).*

X-ray scattering provided further information on the structure of the different phases observed in DSC. The high temperature phases above the strong endothermic phase transition were characterized by powder X-Ray diffraction at 373K for **14** and at 573K for **13** [Tchebotareva 03]. Both diffraction patterns could be assigned to an ordered hexagonal columnar phase. In both cases, the (001)-reflex which corresponds to the distance between two neighboring discs in the column was observed at about 0.36 nm. This indicates periodic, non-tilted stacking of the molecules within the columns.

Cooling to the low temperature phases involves considerable changes in the structures of both systems. Fig. 6.3 displays the 2D diffractogram of an extruded fiber of HBC-C_{10}COOH together with the equatorial intensity distribution, which was measured at RT after cooling from the mesophase. The pattern of **14** was found to strongly resemble the pattern of the parent compound HBC-$C_{8,2}^{rac}$ [Fechtenkötter 01b]. For comparison, the equatorial intensity distribution of HBC-$C_{8,2}^{rac}$ is also shown in Fig. 6.3. The analysis of the pattern showed that in the solid phase of **14** the columns are packed in a rectangular 2D lattice. The cell parameters of the rectangular unit cell were calculated to a = 2.21 nm and b = 3.83 nm, which is slightly bigger than the unit cell of the parent compound **10** (a = 2 nm, b = 3.46 nm). The reflexes along the meridional, which correspond to the distance between the discs in the column, are divided into four and shifted by approximately 40° from the meridional direction, which indicates that the discs are tilted with respect to the columnar axis. This tilt also leads to a longer periodicity along the fiber axis of h=0.5nm, which was already observed in other HBCs with a tilted arrangement of the discs [Fechtenkötter 01a, Fischbach 02]. The similarity of the structure of the phases formed by **14** and **10**, as well as the similar phase transition temperatures, indicate that the introduction of the long C_{10}COOH chain does not lead to significant changes in both the columnar packing and the $\pi - \pi$ stacking.

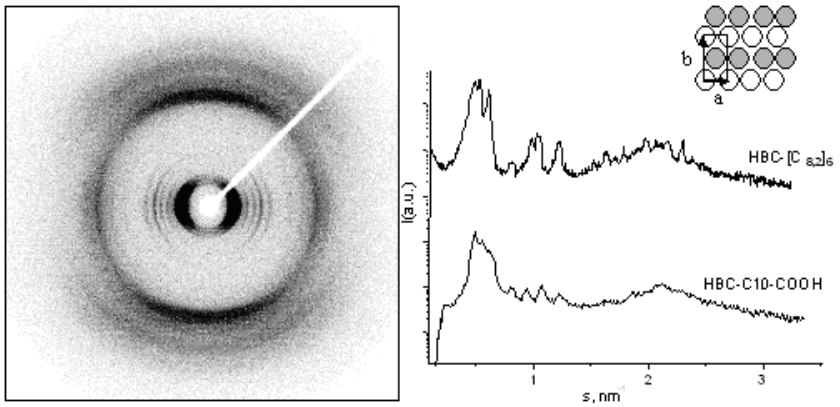

Figure 6.3: *X-ray diffractogram and equatorial intensity distribution for the low-temperature phase of* **14** *in comparison with the equatorial intensity distribution of HBC-*$C_{8,2}^{ac}$ *(***10***).*

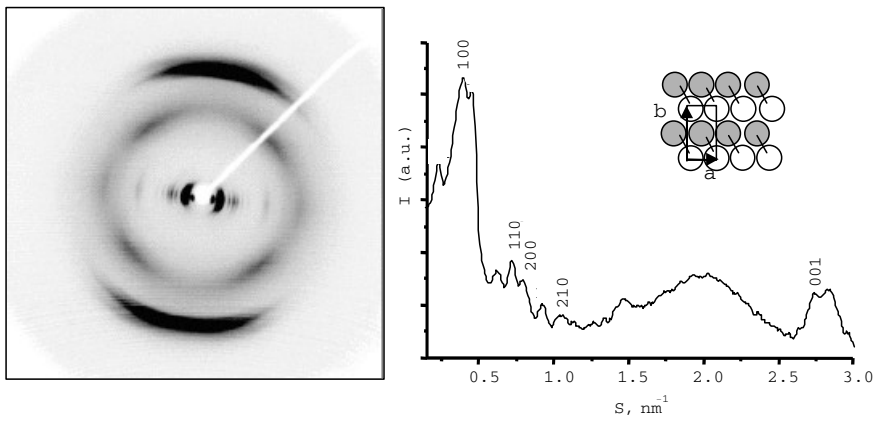

Figure 6.4: *X-ray diffractogram and equatorial intensity distribution for the solid phase of* **13***.*

In contrast, the room temperature 2D diffractograms of extruded fibers of **13** and **15** strongly differ from the pattern of **14**. The 2D diffractogram of **13** without prior thermal treatment (not shown here) revealed an undefined structure with broad peaks in the equatorial plane. A sharp meridional reflex corresponding to a disc distance of 0.36nm was observed, which indicates a non-tilted arrangement of the discs within the columns. Since DSC revealed a strong hysteresis effect (irreversible transition detected on 1st heating scan in DSC), the sample was heated to above 70 °C and subsequently cooled down for a second measurement. This procedure lead to the melting of non-equilibrated structures and, thus, a much better resolved diffraction pattern was obtained, which is shown in Fig. 6.4. The analysis showed that **13** adopts a hexagonal arrangement of the columns with a non-tilted packing of the discs in the column. The characteristic reflexes for the hexagonal arrangement were fitted to an orthorhombic unit cell

with cell parameters a = 2.55 nm and b = 4.42 nm. The occurrence of additional reflexes was taken as an indication for a lamellar arrangement between column rows (depicted in the inset of Fig. 6.4). An unambiguous assignment of all reflexes was not possible.
Clearly, the shorter acid chain in **13** not only tremendously raises the phase transition temperature to the LC phase, but also significantly changes the structure in the solid phase. The solid-state NMR experiments presented in the following show that these differences can be understood on the basis of the formation of hydrogen bonded acid dimers.

6.1.2 Solid-state NMR

Of course, the presence of free acid groups, which are capable of hydrogen bonding, strongly suggests that the structure of the investigated HBC-acids is also governed by hydrogen bonding. The formation of hydrogen bonded acid dimers is conveniently investigated by solid-state NMR. Solid-state NMR was already successfully applied for unravelling the interplay between acid dimer formation and the phase behavior in a familiar system, HBC[C10COOH]$_6$, a hexa-*peri*-hexabenzocoronene with six symmetrically attached C_{10}COOH chains [Brown 00b]. There, ^{1}H solid-state NMR methods employing fast (ν_R=30kHz) MAS were used, which are quite powerful in such systems, because the position of the chemical shift of the acid proton is very sensitive to the strength and geometry of hydrogen bridges [Berglund 80, Becker 96].

6.1.2.1 One-dimensional ^{1}H MAS NMR

In order to investigate acid dimer formation in the three HBC-acids, temperature dependent ^{1}H MAS NMR spectra were recorded. As can be seen in Fig. 6.5, the acid proton peak is resolved in the spectra of all samples. The high chemical shift of the acid protons of > 12 ppm proves that in all samples hydrogen bonds are formed. Regarding the proton spectra at elevated temperatures (Fig. 6.6), significant differences between the three samples are observed.
In Fig. 6.7, the chemical shift of the acid protons is plotted versus temperature for all three samples. The samples were heated as-synthesized, cooled down and heated again for the measurement of the second heating curve. For HBC-C_{10}COOH the first and second heating curve do not differ within the experimental error. However, for HBC-C_3COOH significant differences between first and second heating are encountered. A similar behavior was already observed in the DSC curves and can be understood on the basis of structural distortions introduced when precipitating the sample from solution. On heating the sample, obviously the material finds ways to rearrange and improve the molecular packing. This is also indicated by the fact that the X-ray patterns were found to look much more structurized after heating and slowly cooling the sample.

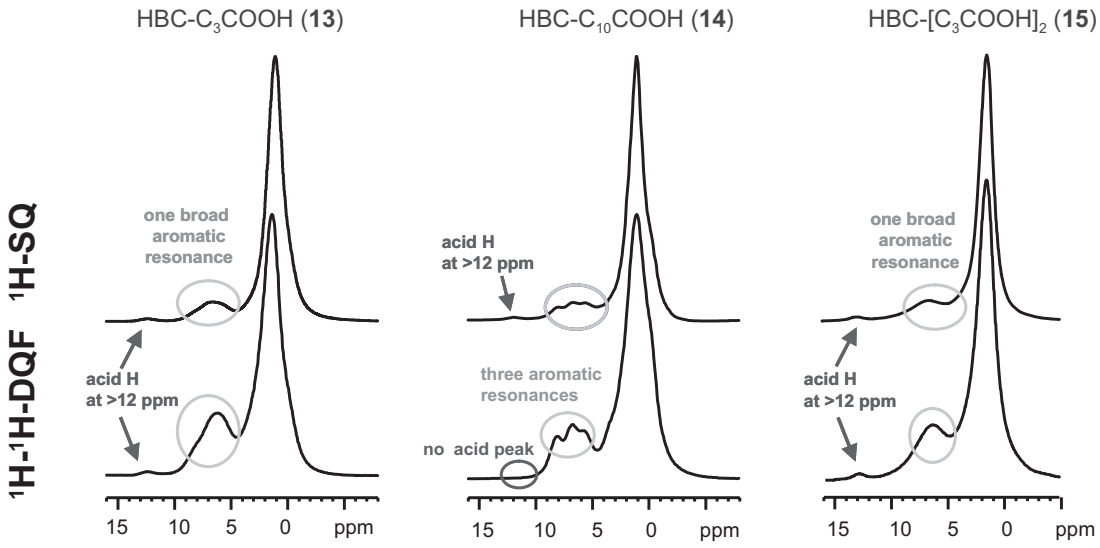

Figure 6.5: ^1H *SQ (top) and DQ-filtered (bottom) spectra of* **13**, **14** *and* **15** *at 30 kHz MAS, T = 48°C and* $\tau_{exc} = 1\tau_R$ *for the DQ spectra.*

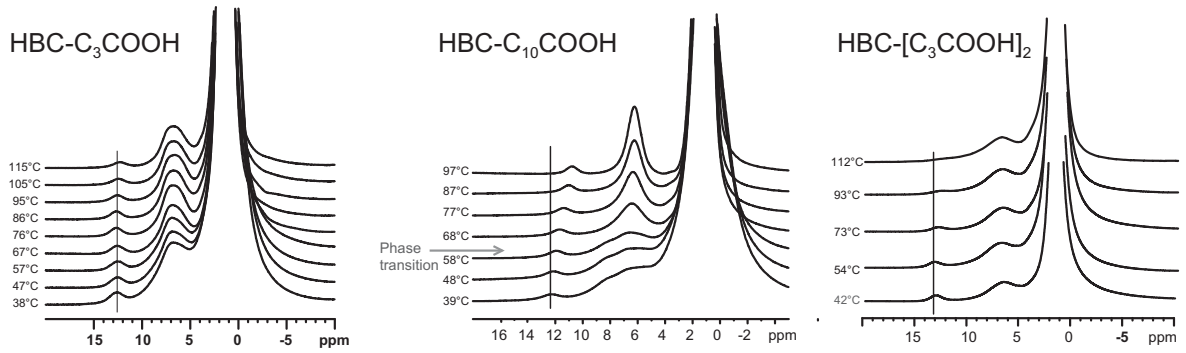

Figure 6.6: ^1H *MAS spectra of* **13**, **14** *and* **15** *at 25 kHz MAS and variable temperatures.*

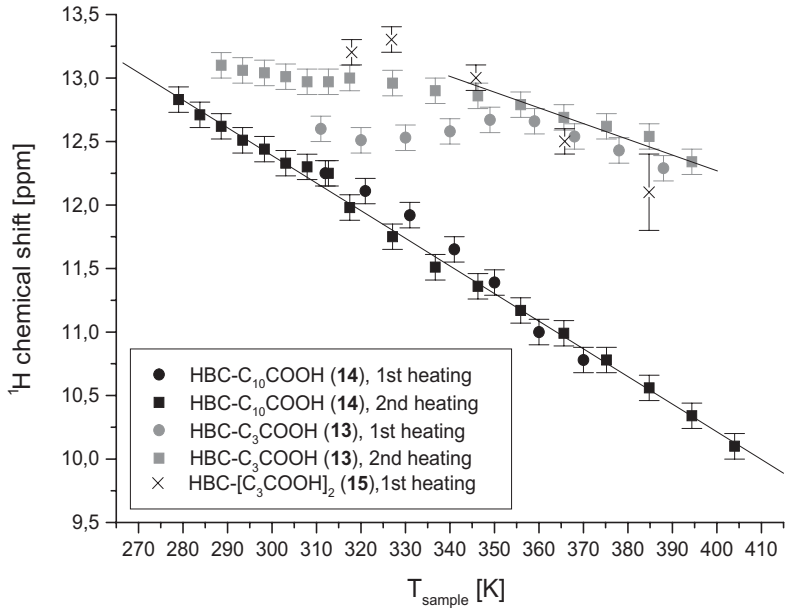

Figure 6.7: *Dependence of the ^1H chemical shift of the acid protons of* **13***,* **14** *and* **15** *on the temperature.*

For the following discussion we focus on the second heating curves. The acid peak of HBC-C_3COOH is located at around 12.5 ppm and decreases only slightly with temperature. The same is the case for the diacid HBC-[C_3COOH]$_2$. Such a high chemical shift of 10-13 ppm is typical for the protons involved in hydrogen bonds, whereas a proton of a free carboxylic acid typically has a chemical shift of around 9 ppm [Berglund 80, Becker 96]. This indicates the presence of strong hydrogen bonds in HBC-C3COOH. In contrast, the peak position of the acid proton peak of HBC-C_{10}COOH shifts almost linearly with increasing temperatures from $\sim$12.5 ppm down to $\sim$10 ppm. Such a behavior was already observed in the familiar HBC[C_{10}COOH]$_6$ [Brown 00b] and was explained by means of a chemical exchange process between the free acid and a hydrogen-bonded acid dimer, as depicted in Fig. 6.8. The free

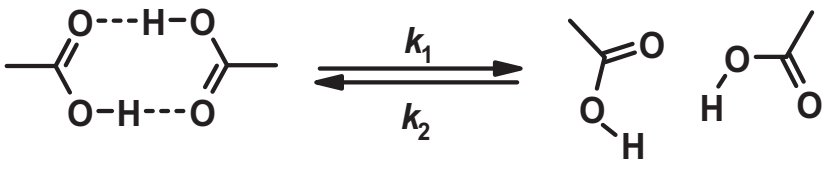

Figure 6.8: *Equilibrium between free and dimerized carboxylic acid groups.*

and the dimerized acid are in a dynamical equilibrium, which involves permanent making and breaking of hydrogen bonds. In the spectra, the two peaks of the free acid and the acid dimer coalesce to a single peak located at an intermediate position which is determined by the rate constants of the equilibrium. At higher temperatures, the equilibrium is shifted towards the

free acid, so the chemical shift moves towards the value of the free acid at 9 ppm. As described in detail in ref. [Brown 00b], the plot of the proton chemical shift versus temperature bears information on the thermodynamic parameters of the equilibrium. However, a detailed analysis requires knowledge of the exact chemical shift of the free and the dimerized acid, which should be detectable as plateau values at high and low temperatures. Obviously, the temperature range experimentally accessible here is too small to reach the plateaus. Only for **13** and **15** a plateau corresponding to the dimerized acid is reached at 13.3 ppm. Therefore, it is only possible to estimate the thermodynamic parameters for the acid dimer formation by estimating the chemical shift of the free acid to 9 ppm and the chemical shift of the acid dimer to 13.3 ppm. Following the procedure described in detail in [Brown 00b], for HBC-C_{10}COOH a standard reaction enthalpy ΔH = 32 kJ/mol and an entropy ΔS = 93 kJ/mol and for HBC-C_3COOH ΔH = 36 kJ/mol and ΔS = 77 kJ/mol is obtained. For **15** such an analysis was not undertaken, because not enough data points were recorded. Nonetheless, from the ^{1}H spectra presented in Fig. 6.6 it is clear that the diacid **15** strongly resembles the short-chain monoacid **13**. The energy for the formation of a hydrogen bond is typically 10-40 kJ/mol. In an acid dimer, usually two hydrogen bonds are present and, thus, the observed values of ΔH are within the expected range. The higher ΔH obtained for **13** fits to the view that the acid dimer in HBC-C_3COOH is more stable than in HBC-C_{10}COOH.
Interestingly, in the plot of the chemical shift vs. temperature of HBC-C_{10}COOH no significant change was observed upon the phase transition to the mesophase, as opposed to HBC[C_{10}COOH]$_6$, where a marked jump of the chemical shift of the acid proton from 10.1 ppm to 9.0 ppm upon the phase transition was observed [Brown 00b]. Obviously, in HBC-C_{10}COOH the phase transition does not have a pronounced influence on the tendency to form acid dimers and vice versa.

6.1.2.2 ^{1}H Double-Quantum (DQ) MAS NMR

The formation of carboxylic acid dimers means that the hydrogen bonded acid protons come quite close to each other with a typical through space H-H separation of between 0.25 and 0.3nm. The existence of such pairs can readily be detected by ^{1}H DQ MAS NMR. In ^{1}H -^{1}H DQ MAS NMR, only signal of sufficiently strong dipolar coupled protons which are not subject to chemical exchange on the experimental timescale (approx. 100μs) or faster passes the double-quantum filter. In Fig. 6.5, ^{1}H -^{1}H DQ filtered spectra are presented in comparison with single-quantum (SQ) spectra. In the DQ-filtered spectra of HBC-C_{10}COOH, the acid signal is completely missing, indicating fast chemical exchange of these protons. In contrast, in the spectra of the short chain acids **13** and **15** the acid peak is present at around 12.5 ppm. Therefore, the acid protons of both **13** and **15** are not subject to fast chemical exchange.
In the spectra of Fig. 6.5 another striking difference meets the eye when regarding the aromatic proton peaks. Whereas the spectra of the C3-acids exhibit only one broad, featureless aromatic peak, the spectra of HBC-C_{10}COOH clearly show three distinguishable peaks. Such

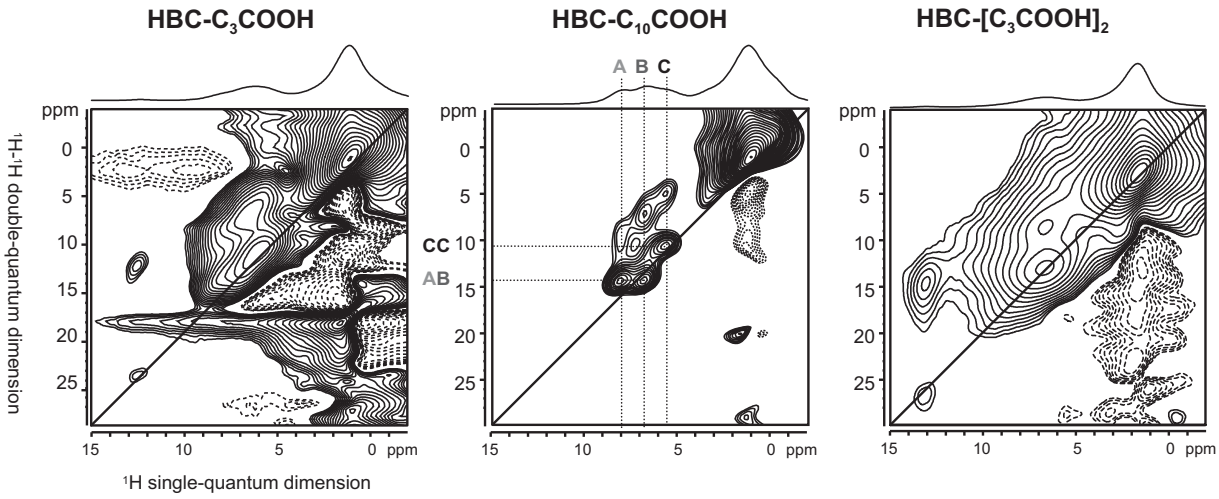

Figure 6.9: *^1H -^1H DQ spectra of* **13**, **14** *and* **15** *at 30 kHz MAS and $\tau_{exc} = 1\tau_R$. The spectra exhibit more or less strong phase distortions from the dominating alkyl peak. This problem could be overcome by WATERGATE peak suppression as described in the text.*

a behavior is well-known from familiar systems [Brown 99, Brown 00a]. As described in the previous chapter, the splitting of the one expected resonance in three separated peaks is due to the tilt of the discs with respect to the columnar axis. Therefore, solid-state NMR confirms the finding of the X-ray investigations that HBC-C_{10}COOH is tilted with respect to the columnar axis in its solid phase, whereas the C3-acids are not.

Further insight is provided by the two-dimensional ^{1}H -^{1}H DQ spectra, which are shown in Fig. 6.9. The spectra are dominated by the strong alkyl peaks, which are responsible for the strong phase distortions encountered in the spectra. In the case of HBC-C_3COOH it is not possible to tell whether peaks due to DQ coherences involving the acid proton are real peaks or just artifacts arising from the phase distortions of the alkyl signals. Hence, in order to remove the dominating alkyl peak WATERGATE peak suppression was utilized for the two mono-acids. WATERGATE peak suppression is well-known from solution NMR to suppress intense water/solvent signals and was adapted to solid-state NMR under MAS [Fischbach 03]. Most importantly, the WATERGATE peak suppression scheme was successfully incorporated into the BABA sequence providing 2D DQ spectra which do not suffer from the phase distortions induced by the alkyl chains. The details of the WATERGATE scheme are described in appendix D.2. On the top of Fig. 6.10, one-dimensional ^{1}H spectra acquired with and without WATERGATE peak suppression of the alkyl peak are displayed. Clearly, in the spectra with WATERGATE peak suppression the features of the aromatic and acid peaks of interest emerge much more intense, since the dominating alkyl peak is strongly reduced. In the ^{1}H -^{1}H DQ spectra (bottom of Fig. 6.10) the severe phase distortions arising from the alkyl peaks are suppressed well below the intensity level of the peaks of interest. A marginal drawback of the peak suppression with WATERGATE is that cross-peaks closer to the suppressed peak are

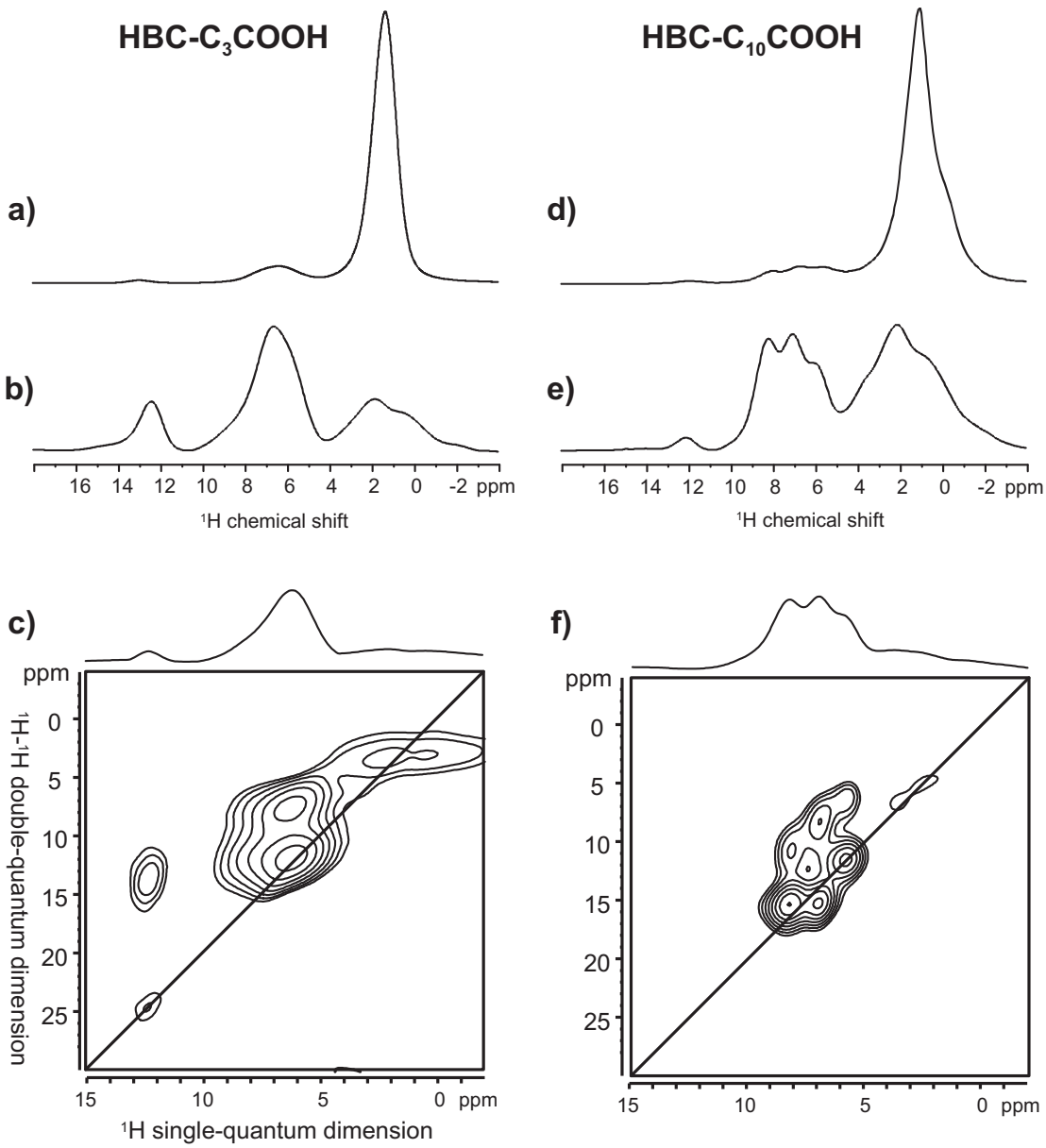

Figure 6.10: *Comparison of the* ^1H *spectra of* **13** *and* **14** *without [(a) and (d)] and with WATERGATE suppression [(b) and (e)]. On the bottom,* ^1H *-*^1H *DQ spectra with WATERGATE peak suppression are shown. Compared to the spectra shown in Fig. 6.9, the peaks of the coherences of interest (involving acid and aromatic protons) are much more pronounced.*

less intense than their counterparts, since they lose some intensity due to the finite bandwidth of WATERGATE peak suppression.
Comparing the 2D DQ spectra of **13** (Fig. 6.10c), **14** (Fig. 6.10f) and **15** (right of Fig. 6.9), significant differences become obvious: The spectra of the short chain acids **13** and **15** have an identical peak pattern: Each spectrum has a diagonal peak at (12.5 ppm,25 ppm), which indicates the presence of acid protons coupled to each other. This is indicative for an acid dimer, where the two acid protons form dipolar coupled pairs. Also, a cross-peak at (12.5 ppm, 13.5 ppm) is detected, which corresponds to a coupling between the acid proton and neighboring aliphatic protons. In contrast, these two peaks do not occur in the 2D DQ spectrum of **14**, where no acid peak intensity is detected at all. This could already be expected from the 1D double-quantum filtered spectra, where also no acid peak was present. The missing acid diagonal peak indicates the absence of a stable acid dimer in **14**. Furthermore, the missing cross-peak to aliphatic protons indicates that the acid group must be very mobile, thus averaging the dipole-dipole coupling between the acid proton and neighboring aliphatic protons. In the aromatic region of the 2D double-quantum spectra, the differences between the short chain acids (**13** and **15**) and the long chain acid **14** are very pronounced as well: The spectrum of **14** features the typical signal pattern known from various other HBCs with a tilted packing arrangement [Brown 99, Brown 00a], with a diagonal peak at (6.0 ppm,12 ppm) and cross-peaks at (7.2ppm,15.8ppm) and (8.5ppm,15.8ppm), respectively. In contrast, the spectra of the short chain acids exhibit only a broad featureless aromatic diagonal peak at (6.2 ppm,11 ppm) as typical for non-tilted packing arrangements. In the spectra also cross-peaks corresponding to couplings between aromatic protons and alkyl protons are present at (6 ppm,7 ppm) for **13** and **15** and at (8.5 ppm,10.5 ppm), (7.2 ppm, 8.8 ppm) and (6.0 ppm,7.0 ppm) for **14**, respectively. Summarizing the results from proton solid-state NMR, it can be concluded that the difference in the phase behavior of the investigated HBC-acids is associated by a different stability of the acid dimers dimers formed in the material. Also, the results from X-ray scattering concerning the intracolumnar arrangement of the discs were confirmed.

6.1.2.3 Heteronuclear ^{1}H -^{13}C Spinning Sideband Patterns

More insight into the nature of the phases formed by the HBC-acids can be gained from investigating molecular dynamics, which is again performed by means of REPT-HDOR SB patterns. In the following, the comparative study is restricted to **13** and **14**, since the behavior of **15** was found to be analogous to **13**. In Fig. 6.11 a and Fig. 6.11 b, ^{13}C cross-polarization (CP) spectra of the two HBC-acids are shown. In both spectra, the resonance of the aromatic C-H carbons at around 120ppm is clearly resolved from the other carbon resonances. In Fig. 6.11c-f REPT-HDOR sideband patterns of the aromatic C-H peaks are shown together with the corresponding best fits and dipole-dipole coupling constants. At around 40 °C the sideband patterns of **13** and **14** are very similar and correspond to dipole-dipole coupling constants of $D_{is}/2\pi$ = (20.4 $\pm$ 0.5) kHz for **13** and $D_{is}/2\pi$ = (22.0 $\pm$ 0.5) kHz for **14**, which

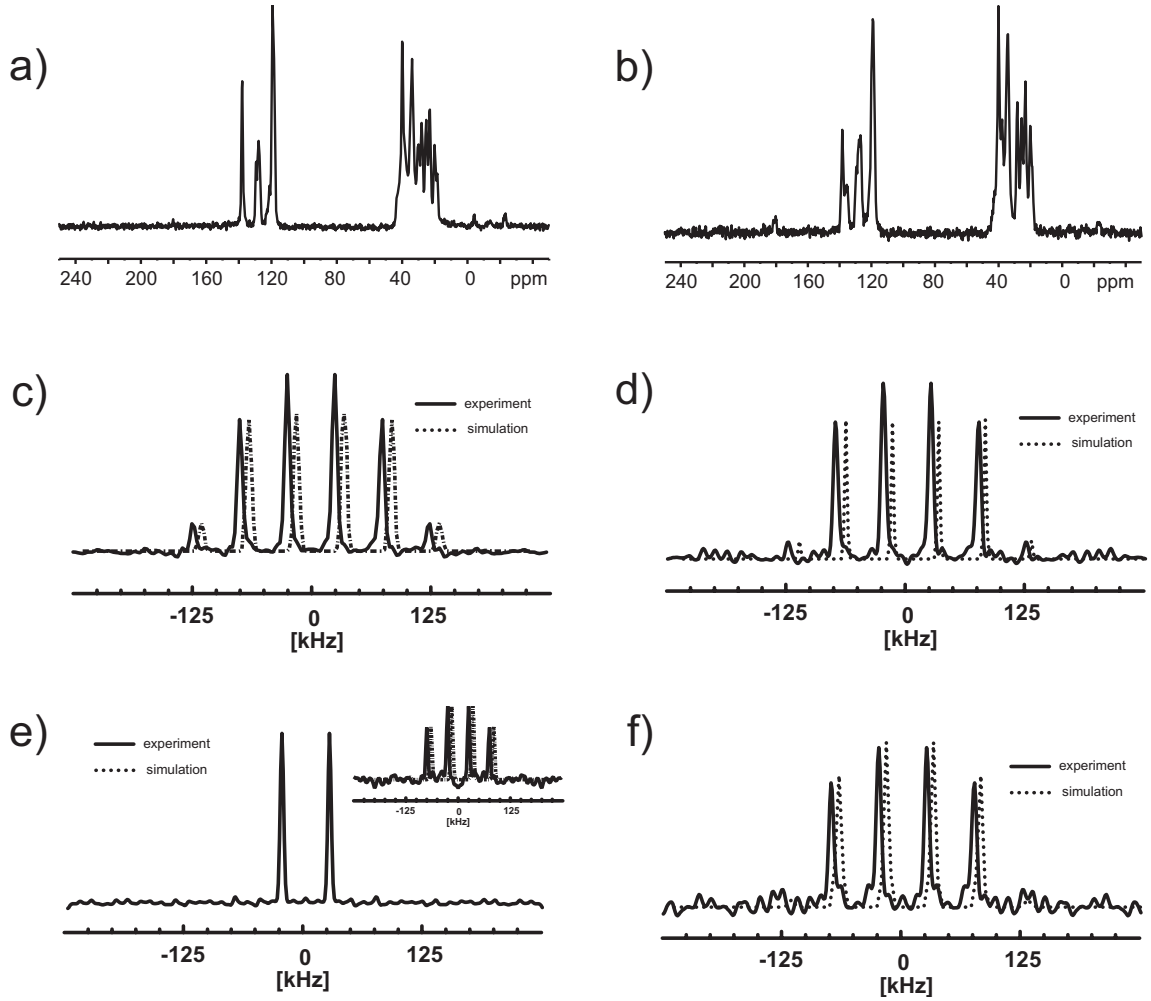

Figure 6.11: *^{13}C CP spectra of HBC-C_{10}COOH (a) and HBC-C_3COOH (b) at 25 kHz MAS and T = 40 °C. (c)-(f) show the REPT-HDOR sideband patterns ($\tau_{rcpl} = 2\tau_R$) at 25 kHz MAS extracted for the aromatic C-H peak at 120 ppm:*
c) HBC-C_{10}COOH, T = 40 °C, $D_{is}/2\pi$ = (22.0 ± 0.5) kHz
d) HBC-C_3COOH, T = 40 °C, $D_{is}/2\pi$ = (20.4 ± 0.5) kHz
e) HBC-C_{10}COOH, T = 93 °C, inset: $\tau_{rcpl} = 4\tau_R$, $D_{is}/2\pi$ = (8.6 ± 0.5) kHz → S = 39%
f) HBC-C_3COOH, T = 102 °C, $D_{is}/2\pi$ = (17.6 ± 0.5) kHz → S = 86%

is typical for a rigid, directly bonded ^{1}H -^{13}C spin pair. Therefore, core dynamics on the fast timescale (correlation times above 10^4Hz), which would result in a reduced dipole-dipole coupling constant, can be excluded for both samples at this temperature.

On heating **14** to its mesophase, the sideband pattern changes dramatically. At 93 °C the sideband pattern of the aromatic CH peak exhibits only first order sidebands, which indicates significant reduction of the dipole-dipole coupling constant by molecular motion. Since sidebands of third or higher order are required for the extraction of dipole-dipole coupling constants, the sideband pattern was re-measured with a longer recoupling time of four rotor periods. From this pattern (depicted in the inset of Fig. 6.11) the dipole-dipole coupling constant was determined to $D_{is}/2\pi$ = (8.6 $\pm$ 0.5) kHz, which corresponds to a reduction to 39% of the rigid dipole-dipole coupling. This strong reduction indicates fast core dynamics with large motional amplitudes as typical for columnar mesophases. It should be pointed out that the observation of large amplitude motions or even column rotation does not contradict the presence of acid dimers. Since the acid dimers are subject to continuous making and breaking processes, the rotation can take place just during those times when the acid dimers are 'open'. In addition, since the alkyl chains carrying the acid end groups are quite long, large amplitude motions can also take place even if the acid dimers are closed. As shown in Fig. 6.12, from the sideband patterns it cannot be distinguished whether a full rotation or a turning motion with an amplitude of $\pm$ 90 ° or more takes place. Alternatively, *intra*columnar dimers could be formed, which naturally do not hinder the column rotation. Assuming fast rotation around the columnar axis as the motional process, a reduction of the dipole-dipole coupling by a factor of two would be expected for an ideal rotation. Any further reduction is due to out-of-plane motion. Calculating the order parameter for a column including fast rotation (according to Eq. (7.1)), one obtains $S_{col.rot.}$ = 78% for compound **14**. This is almost identical to the order parameter of the symmetric parent compound, HBC-$C_{8,2}^{rac}$ ($S_{col.rot.}$ = 79%, subsection 5.3.2).

In contrast to this, the sideband pattern of **13** at 102 °C is only slightly changed and can be fitted to a dipole-dipole coupling constant of $D_{is}/2\pi$ = (17.6 $\pm$ 0.5) kHz, which corresponds to a much lower reduction to 86% of the rigid dipole-dipole coupling. This slight reduction indicates small angle librations, but definitely excludes a column rotation or large amplitude motions, as would be typical for columnar liquid crystalline phases. In analogy to the strategy described in subsection 5.3.3, the observed reduction factor of 86% can be used to get an estimate of the librational amplitude from Fig. 4.18. Assuming a gaussian reorientation distribution, one obtains a FWHM of the gaussian distribution of $\Delta\beta \approx 27°$.

Summarizing the results from the REPT-HDOR patterns, it can be concluded that HBC-C_{10}COOH (**14**) undergoes at 70 °C a transition to a columnar liquid crystalline phase, which is characterized by large amplitude motions of the aromatic cores. In contrast, in HBC-C_3COOH (**13**) large amplitude motion of the aromatic cores is suppressed at least up to 102 °C.

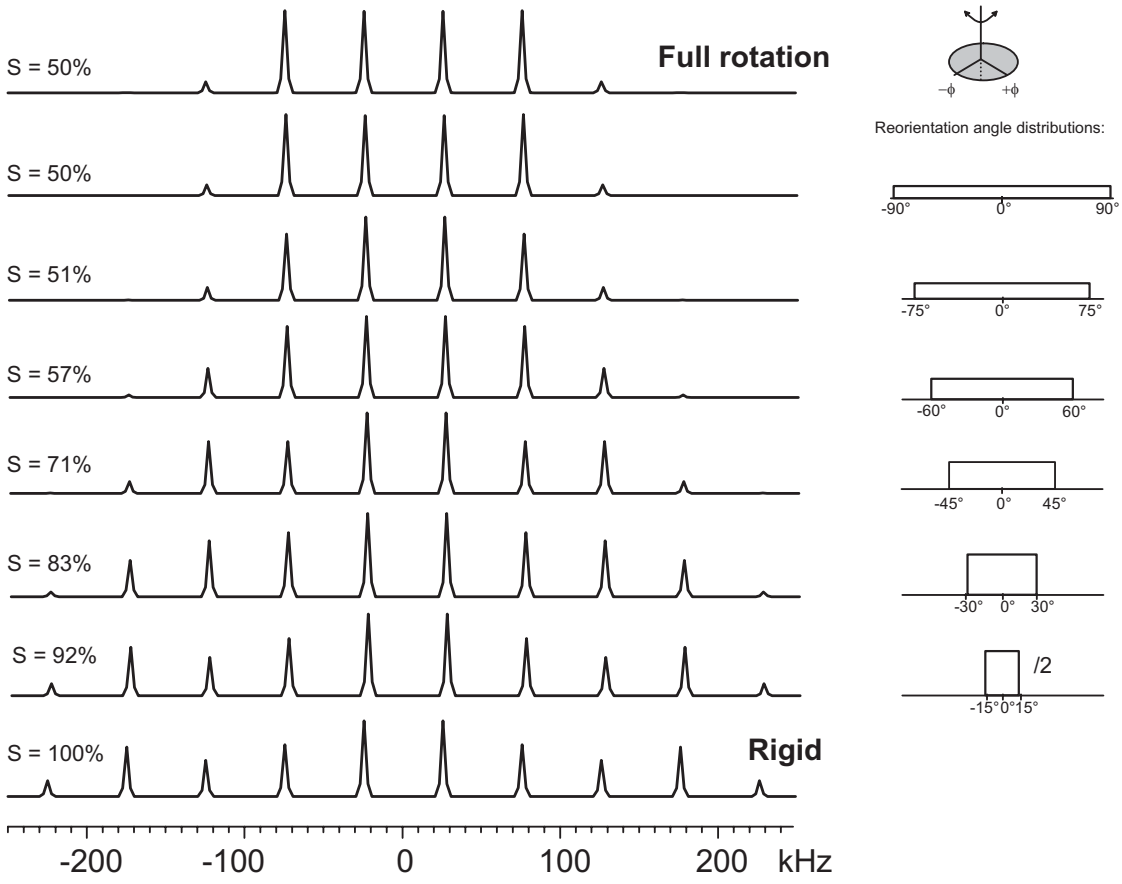

Figure 6.12: *Calculated REPT-HDOR sideband patterns ($\tau_{rcpl} = 4\tau_R$, 25 kHz MAS) for a C-H spin pair ($r_{is} = 1.14\mathring{A}$) undergoing no motion (bottom) or underlying rotational diffusion with different amplitudes. The reorientation angle distributions were chosen as box functions as depicted on the right of the corresponding sideband patterns. The calculated patterns were fitted to yield the reduced dipole-dipole coupling constants. The reduction factors obtained from those are indicated in the figure. Even though box functions are physically unlikely reorientation distributions, the calculations indicate that low reduction factors are only observed for large amplitude motions. Clearly, a rotational diffusion with an amplitude of $\pm 90\,^\circ$ cannot be distinguished from a full rotation (top).*

6.1.3 Discussion

The results presented above show that the phase behavior in HBCs bearing carboxyl-terminated alkyl sidechains strongly depends on the length of this sidechain. Since the acid groups are able to form hydrogen-bonded dimers, hydrogen-bonding definitely has an influence on the observed structural and dynamical properties.
^{1}H solid-state NMR proved that in all three considered HBC-acids (**13**, **14** and **15**) acid dimers are formed by hydrogen bonding. The observed decrease of the chemical shift of the acid proton with increasing temperature indicates an equilibrium between free and dimerized acids, as was observed in a related system, HBC-[C_{10}-COOH]$_6$ [Brown 00b]. The fact that the equilibrium shifts at much lower temperatures towards the free acid in **14** than in **13** and **15** can be taken as an indication for a less stable dimer in **14**. Also, the non-existing DQ intensity of the acid proton peak of **14** proves the fast making and breaking of hydrogen bonds in this system. In contrast, the existence of DQ intensity of the C3-acid protons clearly indicates that the acid protons attached to the short chains do not undergo exchange on the timescale of the experiment. Only at higher temperatures (spectra not shown here) the DQ intensity of the acid proton peak of **13** and **15** vanishes, too. This difference in the formation of the acid dimers can be attributed to the different lengths of the sidechain bearing the carboxyl group. The longer chain is presumably more mobile and, therefore, the acid dimers break more easily. An indication for the higher mobility of the chain end of the long C10-chain is the fact that no DQ cross-peak between the acid proton and aliphatic protons is observed for HBC-C_{10}COOH, but for HBC-C_3COOH and HBC-[C_3COOH]$_2$. At this point of the discussion, it should be emphasized that even though the acid dimer in **14** is not stable over a μs timescale, the observed high chemical shift still proves that, on average, even in **14** the acid dimers are closed for longer times than they are open.
Since the acid dimer is the predominating form in all three considered acids, another effect might contribute to the pronounced differences in the phase behavior, which is the effect of the spacer length in dimers of discotic molecules. This effect has already been subject to several studies [Lillya 85, Boden 99a]. In a study of Zamir et al. [Zamir 97], alkanoyloxybenzene dimers with covalent linkers of various lengths were investigated by X-Ray and solid-state NMR. There, pronounced differences in the mobility and phase behavior of the systems were found with different spacer length. Short spacers which exactly bridge the intercolumnar distance in the material prevented large amplitude core motion. Therefore, no mesophase could be formed. However, systems with longer spacers were found to form columnar mesophases isomorphic to those of the monomers.
Most studies of discotic dimers available from the literature assume the bridging to be preferably intercolumnar because of the lower strain in all-trans chains (as they are present in intercolumnar dimers) as compared to chains which are folded to meet spatial requirements for intracolumnar bridging. A molecular modelling study of Boden et al. [Boden 99a] on triphenylene dimers bridged by flexible O(CH_2)$_n$O polymethylene chains investigated the energy

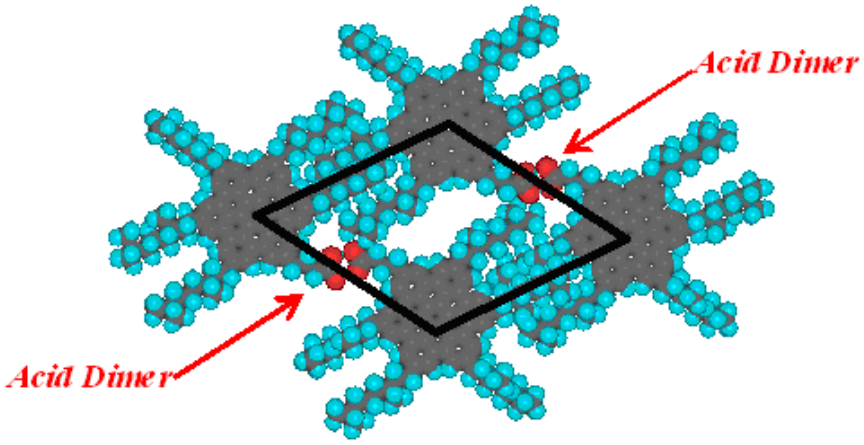

Figure 6.13: *Unit cell of the two-dimensional columnar lattice formed by HBC-C_3COOH. Clearly, if the acid groups are dimerized, the resulting 'spacer' exactly matches the intercolumnar distance.*

differences between all-trans chains and chains with a conformation adapted to intracolumnar bridging. It was shown that low strain bridging in an intracolumnar manner required only comparably short spacers with n>2 bridging methylene units. However, the shortest chain, for which a columnar mesophase was observed, had n=8 methylene units, which was found to be one methylene unit more than required for intercolumnar bridging.
Comparing these results with the HBC-acids investigated in this study, exactly the same observations are made with the only difference that the linkers are not covalently bonded, but formed by hydrogen bonding. HBC-C_{10}COOH with a long 'spacer' exhibits almost exactly the same phase behavior as its parent compound, HBC-$C_{8,2}^{rac}$. The phases formed by HBC-C_{10}COOH are isomorphic to those of HBC-$C_{8,2}^{rac}$ with the only difference being the slightly lowered phase transition of 70 °C instead of 81 °C. The C3-acids, however, effectively form 'spacers' with a length exactly matching the intercolumnar distance, as depicted in Fig. 6.13. This short 'spacer' excludes large amplitude core motions, which are a prerequisite for the formation of a discotic mesophase. In principle, in the C3-acids also intracolumnar bridges could be present, which would of course not hinder large amplitude core motions. However, an hydrogen-bonded acid dimer is rather stiff and, hence, intracolumnar dimers are supposedly not formed in the C3-acids, since this would imply too much strain on the chains. Also, the observation of a superstructure in the X-ray diffractograms of HBC-C_3COOH hints at the presence of acid dimers, whose formation might account for the observed lamellar superstructure.
To further support these conclusions, the results obtained here for 'non-covalently' bonded HBC-dimers will be compared to the results from covalently bonded HBC-dimers in section 6.3.

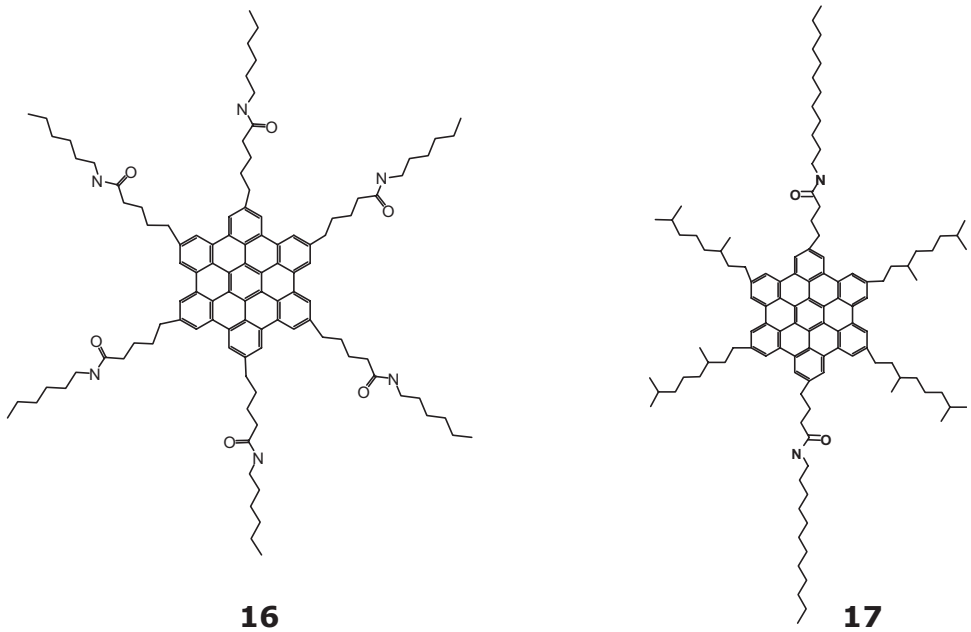

Figure 6.14: *Chemical structures of the two investigated HBC derivatives bearing amide functionalities within their sidechains.*

6.2 Hydrogen Bonding in HBCs with Amide Functionalities

In this section, two HBC derivatives with amide groups in their sidechains are discussed, whose chemical structures are depicted in Fig. 6.14. Since amide functionalities are also capable of forming hydrogen bonds, it is of interest to compare the effect of the amide functionalities on the phase behavior of HBCs to the effect of the carboxylic acid functionalities, which was studied in the previous section.

The two investigated materials differ in the number of amide groups per molecule. Whereas **16** is symmetrically substituted with all six sidechains bearing amide groups [Wang 03], **17** has only two amide groups in two opposite sidechains [Wasserfallen 03]. Both materials are nearly insoluble in both unpolar and polar solvents. Hence, the structure could not be unambiguously characterized with solution state NMR. The insolubility was attributed to a dense hydrogen bonded network. This network is presumably more rigid in **16**, as is indicated by the fact that **16** does not melt up to 219 °C. In contrast, **17** undergoes a phase transition at around 90 °C to a presumably hexagonal columnar mesophase. However, experimental proof of the existence of strong hydrogen bonding in these two materials was not available yet. Since the amide proton chemical shift is known to be very sensitive to the strength and geometry of hydrogen bonds [Yamauchi 00, Yamauchi 02], proton solid-state NMR was carried out to address this question. In Fig. 6.15a and b, ^{1}H MAS spectra of **16** and **17** are shown. Unfortunately, in the one-dimensional ^{1}H spectra, the peaks of amide and aromatic protons are not resolved. Hence, two-dimensional ^{1}H -^{1}H DQ spectra were measured, which are shown

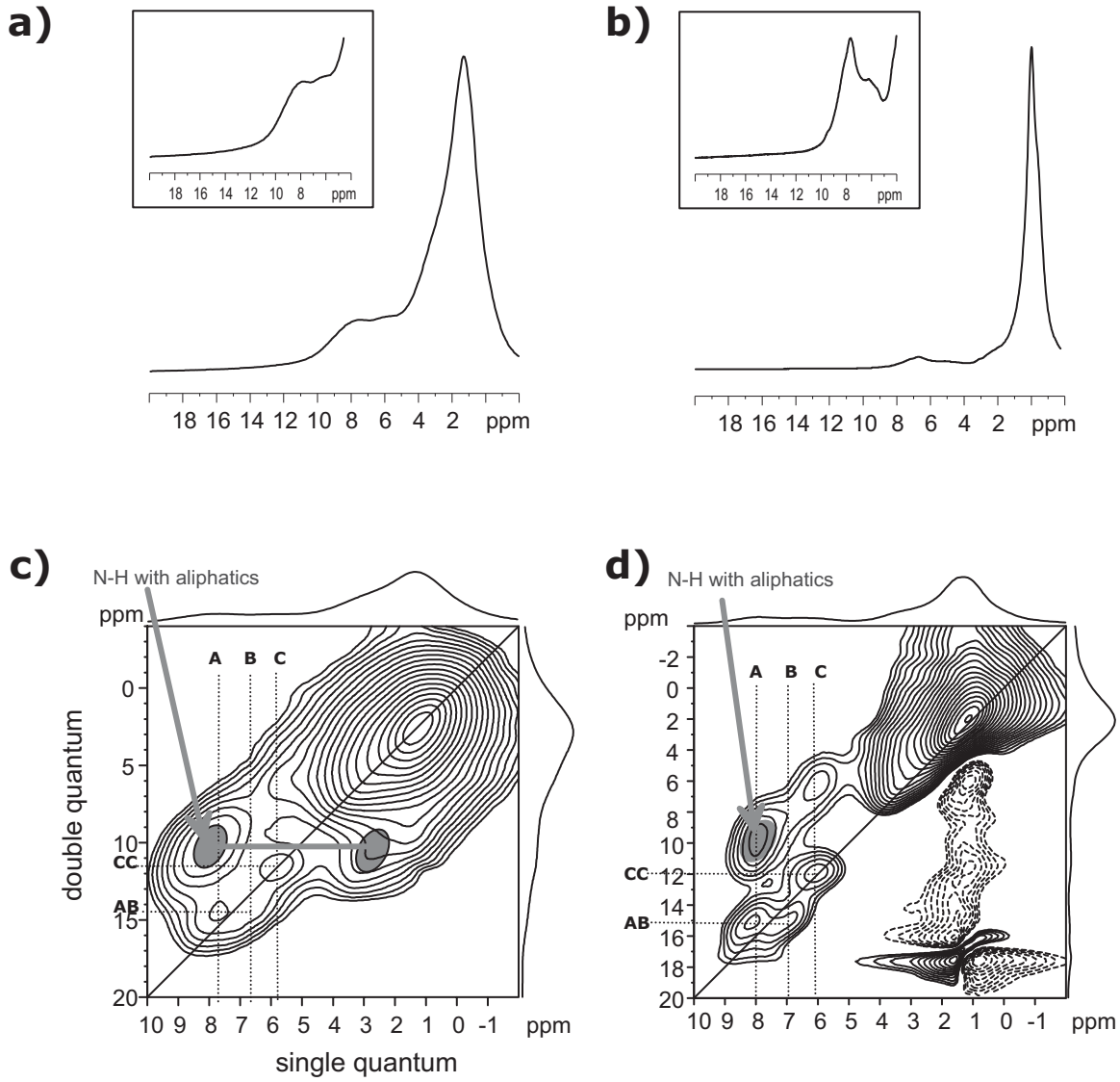

Figure 6.15: *^1H spectra of* **16** *and* **17** *at 30 kHz MAS and T = 48 °C: (a) ^1H -SQ,* **16***; (b) ^1H -SQ,* **17***; (c) ^1H -^1H DQ,* **16***; (d) ^1H -^1H DQ,* **17***.*

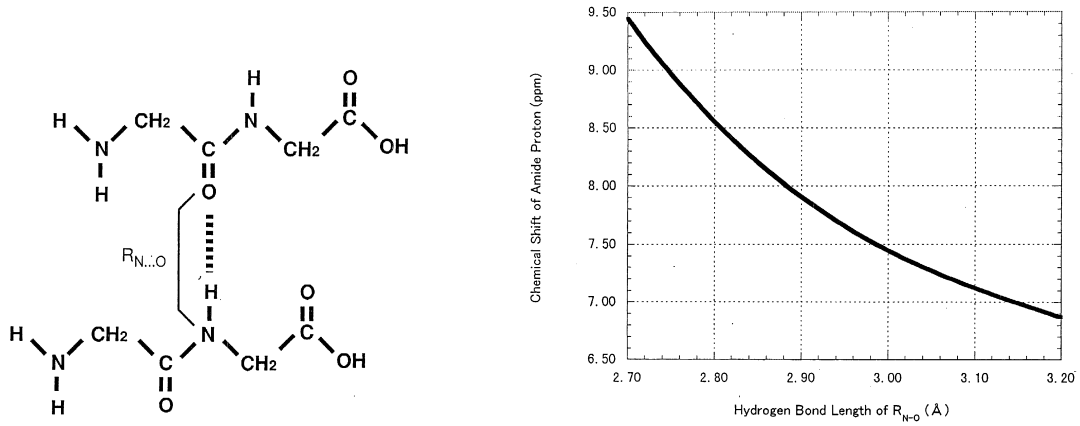

Figure 6.16: *Calculated dependence of the ^1H chemical shieldings of hydrogen-bonded Gly amide protons of two hydrogen-bonded GlyGly molecules (shown on the left) on R_{N-O} [taken from [Yamauchi 00]].*

in Fig. 6.15 c and d. In both spectra an intense cross-peak at around (8.2 ppm, 10.0 ppm) is present. In the spectrum of **16** this cross-peak is clearly too intense for a DQ coherence between aromatic and aliphatic protons. Hence, at least some intensity of this cross peak can be ascribed to a coherence between amide and aliphatic protons, which means that the amide protons in **16** have a chemical shift of around 8.2 ppm. In the spectrum of **17** the intensity of the cross-peak is not really exceeding the expectations for an aromatic-aliphatic coherence. However, it should be noted that in **17** only two amide groups per molecule are present and, hence, the amide proton peak is not expected to be as intense as in **16**. Since no other peak is detected in the spectrum, which could be attributed to the amide protons, it is reasonable to assume that, in analogy to **16**, the amide protons of **17** are located at 8.2 ppm.
The extracted chemical shift of the amide protons of around 8.2 ppm can be compared to chemical shift values of amide protons reported in the literature [Yamauchi 00, Yamauchi 02]. It was found that the chemical shift of the amide protons sensitively depends on the distance between the hydrogen bridged oxygen and nitrogen, R_{N-O}. In Fig. 6.16 (taken from [Yamauchi 00]), calculated chemical ^{1}H shieldings (σ) of hydrogen-bonded Gly amide protons are shown. According to this, the observed chemical shift of 8.2 ppm corresponds to a distance $R_{N-O} \sim 2.8\mathring{A}$, which is a typical distance for such hydrogen bonds. For 'free' amide protons in a nonpolar solvent ($CDCl_3$), chemical shifts between 5.0 ppm and 5.5 ppm are known from the literature [Ishimoto 99]. Consequently, the observed high ppm value clearly proves that the amide protons undergo hydrogen bonding, even though the estimation of the N-O distance is very crude.
Of course, the ^{1}H -^{1}H DQ quantum spectra also provide information about the disc stacking arrangement. The DQ signal pattern of the aromatic protons of **17** clearly corresponds to a 'herringbone'-type of arrangement, as depicted in Fig. 5.11. In the DQ spectrum of **16**, the pattern is not as pronounced as in the DQ spectrum of **17** but nonetheless resembles the typi-

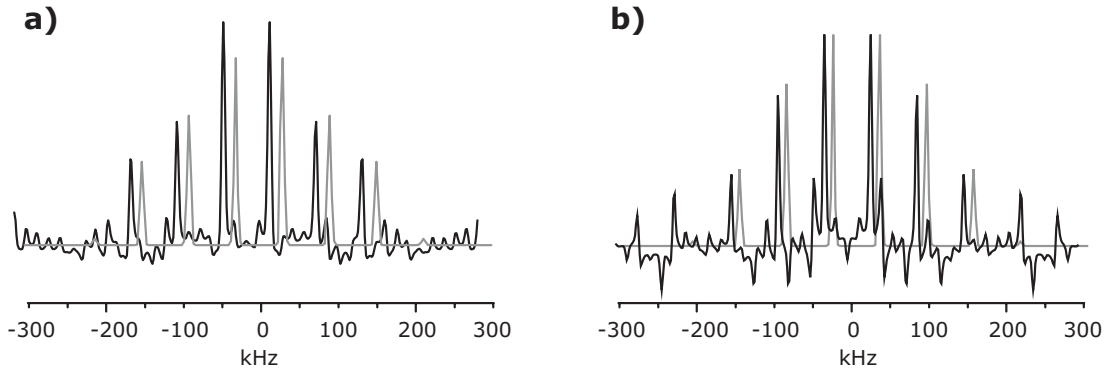

Figure 6.17: *REPT-HDOR SB pattern of* **16** *(a) and* **17** *(b) at 30 kHz MAS, $\tau_{rec} = 3\tau_R$ and T = 48 °C. The underlying grey patterns are the best-fit patterns with $D_{is}/2\pi$ = (20.8 ± 0.5) kHz (a) and $D_{is}/2\pi$ = (19.9 ± 1.0) kHz (b), respectively.*

cal features of tilted columnar stacks. This points at a 'herringbone'-type arrangement in **16** which is not as well defined as in **17**.
The molecular dynamics was probed by REPT-HDOR sideband patterns, which are shown in Fig. 6.17. The low temperature patterns of the core CH resonance of both **16** and **17** correspond to basically rigid dipole-dipole coupling constants, indicating that the aromatic cores are rigid in both materials.

Summarizing the results on HBCs with amide functionalities, it can be said that the phase behavior in these materials is governed by hydrogen bonding of the amide groups. Even though the formation of amide hydrogen bonds does not seem to hinder a tilt of the discs with respect to the columnar axis, the formation of a columnar mesophase is clearly hindered, which is reflected in the fact that **16** does not melt up to 219 °C. Comparing the results for **16** and **17**, it becomes obvious that the effect of six amide groups per molecule is naturally much more pronounced than the effect of only two amide groups per molecule. For example, the phase transition temperature of **16** and **17** are increased due to the additional hydrogen bonding by 138 °C and only 9 °C, respectively, as compared to the parent compound without amide functionalities HBC-$C_{8,2}^{rac}$ (**10**). Also, while the core packing of **17** is unchanged as compared to **10**, the core packing is considerably less ordered in **16**, as is clear from the ^{1}H -^{1}H DQ spectra.

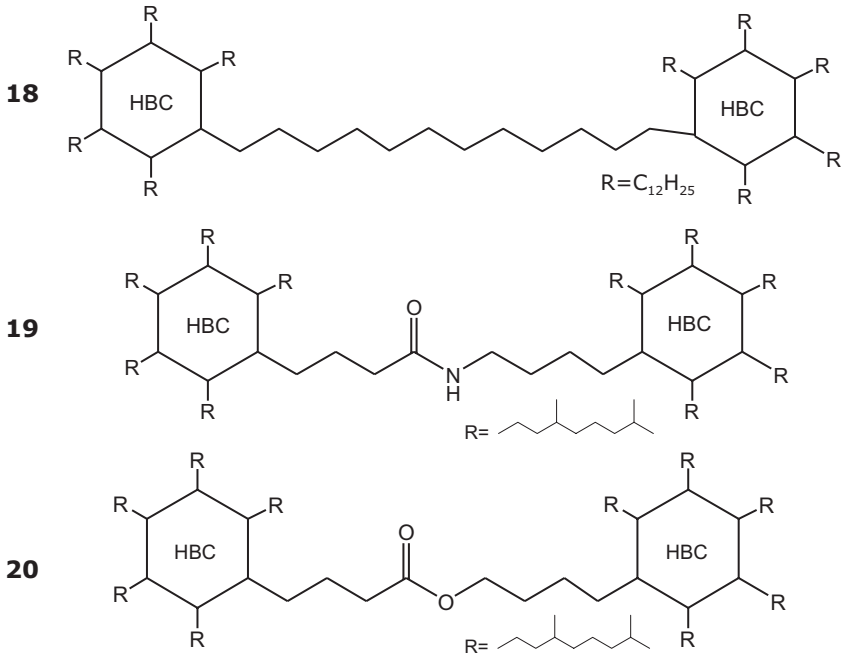

Figure 6.18: *Chemical structures of the investigated covalently bonded HBC dimers.*

6.3 Covalently Bonded HBC Dimers

As mentioned above, supramolecular ordering can be controlled by linking the building blocks. For discotic liquid crystals, the formation of covalently bonded dimers is such a method. Discotic triphenylene dimers with a flexible alkyl spacer have extensively been studied and were found to form a supercooled stable glassy D_h phase [Boden 95]. Crystallization was found to be efficiently suppressed, while the thermal interval of liquid crystallinity is broadened, which is of high interest for potential device applications. ^{2}H and ^{13}C solid-state NMR studies on other discotic dimers showed that the rotational freedom is greatly reduced unless the linking spacer is relatively long [Zamir 94, Zamir 97].

In this section, the phase behavior of covalently linked HBC dimers is considered. In order to unravel the influence of the linker-type on the phase behavior, three HBC dimers with different linkers were investigated, whose chemical structures are depicted in Fig. 6.18. The HBC alkyl-dimer **18** is linked by an unfunctionalized dodecyl-chain [Ito 00a]. To account for the influence of functionalities in the spacer, two HBC dimers with an identical spacer length of 9 atoms were investigated, the ester-dimer **20** and the amide-dimer **19**, which adds the possibility of hydrogen bonding [Tchebotareva 03].

The mesophase of the alkyl-dimer **18**, which is formed at temperatures above 53 °C, was previously characterized by DSC, POM and X-ray [Ito 00a]. It was found to be a Col_{ho} phase, isomorphic to the one of the corresponding monomer HBC-C_{12} (**5**). Compared to **5**, the phase transition temperature is lowered by more than 50 °C from 107 °C to 53 °C.

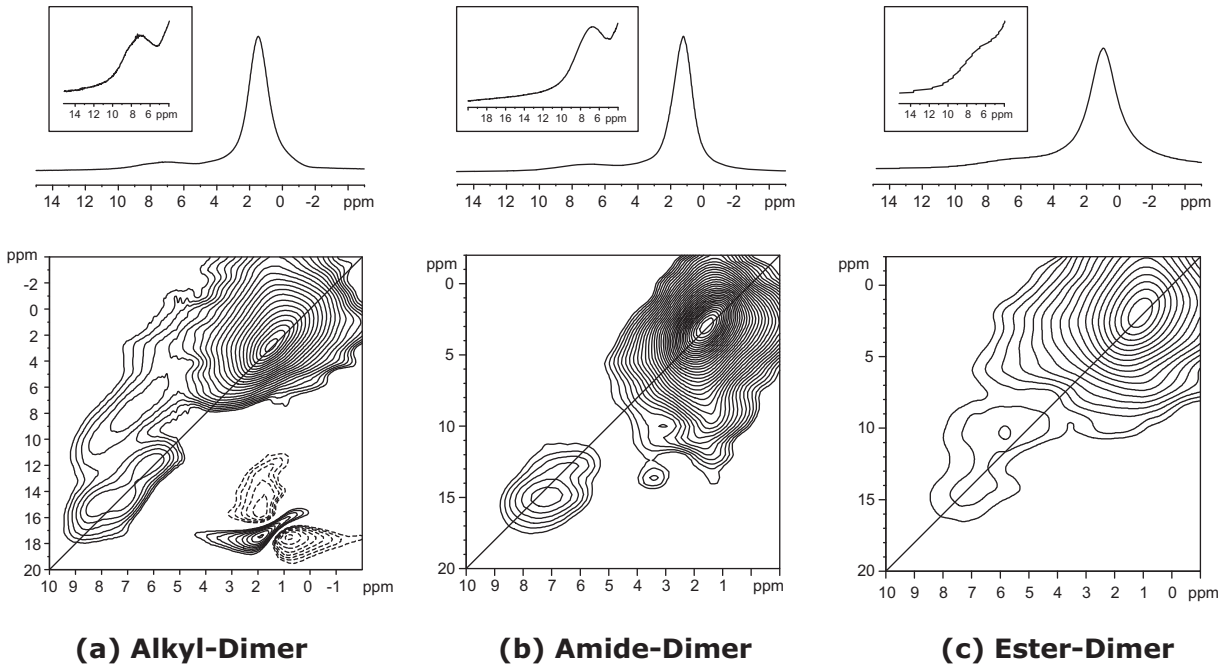

Figure 6.19: *^{1}H SQ (top) and ^{1}H -^{1}H DQ (bottom) spectra of the investigated HBC dimers:*
(a) **18***: 30 kHz MAS, $\tau_{exc} = 1\tau_R$, T = 48 °C*
(b) **19***: 25 kHz MAS, $\tau_{exc} = 1\tau_R$, T = 44 °C*
(c) **20***: 22.5 kHz MAS, $\tau_{exc} = 1\tau_R$, T = 2 °C.*

The amide linked dimer **19** forms no mesophase up to 220 °C [Tchebotareva 03]. In contrast, the ester linked dimer **20** has a reversible transition to a columnar mesophase at 14 °C, which is more than 60 °C lower than the phase transition in the corresponding monomer **10** [Tchebotareva 03]. X-ray measurements of both **19** and **20** revealed a hexagonal packing of columns at room temperature. X-ray reflexes indicate distances of around 0.35 nm and the absence of tilting of the discs within the columns. Given the similarity in the molecular structures, it is no surprise that the 2D hexagonal unit cells have identical cell parameters a = 2.54 nm. In the small angle region of the diffractogram of **19**, an additional peak at s = 0.26 nm was observed, which was attributed to a superstructure, in which the dimers adopt some specific orientation within the hexagonal unit cell.
The solid-state NMR experiments presented in the following provide further characterization of the different phases and address in particular the question of the origin of the observed strong differences in the phase behavior of the amide and the ester linked HBC dimer.

6.3.1 ^{1}H NMR

In Fig. 6.19, ^{1}H SQ and two-dimensional ^{1}H -^{1}H DQ spectra of the three HBC dimers in their respective solid phases are shown. The ^{1}H SQ spectra are dominated by the strong, broad alkyl peak. Since the ^{1}H -^{1}H DQ spectra provide much better resolution, these are discussed in the following. The spectrum of **18** features the typical DQ signal pattern of a 'herringbone'-type packing arrangement in the aromatic region, which was also observed for the corresponding monomer **5**. Hence, in the solid-phase of **18** the discs are tilted with respect to the columnar axis. In contrast, in the DQ spectra of both **19** and **20** no such distinct DQ signal pattern could be observed, indicating the absence of a 'herringbone'-type packing arrangement in these materials. However, it should be noted that the spectrum of **20** could be measured only at a spinning rate of 22.5 kHz for experimental reasons[1]. Hence, the spectrum of **20** is not at maximum resolution, and a 'herringbone'-type of arrangement cannot be excluded completely for this compound. Unfortunately, the resonance of the amide proton of **19** could not be detected, which is not surprising, since each molecule contains only one amide proton. Presumably, the amide proton resonance lies underneath the resonance of the aromatic protons between 6-8 ppm. Hence, one cannot tell from the ^{1}H spectra whether in the solid phase of **19** hydrogen bonded amide-dimers are formed or not.

6.3.2 ^{1}H -^{13}C REPT-HDOR

In order to further characterize the phases formed by the HBC dimers, the dynamics of the aromatic cores were studied by measuring heteronuclear ^{1}H -^{13}C dipole-dipole coupling constants by means of REREDOR or REPT-HDOR spinning sideband patterns. Compared to the ^{2}H NMR approach used in earlier studies of discotic dimers [Zamir 97], this approach benefits from the fact that no isotopic enrichment is needed. The heteronuclear dipole-dipole coupling constants of the core CH immediately provide information on the core dynamics.
The sideband patterns, together with the corresponding best-fits, are depicted in Fig. 6.20. For **18**, a ^{1}H -^{13}C dipole-dipole coupling constant of $D_{is}/2\pi$=(19.0$\pm$1.0)kHz was measured at T = 38 °C. This corresponds to a more or less rigid coupling and, hence, the aromatic cores of **18** are rigid on the fast timescale above 10^4 Hz, which was already observed in the solid phase of the corresponding monomer HBC-C_{12}.
For **19**, the REPT-HDOR SB pattern of the core CH corresponds to an almost rigid dipole-dipole coupling constant of $D_{is}/2\pi$ = (19.1 $\pm$ 0.5) kHz even at T = 112 °C, which indicates that the aromatic cores of the amide-linked dimer undergo only small amplitude motions. In contrast, for the core CH of **20** only the low temperature (T = 6 °C) sideband pattern corresponds to an almost rigid dipole-dipole coupling $D_{is}/2\pi$ = (19.1 $\pm$ 1.0) kHz. At T = 44 °C,

[1]The sample needed to be cooled for the measurements, which generally leads to less stable sample spinning for MAS experiments and thereby excludes the possibility to spin at the highest spinning rates.

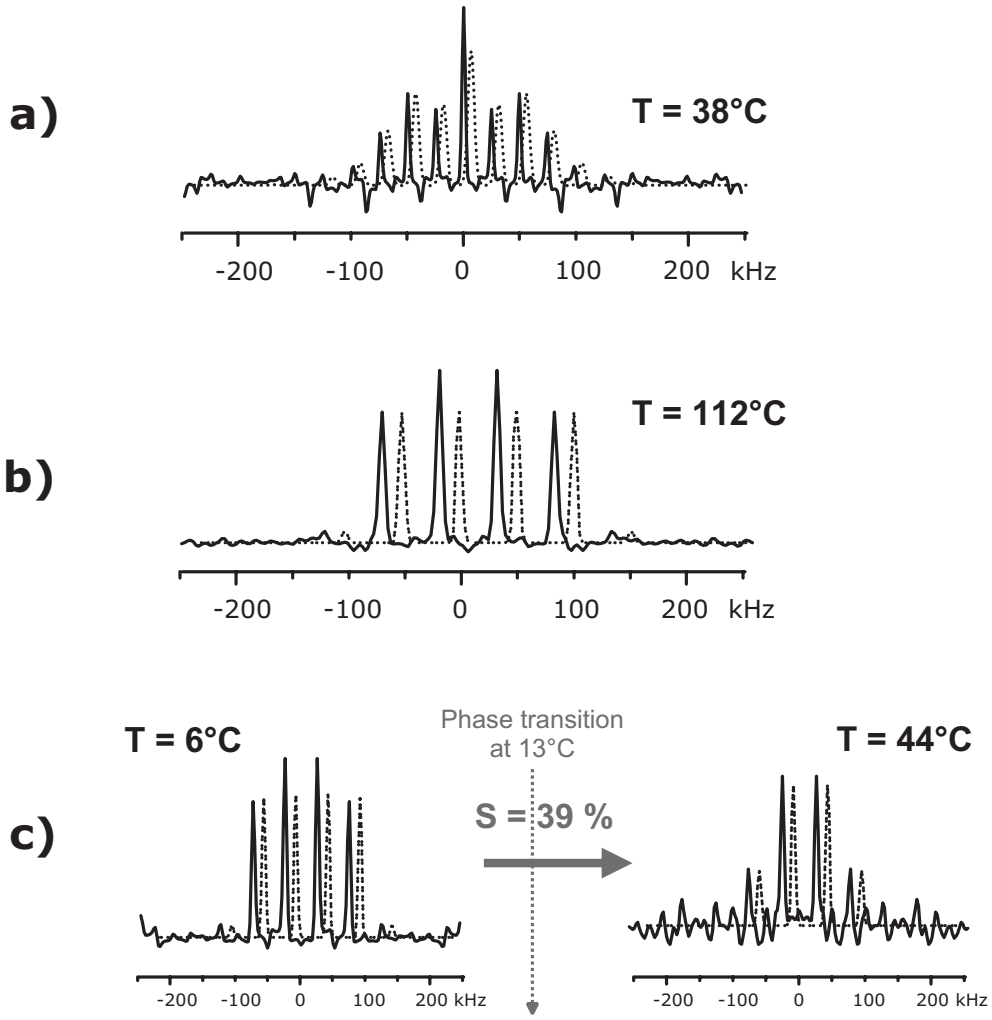

Figure 6.20: *REREDOR SB pattern of the core CH of the HBC dimer* **18** *(a) and REPT-HDOR SB patterns of the HBC dimers* **19** *(b) and* **20** *(c). The dotted lines are the best-fit patterns with the corresponding dipole-dipole coupling constants listed in the text.*

the dipole-dipole coupling constant is strongly reduced to $D_{is}/2\pi$ = (7.5 $\pm$ 1.5) kHz. This corresponds to a reduction to 39% of the rigid dipole-dipole coupling, which clearly indicates the presence of large amplitude core motions in the LC phase of **20**.

6.3.3 Discussion

Summarizing the results of this section, it can be concluded that the properties of the covalently linked HBC-dimers strongly depend on the linker-type. However, the dimer **18** has straight dodecyl sidechains, while **19** and **20** carry branched chains, so that the observed differences in the phase behavior of **18** and **19**/**20** can not solely be attributed to the differences in the linkers alone.
Irrespective of this, the phase behavior of the alkyl-linked dimer **18** can be compared to the corresponding monomer HBC-C_{12} (**5**). The phases formed by **18** were found to be isomorphic to the phases of **5**, only the phase transition temperature is significantly lowered by more than 50 °C in **18** as compared to **5**. Such a behavior is well known from other discotic molecules with long, flexible alkyl spacers [Zamir 97]. Obviously, the flexible spacers are long enough to allow for large amplitude motions of the aromatic cores, which is a prerequisite for the formation of a columnar mesophase. Also, they seem to introduce a significant amount of disorder, which leads to the significant decrease of the melting temperature.
The behavior of the amide- and ester-linked dimers **19** and **20** can be compared to the corresponding unfunctionalized monomer HBC-$C_{8,2}^{rac}$ (**10**) with identical sidechains. While the ester-dimer **20** melts at 14 °C, which is more than 60 °C lower than **10**, the amide-dimer **19** melts above 200 °C and fast core motion is suppressed up to at least 112 °C. This difference is somewhat surprising, since the spacer lengths of **19** and **20** are identical. A possible explanation might be 'secondary' interactions of the amide groups, which are capable of forming hydrogen bonds with the amide groups of the neighboring dimers and, thus, stabilize the rigid structure.

At this point it is instructive to compare these results to the results of the non-covalently linked HBC-dimers as formed by the HBC-acids discussed in section 6.1. For this purpose, the respective phase transition temperatures, solid-state packing arrangements and dynamical parameters are listed in table 6.1. For the HBC-acids, it was found that the phase behavior strongly depends on the length of the 'spacer' which is formed by hydrogen bonding of the carboxylic acid groups. While for HBC-C_{10}COOH with its long spacers, a phase behavior analogous to the corresponding monomer was found, the short C3-chain acids **13** and **15** exhibit a behavior analogously to the amide-dimer **19** (i.e. suppression of the formation of a liquid crystalline phase at least up to 200 °C). Since **13**, **15** and **19** have an identical 'spacer' length (nine atoms), the phase behavior of the amide-dimer supports the hypothesis that the spacer length governs the phase behavior. However, the results obtained for the ester dimer,

Table 6.1: *Comparison of phase transition temperatures, solid state packing and molecular dynamics of the covalently and non-covalently bonded HBC dimers and the respective unfunctionalized parent materials (K = crystalline phase, X = solid phase, Col_{ho} = ordered hexagonal columnar mesophase, I = isotropization).*

Compound		Transition	T(°C)	'herring-bone' packing	D_{is} of core CH [kHz] (at T)	S [%]	column rotation ($S_{col.rot.}$ [%])
HBC-$C_{8,2}^{rac}$	**10**	K → Col_{ho}	81	yes	21.7 ± 0.6 (38 °C)		
		Col_{ho} → I	420		8.6 ± 0.3 (105 °C)	40	yes (79)
HBC-C_3COOH	**13**	X → Col_{ho}	221	no	20.4 ± 0.5 (40 °C)		
					17.6 ± 0.5 (102°C)	86	no
HBC-C_{10}COOH	**14**	K → Col_{ho}	70	yes	22.0 ± 0.5 (40 °C)		
					8.6 ± 0.5 (93 °C)	39	yes (78)
Amide-Dimer	**19**	X → Col	220	no	19.1 ± 0.5 (112 °C)	–	no
Ester-Dimer	**20**	X → Col	14	potentially	19.1 ± 1.0 (6 °C)		
					7.5 ± 1.5 (44 °C)	39	yes (78)
HBC-C_{12}[a]	**5**	K_1 → K_2	42	yes	20.9 ± 0.5 (35 °C)		
		K_2 → Col_{ho}	107		8.2 ± 0.9 (120 °C)	39	yes (78)
Alkyl-Dimer	**18**	K → Col_{ho}	53	yes	19.0 ± 1.0 (38°C)		

[a] Data were taken from [Saalwächter 00].

which also has a spacer length of nine atoms, but forms a columnar mesophase already at 14 °C, show that this simple view is too simple. Of course, one can attribute the differences between ester and amide linked dimer by additional hydrogen bonding via the amide protons. However, this naturally does not account for the difference between the ester-linked dimer and the C_3-acids. Hence, another explanation for the pronounced differences in the phase behavior of these dimers with *identical* spacer length seems more feasible, which is based on considering the rigidity of the linkage. It is well known that an amide group is much more rigid and confined to a planar structure than an ester group. An acid dimer (as present in the HBC-acids) is even more rigid and confined to a planar geometry. The length of the spacer chains (nine atoms) fits exactly the intercolumnar distance. Hence, intercolumnar linkages can be formed, which, once formed, restrict large amplitude motions of the cores. This situation is already known to prevent mesophase formation, if only *inter*columnar linkages are considered [Boden 99a]. However, there is still the possibility of the formation of *intra*columnar linkages, which require shorter, but flexible spacers. Clearly, the amide- and acid-functionalized linkage is much less flexible than the ester linkage. Hence, *intra*columnar linkages might very well be present in the case of the ester linkage, which naturally do not suppress a mesophase formation. In the case of the amide and the acid dimer linkage, such *intra*columnar linkages appear to be much more strained and, thus, are presumably not formed, which in turn prevents the formation of a mesophase.

A point not mentioned yet is that the structures observed for the covalently linked dimers most probably do not represent the most stable structures from a thermodynamical point of view, since these materials could not be annealed by thermal treatment (which would require sufficiently low melting temperatures). Hence, it might very well be that the encountered differences are predetermined by the way the materials crystallize from solution. Potentially, the ester-dimer is already present in a folded state in solution (i.e. the two aromatic discs of the dimer are lying on top of each other), which is kept during precipitation, whereas the amide dimer is present in a 'stretched' conformation with the aromatic planes of the same molecule being well-separated. The precipitated structures are essentially non-covalent 3D networks, which cannot be broken by thermal treatment. The non-covalent nature (hydrogen bonding) of the network formed by HBC-C_3COOH makes self-healing processes of the network possible. This is reflected by the fact that the X-ray patterns of HBC-C_3COOH exhibit sharper reflections (i.e. the packing is better defined) than the X-ray patterns of the amide-dimer **19**.

Concluding this section it can be said that the phase behavior in covalently and non-covalently bonded HBC dimers depends not only on the length but also on the functionalization and rigidity of the spacer connecting the two HBC discs.

Chapter 7

Structure and Dynamics of Discotic Mesogens with Potential Electron Carrier Properties

Most of the discotic mesogens reported so far are better hole carriers than electron carriers [Eichhorn 00]. However, for potential device applications also electron carriers are needed. To date, only few examples of electron carrier discotic mesogens exist [Boden 94, Struijk 00, Craats 00, Boden 01]. Hexaazatrinaphthylenes (HATNA) have six nitrogen atoms in the aromatic core [Kestemont 01]. This is anticipated to significantly increase the first reduction potential and, thus, to facilitate electron injection and reduce the tendency of charge trapping [Uckert 00]. In the literature, four derivatives with thioether sidechains of different lengths have been reported, ranging from hexyl- to dodecyl-sidechains [Kestemont 01]. The investigations presented in this chapter are restricted to the dodecyl-substituted material HATNA-SC_{12} (**21** in Fig. 7.1), which has the simplest phase behavior- as determined by DSC- and the lowest transition temperature to the LC phase. The material was synthesized and provided by the group of Prof. Y. Geerts (ULB Bruxelles). The first section summarizes results from previous DSC and X-ray investigations [Lehmann 03], while thereafter the results from the solid-state NMR investigations will be presented.

7.1 DSC and X-ray

The DSC curves of **21** of subsequent heating and cooling scans are depicted in Fig. 7.2. In the first heating curve, a large endothermic peak is observed, which arises from the melting of the Cr_0 phase at 90 °C. In subsequent scans a single transition with a comparably smaller transition enthalpy is observed close to 100 °C. Above the melting temperature, only one LC

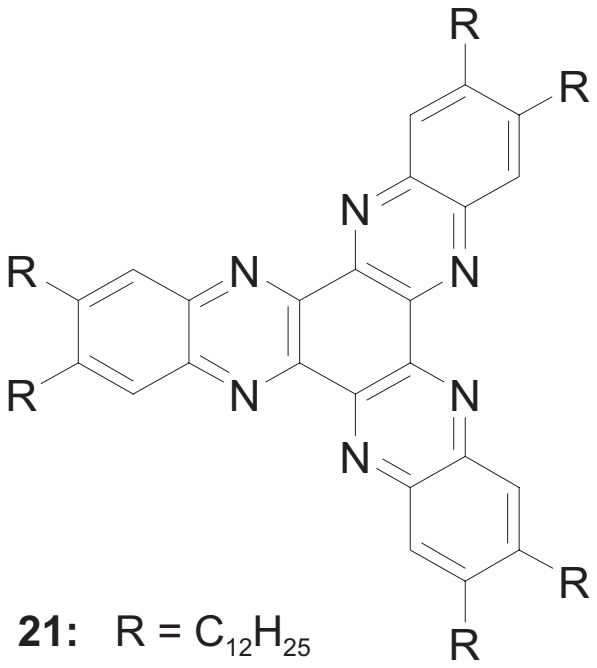

Figure 7.1: *Chemical structure of HATNA-SC*$_{12}$ *(***21***).*

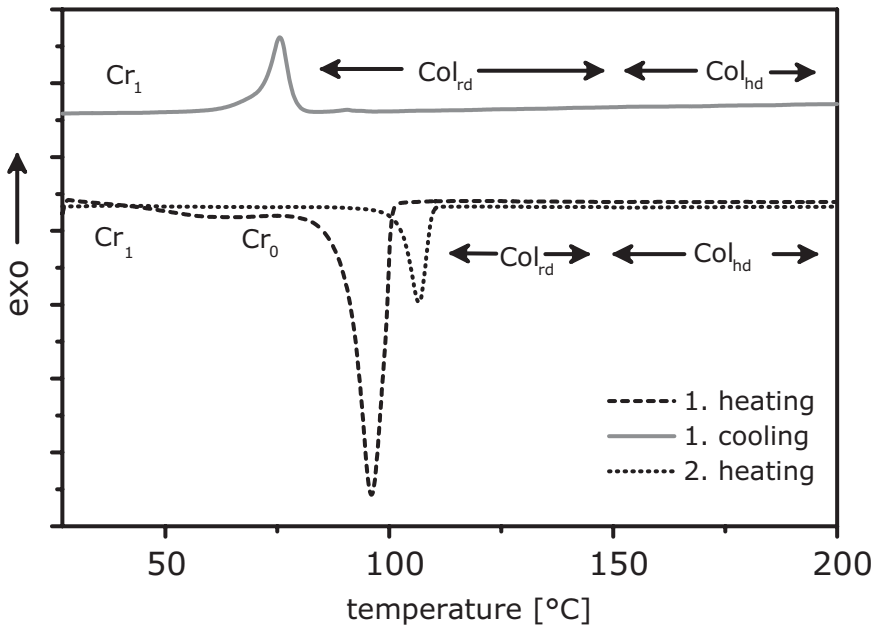

Figure 7.2: *DSC traces of* **21**.

Table 7.1: *Thermotropic behavior of* **21**.

DSC trace	Phase transitions, transition temperature (onset) [°C]/ transition enthalpy $[\frac{kJ}{mol}]$ [a]
1. heating	Cr_0 90/134 Col_{rd} 149/- Col_{hd}
1. cooling	Col_{hd} 147/- Col_{rd} 79/-32.4 Cr_1
2. heating	Cr_1 99/31.7 Col_{rd} 149/- Col_{hd}

[a] the transition to the hexagonal columnar phase has only been observed by means of X-ray diffraction.

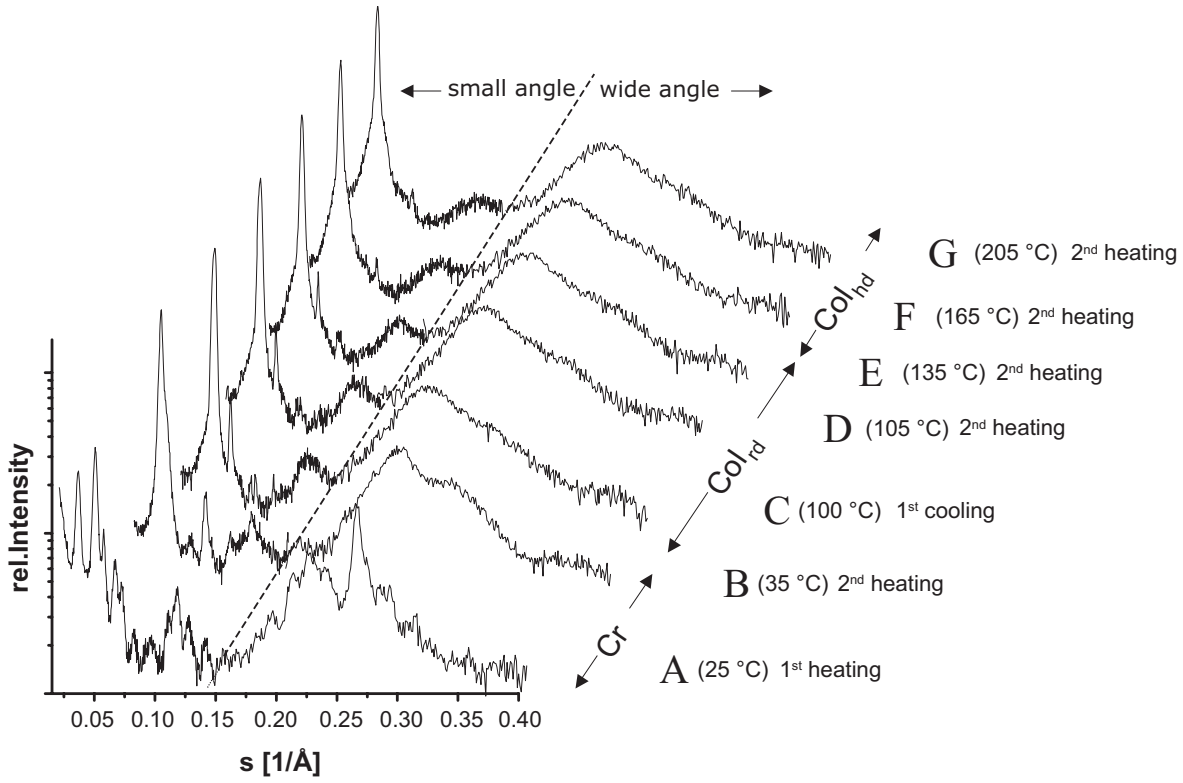

Figure 7.3: *Temperature dependent powder X-ray patterns of* **21**. *The X-ray diffractograms have been measured with the synchrotron facilities in Hamburg and will be published in [Lehmann 03].*

phase is identified by DSC. However, temperature dependent X-ray powder diffraction revealed that a second phase is formed above 149 °C (see below). The transition temperatures and enthalpies are summarized in table 7.1.

Fig. 7.3 shows temperature dependent powder patterns of **21**. The first X-ray pattern (A) was recorded on an as-synthesized sample before the first heating at room temperature (RT). The material is clearly in a crystalline phase. Indexing of the reflexes turned out to be quite ambiguous and is therefore not presented here. The second pattern (B) was also recorded in the

low temperature phase, but *after* the first heating cycle. Evidently, the irreversible behavior observed in DSC is reflected in the X-ray diffractograms, since the original structure could not be recovered by cooling. The absence of a sharp signal at wide angles provides evidence that a regular π-stacking is not present in this phase.
The patterns (C-G) in Fig. 7.3 were measured above the melting transitions at 99°C. The absence of mixed reflections hkl was taken as an indication for the disappearance of the positional long-range order (as is present in the Cr_0 phase) and, consequently, for the formation of a liquid crystal phase. In the wide-angle region, only a broad halo arising from the alkyl chains is observed. The small angle regions exhibit considerable changes upon increasing the temperature. The detailed analysis lead to the assignment of two liquid crystalline phases with the higher temperature LC phase formed at above 149 °C. The lower temperature LC phase could be assigned to a Col_{rd} phase with a non-centered rectangular unit cell (a = 46.6$\mathring{A}$, b = 27.6 $\mathring{A}$) as depicted in Fig. 7.4. At 149 °C, the 210 reflection which determines the rectangular symmetry of the two-dimensional lattice vanishes and only two reflections whose reciprocal spacings follow the ratio $1 : \sqrt{3}$ persist. Thus, above this temperature the columnar mesophase is hexagonal (Col_{hd}).
In order to gain more information about the mesophase structure, 2D X-ray studies on extruded filaments have been carried out, the details of which are described in [Lehmann 03]. In the Col_{rd} phase at 135 °C a disordered stacking of mesogens along columns with a spacing of 8.7 $\mathring{A}$ was observed. Such a large intra-columnar distance could only be explained if the next neighbors in the column cannot be transformed into each other by a simple translation along the column axis. Also, a tilt of approximately 23° with respect to the columnar axis was detected. Based on these observations, two possible stacking arrangements were proposed, which are schematically depicted in Fig. 7.4. In order to account for the large spacing (i.e. a periodicity of two molecules along the columnar axis), neighboring mesogens must either be translationally displaced, as depicted in I, or they must be rotationally displaced (staggered), as illustrated in II. Of course, the two schematic drawings comprise only extreme cases and, most probably, a combination of both is present in the mobile LC phase. In contrast, at 170 °C in the Col_{hd} phase the 2D X-ray pattern was assigned to a non-tilted arrangement of the discs within the columns.

7.2 ^{1}H Spectra

^{1}H MAS experiments were carried out in order to obtain additional information on the packing and the dynamics in the various phases. In Fig. 7.5 temperature dependent ^{1}H MAS spectra are shown, which were recorded by heating the as-synthesized sample. Up to the phase transition temperature, the spectra do not change significantly. The phase transition at 90 °C comes along with a pronounced line narrowing. The LC phase spectra are much better resolved with comparably narrow peaks, which indicate rapid motional processes. In the aromatic region,

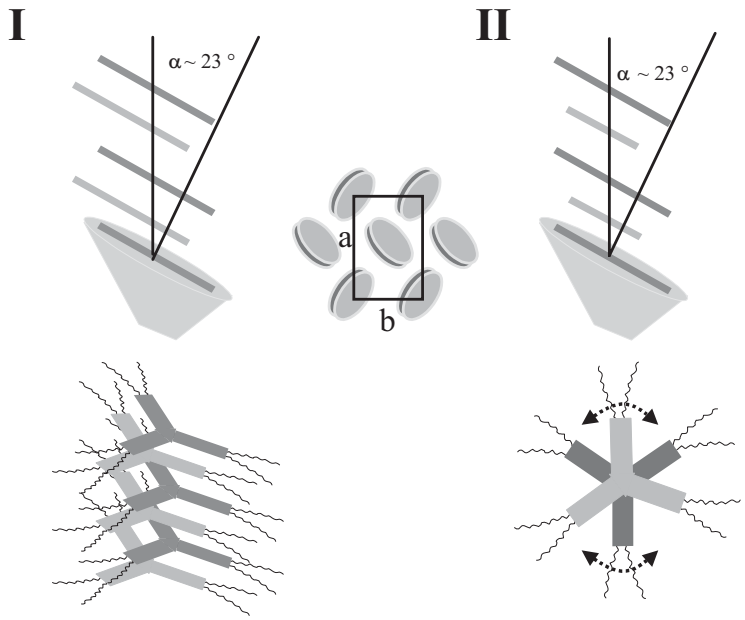

Figure 7.4: *Possible stacking of discotic HATNA mesogens along a column in the rectangular columnar mesophase. The mesogens could be translationally displaced (I) or rotationally displaced (II).*

a single peak at 6.4 ppm is observed, which corresponds to a shift by more than 1.5 ppm as compared to the chemical shift of 8.2 ppm in solution (250 MHz, $CDCl_3$, 30 °C). Therefore, the aromatic protons still experience strong additional shifts in the LC phase due to the aromatic ring currents of neighboring molecules. Since in the X-ray diffractograms a strong difference between an as-synthesized and a thermally annealed (i.e. previously heated to the LC phase) sample was observed, ^{1}H spectra were recorded in both the Cr_0 phase (i.e. of the as-synthesized sample) and the Cr_1 phase (i.e. of the annealed sample). The ^{1}H spectra in both Cr phases are dominated by the broad peak of the alkyl protons. In order to better resolve the aromatic region, the alkyl peak was suppressed by a PFG-assisted WATERGATE peak suppression scheme, the details of which are described in appendix D.2. The spectra with and without WATERGATE peak suppression are compared in Fig. 7.6. In the spectra with WATERGATE, a well-resolved aromatic peak is present at around 7 ppm, which has a slight shoulder at around 8 ppm. Comparing the spectra of the as-synthesized and the annealed sample without WATERGATE peak suppression, it becomes obvious that the alkyl peak is much smaller in the case of the annealed sample, as is indicated in Fig. 7.6 by the grey lines which denote the full-width at half maximum. Obviously, in the annealed sample the sidechains are considerably more mobile leading to the narrower peak. This observation might also account for the high transition enthalpy in the first DSC scan, which is significantly smaller in subsequent scans. In the first scan, more energy might be needed for the melting of the more rigid alkyl chains than in subsequent scans.

^{1}H -^{1}H double-quantum (DQ) spectra were recorded to unravel neighborhood-relations be-

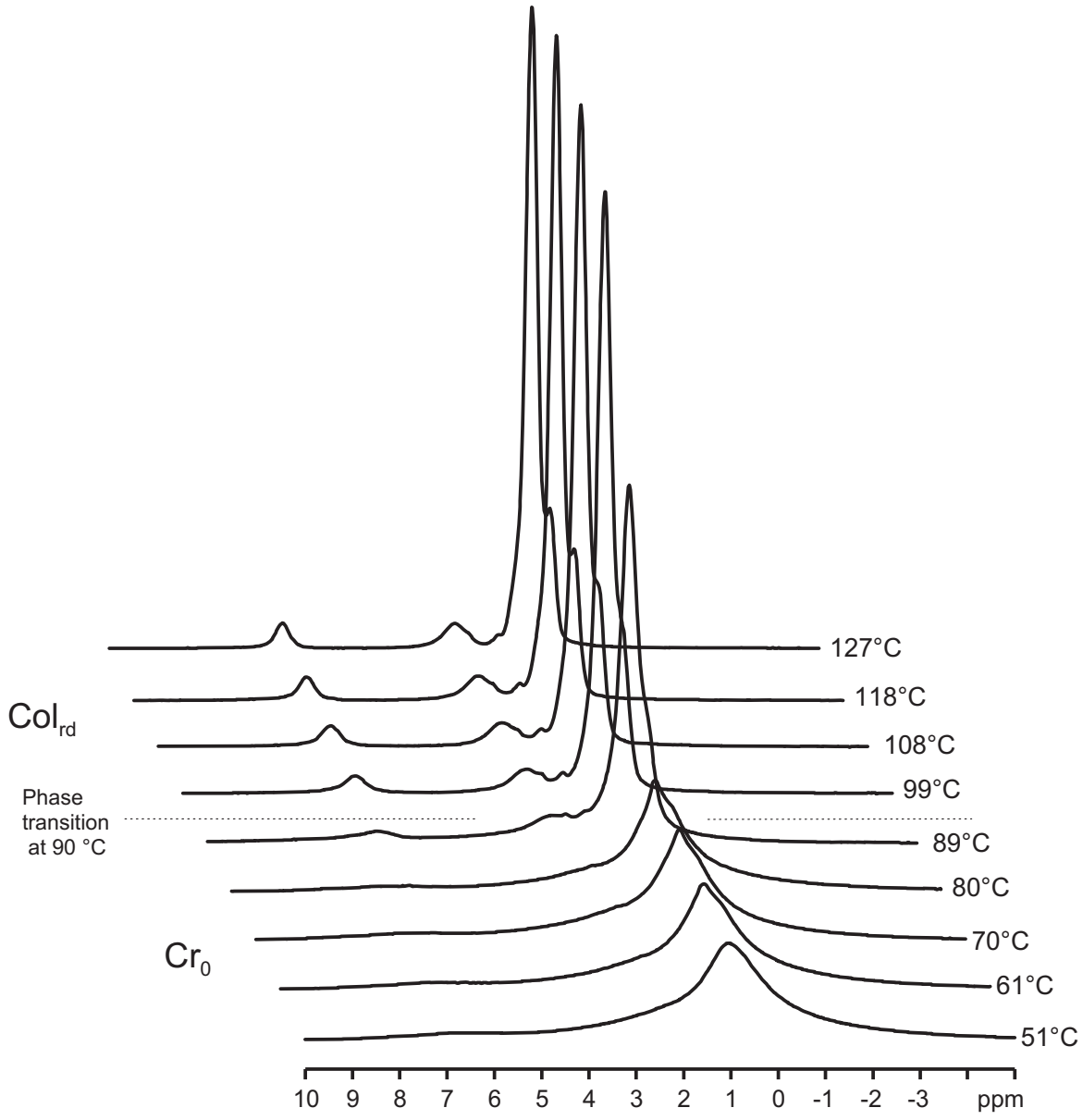

Figure 7.5: *Temperature dependent ^1H spectra of* **21** *at 30 kHz MAS, measured on heating the as-synthesized sample.*

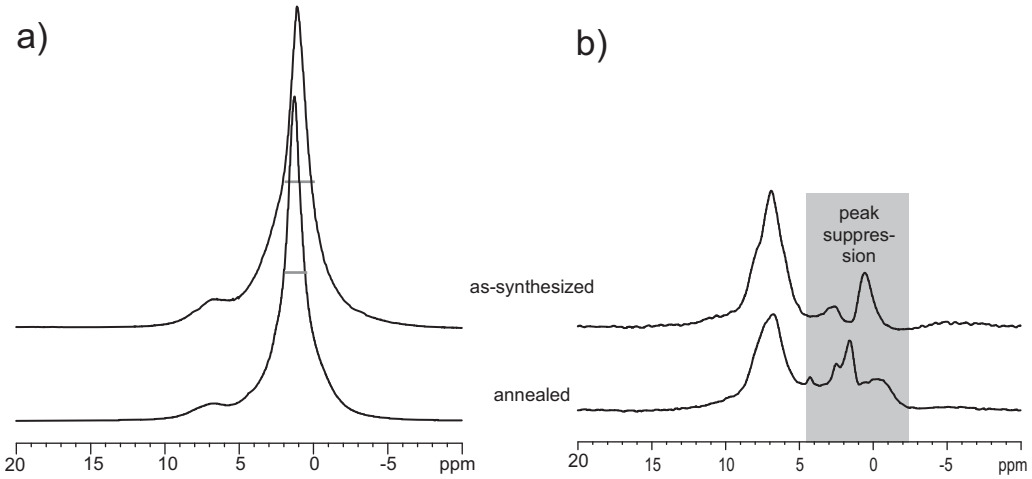

Figure 7.6: *^1H spectra of* **21** *at 30 kHz MAS and T = 48 °C of the as-synthesized sample (top) and a sample, which was previously heated to the LC phase. In (b) the corresponding spectra using WATERGATE suppression of the strong aliphatic peak are shown. The grey shaded area in (b) is where the peak suppression was applied. The 'peaks' in this area are artifacts from the suppression.*

tween protons. The crystal phase spectra were measured at 48 °C and are shown in Fig. 7.7 a for the as-synthesized sample and in Fig. 7.7 b for the annealed sample. Comparing these two spectra, it is obvious that the spectrum of the annealed sample suffers much more from severe phase distortions of the alkyl peak. These phase distortions are indicative for considerable sidechain mobility, which leads to the loss of coherence during the course of the experiment and, thereby, also to the loss of phase information. Hence, the ^{1}H -^{1}H DQ spectra confirm the finding that the sidechains in the annealed sample are more mobile. In order to resolve the peak pattern of the aromatic protons better, the spectrum of the annealed sample was measured with WATERGATE peak suppression (shown in Fig. 7.7c). In the following, the spectra in Fig. 7.7 a and c are compared. Clearly, the peak pattern in the aromatic region is identical in both spectra. As expected, cross-peaks between the aromatic protons and the SCH_2 protons are observed at (7.0 ppm, 9.7 ppm) and (2.7 ppm, 9.7 ppm)[1] (marked in green), which indicate a dipole-dipole couplings between the aromatic protons and the SCH_2 protons. Interestingly, also a diagonal peak of the aromatic protons (marked blue) at around (7 ppm, 14 ppm) is present. This indicates sufficiently strong dipole-dipole coupling between the aromatic protons, i.e. a sufficiently close proximity between two aromatic protons. Looking at the molecular structure (depicted on the lower left of Fig. 7.7), this observation is surprising, because the closest distance between aromatic protons within one molecule is about 5 $\mathring{A}$, which should not lead to an observable diagonal peak under these experimental conditions. The presence of a DQ coherence between two aromatic protons is therefore possibly due to a

[1]The second cross-peak is not present in the spectrum of Fig. 7.7 c, because the WATERGATE peak suppression scheme was applied before detection and, hence, suppresses all signal which is located in the single-quantum dimension at or close to the position of the suppressed peak.

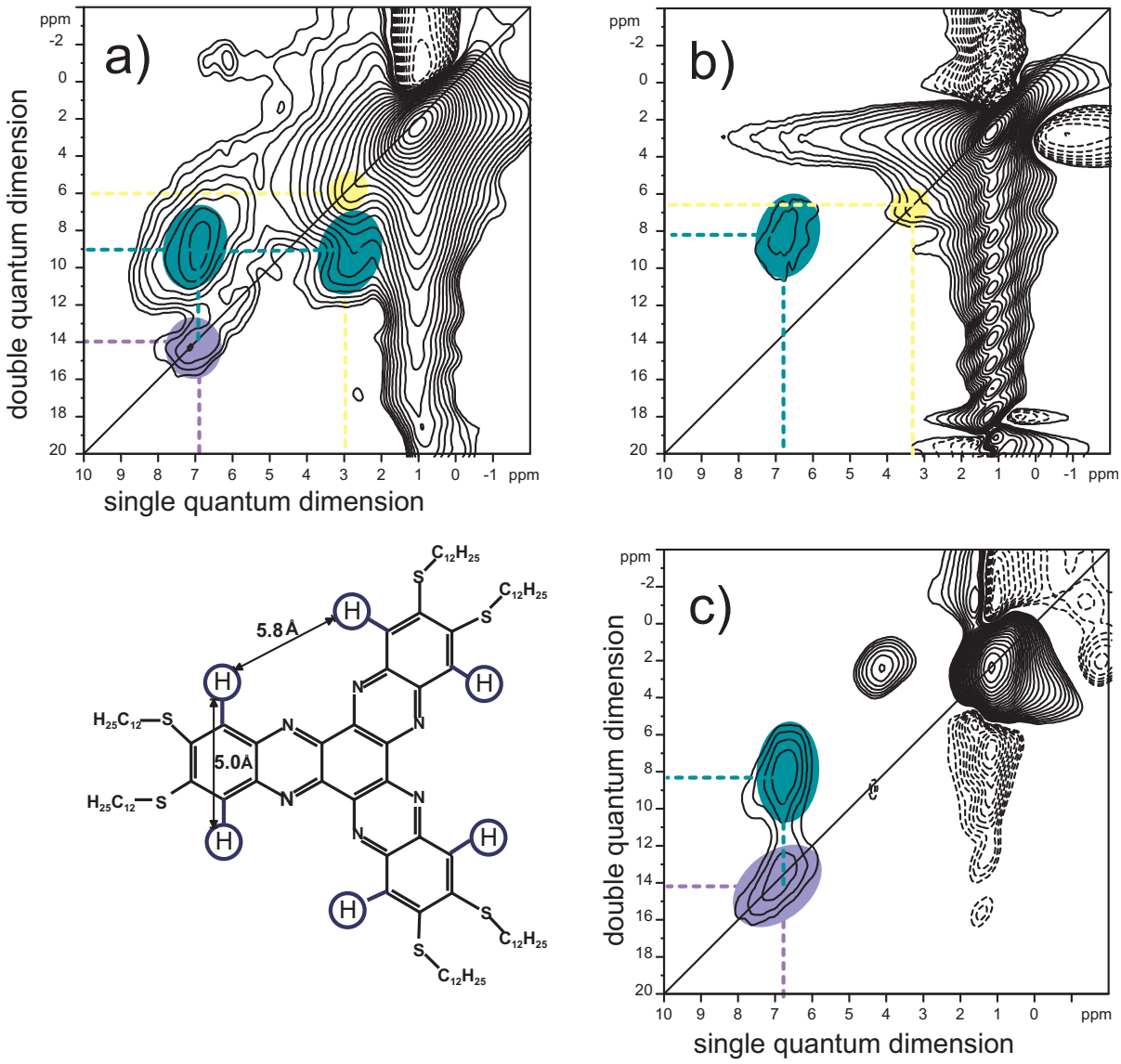

Figure 7.7: ^{1}H -^{1}H *DQ spectra of* **21** *at 30 kHz MAS, 48 °C and* $\tau_{exc} = 4\tau_R$. *In (a) the spectrum of the as-synthesized sample is shown. (b) and (c) are spectra of a thermally annealed sample. Clearly, spectrum (b) suffers from strong phase distortions arising from the dominating alkyl peak. Hence, spectrum (b) was re-measured utilizing WATERGATE peak suppression of the alkyl peak. This WATERGATE spectrum is shown in (c). In both (a) and (c) a diagonal peak at (7 ppm, 14 ppm) (marked in blue) is observed, which indicates a coherence arising from the coupling of two aromatic protons.*

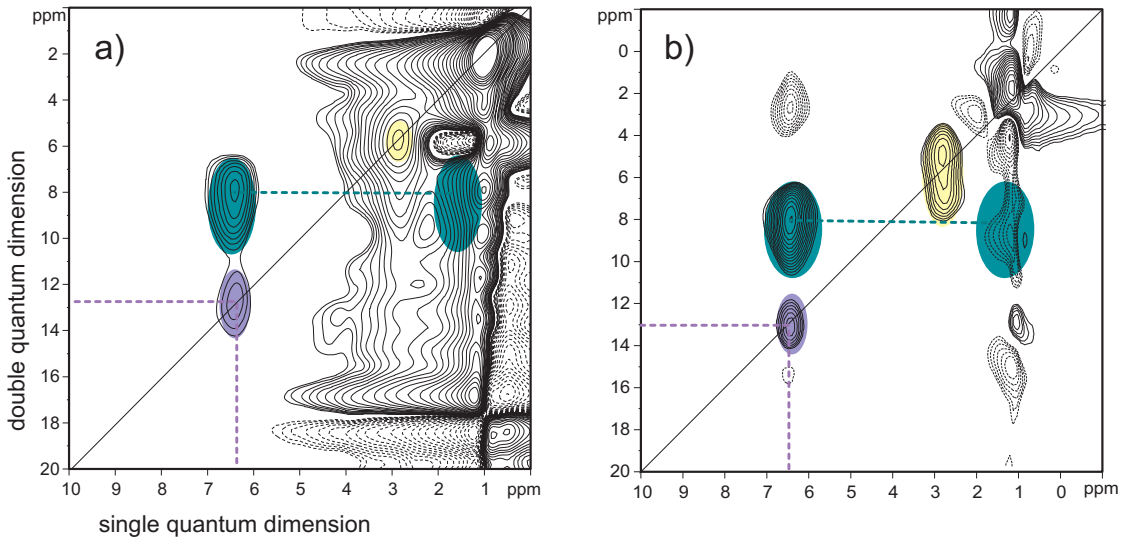

Figure 7.8: *^1H -^1H DQ spectra of* **21** *in its Col_{rd} phase at around 110 °C and 30 kHz MAS. Spectrum (a) was measured with an excitation time of four rotor periods. Since in (a) also strong phase distortions are present, spectrum (b) was recorded utilizing WATERGATE peak suppression of the alkyl peak and a longer excitation time of 8 rotor periods.*

coupling between aromatic protons from different molecules, which must be closer than 5 $\mathring{A}$ in the solid-state packing. Of course, it was tried to quantify the dipole-dipole coupling strength (and thereof the distance between the coupled protons) by acquiring ^{1}H -^{1}H spinning sideband patterns with the BABA experiment. Unfortunately, even with excitation times as long as 1.3 ms no sidebands of orders higher than one could be generated. Hence, the observed coupling is either very small (below 500 Hz i.e. the distance between the dipolar coupled nuclei is above 6$\mathring{A}$) or a relaxation process prevents the generation of higher order sidebands. It should be noted that the signal intensity of the aromatic diagonal peak is much smaller than the signal intensity of the cross-peaks between the aromatic and the aliphatic protons. Hence, the observed dipole-dipole coupling between aromatic protons is definitely very weak and maybe even intermolecular.

Since in the LC phase the aromatic cores undergo fast motional processes (see below), the absence of an aromatic diagonal peak in the LC phase would prove that the observed dipole-dipole coupling between aromatic protons is intermolecular. Hence, ^{1}H -^{1}H DQ spectra were recorded in the LC phase at around 110 °C both with and without WATERGATE peak suppression, which are depicted in Fig. 7.8. In both spectra, a diagonal peak at at (6.4 ppm, 12.8 ppm) is observed, which indicates the presence of a DQ coherence between aromatic protons in the LC phase. At first sight, this suggests that the observed dipole-dipole coupling between the aromatic protons is intramolecular. However, as mentioned above, due to the long distance to the next proton intramolecular couplings are very weak and should not lead to observable coherence peaks. Hence, the observed peak must arise from intermolecular couplings

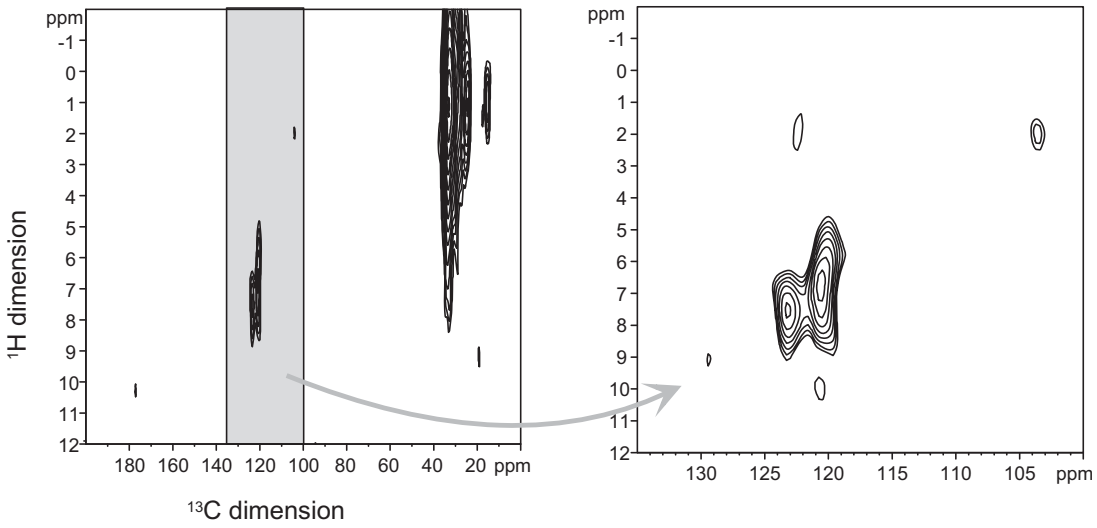

Figure 7.9: *^{1}H -^{13}C correlation spectrum (REPT-HSQC) of an annealed sample of* **21** *in its Cr$_1$ phase at around 48 °C, 30 kHz MAS and $\tau_{rcpl} = 1\tau_R$.*

even in the LC phase. Of course, a correlated motional process, in which several discs rotate as a whole without their relative positions being changed, would be hypothetically possible. However, this seems to be highly improbable considering the significant amount of mobility and disorder in the LC phase. Alternatively, it might be that the discs undergo up and down reorientations in the LC phase as depicted in Fig. 7.12. During such a motion the aromatic protons of two neighboring molecules might come quite close to each other, even closer than the normal $\pi - \pi$ distance of around 3.5 $\mathring{A}$. Such a close distance naturally would give rise to an observable DQ coherence. The fact, that no sidebands could be generated, would then be indicative for the dynamic average over the various proton-proton distances met during such an up and down motion.

7.3 ^{1}H -^{13}C Correlation Spectra

The aromatic peaks in the ^{1}H -^{1}H spectra of the Cr phases are comparably broad and quite featureless. Hence, in order to check for a characteristic peak pattern (which would be characteristic for the solid-state packing arrangement), heteronuclear ^{1}H -^{13}C correlation spectra were recorded with the REPT-HSQC technique. In Fig. 7.9 the ^{1}H -^{13}C correlation spectrum of an annealed sample of **21** is shown. The recoupling time was chosen short to obtain only peaks for directly bonded ^{1}H -^{13}C pairs. In the aromatic region clearly two correlation peaks (arising from aromatic core CH) can be distinguished, one at (123 ppm, 7.5 ppm) and the other at (120.5 ppm, 6.8 ppm). Thus, in the packing at least two different local environments for the aromatic CH groups must be present. This information alone is unfortunately not enough

to propose a structural model. Future investigations are planned, where a fiber is extruded from the LC phase directly into the NMR rotor. Since the same fiber could also be used for the acquisition of WAXS patterns, the combination of the 2D WAXS data together with the solid-state NMR results might prove fruitful for unravelling the structure in the Cr_1 phase. In contrast, the ^{1}H -^{13}C correlation spectrum of the as-synthesized sample (not shown here) does not feature two such well-defined aromatic correlation peaks. This might be attributed to the fact that when precipitating from solution the (partial) crystallization of the alkyl chains governs the packing. Since the packing of the alkyl chains is well-known to be incommensurable to the packing of the aromatic cores in discotic liquid crystals [deGennes 83], the (partial) crystallization of the alkyl chains might hinder an optimal packing of the aromatic cores.
In contrast, when cooling from the LC phases, the alykl chains do not crystallize properly and the aromatic cores might be governing the stacking and, thus, a better ordered core stacking would be observed, which might account for the two distinct environments for the aromatic protons in the packing.

7.4 Dynamics in the Crystal Phase Cr_1

Fast molecular dynamics of both the aromatic core and the sidechains are conveniently probed by measuring ^{1}H -^{13}C dipole-dipole coupling constants with the REREDOR technique. Hereby, reduced (as compared to the rigid value, which is around 21 kHz for a directly bonded C-H spin pair) dipole-dipole coupling constants are indicative for motion with correlation times on or below the μs timescale. In Fig. 7.10 the results for an annealed sample are displayed: In (a) the first slice of the two-dimensional data set (t_1 = 0) is shown together with the assignment of the observed ^{13}C resonances. The sideband (SB) patterns corresponding to the various resonances are shown in (b). The patterns of the aromatic resonances correspond to dipole-dipole coupling constants of $D_{is}/2\pi$ = 22 $\pm$ 1 kHz. Hence, the aromatic cores are rigid on the μs timescale. In contrast, the SB patterns of the sidechain CH_2 groups yield significantly reduced dipole-dipole coupling constants, which are listed in the figure. Assuming a rigid coupling of $D_{is}^{rigid}/2\pi$ = 21 kHz, reduction factors can be calculated according to $S = \frac{D_{is}^{observed}}{D_{is}^{rigid}}$. The reduction factors S (also listed in the figure) decrease with the distance from the aromatic core. Hence, the mobility increases with the distance from the aromatic core. Such a mobility gradient along the chain is a typical phenomenon in discotic liquid crystals and was also observed for the HBC derivatives discussed in chapter 5.
Of course, the absence of any fast core motion does not exclude slow motional processes on the s to ms timescale. Such slow reorientation processes were, for example, observed in HBC-PhC_{12} [Fischbach 02]. Slow dynamics was tested for with the CODEX experiment [deAzevedo 99, deAzevedo 00], a one-dimensional exchange experiment under MAS, where a signal decay occurring on increasing a mixing time is indicative for slow exchange processes. Spectra were recorded at around 50 °C and at around 70 °C (spectra not shown here).

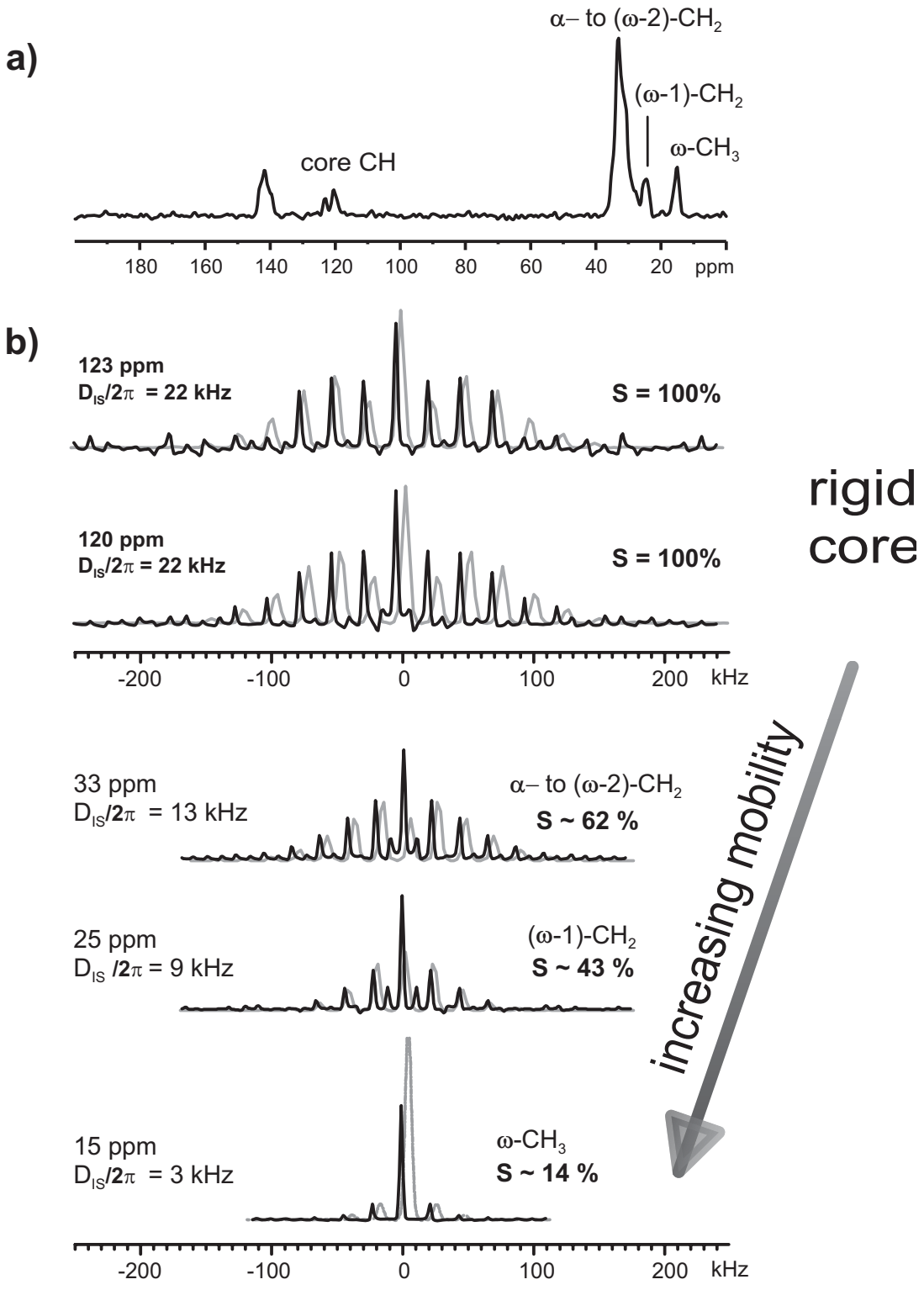

Figure 7.10: *REREDOR of an annealed sample of* **21** *in its Cr_1 phase measured at 25 kHz MAS and $\tau_{rcpl} = 2\tau_R$. In (a), the first slice (t_1 = 0) is shown together with the corresponding peak assignment. In (b), the extracted SB patterns of the various resonances are shown in black together with the best fit (by eye) patterns (underlying patterns in grey).*

Since no signal decay could be detected on increasing the mixing time from 50 ms to 1s, large-amplitude motion of the aromatic cores on this timescale can be excluded.

7.5 LC Phase Dynamics as Probed by Deuteron NMR

To obtain quantitative information on the mobility in the liquid crystalline phases by ^{13}C detected NMR experiments turned out to be difficult, since adverse relaxation behavior lead to complete signal loss of the core CH resonance in the ^{13}C detected LC phase spectra. Even though this observation indicates core motions, a quantitative analysis (i.e. the determination of a dynamical order parameter) of the core motion was naturally not possible.
Hence, to obtain the desired order parameter, the material was selectively enriched with deuterium at the core CH position for ^{2}H NMR experiments. A line shape analysis of ^{2}H solid echo spectra [Spiess 81] is an established method to probe molecular dynamics in discotic liquid crystals [Herwig 96, Leisen 92]. In Fig. 7.11, solid echo spectra of the core deuterated compound are shown. In the crystal phase, rigid PAKE-patterns [Pake 48] are measured with a quadrupole splitting of $\delta_Q/2\pi$ = 130 kHz. Interestingly, the signal-intensity in the middle of the patterns is significantly higher than in the simulated spectra. Since this effect becomes more pronounced at higher temperatures, it might be due to some moieties in the sample, which undergo ill-defined intermediate motions, which superimposes a broad gaussian-type pattern (as it is solely observed in the spectrum at 120 °C) on the spectrum. However, the excess signal intensity in the middle of the patterns might as well be due to experimental artifacts. If the acquisition does not start precisely at the echo maximum, such additional intensity can arise. In all spectra at higher temperatures (above 90 °C) an additional isotropic signal of varying intensity at ω_0 is present. This phenomenon is well-known from liquid crystalline systems with deuterated dopants [Emsley 85, Kranig 90]. There, the isotropic signal arises from molecules outside the columns, which can undergo isotropic motions. Obviously, parts of the sample form smaller assemblies with less order and higher mobilities. Especially at the domain boundaries one can easily envisage smaller amounts of less ordered material. Above the phase transition to the Col$_{rd}$ phase, a broad gaussian shaped spectrum is observed, which is indicative for ill-defined motions (i.e. no defined reorientation angle) on the intermediate timescale (as indicated by the severely reduced signal intensity). Notably, the loss of the characteristic horns indicates that the molecular process must lead to a motionally averaged quadrupole tensor with a high $\bar{\eta}$.
After heating above 149 °C into the Col$_{hd}$ phase, a well-defined motionally reduced pattern is observed, which corresponds to a quadrupole splitting of $\delta_Q/2\pi$ = 25 kHz. In a hexagonal discotic phase with a non-tilted disc arrangement, the most prominent motional process is the rotation about the column axis [Emsley 85]. Such a well-defined motionally reduced pattern is only obtained if the motionally averaged asymmetry parameter is $\bar{\eta}$=0. Since the column rotation renders $\bar{\eta}$=0, it can be concluded that in the Col$_{hd}$ phase a fast rotation around the

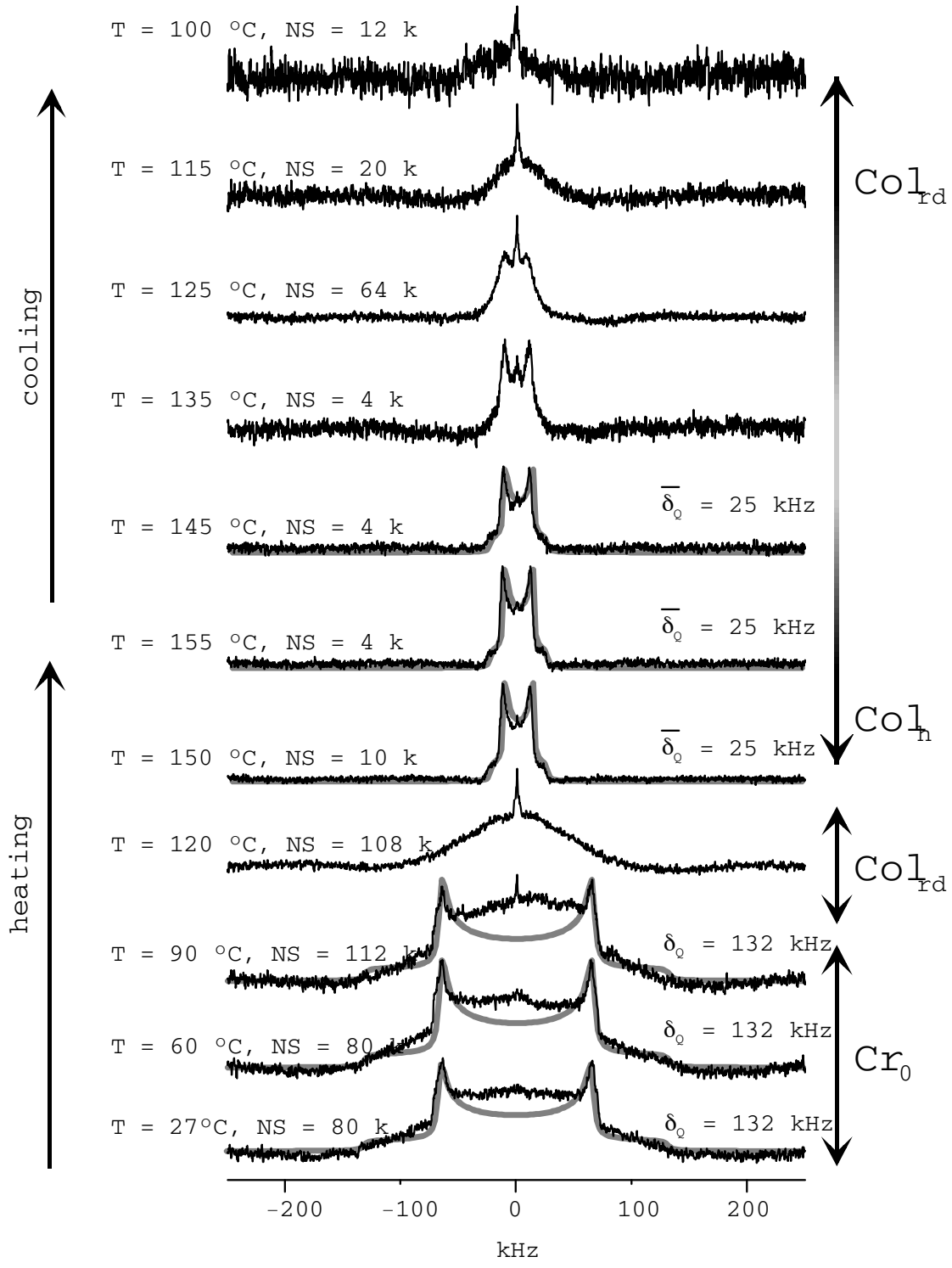

Figure 7.11: *^{2}H solid echo spectra of a core deuterated sample of* **21**. *The underlying grey patterns were calculated with the WEBLAB program package [Macho 01] using the quadrupole splittings indicated on the right. Note that the spectra were acquired with different numbers of scans (NS), which are indicated in the figure (1 k = 1024).*

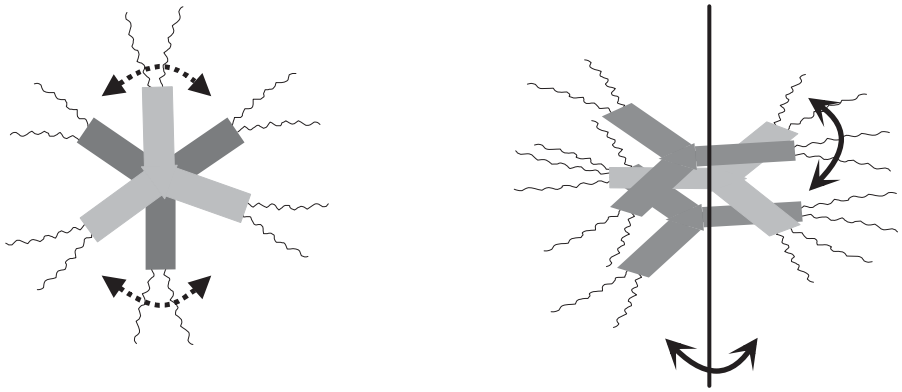

Figure 7.12: *Possible explanation of the low order parameter observed in the Col$_{hd}$ phase of* **21***: Due to their special shape, the molecules have a lot of space for up and down motions in the column, if they are rotationally displaced.*

columnar axis takes place. This axial rotation leads to a motionally averaged PAKE-pattern which is reduced in width by a factor of two compared with that of a rigid solid. Further reduction indicates limited order, i.e., in particular out-of-plane motions. Hence, an order parameter can be defined (in analogy to the one defined in Eq. (7.1) for the reduction of the heteronuclear dipole-dipole couplings) according to

$$S_{col.rot.} = \frac{2\delta_Q^{LC}}{\delta_Q^{rigid}}\,; \qquad 0 \leq S \leq 1. \tag{7.1}$$

This order parameter is $S_{col.rot.}$ = 1 for a perfect in-plane rotation of the discs. With the rigid splitting of 130 kHz and the reduced quadrupole splitting of 25 kHz observed in the Col$_{hd}$ phase we obtain $S_{col.rot.}$ = 0.38. This is an extremely low order parameter compared to other discotic liquid crystalline materials. For example, the glass-forming (2S,3S)-2-chloro-3-methylpentanoyloxypentakis(pentyloxy)triphenylene [Vallerien 90] has an order parameter of $S_{col.rot.}$ = 0.95. The order parameters observed in the HBC derivatives described in the previous chapters of this thesis were found to vary between $S_{col.rot.}$ = 0.66 and $S_{col.rot.}$ = 0.94. A possible explanation for this very low order parameter is that, due to their special 'three-armed star' shape, the molecules have a lot of space available for up and down motions in the column, if they are packed in a rotationally displaced fashion as depicted in Fig. 7.12. These out-of-plane motions might then lead to the observed low order parameter. Also, the very low order parameter could be due to the presence of the six nitrogen atoms in the core that are partially negatively charged, which might disrupt the columnar order by electrostatic repulsion. The columar arrangement would nonetheless be enforced by the microphase separation of aliphatic and aromatic parts. It should be noted that, in principle, the observed strong reduction of the quadrupole coupling could be explained by a tilt of the molecules with respect

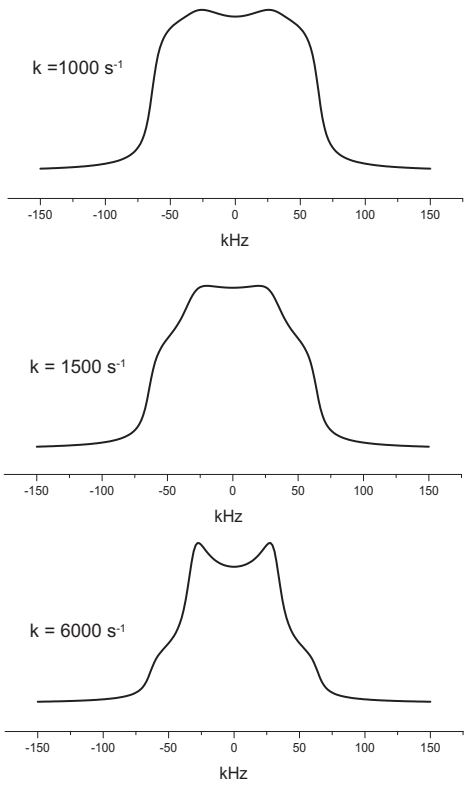

Figure 7.13: *Calculated ^2H spectra for in-plane 120° jumps of the HATNA molecules for different jump rates k. The calculations were carried out with the WEBLAB program (http:\\www.mpip-mainz.mpg.de/weblab40/ [Macho 01]) with the following parameters: cone angle θ=90°, flip angle ϕ=120°, pulse delay 20 μs. The lineshape is Lorentzian with 10 kHz line broadening.*

to the column axis. However, this possibility can safely be excluded from the 2D WAXS investigations.

On cooling the sample, the ^{2}H spectra again become broad and featureless, when entering the Col$_{rd}$ phase, and an unambiguous, detailed analysis of these line shapes is naturally not possible. Notably, the spectra at temperatures right below the phase transition temperature at 147° (as detected in X-ray), still exhibit two broadened horns corresponding to the same splitting of 25 kHz. This indicates that in this temperature range the two LC phases might coexist. Also, it should be noted that dynamics as detected by NMR not necessarily goes along with structural changes as they are detected by X-ray scattering. Since in the fast motional limit a three site jump cannot be distinguished from a free rotation, it seems feasible to test, whether the observed intermediate lineshapes could be explained by simple three site jumps around the C$_3$ symmetry axis of the molecules. In Fig. 7.13 calculated spectra for intermediate jump rates are depicted. Clearly, these spectra do not fully resemble the experimental spectra. Nonethesless, even such a simple motional model leads to a smearing of the characteristic horns. Additional out-of-plane motions might than lead to the complete smearing of

the spectra. The gaussian shape of the experimental spectra in the Col_{rd} phase is certainly due ill-defined motional amplitudes, which fits to the observation of a disordered stacking of the mesogens in the columns from X-ray.

7.6 Conclusions

Summarizing the results of the solid-state NMR investigations on HATNA-SC_{12}, it can be said that the special shape of the HATNA core obviously leads to an increased amount of disorder in the columnar LC phase packing, which is reflected in both the X-ray diffractograms [Lehmann 03] and the dynamical order parameters determined by ^{2}H NMR. In both X-ray and ^{1}H solid-state NMR of the crystal phases, strong differences were observed between an as-synthesized sample and a thermally annealed sample, which was previously heated to the LC phase. The ^{1}H linewidths of the aliphatic peak indicate increased sidechain mobility in the annealed material. Obviously, the material crystallizes in an ordered manner when precipitated from solution during synthesis, but is kinetically trapped in a more disordered arrangement when it crystallizes from the neat LC phase. This observation is also corroborated in the charge carrier mobility measurements carried out with the PR-TRMC (*p*ulse-*r*adiolysis *t*ime-*r*esolved *m*icrowave *c*onductivity) technique [Craats 00], which are shown in Fig. 7.14. During the first heating a significant drop in the charge carrier mobility is observed upon entering the LC phase, which much less pronounced in the cooling trace. Obviously, the charge carrier mobility is higher in more ordered phases. This phenomenon was already observed in HBC-C_{12} (**5**), where the highest charge carrier mobility was measured in the highly ordered crystalline phase [Craats 99].

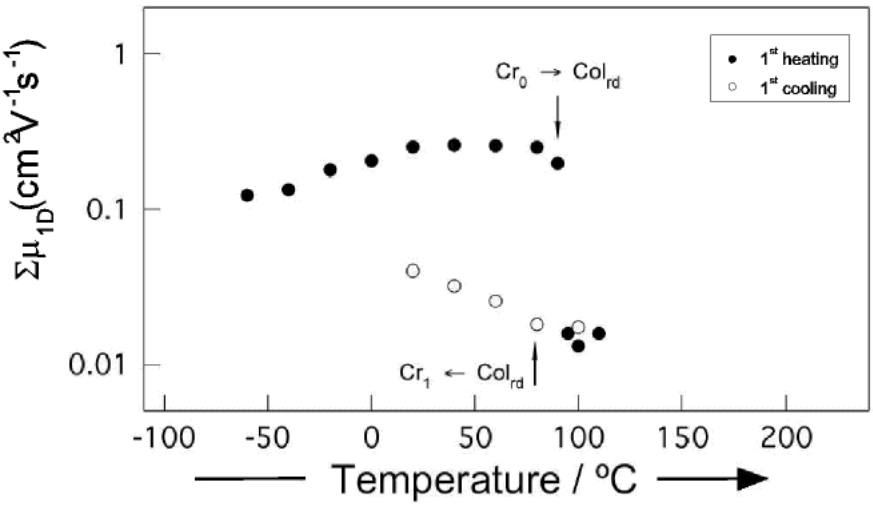

Figure 7.14: *Temperature dependence of the charge carrier mobilities of* **21** *as measured with the PR-TRMC technique [provided by J. Piris, TU Delft, The Netherlands].*

Chapter 8

Conclusions

The topic of this thesis was the investigation of structure, order and dynamics in various discotic mesogens by advanced solid-state NMR as well as the development of recoupling experiments in MAS NMR to tackle these questions. In the past, studies of liquid crystalline systems were traditionally carried out by ^{2}H NMR on selectively deuterated samples [Emsley 85]. However, in systems, as complex as the ones considered here, isotopic enrichment is synthetically demanding and often not feasible. Therefore, the spectroscopic strategy applied here aimed at avoiding the effort of isotopic enrichment by replacing ^{2}H NMR with recoupling techniques involving ^{1}H and ^{13}C NMR under very fast MAS [Schnell 01b, Saalwächter 01b, Saalwächter 02c, Hong 00]. The discotic mesogens predominantely studied in this thesis are hexa-*peri*-hexabenzocoronene (HBC) derivatives which are due to their high one-dimensional charge carrier mobilities of particular interest for potential optoelectronic device applications.

SUPRAMOLECULAR STACKING IN COLUMNAR PHASES

The supramolecular stacking arrangement of the discotic cores was mainly probed by 2D ^{1}H -^{1}H double-quantum (DQ) methods. Since the ^{1}H chemical shift is very sensitive to electron densities of neighboring aromatic groups, it can be used for probing the arrangement of π-electron systems in the vicinity and, in particular, to identify $\pi - \pi$ stacking [Brown 99]. Technically, however, it turned out that in many of the investigated systems the intense NMR signals of the long alkyl sidechains caused severe phase problems which considerably disrupted the weak signals of interest. These problems could be successfully solved by adapting the WATERGATE suppression technique [Sklenar 93] for solid-state NMR, as was described in detail in appendix D.2. The robustness of this technique and the simplicity with which it can be incorporated into existing ^{1}H MAS experiments makes it a valuable tool for ^{1}H solid-state NMR.

In contrast to the ^{1}H chemical shift, the isotropic ^{13}C chemical shift is, effectively, by far not as sensitive to $\pi - \pi$ packing effects. Nonetheless, as shown in **chapter 5**, the princi-

pal values of the ^{13}C chemical shift anisotropy (CSA) were found to exhibit a considerable sensitivity to such packing effects. However, in the past, the determination of the principal values of the ^{13}C CSA either involved isotopic enrichment or particularly involved experiments. As demonstrated in **chapter 5**, with the relatively new SUPER experiment [Liu 02] the ^{13}C CSA values can easily be determined in a site-resolved fashion in natural abundance even in complex supramolecular materials. Moreover, the comparison of experimental and calculated CSA data might in principle be used for the elucidation of the solid-state packing, too. This is of interest for systems whose ^{1}H NMR spectra are not sufficiently resolved or where no protons are present in the chemical structure at the position of interest.

MOLECULAR DYNAMICS AND ORIENTATION

The dynamics of individual molecular segments in the mesogens was probed by MAS sideband patterns that arise from reconversion rotor encoding (RRE) in 2D recoupling experiments. These sideband patterns provide sensitive means to determine dipole-dipole coupling constants and/or chemical-shift anisotropies, which are characteristically reduced by molecular motion occuring at rates $> 10^3 s^{-1}$. In **chapter 4** it was demonstrated that these sideband patterns can also be strongly affected by sample orientation. Under MAS it is possible to recouple either the ω_R- or the $2\omega_R$-modulated terms of an interaction Hamiltonian, both of which exhibit different orientation dependencies [Glaubitz 01]. The two types of recoupling experiments provide complementary information on orientation effects and, in principle, make it possible to distinguish effects of motion and orientation. Studying such effects by NMR is particularly interesting for materials which can easily be aligned, such as discotic liquid crystals. For a macroscopically aligned material, HBC-PhC_{12}, an orientational order parameter could be determined from NMR, which is consistent with the results from X-ray scattering. The possibility to obtain orientational order parameters of molecular segments with ^{13}C chemical shift site resolution represents a valuable supplement to routinely available X-ray data whenever structural details of molecular subunits become relevant. Such a case was met for the *exo*-phenylene rings in HBC-PhC_{12}, whose orientation with respect to the aromatic core is solely accessible by NMR.

SIDECHAINS AND FUNCTIONALIZATION

In **chapters 5** and **6**, discotic mesogens based on a hexa-*peri*-hexabenzocoronene core were investigated in detail. The influence of branched sidechains as opposed to linear ones was studied in **chapter 5**. Branched sidechains are preferred for applications, because they lower the phase transition temperatures and, thereby, lead to a better processability of the material [Fechtenkötter 01b]. It was found that the introduction of a branched sidechain does not lead to any pronounced difference in columnar packing arrangements or dynamics in the respective phases. In contrast, in functionalized HBC derivatives, which were considered in **chapter 6**, a strong influence of the sidechain functionalization on dynamics and packing arrangement was observed. Particularly in covalently and non-covalently bonded HBC dimers, the materials' properties substantially depend on the length and the rigidity of the connecting 'spacer'.

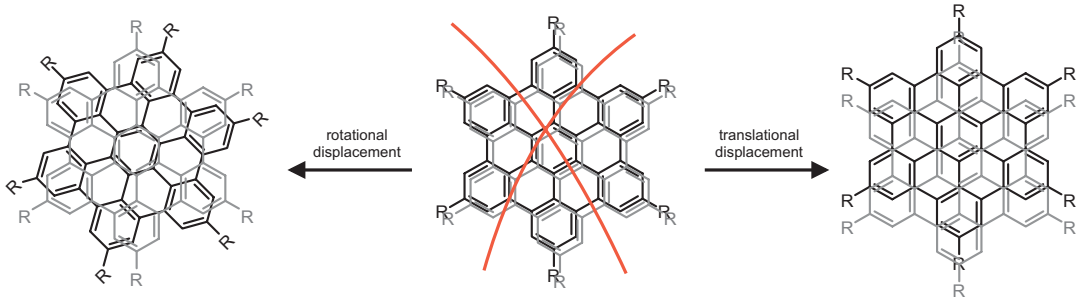

Figure 8.1: *Arrangement of neighboring HBC discs in the columnar stack. The discs are either translationally or rotationally displaced. A face-to-face arrangement (middle) is energetically unfavorable.*

PHASE BEHAVIOR

With the above observations in mind, it is now interesting to ask the question what finally governs the supramolecular arrangement and the phase behavior in these materials. The microphase separation of aromatic cores and aliphatic sidechains is clearly responsible for the columnar arrangement observed in all investigated materials. The core stacking within the columns is obviously primarily controlled by the $\pi - \pi$ interactions. Quantum chemical calculations revealed that a full face-to-face arrangement of the discs in the column is energetically unfavorable ([Gauss 03a] and Fig. 5.16). Hence, neighboring discs are found to be either translationally or rotationally displaced in the columnar stack, as is depicted in Fig. 8.1. For HBCs the typical arrangement is a tilted, 'herringbone'-type stacking of the cores. Only in cases where bulky substituents (e.g. a phenylene ring) or constraints arising from dimer formation prevent the tilted arrangement, a different arrangement of the molecules in the stack is observed. Obviously, control of phase behavior and dynamics in HBC derivatives can be achieved by sidechain functionalization.

COMPARISON TO HATNA DERIVATIVES

The phase and packing behavior of the HATNA derivatives discussed in **chapter 7** is more complicated than that of most HBC derivatives. The solid-state investigations provided additional insight into the structure and dynamics in the various phases. In particular, a dynamic order parameter for the column rotation in the Col_{hd} phase could be determined to $S_{col.rot.}$ = 0.38. This very low order parameter could be attributed to the special three-armed star shape of the molecule, which leaves a lot of space for disordered motions.

The results presented here clearly show that solid-state NMR is a powerful tool for the investigation of complex supramolecular systems. Of course, in such systems solid-state NMR alone will not provide the full information, just as no other characterization method will. Rather, it is the combination of all characterization methods available, which will lead to a sound understanding of structure-property relationships in complex supramolecular systems. Nonetheless, on the way to gain such understanding, solid-state NMR can certainly contribute significantly, and with the recent methodological improvements, some of which were de-

veloped and applied in this thesis, solid-state NMR has become a characterization method that is readily and routinely available to materials scientists.

Appendix

A Tensor Algebra

A.1 Spherical Representation of a Cartesian Tensor

In the following, the relations for transforming a cartesian tensor into the spherical tensor representation will be listed.
If the complete Hamiltonian of an interaction is given in cartesian coordinates by Eq. (2.2), the spherical tensor representation reads as

$$\hat{\boldsymbol{H}} = \hat{\underline{\mathbf{I}}} \cdot \underline{\underline{\mathbf{A}}} \cdot \hat{\underline{\mathbf{S}}} = \sum_{k=0}^{2} \sum_{q=-k}^{k} (-1)^q A_{kq} \hat{T}_{k-q}. \tag{A.1}$$

The irreducible spherical spin tensor operators $\hat{T}_{k-q}$ are listed in table A.1 for the most common interactions. With the spherical unit operators $e_{10} = e_z$ und $e_{1\pm1} = \mp(\frac{1}{\sqrt{2}})(e_x \pm i e_y)$ the A_{kq} are

$$\begin{aligned}
\mathbf{A}_0: \quad A_{00} &= \tfrac{1}{3}(A_{xx} + A_{yy} + A_{zz}) = \tfrac{1}{3}\mathbf{Tr}\{A\} \\
\mathbf{A}_1: \quad A_{10} &= -\tfrac{i}{\sqrt{2}}(A_{xy} - A_{yx}) \quad \left\{ \overset{PAS}{=} -i\sqrt{2}A_{xy} \right\} \\
A_{1\pm1} &= -\tfrac{1}{2}\{(A_{zx} - A_{xz}) \pm i(A_{zy} - A_{yz})\} \quad \left\{ \overset{PAS}{=} A_{xz} \pm iA_{yz} \right\} \\
\mathbf{A}_2: \quad A_{20} &= \sqrt{\tfrac{3}{2}}(A_{zz} - A_{00}) \quad \left\{ \overset{PAS}{=} \sqrt{\tfrac{3}{2}}\delta \right\} \\
A_{2\pm1} &= \mp\{(A_{zx} + A_{xz}) \pm i(A_{zy} + A_{yz})\} \quad \left\{ \overset{PAS}{=} 0 \right\} \\
A_{2\pm2} &= \tfrac{1}{2}\{(A_{xx} - A_{yy}) \pm i(A_{xy} + A_{yx})\} \quad \left\{ \overset{PAS}{=} -\tfrac{1}{2}\delta\eta \right\}
\end{aligned} \tag{A.2}$$

The last terms in curly brackets are the tensor components in the principal axis system (PAS) with the anisotropy parameter, δ, and the asymmetry parameter, η.

Table A.1: *Spherical tensor representation of spin operators (with* $\hat{I}_\pm = \hat{I}_x \pm i\hat{I}_y$*)*

Interaction	T_{00}	T_{10}	$T_{1\pm1}$	T_{20}	$T_{2\pm1}$	$T_{2\pm2}$
Chemical shift	$-\frac{1}{\sqrt{3}}\hat{I}_z B_0$	0	$-\frac{1}{2}\hat{I}_\pm B_0$	$\sqrt{\frac{2}{3}}\hat{I}_z B_0$	$\mp\frac{1}{2}\hat{I}_\pm B_0$	0
Dipole-dipole	0	0	0	$\frac{1}{\sqrt{6}}\left(3\hat{I}_z\hat{S}_z - \hat{\boldsymbol{I}}\hat{\boldsymbol{S}}\right)$	$\mp\frac{1}{2}\left(\hat{I}_z\hat{S}_\pm + \hat{I}_\pm\hat{S}_z\right)$	$\frac{1}{2}\hat{I}_\pm\hat{S}_\pm$
Quadrupole	0	0	0	$\frac{1}{\sqrt{6}}\left(3\hat{I}_z^2 - I(I+1)\right)$	$\mp\frac{1}{2}\left(\hat{I}_z\hat{I}_\pm + \hat{I}_\pm\hat{I}_z\right)$	$\frac{1}{2}\hat{I}_\pm\hat{I}_\pm$

A.2 Rotations and Coordinate Transformations

As shown in the first chapters of this thesis, the evaluation of most NMR experiments involves all kinds of rotations of interaction tensors. Any rotation of a three-dimensional body can be performed by three subsequent rotations by the three Euler angles α, β and γ. Throughout this thesis the sign conventions and definitions of Rose are used [Rose 57], with the Euler angles being defined as follows:
α: rotation about the original *z* axis
β: rotation about the new *y*' axis
γ: rotation about the final *z*" axis
Mathematically, the rotation is carried out by multiplication with the rotation matrix $\underline{\underline{\mathbf{R}}}(\alpha, \beta, \gamma)$:

$$\underline{\underline{\mathbf{R}}}(\alpha, \beta, \gamma) = \underline{\underline{\mathbf{R}}}_{z''}(\gamma)\underline{\underline{\mathbf{R}}}_{y'}(\beta)\underline{\underline{\mathbf{R}}}_{z}(\alpha) \tag{A.3}$$

Since the rotation matrix describes a unitary transformation, it exhibits the following properties:

$$det\underline{\underline{\mathbf{R}}} = 1 \quad \text{und} \quad \underline{\underline{\mathbf{R}}}^{-1} = \underline{\underline{\mathbf{R}}}^{T} \tag{A.4}$$

A rotation by the three Euler angles can also be understood in terms of a transformation from a coordinate system *a* to a coordinate system *b*. Thus, β and α can be seen as the polar angles of the z^b axis in the system *a*. Alternatively, β and $180° - \gamma$ are the polar angles of the z^a axis in the system *b*. It should be noted that the transformation of a vector $\underline{\mathbf{r}}^b$ to the system *b* according to

$$\underline{\mathbf{r}}^b = \underline{\underline{\mathbf{R}}}(\alpha, \beta, \gamma)\underline{\mathbf{r}}^a \tag{A.5}$$

means a passive rotation where the vector $\underline{\mathbf{r}}$ stays fixed and the coordinate system rotates.
Since active rotations where the coordinate system stays fixed and the vector $\underline{\mathbf{r}}$ rotates are

Table A.2: Reduced Wigner rotation matrix elements $d^{(1)}_{pq}$

p \ q	1	0	−1
1	$\frac{1}{2}(1+\cos\beta)$	$-\frac{1}{\sqrt{2}}\sin\beta$	$\frac{1}{2}(1-\cos\beta)$
0	$\frac{1}{\sqrt{2}}\sin\beta$	$\cos\beta$	$-\frac{1}{\sqrt{2}}\sin\beta$
−1	$\frac{1}{2}(1-\cos\beta)$	$\frac{1}{\sqrt{2}}\sin\beta$	$\frac{1}{2}(1+\cos\beta)$

easier to follow, it is common to introduce a "pseudo-active" rotation matrix $\underline{\underline{\tilde{\mathbf{R}}}}$:

$$\begin{aligned}\underline{\underline{\tilde{\mathbf{R}}}}(\alpha,\beta,\gamma) &= \underline{\underline{\mathbf{R}}}^{-1}(\alpha,\beta,\gamma) = \underline{\underline{\mathbf{R}}}^{-1}_{z''}(\gamma)\underline{\underline{\mathbf{R}}}^{-1}_{y'}(\beta)\underline{\underline{\mathbf{R}}}^{-1}_{z}(\alpha) \\ &= \begin{pmatrix} \cos\gamma & \sin\gamma & 0 \\ -\sin\gamma & \cos\gamma & 0 \\ 0 & 0 & 1 \end{pmatrix} \begin{pmatrix} \cos\beta & 0 & -\sin\beta \\ 0 & 1 & 0 \\ \sin\beta & 0 & \cos\beta \end{pmatrix} \begin{pmatrix} \cos\alpha & \sin\alpha & 0 \\ -\sin\alpha & \cos\alpha & 0 \\ 0 & 0 & 1 \end{pmatrix}\end{aligned} \tag{A.6}$$

Turning to rotations of a tensor, the transformation of a cartesian tensor $\underline{\underline{\mathbf{T}}}$ is given by

$$\underline{\underline{\mathbf{T}}}^b = \underline{\underline{\mathbf{R}}}^{-1}(\alpha,\beta,\gamma)\underline{\underline{\mathbf{T}}}^a\underline{\underline{\mathbf{R}}}(\alpha,\beta,\gamma) = \underline{\underline{\tilde{\mathbf{R}}}}(\alpha,\beta,\gamma)\underline{\underline{\mathbf{T}}}^a\underline{\underline{\tilde{\mathbf{R}}}}^{-1}(\alpha,\beta,\gamma). \tag{A.7}$$

Since such matrix multiplications are tedious and costly in terms of computation time, rotations are usually carried out in the spherical tensor representation (see A.1). The rotation of a tensor, which is expressed by the components of a spherical tensor, is given by

$$T^b_{kq} = \sum_{p=-k}^{+k} T^a_{kp} D^k_{pq}(\alpha,\beta,\gamma) \tag{A.8}$$

The T_{kq} transform in the same way as the irreducible representation D_k of the rotational group, which is given by the Wigner rotation matrices D^k_{pq}

$$D^k_{pq} = d^k_{pq}(\beta)e^{-ip\alpha}e^{-iq\gamma} \tag{A.9}$$

The elements d^k_{pq} of the reduced rotation matrices are real and listed in Table A.2 and A.3.

B Simulation Programs

If not indicated otherwise, simulations of the sideband patterns generated by the various recoupling techniques were carried out using routines which calculate the analytical expressions

Table A.3: Reduced Wigner rotation matrix elements $d^{(2)}_{pq}$

p \ q	2	1	0	−1	−2
2	$\frac{1}{4}(1+\cos\beta)^2$	$-\frac{1}{2}(1+\cos\beta)\sin\beta$	$\sqrt{\frac{3}{8}}\sin^2\beta$	$-\frac{1}{2}(1-\cos\beta)\sin\beta$	$\frac{1}{4}(1-\cos\beta)^2$
1	$\frac{1}{2}(1+\cos\beta)\sin\beta$	$\cos^2\beta-\frac{1}{2}(1-\cos\beta)$	$-\sqrt{\frac{3}{8}}\sin 2\beta$	$\frac{1}{2}(1+\cos\beta)-\cos^2\beta$	$-\frac{1}{2}(1-\cos\beta)\sin\beta$
0	$\sqrt{\frac{3}{8}}\sin^2\beta$	$\sqrt{\frac{3}{8}}\sin 2\beta$	$\frac{1}{2}(3\cos^2\beta-1)$	$-\sqrt{\frac{3}{8}}\sin 2\beta$	$\sqrt{\frac{3}{8}}\sin^2\beta$
−1	$\frac{1}{2}(1-\cos\beta)\sin\beta$	$\frac{1}{2}(1+\cos\beta)-\cos^2\beta$	$\sqrt{\frac{3}{8}}\sin 2\beta$	$\cos^2\beta-\frac{1}{2}(1-\cos\beta)$	$-\frac{1}{2}(1+\cos\beta)\sin\beta$
−2	$\frac{1}{4}(1-\cos\beta)^2$	$\frac{1}{2}(1-\cos\beta)\sin\beta$	$\sqrt{\frac{3}{8}}\sin^2\beta$	$\frac{1}{2}(1+\cos\beta)\sin\beta$	$\frac{1}{4}(1+\cos\beta)^2$

for the various experiments.
The Back-to-back and most of the REREDOR sideband patterns were calculated with PV-WAVE routines written by Dr. Ingo Schnell. Most of the other ^{13}C detected recoupling experiments were simulated with a C^{++} program originally written by Dr. Kay Saalwächter, which was modified for the description of the respective experiments. The core program includes functions calculating the integrated phases (Eq. (2.47)) of the various interactions as well as functions calculating the averaged integrated phases under a recoupling pulse train. This program can be adapted to the various experiments by implementing the respective analytical formula. The analytical formula for the various ^{13}C detected experiments are listed in table B.1. The experimental parameters (spinning frequency, investigated nuclei, recoupling time etc.) are then read in from a separate input file. Since this program also includes an option for dynamic pre-averaging of the respective interaction tensors by arbitrary reorientation distributions, it was used for all calculations of sideband patterns including fast motional averaging.
For the investigation of multi-spin effects, simulations based on the propagator formalism were carried out. These calculations were done with the SIMPSON program [Bak 00].

C Powder Averages and the Implementation of Orientation Distributions

When carrying out simulations of solid-state NMR experiments on powdered or partially oriented samples, special care has to be taken to apply a suitable powder averaging procedure. The signal of a powdered sample is given by

$$S(t) = \frac{1}{8\pi}\int_0^{2\pi} d\alpha \int_0^{\pi} d\beta\ sin\beta \int_0^{2\pi} d\gamma\ s(t;\alpha,\beta,\gamma), \tag{C.1}$$

where α, β and γ are the Euler angles denoting the orientation of the PAS in the rotor frame, and $s(t;\alpha,\beta,\gamma)$ characterizes the time evolution of a single crystallite. Under MAS, the initial

Table B.1: *Analytical equations for the ^{13}C detected recoupling pulse sequences with the integrated phases Φ_{csa} and $\Phi_{D_{is}}$ given by Eq. (2.47) and Eq. (2.55).*

CODEX-SB: $S(t_1) = \langle cosN\bar{\Phi}^{(0)} cosN\bar{\Phi}^{(t_1)} + sinN\bar{\Phi}^{(0)} sinN\bar{\Phi}^{(t_1)} \rangle$

CSA-Filter: $S(t_1) = \langle cosN\bar{\Phi}^{(0)} cosN\bar{\Phi}^{(t_1)} + sinN\bar{\Phi}^{(0)} sinN\bar{\Phi}^{(t_1)} - \Phi_{csa}\,|_0^{t_1} + \Phi_{csa}\,|_{t_1}^{2t_1} \rangle$

with:

ω_R-recpl.: $\bar{\Phi}^{(0)} = \Phi_{csa}\,|_0^{\frac{\tau_R}{2}} - \Phi_{csa}\,|_{\frac{\tau_R}{2}}^{\tau_R}$; $\bar{\Phi}^{(t_1)} = \Phi_{csa}\,|_0^{\frac{\tau_R}{2}} - \Phi_{csa}\,|_{\frac{\tau_R}{2}}^{\tau_R}$

$2\omega_R$-recpl.: $\bar{\Phi}^{(0)} = \Phi_{csa}\,|_0^{\frac{\tau_R}{4}} - \Phi_{csa}\,|_{\frac{\tau_R}{4}}^{\frac{\tau_R}{2}} + \Phi_{csa}\,|_{\frac{\tau_R}{2}}^{\frac{3\tau_R}{4}} - \Phi_{csa}\,|_{\frac{3\tau_R}{4}}^{\tau_R}$

$\bar{\Phi}^{(t_1)} = \Phi_{csa}\,|_{t_1}^{\frac{\tau_R}{4}+t_1} - \Phi_{csa}\,|_{\frac{\tau_R}{4}+t_1}^{\frac{\tau_R}{2}+t_1} + \Phi_{csa}\,|_{\frac{\tau_R}{2}+t_1}^{\frac{3\tau_R}{4}+t_1} - \Phi_{csa}\,|_{\frac{3\tau_R}{4}+t_1}^{\tau_R+t_1}$

REPT-HDOR: $S(t_1) = \langle sinN\bar{\Phi}^{(0)} sinN\bar{\Phi}^{(t_1)} \rangle$

REREDOR: $S(t_1) = \langle cosN\bar{\Phi}^{(0)} cosN\bar{\Phi}^{(t_1)} + sinN\bar{\Phi}^{(0)} sinN\bar{\Phi}^{(t_1)} - \Phi_{D_{is}}\,|_0^{t_1} + \Phi_{D_{is}}\,|_{t_1}^{2t_1} \rangle$

with:

ω_R-recpl.: $\bar{\Phi}^{(0)} = \Phi_{D_{is}}\,|_0^{\frac{\tau_R}{2}} - \Phi_{D_{is}}\,|_{\frac{\tau_R}{2}}^{\tau_R}$; $\bar{\Phi}^{(t_1)} = \Phi_{D_{is}}\,|_0^{\frac{\tau_R}{2}} - \Phi_{D_{is}}\,|_{\frac{\tau_R}{2}}^{\tau_R}$

$2\omega_R$-recpl.: $\bar{\Phi}^{(0)} = \Phi_{D_{is}}\,|_0^{\frac{\tau_R}{4}} - \Phi_{D_{is}}\,|_{\frac{\tau_R}{4}}^{\frac{\tau_R}{2}} + \Phi_{D_{is}}\,|_{\frac{\tau_R}{2}}^{\frac{3\tau_R}{4}} - \Phi_{D_{is}}\,|_{\frac{3\tau_R}{4}}^{\tau_R}$

$\bar{\Phi}^{(t_1)} = \Phi_{D_{is}}\,|_{t_1}^{\frac{\tau_R}{4}+t_1} - \Phi_{D_{is}}\,|_{\frac{\tau_R}{4}+t_1}^{\frac{\tau_R}{2}+t_1} + \Phi_{D_{is}}\,|_{\frac{\tau_R}{2}+t_1}^{\frac{3\tau_R}{4}+t_1} - \Phi_{D_{is}}\,|_{\frac{3\tau_R}{4}+t_1}^{\tau_R+t_1}$

rotor phase γ is taken into account separately and one is left with

$$S(t) = \frac{1}{4\pi} \int_0^{2\pi} d\alpha \int_0^{\pi} d\beta \; sin\beta \; s(t;\alpha,\beta), \tag{C.2}$$

which depends only on two variables. For computer simulations, the powder average needs to be implemented in discrete steps. Hence, Eq. (C.2) is approximated by summing up spectra

calculated for each powder orientation $(\alpha_{ij}, \beta_{ij})$ weighted by a factor w_{ij}:

$$S(t) = \sum_{i=1}^{N} \sum_{j=1}^{M} s(t; \alpha_{ij}, \beta_{ij}) w_{ij}, \tag{C.3}$$

where the subscript ij was introduced to indicate that the Euler angles may depend on two indices i and j and may not necessarily be selected independently. The weighting factor w_{ij} is usually normalized according to $\sum_{i=1}^{N} \sum_{j=1}^{M} w_{ij} = 1$. An important point is that both in Eq. (C.1) and Eq. (C.2) an additional factor of sinβ is present, which arises from the spherical symmetry of the problem. Hence, the weighting factor w_{ij} in Eq. (C.3) needs to include a factor sinβ_{ij}, which renders it β dependent, $w_{ij}(\beta)$. Since Eq. (C.3) is an approximation, it is always necessary to check that the powder averaging converges (i.e. the results do not change significantly on increasing the number of powder angles) before choosing the number of crystallite orientations. The number of powder angles and, hence, the calculation time required to reach convergence strongly depends on the powder averaging procedure, i.e. on how the powder angles are distributed over the unit sphere. In the literature, various powder averaging procedures are reported [Wang 95, Hodgkinson 00]. For experiments under MAS, the REPULSION procedure [Bak 97] has turned out to be advantageous. It should be noted that for a single uniaxial interaction only the β angle has to be taken into account. Then, incrementing β in steps between $0°$ and $90°$, while keeping α at an arbitrary value, is sufficient for the powder average.
In the simulations presented here, the powder angle pairs are read in from a separate powder angle file, which is a plain ASCII-file consisting of three columns:

α	β	w
0	0	1
0.2	0	1
...	...	...

The weighting factor makes it particular easy to implement orientation distributions by just modifying it according to the distribution. With an gaussian orientation distribution (Eq. (4.7)) of the general form

$$P(\beta) = exp\left(-\frac{sin^2\beta - c}{k}\right), \tag{C.4}$$

the β-dependent weighting factor is given by

$$w_{ij}(\beta) = sin\beta \cdot exp\left(-\frac{sin^2\beta - c}{k}\right). \tag{C.5}$$

For asymmetric interactions, for each β angle a sufficient number of α angles needs to be considered.

D Experimental Details

D.1 Instrumentation and Experimental Parameters

The NMR experiments were carried out on digital BRUKER Avance-type spectrometers, with B_0-fields corresponding to ^{1}H resonance frequencies of 300.23 MHz (DSX300, 7 T, 85 mm bore magnet), 500.12 MHz (DSX500, 11.74 T, 89 mm bore magnet) and 700.13 MHz (DRX700, 16.4 T, standard 54 mm bore magnet). MAS experiments were carried out using commercial 2.5 mm MAS double-resonance probes, also manufactured by BRUKER with spinning speeds typically ranging from 7 kHz (SUPER) to 30 kHz.
90° pulse lengths varied between 2.0 and 2.5 μs on both channels, corresponding to $\omega_1/2\pi$ = 100-125 kHz. In all ^{13}C -detected experiments, the TPPM scheme was applied for dipolar decoupling [Bennett 95], using approximately 170° pulses and a phase-modulation angle of 30°. Ramped-CP was used for all experiments with an initial cross-polarization step [Metz 94].
The solution-state NMR spectra were measured by M. Wagner on a 500 MHz BRUKER instrument (DSX500).
The deuterium solid-echo spectra were measured with a static single resonance probehead at a deuterium resonance frequency of 107.47 MHz. The echo delay time was 20 μs and the deuterium 90° pulse length was set to 4 μs.
SUPER. The SUPER experiments [Liu 02] were performed at 7 kHz MAS with a scaling factor χ'=0.155 resulting in an effective spectral width of the indirect dimension of ω_R/χ' = 45 kHz, which is sufficiently large for the CSAs of the aromatic sp^2 carbons of interest. The offset was set on the resonance of interest. For the ^{13}C 360° pulses the $\omega_{1,C}$ = 12.12 ω_R condition was satisfied by choosing the pulse strength to be 85 kHz. Special care has to be taken to apply sufficient heteronuclear decoupling during the ^{13}C 360° pulses. Optimum decoupling would be achieved with $\omega_{1,H}/\omega_{1,C} \geq 2$. The high ^{1}H power levels required to fulfill this condition can experimentally only be realized with the small coils of 2.5 mm rotors. In the experiments presented here, the decoupling during the ^{13}C 360° pulses was chosen to be $\omega_{1,H}/2\pi \approx 150$ kHz.
Temperature Calibration. Under fast magic-angle spinning the bearing gas pressure is typically 3.4 bar. At such high pressures, air friction due to the rapid air flow leads to an increase of the temperature inside the rotors. Using the ^{119}Sn resonance of $Sm_2Sn_2O_7$ as a chemical shift thermometer, the temperature correction curve as a function of the bearing gas temperature was calibrated following the procedure described in [Langer 99]. All temperatures reported in this thesis were corrected by this procedure.
WAXS. The WAXS measurements of the oriented filaments presented in chapter 4 were conducted by F. Ebert using a rotating anode (Rigaku 18 kW) X-ray beam with a pinhole collimation and a 2D detector (Siemens) with 1024 x 1024 pixels. A double graphite monochromator for the CuK_α radiation (λ = 0.154 nm) was used. The beam diameter was about 0.5 mm and the sample to detector distance was 80 mm. The patterns were recorded with vertical

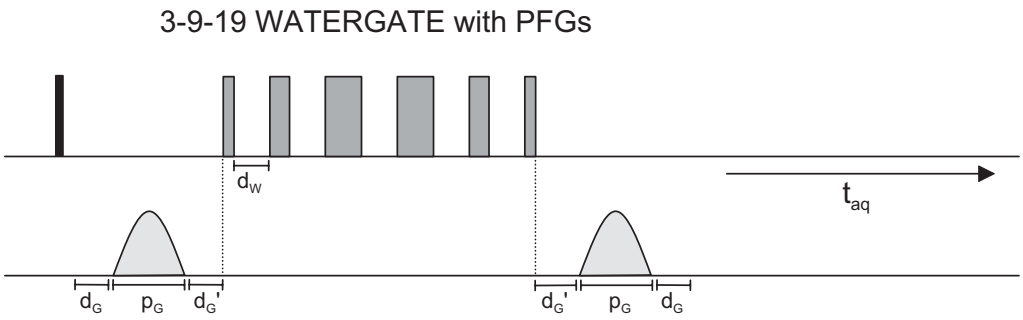

Figure D.1: *PFG-assisted WATERGATE sequence for selective peak suppression, using a 3-9-19 inversion pulse and a pair of pulsed field gradients. At 30 kHz MAS typical timings and settings are d_G = 33 μs, p_G = 100 μs, d_G' = 100 μs, d_W = 33 μs, ΔB = 20...30 G/cm.*

orientation of the filament axis and with the beam perpendicular to the filament.

D.2 WATERGATE Peak Suppression

In the ^{1}H spectra of the liquid crystalline systems, the resonances of interest are often relatively weak and need to be observed despite the presence of strong ^{1}H signal of the long alkyl sidechains. Hence, a PFG-assisted WATERGATE peak suppression scheme was incorporated into the solid-state MAS experiments.
In modern high-resolution NMR, techniques for selective excitation [Kupce 93, Freeman 91] and/or suppression of peaks [Hore 83, Gueron 91] belong to the standard tools and are routinely available on spectrometers. To efficiently select the wanted signals and, at the same time, remove the unwanted ones from the spectrum, pulsed field-gradients (PFGs) have been introduced to the experiments [Bernstein 94, Berger 97], which dephase coherences of unwanted spin signals, while the signals of the wanted coherences are constructively refocused. A particular successful variant for frequency-selective excitation/suppression is the WATERGATE technique introduced by Piotto, Saudek and Sklenar [Piotto 92, Sklenar 93]. The scheme effectively provides a frequency selective inversion pulse, which consists of a sequence of six pulses with durations of 3α-9α-19α-19α-9α-3α with 26α = π and which is usually referred to as '3-9-19' pulse. Effectively, this binomial sequence inverts all resonances within the spectrum except for the frequencies $\omega^k = 2\pi k/\tau_\alpha$, where k is an integer (including zero) and τ_α is the delay between two pulses of the binomial sequence. In combination with two identical PFGs applied before and after the 3-9-19 pulse (see Fig. D.1), WATERGATE efficiently suppresses the signal located at the carrier frequency of the pulse train as well as all signals at $\omega^k = 2\pi k/\tau_\alpha$, because all these signals are dephased twice by the PFGs, while all other signals are refocused. In principle, any selective π pulse, together with an appropriate combination of two PFGs, would serve the same purpose, but experimentally the 3-9-19 pulse has proven to be particularly robust and tolerant with respect to slight misadjustments.

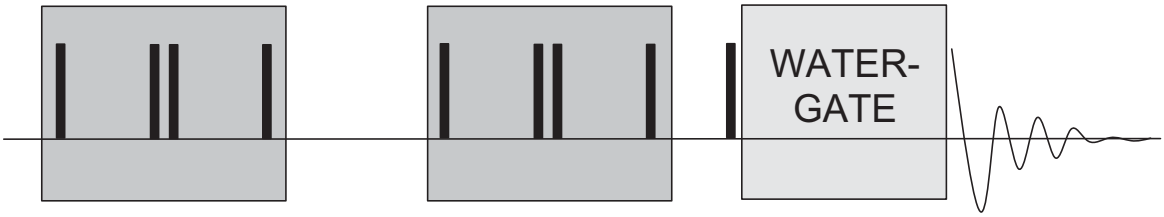

Figure D.2: *Modified Back-to-back pulse sequence for ^{1}H -^{1}H DQ MAS NMR spectroscopy with selective suppression of signals in t_2 by the WATERGATE scheme.*

In order to achieve peak suppression in the DQ spectra, the WATERGATE block was inserted into the Back-to-Back sequence before signal acquisition, as depicted in Fig. D.2. In the two-dimensional variant with a t_1 evolution time between the two BABA recoupling blocks, special care has to be taken concerning the frequency-offset during the t_1 evolution time. For the peak suppression, the RF carrier frequency must be identical to the signal which is to be suppressed. However, this resonance is often located at the edges of the spectrum. If the same carrier frequency is chosen for the t_1 evolution time, the spectrum often does not fit into the spectral window of F_1, which causes severe backfolding in the indirect dimension. In order to avoid those problems, a frequency switch is made for the BABA blocks in such a way that the carrier frequency lies in the middle of the spectrum. Examples for spectra with WATER-GATE peak suppression were already depicted in figures 6.10, 7.6 and 7.7. Technical details of the used MAS probehead and more experimental examples are published in [Fischbach 03]. The suppression efficiencies achieved by the WATERGATE approach are of the order of 1%, which is perfectly sufficient for the described homonuclear solid-state ^{1}H experiments.

E Effects of Intermediate Motions on MAS Recoupling Methods

Throughout this thesis, molecular dynamics has been investigated by measuring motionally averaged dipole-dipole coupling constants with the various recoupling experiments described in chapter 3. This analysis silently took for granted that the underlying motional processes are fast with respect to the timescale of the respective experiment. In this section, the question is adressed how motion in the so-called intermediate motional limit (IMR), effects the outcome of recoupling MAS experiments. Generally, depending on the rate k of the motional process and the strength δ_λ (i.e. the anisotropy parameter of the underlying anisotropic interaction λ), three sorts of motional regimes are distinguished: (i) In the slow motional regime (rates k$\ll \delta$) the molecular motions are that slow that in the course of the experiment practically no reorientation takes place. In this regime, the spectra are obviously not sensitive to the motional process. (ii) The intermediate motional regime is met for k$\approx \delta/2\pi$. (iii) In the fast motional regime (k$\gg \delta$), the molecular motions are comparably fast and the respective interaction tensor is motionally averaged. This averaging is sensitive to the geometry of the underlying motional process but not to the motional correlational times.
Naturally, it is important to know the effects of intermediate motions on the outcome of the repective experiment used for the study of molecular dynamics. From static echo experiments, such as the hahn echo, the Gill-Meiboom sequence or the solid-echo sequence (see section 2.5.4 and [Schmidt-Rohr 94]), it is well known that intermediate motion on the timescale of the respective echo delay time leads to characteristic lineshapes and to a significant loss of signal intensity [Spiess 80]. High-resolution NMR techniques employing magic-angle spinning (MAS) are also known to exhibit intensity loss and complex behavior when dynamics in the sample occurs on timescales comparable to the MAS frequency or the applied pulse schemes and rf-frequencies [Suwelack 80, Vanderhart 81, Schmidt 86]. Specific treatment of the effect of intermediate motions on the laboratory frame recoupling pulse sequences described in chapter 3 can be found in [Saalwächter 02b]. Summarizing those results it can be said that (well-defined) intermediate motions affect the result of recoupling experiments[1] as follows:

- The signal intensity is found to pass through a minimum at approximately $k \approx \delta_\lambda/2\pi$ (see also Fig. E.2). Provided the underlying interaction strength δ_λ is known, the position of the minumum represents a good estimate of the rate constant at the given temperature.
- Upon entering the intermediate motional regime a characteristic signal decay with increasing recoupling time is observed which can be described by an apparent transverse relaxation time T_2^{rcpl}.
  T_2^{rcpl} decreases with increasing rate constants k and does not depend on the spinning frequency to a first approximation in the fast spinning limit.
- Simulations showed that it is apparently the averaged recoupled tensor as described e.g. by Eq. (3.22) which dominates at least the slow branch of the IMR. This is a consequence

[1] such as the various REPT [Saalwächter 01b] or the CSA recoupling techniques [deAzevedo 99, Hong 00]

of the fact that in the fast spinning limit the averaged recoupled Hamiltonian should be unaffected, i.e. no motion takes place on the $1\tau_R$ timescale. Note that the averaged recoupled tensor often exhibits a characteristic (depending on the experiment) scaling factor which also governs at which motional rates the IMR is reached.

For the hexabenzocoronenes studied extensively in chapters 5 and 6, rotation around the columnar axis was found to be the characteristical motional process in the liquid crystalline phases. In the following, the question is adressed how intermediate rates for this particular process affect the outcome of the routinely used ^{1}H -^{13}C spinning sideband patterns. Preliminary work on this question is reported in [Fischbach 00] for HBC-PhC_{12} (**6**). As mentioned in section 5.1, HBC-PhC_{12} undergoes slow (i.e. on the ms timescale) disc reorientations (60° or 120° in-plane jumps) in the solid phase at room temperature, which were detected with the CODEX experiment [Fischbach 02]. The rate of this process was found to increase with temperature and to enter the intermediate motional regime at above 50°C for the CODEX experiments. Above the phase transition to the LC phase at 80°C, fast column rotation was detected by means of REPT-HDOR spinning SB patterns [Fechtenkötter 99]. The signal loss associated with entering the IMR can also be monitored by measuring temperature dependent 1D REPT-HSQC spectra. These are shown in Fig. E.1 for two different recoupling times. Clearly, the core CH peak at 118 ppm (marked by the grey dotted lines) broadens and loses intensity upon approaching the phase transition temperature at 80 °C. For both recoupling times, minimum signal intensity is found at 70 °C. This can now be compared to calculations of the REPT signal intensity for various motional rates which are shown in Fig. E.1. The calculations were carried out with a C^{++} program written by K. Saalwächter which is based on a linearization of the general solution of the stochastic Liouville-von Neumann equation. Practically, the calculation is done by separating the exchange step and the 'normal' quantum-mechanical evolution of the spin system, which allows those to be calculated sequentially. Hereby, care needs to be taken to keep the simulation time step short enough. Practically, this means that the suitability of a chosen time step needs to be checked by repeating the calculation with a shorter time step and test for convergence.

Clearly, both calculated signal intensity curves in Fig. E.2 exhibit a characteristic minimum at intermediate motional rates of around 10 kHz. Hence, it can be concluded that in HBC-PhC_{12} the jump process has at 70 °C a rate on the same order of magnitude. However, it must be stressed, that signal loss during NMR experiments occurs as a result of various other factors, such as the interference of heteronuclear decoupling and motions of the C-H dipolar tensor[2] [Vanderhart 81, Long 94] or recoupling effects of finite pulses [Ishii 95]. Such effects were not included in the calculations and, therefore, the comparison of experimental and calculated signal intensities allows only for qualitative conclusions. As shown in [Saalwächter 02b] a quantative relation of the observed signal intensities to the rate constants k of the motional process requires a suitable reference experiment which is subject to the same adverse effects.

[2]Note that this interference primarily affects the linewidth and not the integral signal intensity. Nevertheless, severe line broadening often appears as a signal loss when the broadened resonance line disappears underneath the experimental noise.

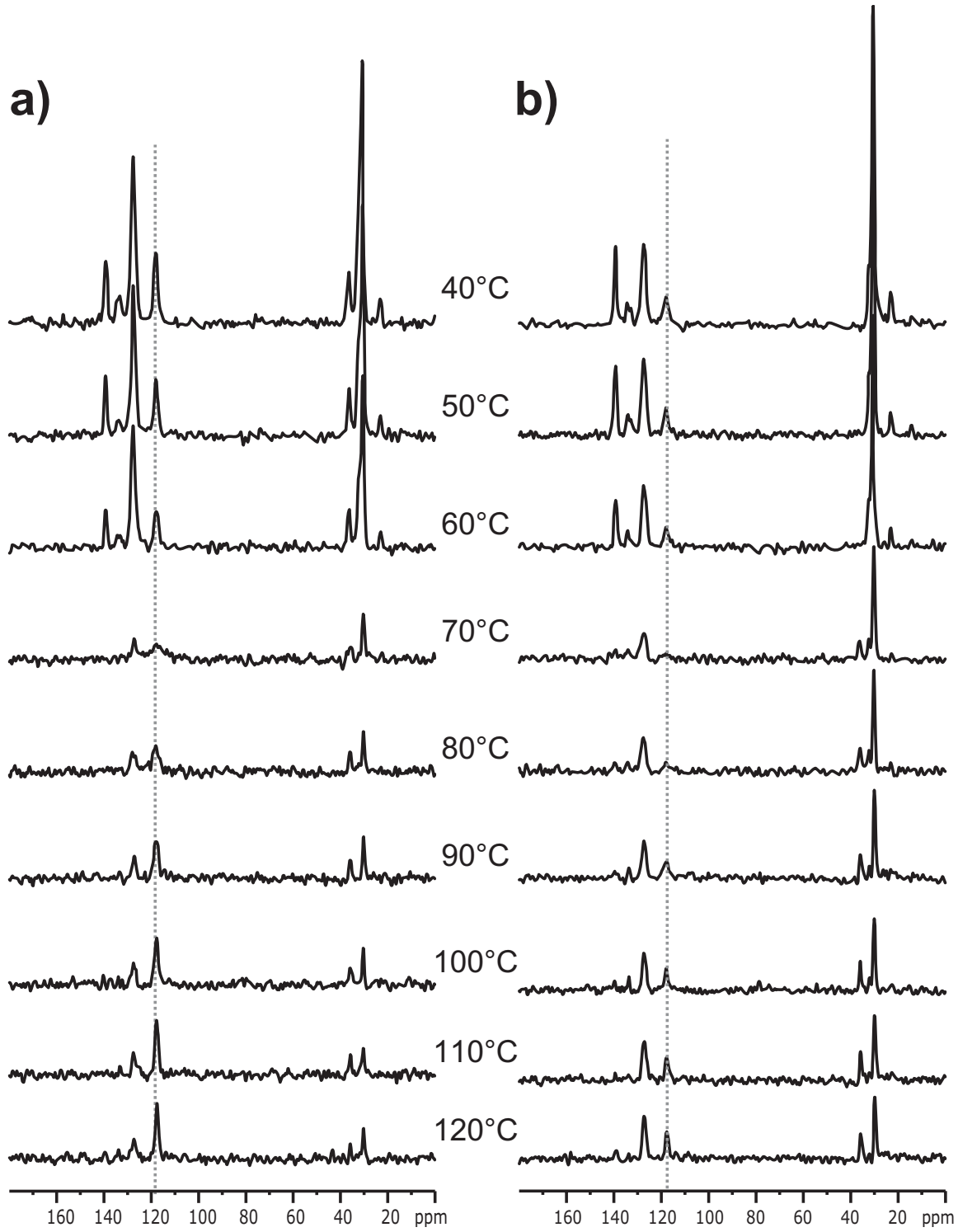

Figure E.1: *1D REPT-HSQC spectra of HBC-PhC$_{12}$ at various temperatures, 25 kHz MAS and recoupling times of $\tau_{rcpl} = 2\tau_R$ (a) and $\tau_{rcpl} = 4\tau_R$, respectively. All spectra were measured with the same experimental setup and identical number of scans and not corrected by the Curie-factor.*

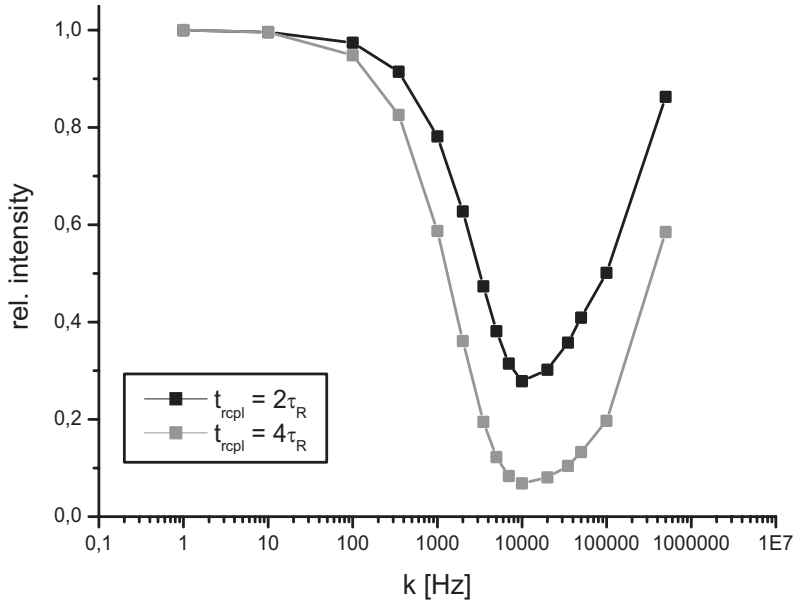

Figure E.2: *Calculated 1D REPT-HSQC signal intensities (25 kHz MAS) of the core CH of an HBC undergoing in-plane 3-site jumps around the columnar axis.*

Comparing the calculated signal intensity curves for two and four rotor periods recoupling time, it becomes obvious that the minimum intensity is much lower (i.e. almost zero) for the longer recoupling time. This might possibly account for the fact that in the REPT-HDOR spectra of HBC-$C^*_{8,2}$ (see section 5.3.2) no signal intensity could be acquired (with a reasonable number of scans) for the core CH at recoupling times longer than 160 μs. Maybe, the column rotation is still in the intermediate motional limit which would cause the pronounced signal loss especially at longer recoupling times. The effect of intermediate motional rates on REPT-HDOR SB patterns is shown in Fig. E.3. Clearly, upon passing through the intermediate motional regime (k$\approx \delta/2\pi$) a transition from spectra exhibiting SB up to fifth order to spectra exhibiting only SB up to third order takes place. Notably, spectra differing from the limiting cases are only seen in a quite narrow interval in the IMR where also the integral intensity of the spectra is at a minimum. Hence, as also shown in more detail in [Saalwächter 00], the measurement of tensor parameters by sideband pattern analysis is possible with very good accuracy for most motional rates. Only in the very small region (in terms of rate constants k) of the IMR the analysis of sideband patterns might yield erroneous results.

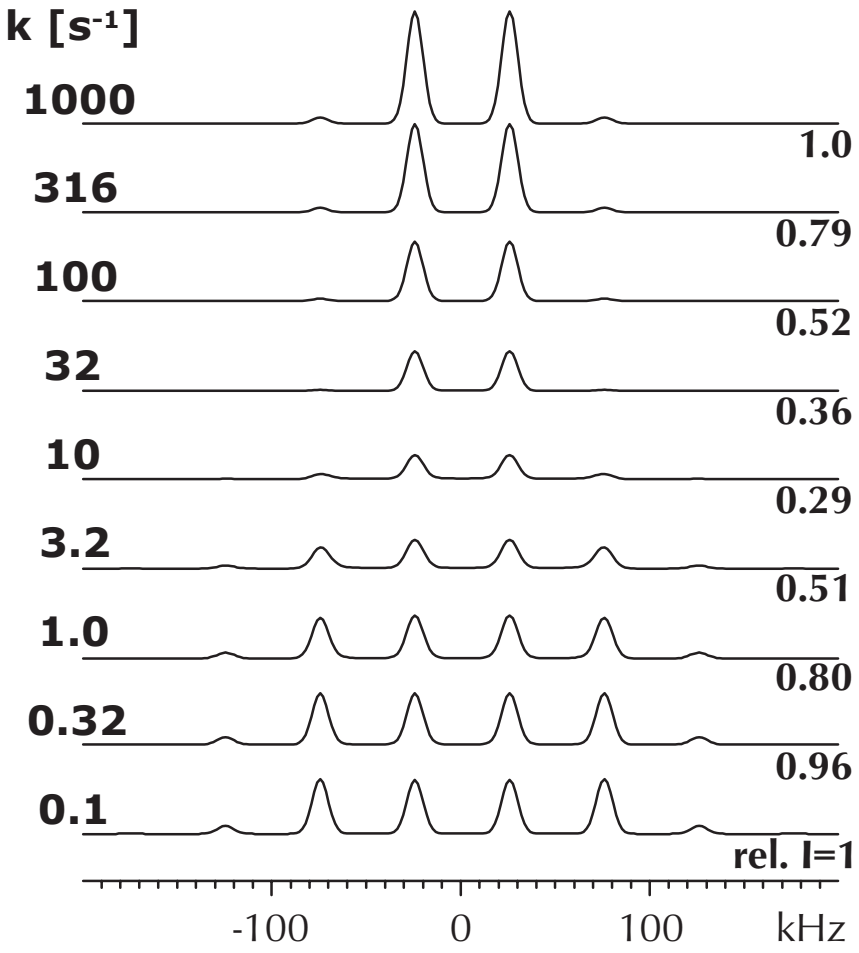

Figure E.3: *Calculated ^{1}H -^{13}C REPT-HDOR sideband patterns ($\tau_{rcpl} = 80\mu s$) for the core CH of an HBC undergoing three-site jumps around the columnar axis with various motional rates k [Figure provided by K. Saalwächter].*

Bibliography

[Abragam 61] A. Abragam. The Principles of Nuclear Magnetism. Oxford Univ. Press, Oxford (1961).

[Abramowitz 72] M. Abramowitz, I. A. Stegun. Handbook of Mathematical Functions. Dover Publications, Inc., New York (1972).

[Ahlrichs 89] R. Ahlrichs, M. Bär, M. Häser, H. Horn, C. Kölmel. Electronic Structure Calculations on Workstation Computers: The Program System Turbomole. *Chem. Phys. Lett.* **162**, 165–169 (1989).

[Andrew 58] E. R. Andrew, A. Bradbury, R. G. Eades. Nuclear Magnetic Resonance Spectra from a Crystal Rotated at High Speed. *Nature* **182**, 1659 (1958).

[Bak 97] M. Bak, N. C. Nielsen. REPULSION, A Novel Approach to Efficient Powder Averaging in Solid-State NMR. *J. Magn. Reson.* **125**, 132–139 (1997).

[Bak 00] M. Bak, J. T. Rasmussen, N. C. Nielsen. SIMPSON: A General Simulation Program for Solid-State NMR Spectroscopy. *J. Magn. Reson.* **147**, 296–330 (2000).

[Baumeister 82] U. Baumeister, H. Hartung, M. Jaskolski. The Crystal and Molecular Structure of 4'-Cyanophenyl-4-normal-pentylbenzoate. *Mol. Cryst. Liq. Cryst.* **88**, 167–181 (1982).

[Becke 88] A. D. Becke. Density-functional Exchange-energy Approximation with Correct Asymptotic-Behavior. *Phys. Rev. A* **38**, 3098–3100 (1988).

[Becker 96] E. D. Becker. Hydrogen bonding, Ch. 4, pp. 2409–2415. Wiley, Chichester (1996).

[Bennett 95] A. E. Bennett, C. M. Rienstra, M. Auger, K. V. Lakshmi, R. G. Griffin. Heteronuclear Decoupling in Rotating Solids. *J. Chem. Phys.* **103**, 6951–6958 (1995).

[Berger 97] S. Berger. NMR Techniques Employing Selective Radiofrequency Pulses in Combination with Pulsed Field Gradients. *Progr. Nucl. Magn. Res. Spectr.* **30**, 137–156 (1997).

[Berglund 80] B. Berglund, R. W. Vaughan. Correlations between Proton Chemical Shift Tensors, Deuterium Quadrupole Couplings, and Bond Distances for Hydrogen Bonds in Solids. *J. Chem. Phys.* **73**, 2037–2043 (1980).

[Bernstein 94] M. A. Bernstein, L. A. Timble. High-resolution NMR Experiments which use Frequency-selective RF Pulses in Combination with Magnetic-field Gradients. *Magn. Res. Chem.* **32**, 107–110 (1994).

[Bloch 46] F. Bloch. Nuclear Induction. *Phys. Rev.* **70**, 460–474 (1946).

[Bloembergen 53] N. Bloembergen, T. J. Rowland. On the Nuclear Magnetic Resonance in Metals and Alloys. *Acta Metall.* **1**, 731–746 (1953).

[Blümich 90] B. Blümich, A. Hagemeyer, D. Schaefer, K. Schmidt-Rohr, H. W. Spiess. Solid State NMR Spectroscopy in Polymer Science. *Adv. Mat.* **2**, 72–81 (1990).

[Boden 94] N. Boden, R. C. Borner, R. J. Bushby, J. Clements. First Observation of an n-Doped Quasi-One-Dimensional Electronically-Conducting Discotic Liquid Crystal. *J. Am. Chem. Soc.* **116**, 10807–10808 (1994).

[Boden 95] N. Boden, R. J. Bushby, A. N. Cammidge, P. S. Martin. Glass-forming Discotic Liquid-crystalline Oligomers. *J. Mater. Chem.* **5**, 1857–1860 (1995).

[Boden 99a] N. Boden, R. J. Bushby, A. N. Cammidge, A. El-Mansoury, P. S. Martin, Z. Lu. The Creation of Long-lasting Glassy Columnar Discotic Liquid Crystals using 'Dimeric' Mesogens. *J. Mater. Chem.* **9**, 1391–1402 (1999).

[Boden 99b] N. Boden, R. J. Bushby, J. Clements, B. Movaghar. Device Applications of Charge Transport in Discotic Liquid Crystals. *J. Mater. Chem.* **9**, 2081–2086 (1999).

[Boden 01] N. Boden, R. J. Bushby, K. Donovan, Q. Y. Liu, Z. B. Lu, T. Kreouzis, A. Wood. 2,3,7,8,12,13-Hexakis[2-(2-methoxyethoxy)ethoxy]-tricycloquinazoline: A Discogen which allows enhanced Levels of n-Doping. *Liquid Crystals* **28**, 1739–1748 (2001).

[Boeffel 83] C. Boeffel, B. Hisgen, U. Pschorn, H. Ringsdorf, H. W. Spiess. Structure and Dynamcis of Liquid Crystalline Polymers from Deuteron NMR. *Israel J. Chem.* **23**, 388–394 (1983).

[Breitmaier 93] E. Breitmaier. Structure Elucidation by NMR in Organic Chemistry. J. Wiley & Sons Ltd., Chichester (1993).

[Brinkmann 00] A. Brinkmann, M. Edén, M. H. Levitt. Synchronous Helical Pulse Sequences in Magic-angle Spinning Nuclear Magnetic Resonance. *J. Chem. Phys.* **112**, 8539–8554 (2000).

[Brown 99] S. P. Brown, I. Schnell, J. D. Brand, K. Müllen, H. W. Spiess. An Investigation of $\pi - \pi$ Packing in a Columnar Hexabenzocoronene by Fast Magic-Angle Spinning and Double-Quantum ^{1}H Solid-State NMR Spectroscopy. *J. Am. Chem. Soc.* **121**, 6712–6718 (1999).

[Brown 00a] S. P. Brown, I. Schnell, J. D. Brand, K. Müllen, H. W. Spiess. A ^1H Double-quantum Magic-angle Spinning Solid-state NMR Investigation of Packing and Dynamics in Triphenylene and Hexabenzocoronene Derivatives. *J. Mol. Struc.* **521**, 179–195 (2000).

[Brown 00b] S. P. Brown, I. Schnell, J. D. Brand, K. Müllen, H. W. Spiess. The Competing Effects of $\pi - \pi$ Packing and Hydrogen Bonding in a Hexabenzocoronene Carboxylic Acid Derivative: A ^1H Solid-state MAS NMR Investigation. *Phys. Chem. Chem. Phys.* **2**, 1735–1745 (2000).

[Brown 01] S. P. Brown, H. W. Spiess. Advanced Solid-state NMR Methods for the Elucidation of Structure and Dynamics of Molecular, Macromolecular and Supramolecular systems. *Chem. Rev.* **101**, 4125–4155 (2001).

[Brunsfeld 01] L. Brunsfeld, B. J. B. Folmer, E. W. Meijer, R. P. Sijbesma. Supramolecular Polymers. *Chem. Rev.* **101**, 4071–4097 (2001).

[Bushby 02] R. J. Bushby. Discotic Liquid Crystals 25 Years on. *Curr. Opinion in Colloid & Interface science* **7**, 343–354 (2002).

[Carravetta 00] M. Carravetta, M. Edén, X. Zhao, A. Brinkmann, M. H. Levitt. Symmetry Principles for the Design of Radiofrequency Pulse Sequences in the Nuclear Magnetic Resonance of Rotating Solids. *Chem. Phys. Lett.* **321**, 205–215 (2000).

[Cavanagh 96] J. Cavanagh, W. J. Fairbrother, A. G. Palmer III, N. J. Skelton. Protein NMR Spectroscopy - Principles and Practise. Academic Press, San Diego, CA (1996).

[Chandrasekhar 77] S. Chandrasekhar, B. K. Sadashiva, K. A. Suresh. Liquid-Crystals of Disc-like Molecules. *Pramana* **7**, 471–480 (1977).

[Chandrasekhar 98] S. Chandrasekhar. Discotic Liquid Crystals: Their Structures and Physical Properties. In D. Demus, J. Goodby, G. W. Gray, H. W. Spiess, V. Vill (eds.), Handbook of Liquid Crystals, Volume 2B, pp. 749–780. Wiley-VCH, Weinheim (1998).

[Chmelka 93] B. F. Chmelka, K. Schmidt-Rohr, H. W. Spiess. Molecular Orientation Distributions in Poly(ethyleneterephthalate) Thin Films and Fibers from Multidimensional DECODER NMR spectroscopy. *Macromolecules* **26**, 2282–2296 (1993).

[Courtieu 82] J. Courtieu, D. W. Alderman, D. M. Grant, J. P. Bayles. Director Dynamics and NMR Applications of Nematic Liquid Crystals Spinning at Various Angles from the Magnetic Field. *J. Chem. Phys.* **77**, 723–730 (1982).

[Craats 99] A. M. van de Craats, J. M. Warman, A. Fechtenkoetter, J. D. Brand, M.Harbison, K. Müllen. Record Charge Carrier Mobility in a Room-Temperature Discotic Liquid-Crystalline Derivative of Hexabenzocoronene. *Adv. Mater.* **11**, 1469–1472 (1999).

[Craats 00] A. M. van de Craats. *Charge Transport in Self-Assembling Discotic Liquid Crystalline Materials*. Dissertation, Delft University of Technology (2000).

[Craats 03] A. M. van de Craats, N. Stutzmann, O. Bunk, M. M. Nielsen, M. Watson, K. Müllen, H. D. Chanzy, H. Sirringhaus, R. H. Friend. Meso-Epitaxial Solution-Growth of Self-Organizing Discotic Liquid-Crystalline Semiconductors. *Adv. Mater.* **15**, 495–499 (2003).

[Davis 76] J. H. Davis, K. R. Jeffrey, M. Bloom, M. I. Valic, T. P. Higgs. Quadrupolar Echo Deuteron Magnetic Resonance Spectroscopy in Ordered Hydrocarbon Chains. *Chem. Phys. Lett.* **42**, 390–394 (1976).

[De Paul 00] S. M. De Paul, K. Saalwächter, R. Graf, H. W. Spiess. Sideband Patterns from Rotor-Encoded Longitudinal Magnetization in MAS Recoupling Experiments. *J. Magn. Reson.* **146**, 140–156 (2000).

[deAzevedo 99] E. R. deAzevedo, W.-G. Hu, T. J. Bonagamba, K. Schmidt-Rohr. Centerband-Only Detection of Exchange: Efficient Analysis of Dynamics in Solids by NMR. *J. Am. Chem. Soc.* **121**, 8411–8412 (1999).

[deAzevedo 00] E. R. deAzevedo, W.-G. Hu, T. J. Bonagamba, K. Schmidt-Rohr. Principles of Centerband-Only Detection of Exchange in Solid-State NMR, and Extensions to 4-Time CODEX. *J. Chem. Phys.* **112**, 8988–9001 (2000).

[deGennes 83] P. G. deGennes. Skoulios Pinched Regions and Incommensurate Structures. *J. Phys. Lett.* **44**, 664–657 (1983).

[Detken 02] A. Detken, E. H. Hardy, M. Ernst, B. H. Meier. Simple and Efficient Decoupling in Magic-angle Spinning Solid-state NMR: the XiX Scheme. *Chem. Phys. Lett.* **356**, 298–304 (2002).

[Ditchfield 74] R. Ditchfield. Self-consistent Perturbation-Theory of Diamagnetism. 1. Gauge-invariant LCAO Method for NMR Chemical-shifts. *Mol. Phys.* **27**, 789–807 (1974).

[Dixon 82] W. T. Dixon. NMR Spectra in Spinning Samples (TOSS). *J. Chem. Phys.* **77**, 1800–1809 (1982).

[Dötz 00] F. Dötz, J. D. Brand, S. Ito, L. Ghergel, K. Müllen. Synthesis of Large Polyaromatic Hydrocarbons: Variation of Size and Periphery. *J. Am. Chem. Soc.* **122**, 7707–7717 (2000).

[Dusold 00] S. Dusold, A. Sebald. Dipolar Recoupling under Magic-Angle Spinning Conditions. In Annual reports on NMR spectroscopy, Volume 41, pp. 185–264. Academic Press (2000).

[Ebert 03] F. Ebert, T. Thurn-Albrecht. Controlling the Orientation of Semicrystalline Polymers by Crystallization in Magnetic Fields. *Macromolecules* **36**, 8685–8694 (2003).

[Eichhorn 00] H. Eichhorn. Mesomorphic Phthalocyanines, Tetraazaprophyrins, Porphyrins and Triphenylenes as Charge-Transporting Materials. *J. Porphyrines Phthalocyanines* **4**, 88–102 (2000).

[Emsley 85] J. W. Emsley. Nuclear Magnetic Resonance of Liquid Crystals, Nato ASI Series. D. Reidel Publishing Company, Dordrecht (1985).

[Ernst 01] M. Ernst, A. Samoson, B. H. Meier. Low-power Decoupling in Fast Magic-angle Spinning NMR. *Chem. Phys. Lett.* **348**, 293–302 (2001).

[Ernst 03] M. Ernst. Heteronuclear Spin Decoupling in Solid-state NMR under Magic-angle Sample Spinning. *J. Magn. Reson.* **162**, 1–34 (2003).

[Evans 95] J. N. S. Evans. Biomolecular NMR Spectroscopy. Oxford University Press, Oxford (1995).

[Facelli 93] J. C. Facelli, D. M. Grant. Determination of Molecular Symmetry in Crystalline Naphthalene using Solid-state NMR. *Nature* **365**, 325–327 (1993).

[Fechtenkötter 99] A. Fechtenkötter, K. Saalwächter, M. A. Harbison, K. Müllen, H. W. Spiess. Highly Ordered Columnar Structures from Hexa-*peri*-hexabenzocoronenes — Synthesis, X-ray Diffraction, and Solid-State Heteronuclear Multiple-Quantum NMR Investigations. *Angew. Chem. Int. Ed. Engl.* **38**, 3039–3042 (1999).

[Fechtenkötter 01a] A. Fechtenkötter. *Liquid Crystalline Hexabenzocoronenes as Organic Molecular Materials - Synthesis, Characterization and Application*. Dissertation, Universität Mainz (2001).

[Fechtenkötter 01b] A. Fechtenkötter, N. Tchebotareva, M. Watson, K. Müllen. Discotic Liquid Crystalline Hexabenzocoronenes Carrying Chiral and Branched Alkyl Chains: Supramolecular Engineering and Improved Synthetic Methods. *Tetrahedron* **57**, 3769–3783 (2001).

[Feike 96] M. Feike, D. E. Demco, R. Graf, J. Gottwald, S. Hafner, H. W. Spiess. Broadband Multiple-Quantum NMR Spectroscopy. *J. Magn. Reson. A* **122**, 214–221 (1996).

[Fischbach 00] I. Fischbach. *Festkörper-NMR-spektroskopische Untersuchungen zur Dynamik in Hexabenzocoronenen*. Diplomarbeit, Universität Mainz (2000).

[Fischbach 02] I. Fischbach, K. Saalwächter, T. Pakula, P. Minkin, A. Fechtenkötter, K. Müllen, H. W. Spiess. Structure and Dynamics in Columnar Discotic Materials: A Com-

bined X-ray and Solid-State NMR Study of Hexabenzocoronene Derivatives. *J. Phys. Chem. B* **106**, 6408–6418 (2002).

[Fischbach 03] I. Fischbach, K. Thieme, A. Hoffmann, M. Hehn, I. Schnell. PFG-Assisted Selection and Suppression of ^{1}H NMR Signals in the Solid State under fast MAS. *J. Magn. Res.* **65**, 102–115 (2003).

[Fredericks 96] J. R. Fredericks, A. D. Hamilton. Hydrogen Bonding Control of Molecular Self-Assembly: Recent advances in Design, Synthesis and Analysis. In J. L. Atwood, J. E. D. Davies, D. D. MacNicol, F. Vögtle, J.-M. Lehn (eds.), Comprehensive Supramolecular Chemistry, Volume 9, pp. 565–594. Pergamon, New York (1996).

[Freeman 91] R. Freeman. Selective Excitation in High-resolution NMR. *Chem. Rev.* **91**, 1397–1412 (1991).

[Friedrich 98] U. Friedrich, I. Schnell, S. P. Brown, A. Lupulescu, D. E. Demco, H. W. Spiess. Spinning-sideband patterns in multiple-quantum magic-angle spinning NMR spectroscopy. *Mol. Phys.* **95**, 1209–1227 (1998).

[Fung 00] B. M. Fung, A. K. Kithrin, K. Ermolaev. An Improved Broadband Decoupling Sequence for Liquid Crystals and Solids. *J. Magn. Res.* **142**, 97–101 (2000).

[Gan 97] Z. Gan, R. R. Ernst. Frequency- and Phase-modulated Heteronuclear Decoupling in Rotating Solids. *Solid State Nucl. Magn. Res.* **8**, 153–159 (1997).

[Gauss 03a] J. Gauss, C. Ochsenfeld, et al. (2003). publication in preparation.

[Gauss 03b] Prof. Dr. J. Gauss (2003). oral communication.

[Geen 95] H. Geen, J. J. Titman, J. Gottwald, H. W. Spiess. Spinning Sidebands in the Fast-MAS Multiple-Quantum Spectra of Protons in Solids. *J. Magn. Reson. A* **114**, 264–267 (1995).

[Glaubitz 01] C. Glaubitz, M. Carravetta, M. Eden, M. H. Levitt. Towards Dipolar Recoupling in Macroscopically Ordered Samples of Membrane Proteins Rotating at the Magic Angle. In S. R. Kühne, H. J. M. deGroot (eds.), Perspectives on Solid-state NMR in Biology, pp. 71–81. Kluwer Academic Publishers (2001).

[Goldfarb 83] D. Goldfarb, Z. Luz, H. Zimmermann. Deuterium Magnetic Resonance in the Discotic Columnar Mesophases of Hexaalkoxytriphenylenes: The Conformation of the Aliphatic Sidechains. *J. Chem. Phys.* **78**, 7065–7072 (1983).

[Gottwald 95] J. Gottwald, D. E. Demco, R. Graf, H. W. Spiess. High-resolution Double-quantum NMR Spectroscopy of Homonuclear Spin Pairs and Proton Connectivities in Solids. *Chem. Phys. Lett.* **243**, 314–323 (1995).

[Goward 03a] G. Goward, K. Saalwächter, I. Fischbach, H. W. Spiess. Reorientation Phenomena in Imidazolium Methyl Sulfonate as Probed by Advanced Solid-State NMR. *J. Am. Chem. Soc.* **125**, 5792–5800 (2003).

[Goward 03b] G. Goward, D. Sebastiani, I. Schnell, H. W. Spiess, H.-D. Kim, H. Ishida. Benzoxazine Oligomers: Evidence for a Helical Structure from Solid-State NMR Spectroscopy and DFT-Based Dynamics and Chemical Shift Calculations. *SS-NMR ACS Proceedings* (2003). accepted for publication.

[Graf 96] R. Graf, D. E. Demco, J. Gottwald, S. Hafner, H. W. Spiess. Dipolar couplings and internuclear distances by double-quantum nuclear magnetic resonance spectroscopy of solids. *J. Chem. Phys.* **106**, 885–895 (1996).

[Graf 98a] R. Graf. *Hochauflösende Doppelquanten-NMR-Spektroskopie an amorphen Polymeren*. Dissertation, Universität Mainz (1998).

[Graf 98b] R. Graf, D. E. Demco, S. Hafner, H. W. Spiess. Selective Residual Dipolar Couplings in Cross-linked Elastomers by ^{1}H Double-quantum NMR Spectroscopy. *Solid State Nucl. Magn. Reson.* **12**, 139–152 (1998).

[Gueron 91] M. Gueron, P. Plateau, M. Decorps. Solvent Signal Suppression in NMR. *Progr. Nucl. Magn. Reson. Spectr.* **23**, 135–209 (1991).

[Gullion 89a] T. Gullion, J. Schaefer. Detection of Weak Heteronuclear Dipolar Coupling by Rotational-Echo Double-Resonance Nuclear Magnetic Resonance. *Adv. Magn. Reson.* **13**, 57–83 (1989).

[Gullion 89b] T. Gullion, J. Schaefer. Rotational-Echo Double-Resonance NMR. *J. Magn. Reson.* **81**, 196–200 (1989).

[Gullion 90] T. Gullion, D. B. Baker, M. S. Conradi. New, Compensated Carr-Purcell Sequences. *J. Magn. Reson.* **89**, 479–484 (1990).

[Gullion 97] T. Gullion. Measurement of Heteronuclear Dipolar Interactions by Rotational-Echo, Double-Resonance Nuclear Magnetic Resonance. *Magn. Reson. Rev.* **17**, 83–131 (1997).

[Hahn 50] E. L. Hahn. Spin Echoes. *Phys. Rev.* **80**, 580–594 (1950).

[Harbison 87] G. S. Harbison, V.-D. Vogt, H. W. Spiess. Structure and Order in Partially Oriented Solids: Characterization by 2D-magic-angle-spinning NMR. *J. Chem. Phys.* **86**, 1206–1218 (1987).

[Häser 92] M. Häser, R. Ahlrichs, H. P. Baron, P.Weis, H. Horn. Direct Computation of 2nd-order SCF Properties of Large Molecules on Workstation Computers with an Application to Large Carbon Clusters. *Theor. Chim. Acta* **83**, 455–470 (1992).

[Herwig 96] P. Herwig, C. W. Kayser, K. Müllen, H. W. Spiess. Columnar Mesophases of Alkylated Hexa-*peri*-hexabenzocoronenes with Remarkably Large Phase Widths. *Adv. Mater.* **8**, 510–513 (1996).

[Herwig 00] P. Herwig, V. Enkelmann, O. Schmelz, K. Müllen. Synthesis and Structural Characterization of Hexa-*tert*-butyl-hexa-*peri*-hexabenzocoronene, its Radical Cation Salt and its Tricarbonylchromium Complex. *Chem. Eur. J.* **6**, 1834–1838 (2000).

[Herzfeld 80] J. Herzfeld, A. E. Berger. Sideband Intensities in NMR Spectra of Samples Spinning at the Magic Angle. *J. Chem. Phys.* **73**, 6021–6030 (1980).

[Hing 92] A. W. Hing, S. Vega, J. Schaefer. Transferred-Echo Double-Resonance NMR. *J. Magn. Reson.* **96**, 205–209 (1992).

[Hirschinger 91] J. Hirschinger, W. Kranig, H. W. Spiess. A Deuteron NMR Study of Axial Motion and Side Chain Conformation in the Mesophase of Discotic Liquid Crystal Main-chain Polymers. *Colloid Polym. Sci.* **269**, 993–1002 (1991).

[Hodgkinson 00] P. Hodgkinson, L. Emsley. Numerical Simulation of Solid-state NMR Experiments. *Progr. NMR Spectrosc.* **36**, 201–239 (2000).

[Hong 00] M. Hong. Solid-state NMR Determination of $^{13}C\alpha$ Chemical Shift Anisotropies for the Identification of Protein Secondary Structure. *J. Am. Chem. Soc.* **122**, 3762–3770 (2000).

[Hore 83] P. J. Hore. Solvent Suppression in Fourier Transform Nuclear Magnetic Resonance. *J. Magn. Res.* **55**, 283–300 (1983).

[Ishii 95] Y. Ishii, J. Ashida, T. Terao. ^{13}C -^{1}H Dipolar Recoupling Dynamics in ^{13}C Multiple-pulse Solid-state NMR. *Chem. Phys. Lett.* **246**, 439–445 (1995).

[Ishimoto 99] B. Ishimoto, K. Tonan, S. Ikawa. Coupling of Intramolecular Hydrogen Bonding to the *cis*-to-*trans* Isomerization of a Proline Imide Bond of Small Model Peptides. *Spectrochimica Acta Part A* **56**, 201–209 (1999).

[Ito 00a] S. Ito, P. T. Herwig, T. Böhme, J. P. Rabe, W. Rettig, K. Müllen. Bishexa*peri*hexabenzocoronenyl: A "Superbiphenyl". *J. Am. Chem. Soc.* **122**, 7698–7706 (2000).

[Ito 00b] S. Ito, M. Wehmeier, J. D. Brand, C. Kübel, R. Epsch, J. P. Rabe, K. Müllen. Synthesis and Self-assembly of Functionalized Hexa-*peri*-hexabenzocoronenes. *Chem. Eur. J.* **6**, 4327–4342 (2000).

[Jaroniec 00] C. P. Jaroniec, B. A. Tounge, C. M. Riestra, J. Herzfeld, R. G. Griffin. Recoupling of Heteronuclear Dipolar Interactions with Rotational-Echo Double-Resonance at High Magic-Angle Spinning Frequencies. *J. Magn. Res.* **146**, 132–139 (2000).

[Kayser 99] C. W. Kayser. *Molekulare Ordnung und Dynamik verschiedener Kolumnarer Diskotischer Flüssigkristalle*. Dissertation, Universität Mainz (1999).

[Kestemont 01] G. Kestemont, V. de Halleux, M. Lehmann, D. A. Ivanov, M. Watson, Y. H. Geerts. Discotic Mesogens with Potential Electron Carrier Properties. *Chem. Commun.*pp. 2074–2075 (2001).

[Khitrin 03] A. K. Khitrin, Toshimichi Fujiwara, Hideo Akutsu. Phase-modulated Heteronuclear Decoupling in NMR of Solids. *J. Magn. Reson.* **162**, 46–53 (2003).

[Kleppinger 97] R. Kleppinger, C. P. Lillya, C. M. Yang. Discotic Liquid Crystals through Molecular Self-assembly. *J. Am. Chem. Soc.* **119**, 4097–4102 (1997).

[Kraft 99] A. Kraft, F. Osterod, R. Fröhlich. Bidirectional Association of Branched Non-covalent Complexes of Tetrazoles and 1,3,5-Tris(4,5-dihydroimidazol-2-yl)benzene in Solution. *J. Org. Chem.* **64**, 6425–6433 (1999).

[Kranig 90] W. Kranig, C. Boeffel, H. W. Spiess. ^{2}H NMR Studies of Phase Behavior and Molecular Motions of Doped Liquid-crystalline Systems. *Liquid Crystals* **8**, 375–388 (1990).

[Kruerke 00] D. Kruerke, N. Gough, G. Heppke, S. T. Lagerwall. Electrically Tuneable Cholesteric Mirror. *Mol. Cryst. Liquid Cryst.* **351**, 69 (2000).

[Kupce 93] E. Kupce, R. Freeman. Techniques for Multisite Excitation. *J. Magn. Res. A* **105**, 234–238 (1993).

[Langer 99] B. Langer, I. Schnell, H. W. Spiess, A.-R. Grimmer. Temperature Calibration under Ultrafast MAS Conditions. *J. Magn. Reson.* **138**, 182–186 (1999).

[Langer 01] B. Langer. *Untersuchung supramolekularer Ordnungsphänomene mittels* ^{1}*H-MAS-Mehrquanten-NMR-Spektroskopie in festen und in flüssigkristallinen Phasen*. Dissertation, Universität Mainz (2001).

[Lee 95] Y. K. Lee, N. D. Kurur, M. Helmle, O. G. Johannessen, N. C. Nielsen, M. H. Levitt. Efficient Dipolar Recoupling in the NMR of Rotating Solids. A Sevenfold Symmetric Radiofrequency Pulse Sequence. *Chem. Phys. Lett.* **242**, 304–309 (1995).

[Lee 02] C. J. Lee, S. J. Lee, J. Y. Chang. Synthesis of a Polymerizable Discotic Liquid Crystalline Compound with a 1,3,5-triazine Core. *Tetrahedron Lett.* **43**, 3863–3866 (2002).

[Lehmann 03] M. Lehmann, G. Kestemont, R. G. Aspe, D. A. Ivanov, R. Gearba, C. Buess-Herman, M. J. H. Koch, M. G. Dibije, J. Piris, M. P. de Haas, J. Warman, M. Watson, J. Cornil, Y. H. Geerts. *Chemistry* (2003). manuscript in preparation.

[Lehn 78] J.-M. Lehn. Cryptates - Inclusion Complexes of Macropolycyclic Receptor Molecules. *Pure Appl. Chem.* **50**, 871–892 (1978).

[Lehn 95] J.-M. Lehn. Supramolecular Chemistry. VCH, Weinheim (1995).

[Leisen 92] J. Leisen, M. Werth, C. Boeffel, H. W. Spiess. Molecular Dynamics at the Glass Transition: One Dimensional and Two-dimensional Nuclear Magnetic Resonance Studies of a Glass-forming Discotic Liquid Crystal. *J. Chem. Phys.* **97**, 3749–3759 (1992).

[Levelut 83] A. M. Levelut. Structures of Mesophases of Disc-like Molecules. *J. Chim. Phys.* **80**, 149–161 (1983).

[Lillya 85] C. P. Lillya, Y. L. N. Murthy. Discotic Twins. *Mol. Cryst. Liq. Cryst. Letters* **2**, 121–125 (1985).

[Liu 02] S.-F. Liu, K. Schmidt-Rohr. A Robust Technique for Two-dimensional Separation of Undistorted Chemical-shift Anisotropy Powder Patterns in Magic-angle-spinning NMR. *J. Magn. Res.* **155**, 15–28 (2002).

[London 37] F. London. *J. Phys. Rad.* **8**, 397 (1937).

[Long 94] J. R. Long, B. Q. Sun, A. Bowen, R. G. Griffin. Molecular dynamics and magic angle spinning NMR. *J. Am. Chem. Soc.* **116**, 11950–11956 (1994).

[Lowe 59] I. J. Lowe. Free Induction Decays of Rotating Solids. *Phys. Rev. Lett.* **2**, 285–287 (1959).

[Macho 01] V. Macho, L. Brombacher, H. W. Spiess. The NMR-WEBLAB: an Internet Approach to NMR Lineshape Analysis. *Appl. Magn. Res.* **20**, 405–432 (2001).

[Maricq 79] M. M. Maricq, J. S. Waugh. NMR in Rotating Solids. *J. Chem. Phys.* **70**, 3300–3316 (1979).

[Marion 83] D. Marion, K. Wüthrich. Application of Phase Sensitive Two-dimensional Correlated Spectroscopy (COSY) for Measurements of H-1 H-1 Spin-spin Coupling-constants in Proteins. *Biochem. Biophys. Res. Commun.* **113**, 967–974 (1983).

[Marion 89] D. Marion, M. Ikura, R. Tschudin, A. Bax. Rapid Recording of 2D NMR-Spectra without Phase Cycling- Application to the Study of Hydrogen-Exchange in Proteins. *J. Magn. Res.* **85**, 393–399 (1989).

[Mehring 83] M. Mehring. High Resolution NMR of Solids. Springer-Verlag, Berlin (1983).

[Metz 94] G. Metz, X. Wu, S. O. Smith. Ramped-Amplitude Cross Polarization in Magic-Angle-Spinning NMR. *J. Magn. Reson. A* **110**, 219–227 (1994).

[Morris 79] G. A. Morris, R. Freeman. Enhancement of Nuclear Magnetic Resonance Signals by Polarization Transfer. *J. Am. Chem. Soc.* **101**, 760–761 (1979).

[Munowitz 87] M. Munowitz, A. Pines. Principles and Applications of Multiple-Quantum NMR. *Adv. Chem. Phys.* **66**, 1–152 (1987).

[Naito 81] A. Naito, S. Ganapathy, K. Akasaka, C. A. McDowell. Chemical Shielding Tensor and ^{13}C -^{14}N Dipolar Splitting in Single Crystals of L-Alanine. *J. Chem. Phys.* **74**, 3190–3197 (1981).

[Neidhöfer 03] M. Neidhöfer. *Festkörper-NMR-Spektroskopie: Lokale Ordnungsphänomene in Flüssigkristallen und polymeren Systemen*. Dissertation, Universität Mainz (2003).

[Nielsen 94] N. C. Nielsen, H. Bilsøe, H. J. Jakobsen, M.H. Levitt. Double-quantum Homonuclear Rotary Resonance: Efficient Dipolar Recovery in Magic-angle Spinning Nuclear Magnetic Resonance. *J. Chem. Phys.* **101**, 1805–1812 (1994).

[Oas 88] T. G. Oas, R. G. Griffin, M. H. Levitt. Rotary Resonance Recoupling of Dipolar Interactions in Solid-state Nuclear Magnetic Resonance Spectroscopy. *J. Chem. Phys.* **89**, 692–695 (1988).

[Ochsenfeld 00] C. Ochsenfeld. An *ab initio* Study of the Relation between NMR Chemical Shifts and Solid-state Structures: Hexabenzocoronene Derivatives. *Phys. Chem. Chem. Phys.* **2**, 2153–2159 (2000).

[Ochsenfeld 01] C. Ochsenfeld, S. P. Brown, I. Schnell, J. Gauss, H. W. Spiess. Structure assignment in the solid state by the coupling of quantum mechanical calculations with NMR experiments: A columnar hexabenzocoronene derivative. *J. Am. Chem. Soc.* **123**, 2597–2606 (2001).

[Okazaki 00] M. Okazaki, K. Kawata, H. Nishikawa, M. Negoro. Polymerizable Discoticnematic Triphenylene Derivatives and their Application to an Optically Anisotropic Film. *Polym. Adv. Technol.* **11**, 398–403 (2000).

[Opella 77] S. J. Opella, J. S. Waugh. Two-dimensional ^{13}C NMR of Highly Oriented Polyethylene. *J. Chem. Phys.* **66**, 4919–4924 (1977).

[Paëpe 03] G. De Paëpe, D. Sakellariou, P. Hodgkinson, S. Hediger, L. Emsley. Heteronuclear Decoupling in NMR of Liquid Crystals Using Continuous Phase Modulation. *Chem. Phys. Lett.* **368**, 511–522 (2003).

[Pake 48] G. E. Pake. Nuclear Resonance Absorption in Hydrated Crystals: Fine Structure of the Proton Line. *J. Chem. Phys.* **16**, 327–336 (1948).

[Parr 89] R. G. Parr, W. Yang. Density Functional Theory of Atoms and Molecules. Oxford University Press, New York (1989).

[Percec 02] V. Percec, M. Glodde, T. K. Bera, Y. Miura, I. Shiyanovskaya, K. D. Singer, V. S. K. Balagurusamy, P. A. Heiney, I. Schnell, A. Rapp, H. W. Spiess, S. D. Hudson, H. Duan. Self-organisation of Supramolecular Helical Dendrimers into Complex Electronic Materials. *Nature* **419**, 384–387 (2002).

[Perdew 86] J. P. Perdew. Density-Functional Approximation for the Correlation-energy of the Inhomogeneous Electron-gas. *Phys. Rev. B* **33**, 8822–8824 (1986).

[Pines 72] A. Pines, W.-K. Rhim, J. S. Waugh. Homogeneous and Inhomogeneous Nuclear Spin Echos in Solids. *J. Magn. Reson.* **6**, 457–465 (1972).

[Pines 73] A. Pines, M. G. Gibby, J. S. Waugh. Proton-enhanced NMR of Dilute Spins in Solids. *J. Chem. Phys.* **59**, 569–590 (1973).

[Piotto 92] M. Piotto, V. Saudek, V. Sklenar. Gradient-tailored Excitation for Single-quantum NMR Spectroscopy of Aqueous Solutions. *J. Biomol. NMR* **2**, 661–665 (1992).

[Pisula 03] W. Pisula (2003). oral communication.

[Powles 63] J. G. Powles, J. H. Strange. Zero Time Resolution Nuclear Magnetic Transients in Solids. *Proc. Phys. Soc. Lond.* **82**, 60 (1963).

[Prins 01] L. J. Prins, D. N. Reinhoudt, P. Timmermann. Noncovalent Synthesis using Hydrogen Bonding. *Angew. Chem. Int. Ed.* **40**, 2383–2426 (2001).

[Purcell 46] E. M. Purcell, H. C. Torrey, R. V. Pound. Resonance Absorption by Nuclear Magnetic Moments in Solids. *Phys. Rev.* **69**, 37–38 (1946).

[Rose 57] M. E. Rose. Elementary Theory of Angular Momentum. Wiley, London (1957).

[Saalwächter 99] K. Saalwächter, R. Graf, H. W. Spiess. Recoupled Polarization Transfer Heteronuclear Multiple-Quantum Correlation in Solids under Ultra-fast MAS. *J. Magn. Reson.* **140**, 471–476 (1999).

[Saalwächter 00] K. Saalwächter. *Heteronuclear Recoupling Methods in Solid-State NMR* . Dissertation, Universität Mainz (2000).

[Saalwächter 01a] K. Saalwächter, R. Graf, H. W. Spiess. Recoupled Polarization-Transfer Methods for Solid-State ^{1}H-^{13}C Heteronuclear Correlation in the Limit of Fast MAS. *J. Magn. Reson.* **148**, 398–418 (2001).

[Saalwächter 01b] K. Saalwächter, H. W. Spiess. Heteronuclear ^{1}H-^{13}C Multiple-spin Correlation in Solid-state Nuclear Magnetic Resonance: Combining Rotational-echo Double-resonance Recoupling and Multiple-quantum Spectroscopy. *J. Chem. Phys.* **114**, 5707–5728 (2001).

[Saalwächter 02a] K. Saalwächter. Methyl Groups as Local Probes for Polymer Dynamics as Investigated by ^{1}H Double-Quantum Magic-Angle Spinning NMR Spectroscopy. *Chem. Phys. Lett.* **362**, 331–340 (2002).

[Saalwächter 02b] K. Saalwächter, I. Fischbach. The Application of MAS Recoupling Methods in the Intermediate Motional Regime. *J. Magn. Res.* **157**, 17–30 (2002).

[Saalwächter 02c] K. Saalwächter, I. Schnell. REDOR-based Heteronuclear Dipolar Correlation Experiments in Multi-spin Systems: Rotor-encoding, Directing and Multiple Distance and Angle Determination. *Solid State Nucl. Magn. Res.* **22**, 154–187 (2002).

[Salzmann 98] R. Salzmann, C. J. Ziegler, N. Godbout, M. T. McMahon, K. S. Suslick, E. Oldfield. Carbonyl Complexes of Iron(II), Ruthenium (II) and Osmium(II) 5,10,15,20-Tetraphenylporphyrinates: A comparative Investigation by X-ray Crystallography, Solid-State NMR Spectroscopy and Density Functional Theory. *J. Am. Chem. Soc.* **120**, 11323–11334 (1998).

[Samoson 03] A. Samoson, Tiit Tuherm. High performance MAS (2003). Poster contribution at the ENC 2003.

[Schäfer 92] A. Schäfer, H. Horn, R. Ahlrichs. Fully Optimized Contracted Gaussian Basis Sets for Atoms Li to Kr. *J. Chem. Phys.* **97**, 2571–2577 (1992).

[Schmidt-Mende 01] L. Schmidt-Mende, A. Fechtenkötter, K. Müllen, E. Moons, R. H. Friend, J. D. MacKenzie. Self-Organized Discotic Liquid Crystals for High-Efficiency Organic Photovoltaics. *Science* **293**, 1119–1122 (2001).

[Schmidt-Mende 02] L. Schmidt-Mende, A. Fechtenkötter, K. Müllen, R. H. Friend, J. D. MacKenzie. Efficient Organic Photovoltaics from Soluble Discotic Liquid Crystalline Materials. *Physica E* **14**, 263–267 (2002).

[Schmidt-Rohr 91] K. Schmidt-Rohr, H. W. Spiess. Chain Diffusion between Crystalline and Amorphous Regions in Polyethylene detected by 2D Exchange C-13 NMR. *Macromolecules* **24**, 5288–5293 (1991).

[Schmidt-Rohr 92] K. Schmidt-Rohr, M. Hehn, D. Schaefer, H. W. Spiess. Two-dimensional Nuclear Magnetic Resonance with Sample Flip for Characterizing Orientation Distributions, and its Analogy to X-ray Scattering. *J. Chem. Phys.* **97**, 2247–2262 (1992).

[Schmidt-Rohr 94] K. Schmidt-Rohr, H. W. Spiess. Multidimensional Solid-State NMR and Polymers. Academic Press, London (1994).

[Schmidt 86] A. Schmidt, S. O. Smith, D. P. Raleigh, J. E. Roberts, R. G. Griffin, S. Vega. Chemical Exchange Effects in the NMR Spectra of Rotating Solids. *J. Chem. Phys.* **85**, 4248–4253 (1986).

[Schnell 96] I. Schnell. *Doppelquanten-NMR-Spektroskopie an polykristallinen Phosphaten*. Diplomarbeit, Universität Mainz (1996).

[Schnell 01a] I. Schnell, B. Langer, S. H. M. Söntjens, M. H. P. van Genderen, R. P. Sijbesma, H. W. Spiess. Inverse Detection and Heteronuclear Editing in ^{1}H-$^{1}5$N Correlation and ^{1}H-^{1}H Double-quantum NMR Spectroscopy in the Solid State under Fast MAS. *J. Magn. Reson.* **150**, 57–70 (2001).

[Schnell 01b] I. Schnell, H. W. Spiess. ADVANCES IN MAGNETIC RESONANCE High-resolution ^{1}H NMR Spectroscopy in the Solid State: Very Fast Sample Rotation and Multiple-quantum Coherences. *J. Magn. Reson.* **151**, 153–227 (2001).

[Schnell 01c] I. Schnell, A. Watts, H. W. Spiess. Double-Quantum Double-Quantum MAS Exchange NMR Spectroscopy: Dipolar-Coupled Spin Pairs as Probes for Slow Molecular Dynamics. *J. Magn. Reson.* **149**, 90–102 (2001).

[Schnell 02] I. Schnell, K. Saalwächter. ^{15}N-^{1}H Bond Length Determination in Natural Abundance by Inverse Detection in Fast-MAS Solid-state NMR spectroscopy. *J. Am. Chem. Soc.* **124**, 10938–10939 (2002).

[Seguy 00] I. Seguy, P. Destruel, H. Bock. An All-columnar Bilayer Light-emitting Diode. *Synthet. Met.* **111**, 15–18 (2000).

[Sklenar 93] V. Sklenar, M. Piotto, R. Leppik, V. Saudek. Gradient-tailored Water Suppression for ^{1}H -^{15}N HSQC Experiments Optimized to Retain Full Sensitivity. *J. Magn. Reson. Ser. A* **102**, 241–245 (1993).

[Slichter 96] C. P. Slichter. Principles of Magnetic Resonance. Springer-Verlag, Berlin (1996).

[Sørensen 83] O. W. Sørensen, G. W. Eich, M. H. Levitt, G. Bodenhausen, R. R. Ernst. Product Operator Formalism for the Description of NMR Pulse Experiments. *Progr. NMR Spectrosc.* **16**, 163–192 (1983).

[Spiess 78] H. W. Spiess. Rotation of Molecules and Nuclear Spin Relaxation. In P. Diehl, E. Fluck, R. Kosfeld (eds.), NMR Basic Principles and Progress, Volume 15, pp. 55–214. Springer-Verlag, Berlin (1978).

[Spiess 80] H. W. Spiess. Deuteron Spin Alignment: A Probe for Studying Ultraslow Motions in Solids and Solid Polymers. *J. Chem. Phys.* **72**, 6755–6762 (1980).

[Spiess 81] H. W. Spiess, H. Sillescu. Solid Echoes in the Slow-Motion Region. *J. Magn. Res.* **42**, 381–389 (1981).

[Stejskal 77] E. O. Stejskal, J. Schaefer, R. A. McKay. High-Resolution, Slow-Spinning Magic-Angle Carbon-13 NMR. *J. Magn. Res.* **25**, 569–573 (1977).

[Struijk 00] C. W. Struijk, A. B. Sieval, J. E. J. Dakhorst, M. van Kijk, P. Kimkes, R. B. M. Koehorst, H. Donker, T. J. Schaafsma, S. J. Picken, A. M. van de Craats, J. M. Warman, H. Zuilhof, E. J. R. Sudhölter. Liquid Crystalline Perylene Diimides: Architecture and Charge Carrier Mobilities. *J. Am. Chem. Soc.* **122**, 11057–11066 (2000).

[Suarez 98] M. Suarez, J.-M. Lehn, S. C. Zimmermann, A. Skoulios, B. Heinrich. Supramolecular liquid crystals. Self-Assembly of a Trimeric Supramolecular Disk and its Self-Oragnization into a Columnar Discotic Mesophase. *J. Am. Chem. Soc.* **120**, 9526–9532 (1998).

[Suwelack 80] D. Suwelack, W. P. Rothwell, J. S. Waugh. Slow Molecular Motion Detected in the NMR Spectra of Rotating Solids. *J. Chem. Phys.* **73**, 2559–2569 (1980).

[Takegoshi 01] K. Takegoshi, J. Mizokami, T. Terao. ^{1}H Decoupling with Third Averaging in Solid NMR. *Chem. Phys. Lett.* **341**, 540–544 (2001).

[Tchebotareva 03] N. Tchebotareva. *Functionalized Hexa-peri-hexabenzocoronene: Synthesis and Supramolecular behavior*. Dissertation, Universität Mainz (2003).

[Thünemann 99] A. F. Thünemann, D. Ruppelt, Shunji Ito, K. Müllen. Supramolecular Architecture of a Functionalized Hexabenzocoronene and its Complex with Polyethyleneimine. *J. Mat. Chem.* **9**, 1055–1057 (1999).

[Thünemann 00] A. F. Thünemann, D. Ruppelt, C. Burger, K. Müllen. Long-range Ordered Columns of a Hexabenzo[bc,ef,hi,kl,no,qr]coronene-polysiloxane Complex: towards Molecular Nanowires. *J. Mat. Chem.* **10**, 1325–1329 (2000).

[Titman 93] J. J. Titman, S. Féaux de Lácroix, H. W. Spiess. Structure and Order in Partially Oriented Solids by Three-dimensional Magic Angle Spinning Nuclear Magnetic Resonance Spectroscopy. *J. Chem. Phys.* **98**, 3816–3826 (1993).

[Tomovic 03] Z. Tomovic, M. D. Watson, K. Müllen. Liquid-Crystals from Graphite Islands: A "Superphenalene"-based Columnar LC (2003). submitted.

[Tracz 03] A. Tracz, J. K. Jeszka, M. D. Watson, W. Pisula, K. Müllen, T. Pakula. Uniaxial Alignment of the Columnar Super-Structure of a Hexa(Alkyl)Hexa-*peri*hexabenzocoronene on Untreated Glass by Simple Solution Processing. *J. Am. Chem. Soc.* **125**, 1682–1683 (2003).

[Tycko 89] R. Tycko, G. Dabbagh, P. A. Mirau. Determination of Chemical-Shift-Anisotropy Lineshapes in a Two-Dimensional Magic-Angle-Spinning NMR Experiment. *J. Magn. Reson.* **85**, 265–274 (1989).

[Uckert 00] F. Uckert, Y.-H. Tak, K. Müllen, H. Bässler. 2,7-Poly(9-fluorenone): A Trap-Free Electron-Injection Material with a High Charge Carrier Mobility for Use in Light-Emitting Diodes. *Adv. Mater.* **12**, 905–906 (2000).

[Vallerien 90] S. U. Vallerien, M. Werth, F. Kremer, H. W. Spiess. Molecular Dynamics and the Glass Transition in a Columnar Liquid Crystal Formed by a Chiral Discotic Mesogen. *Liq. Crystals* **8**, 889–893 (1990).

[Vanderhart 81] D. L. Vanderhart, W. L. Earl, A. N. Garroway. Resolution in ^{13}C NMR of Organic Solids Using High-power Proton Decoupling and Magic-angle Sample Spinning. *J. Magn. Reson.* **44**, 361–401 (1981).

[Voelkel 88] R. Voelkel. High-Resolution Solid-State C-13-NMR Spectroscopy of Polymers. *Angew. Chem. Int. Ed. Engl.* **27**, 1468–1483 (1988).

[Wang 95] D. Wang, G. R. Hanson. A New Method for Simulating Randomly Oriented Powder Spectra: The *S*ydney *Op*era *H*ouse (SOPHE) Method. *J. Magn. Res. A* **117**, 1–8 (1995).

[Wang 03] Z. Wang (2003). manuscript in preparation.

[Wasserfallen 03] D. Wasserfallen (2003). unpublished results.

[Weitekamp 82] D. P. Weitekamp, J. R. Garbow, A. Pines. Determination of Dipole Coupling Constants Using Heteronuclear Multiple Quantum NMR. *J. Chem. Phys.* **77**, 2870–2883 (1982).

[Werth 93] M. Werth, J. Leisen, C. Boeffel, R. Y. Dong, H. W. Spiess. Mobility Changes of Side Chains Ascribed to Density Modulations along Columnar Structures Detected by 2D NMR. *J. Phys. II France* **3**, 53–67 (1993).

[Wind 02] M. Wind, K. Saalwächter, U.-M. Wiesler, K. Müllen, H. W. Spiess. Solid-state NMR Investigations of Molecular Dynamics in Polyphenylene Dendrimers: Evidence of Dense-shell Packing. *Macromolecules* **35**, 10071–10086 (2002).

[Wolinski 90] K. Wolinski, J. F. Hinton, P. Pulay. Efficient Implementation of the Gauge-independent Atomic Orbital Method for NMR Chemical-shift Calculations. *J. Am. Chem. Soc.* **112**, 8251–8260 (1990).

[Yamauchi 00] K. Yamauchi, S. Kuroki, K. Fujii, I. Ando. The Amide Proton Chemical Shift and Hydrogen-bonded Structure of Peptides and Polypeptides in the Solid State as Studied by High-frequency Solid-state NMR. *Chem. Phys. Lett.* **324**, 435–439 (2000).

[Yamauchi 02] K. Yamauchi, S. Kuroki, I. Ando. The Amide Proton Chemical Shift and Hydrogen-bonded Structure of Glycine-containing Peptides and Polypeptides in the Solid State as Studied by Multi-pulse-associated High-speed MAS ^{1}H NMR. *J. Mol. Struc.* **602**, 9–16 (2002).

[Yu 98] Y. Yu, B. M. Fung. An Efficient Broadband Decoupling Sequence for Liquid Crystals. *J. Magn. Res.* **130**, 317–320 (1998).

[Zamir 94] S. Zamir, R. Poupko, Z. Luz, B. Huser, C. Boeffel, H. Zimmermann. Molecular Ordering and Dynamics in the Columnar Mesophase of a New Dimeric Discotic Liquid Crystal as Studied by X-ray Diffraction and Deuterium NMR. *J. Am. Chem. Soc.* **116**, 1973–1980 (1994).

[Zamir 97] S. Zamir, E. J. Wachtel, H. Zimmermann, S. Dai, N. Spielberg, R. Poupko, Z. Luz. Mesomorphic and Dynamic Properties of Discotic Alkanoyloxybenzene Dimers as Studied by X-ray and NMR: The Effect of the Spacer Length. *Liquid Crystals* **23**, 689–698 (1997).

[Zannoni 94] C. Zannoni. On the description of ordering in liquid crystals. In G. R. Luckhurst, C. A. Veracini (eds.), The Molecular Dynamics of Liquid Crystals, NATO ASI Series, Volume 431, pp. 11–36. Kluwer Academic Publishers, Dordrecht, The Netherlands (1994).

[Zhao 01] X. Zhao, M. Edén, M. H. Levitt. Recoupling of Heteronuclear Dipolar Interactions in Solid-state NMR Using Symmetry-based Pulse Sequences. *Chem. Phys. Lett.* **342**, 353–361 (2001).

Acknowledgements/Danksagung

An dieser Stelle möchte ich mich herzlich bei allen bedanken, die zum Gelingen dieser Arbeit beigetragen haben und die letzten zweieinhalb Jahre zu einer schönen und abwechslungsreichen Zeit haben werden lassen. Insbesondere den vielen Kooperationspartnern aus In- und Ausland sei für die fruchtvolle Zusammenarbeit der letzten fast drei Jahre gedankt.

Aus Gründen des Datenschutzes dürfen in dieser online-veröffentlichten Version meiner Dissertation in der Danksagung keine Personen namentlich erwähnt werden. Für die ausführliche Danksagung sei an dieser Stelle daher auf die Druckversion verwiesen.